The effect of double diffusion on the dynamics of turbulent plumes and jets

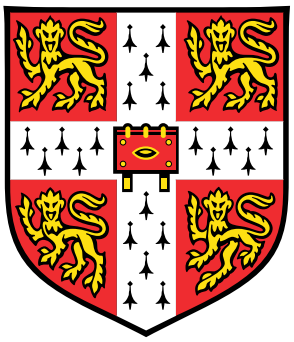

Maksim Dadonau

Supervisor: Prof. P. F. Linden

Department of Applied Mathematics and Theoretical Physics
University of Cambridge

This dissertation is submitted for the degree of
Doctor of Philosophy

Girton College

September 2020

To my mom.

Declaration

I hereby declare that except where specific reference is made to the work of others, the contents of this dissertation are original and have not been submitted in whole or in part for consideration for any other degree or qualification in this, or any other university. This dissertation is my own work and contains nothing which is the outcome of work done in collaboration with others, except as specified in the text and Acknowledgements.

Maksim Dadonau
September 2020

Acknowledgements

Most of all, I would like to thank my supervisor Professor Paul Linden for his endless guidance and encouragement over the last three (and a half) years. I am forever grateful for the numerous stimulating discussions and for all his efforts in helping me to develop both professionally and personally. His door was always open for me and I always knew that he is there to help. Thank you, Paul.

Additional very special thanks go to Dr Jamie Partridge, who was in many ways my 'junior' supervisor. I cannot thank Jamie enough for all the time he spent helping me. Whether it was a broken pump, a bug in the code or a new concept that was difficult to grasp, Jamie was always there. Thank you for the patience and the selflessness with which you dealt with me over these years.

I am also very grateful to my advisor Professor Stuart Dalziel for his continual support and advice over these years. Additionally, I would like to thank Professor Grae Worster and Professor Colm-cille Caulfield for the immensely helpful discussions we had throughout my years at DAMTP.

None of my experiments would have been possible without the wonderful laboratory technicians at the G. K. Batchelor Laboratory. In particular, I would like to thank David Page-Croft, Colin Hitch, Paul Mitton, Andrew Denson, and John Milton for their endless technical support and for making ideas turn into reality. I would also like to thank Mark Hallworth for his assistance throughout my time in the laboratory.

Without a doubt, this journey would not have been easy without my dear friends from all over the world, who gave me the energy and inspiration to keep moving forward. The very special gratitude goes to Maksimas Milta, my oldest and dearest friend, for always being there for me and supporting me throughout my academic journey. I would also like to thank Ilya Ivanitski and Bahram Ismailov for making every holiday back home a very special occasion, as well as Huseyn Mammadov and Afig Aslanov for never failing to provide a great deal of distraction over a weekend in London.

I was also very lucky to work and live alongside lots of wonderful people over my time at Cambridge. Thank you, Amalia Thomas, Ben Jackson, Botty Dimanov, David Parker, Emily Kruger, Jenny Leivadarou, Jonny Tsang, Kanwar Singh, Katherine Grayson and Rajesh Bhagat for making my time at Cambridge so very special.

Finally, I would like to thank Bill & Melinda Gates Foundation and the Gates Cambridge Trust for granting me this opportunity to pursue my research interests and for providing with the support and care I needed to focus on my studies.

Abstract

This thesis presents the experimental investigation of the effect of double diffusion on the dynamics of turbulent plumes and jets. Although it consists of seven distinct chapters, the work presented here can be broadly broken down into two parts.

The first part addresses the effect of double diffusion on the rate of entrainment in turbulent plumes in the salt-fingering configuration. Plumes over a range of source buoyancy fluxes B_0 and source density ratios R_ρ are examined experimentally using two experimental methods. The first method is based on the filling-box technique introduced by Baines (1983), which allows the plume volume flux to be measured directly. The second method uses PIV and LIF to obtain simultaneous two-dimensional measurements of the velocity and scalar fields within the flow. The results obtained using both techniques reveal that when the plumes are double-diffusive ($R_\rho > 0$) the rate of turbulent entrainment is not constant, with an up to 20% reduction in the value of the entrainment coefficient from the value found for single-diffusive plumes, i.e. plumes with $R_\rho = 0$. The scale of reduction is found to be in direct relation to the source density ratio and is inversely related to the distance travelled by the plume, indicating that double-diffusive effects decrease as the plume evolves. Ultimately, double-diffusive plumes attain self-similarity and resemble the behaviour of single-diffusive plumes. We propose an explanation for the observed reduction in the entrainment coefficient on the basis of differential diffusion hindering large-scale engulfment at the edge of the plume.

For the second part, we investigate the effect of double diffusion on the dynamics of initially neutrally-buoyant warm and salty turbulent jets discharged horizontally into stationary cooler freshwater ambient. Jets over a range of source Reynolds numbers and source temperature/salinity combinations are examined. In all cases, we observed sinking jet trajectories and the formation of salt fingers along the lower surface. Increasing the source concentration of both scalar properties led to more pronounced jet sinking trajectories and earlier formation of salt fingers, demonstrating the significance of the double-diffusive processes. We propose that is it the differential double-diffusive fluxes across the jet-ambient turbulent/non-turbulent interfaces that causes the build-up of negative buoyancy and hence the sinking motion. In addition, we make predictions on the onset point of the salt fingers based on the balance between diffusive processes and the jet entrainment, and compare them with the experimental observations.

Table of contents

Nomenclature

Roman Symbols

B	Buoyancy flux	$[L^4T^{-3}]$
b	Plume/jet radius	$[L]$
g	Gravitational acceleration	$[LT^{-2}]$
g'	Buoyancy	$[LT^{-2}]$
Fr	Froude number	$[-]$
Le	Lewis number	$[-]$
M	Momentum flux	$[L^4T^{-2}]$
m	Mass	$[L^4T^{-2}]$
N	Buoyancy frequency	$[T^{-1}]$
Nu	Nusselt number	$[-]$
p	Pressure	$[ML^{-1}T^{-2}]$
Pr	Prandtl number	$[-]$
Q	Volume flux	$[L^3T^{-1}]$
R	Stability ratio	$[-]$
r	Radial co-ordinate	$[L]$
Ra	Rayleigh number	$[-]$
Re	Reynolds number	$[-]$

Ri	Richardson number	$[-]$
Sc	Schmidt number	$[-]$
T	Temperature	$[\Theta]$
t	Time	$[T]$
u	Radial velocity component	$[LT^{-1}]$
w	Streamwise velocity component	$[LT^{-1}]$
V	Volume	$[L^3]$
z_{vo}	Virtual origin correction	$[L]$

Greek Symbols

α	Entrainment coefficient	$[-]$
β	Volumetric expansion coefficient	$[-]$
η_B	Batchelor length scale	L
η_K	Kolmogorov length scale	L
Γ	Plume Richardson number	$[-]$
γ	Double-diffusive flux ratio	$[-]$
κ	Coefficient of molecular diffusivity	$[L^2T^{-1}]$
μ	Kinematic viscosity	$[L^2T^{-1}]$
∇	Gradient operator	$[L^{-1}]$
ν	Dynamic viscosity	$[ML^{-1}T^{-1}]$
ρ	Plume/jet density	$[ML^{-3}]$
ρ_a	Ambient density	$[ML^{-3}]$
ρ_r	Reference density	$[ML^{-3}]$
τ	Non-dimensional time scale	$[-]$
ω	Vorticity	$[T^{-1}]$

Chapter 1

Introduction

1.1 Buoyant flows

From the great diversity of fluid flows that we encounter every day in our lives an astonishing variety are induced by buoyancy. The buoyancy force, which drives the fluid motion, arises from the density differences, which in turn originate from inhomogeneities in various properties, most commonly temperature and concentration of chemical species. Buoyancy-driven flows can be found everywhere and at all scales, from within the molten Earth's core, to our oceans, lakes and atmosphere. Specific examples include the descending motions of downdrafts in the atmosphere, the rise and fall of volcanic ash clouds, or the propagation of smoke in free or enclosed spaces (Hunt, 1991). The ability to accurately predict the mixing and ultimate state of the released fluid in these and other relevant scenarios is critical in environmental and industrial applications. Considerable research attention has therefore been paid to the dynamics of turbulent buoyant releases in a variety of flow configurations.

Depending on the force fields, flow geometries and boundary conditions, there are a multiplicity of buoyancy-driven flows, including gravity currents, thermals, and arguably the two most common: plumes and buoyant jets. It is these two types of free shear flows that will be the focus of this study, which explores the dynamics of turbulent plumes and jets under the influence of double-diffusive processes.

Below we provide a brief account of jets and plumes, outlining their characteristic features, similarities and distinctions. A brief summary of the mechanism of turbulent entainment and the basics of double-diffusive convection are laid out in sections 1.2.2 and 1.3, respectively. An overview of a rather limited relevant literature on double-diffusive plumes and jets is presented in section 1.4. We conclude this Chapter by formulating the problem and the key objectives for this work in section 1.5.

1.2 Plumes & jets

(a)

(b)

Fig. 1.1 Photographs of: (a) thermal plume generated by a fire that destroyed Barcelona's Gran Teatro del Liceo (from Time, February 14, 1994. Courtesy of Gamma-Imaginechina); (b) high-Reynolds-number turbulent jet produced by the test of a rocket (courtesy of Lockheed Martin).

1.2.1 Background

Plumes are convective flows with predominantly vertical motion, which occur whenever buoyant fluid is persistently released from a localised source. In an ideal case of a pure plume, motion is driven by the buoyancy force alone. In contrast, pure jets originate from localised continuous sources of momentum. Although visual features of plumes and jets are rather similar, with examples of both shown in figures 1.1a and 1.1b respectively, their motions originate from and are driven by these two different mechanisms. That is, perhaps, the main distinction between these two types of flows.

Plumes and jets are common in a wide variety of natural and industrial circumstances, with their length scales ranging over several orders of magnitude. In most cases of practical interest plumes and jets are turbulent, exhibiting chaotic motion and having a high Reynolds number $Re = UL/\nu$, where U is a velocity scale of the plume/jet, L a characteristic length scale, e.g. the plume/jet radius, and ν the kinematic viscosity of the fluid. In nature, examples of turbulent plumes include, but are not limited to, seafloor hydrothermal vents, known as 'black-smokers', plumes of freshwater formed by melting of glaciers and icebergs and, most energetic of all,

plumes due to explosive volcanic eruptions (Carazzo et al., 2006). Recent examples of rather dramatic environmental events involving plumes are the eruption of the Icelandic volcano Eyjafjallajökull in 2010 and the Deepwater Horizon oil leak in the Gulf of Mexico in the same year (Burridge et al., 2016). In some extreme cases, plumes can be formed by large explosions or nuclear accidents (Hunt and Van den Bremer, 2010). Examples of turbulent jets due to industrial human activities include jet engines discharging hot gas into the atmosphere and effluent from submerged cooling water outlets of fossil-fuelled power plants.

Pure plumes and jets have received considerable research attention since 1930s. In one of the earliest studies, Schmidt (1941) proposed similarity solutions for steady plumes. Earlier still, Tollmien (1926) had developed similarity solutions for a pure turbulent jet. A little later, Priestley and Ball (1955) developed a plume model based on energy conservation of the mean flow. At around the same time, Morton et al. (1956) developed similarity solutions for pure plumes on the basis of conservation of volume, momentum and buoyancy.

Although of great theoretical interest, the idealised cases considered in these studies are rather uncommon. In particular, in the aforementioned real world scenarios, plumes are rarely driven by the buoyancy force alone. Similarly, it is rather uncommon to encounter a pure jet flow, with no buoyant scalar component within it. Instead, in most practical cases, plume/jet flows are driven by some combination of both buoyancy and momentum. Such flows are commonly termed 'forced plumes' or 'buoyant jets'. These less idealistic fluid flows are normally differentiated on the basis of a flux-balance parameter introduced by Morton (1959), quantifying the balance between buoyancy and momentum, with purely buoyant plumes and pure momentum jets being the two limiting states. One example of a buoyant jet is the discharge of thermal effluent from a steam-electric power plant. The effluent is often warmer and thus lighter than the water in the reservoir it is discharged into, resulting in a rising jet motion. The ability to predict the evolution and ultimate fate of buoyant jet fluid is of crucial importance for ecological, environmental and industrial reasons, and has motivated various authors to investigate the dynamics of buoyant jets theoretically (Chen and Rodi, 1980; Hirst, 1971; Jirka, 2004) and experimentally (Bloomfield and Kerr, 2002; Lane-Serff et al., 1993; Roberts et al., 1997).

Common to both plumes and jets is the process of turbulent entrainment of ambient fluid into the flow. The entrainment process largely determines the dynamics of a jet/plume, and therefore is discussed in detail in the next section. For a basic

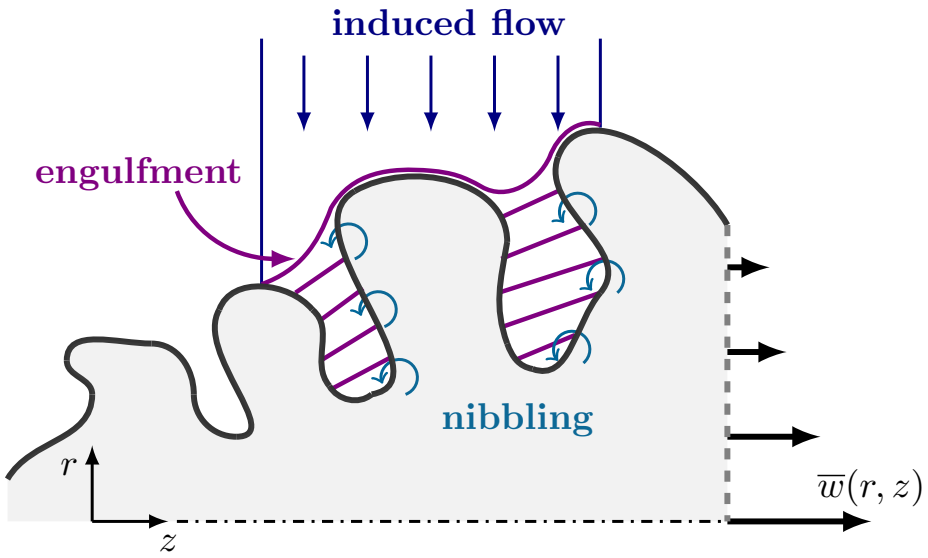

Fig. 1.2 A schematic representation of the entrainment mechanism in a turbulent plume/jet. In this figure $\overline{w}(r,z)$ represents schematically the profile of time-average streamwise velocity.

mathematical description of plume and jet flows, the reader is referred to sections 2.7 and 2.8, respectively.

1.2.2 Turbulent entrainment

Turbulent plumes and jets are characterised by the presence of strong eddying motions occurring at various length and time scales. These turbulent eddies interact with each other and the surrounding fluid, causing the gradual advancement of turbulent flow into the non-turbulent ambient fluid via the process of turbulent entrainment.

Turbulent entrainment in jets and plumes is generally believed to be a multiple-stage process (Turner 1986; Philip and Marusic 2012), as illustrated schematically in figure 1.2. Considering the instantaneous region between the two vertical blue lines, the non-turbulent ambient fluid is first induced towards the turbulent boundary of a plume/jet and engulfed by the motions of large-scale eddies. The engulfed fluid, shown as the shaded regions in the figure, is then 'nibbled' across the turbulent/non-turbulent interface (TNTI) by the action of viscous diffusion of small-scale eddies and is thereby made turbulent.

Although it is generally agreed that both large- and small-scale processes play an important role in the process of turbulent entrainment, there exists an on-going debate on which of the two is the dominant mechanism. Contradictory to the results

in support of 'nibbling' obtained in some recent numerical simulations (Mathew and Basu, 2002) and experiments (Westerweel et al., 2005), a significant amount of early (Gartshore 1966; Townsend 1970; Brown and Roshko 1974) and recent (Burridge et al., 2017) experimental studies suggest that engulfment is the dominant process.

For most practical applications, the variety of scales present in the process of turbulent entrainment makes it impossible (at the current stage) to fully resolve the entrainment process. This in turn, creates the need for effective entrainment modelling techniques. The classical approach to modelling turbulent entrainment, formulated by Morton et al. (1956), takes the profiles of time-averaged vertical velocity (and buoyancy force in the case of a plume) in horizontal sections of turbulent plumes/jets to be of similar form at all heights from the source. From this hypothesis of geometric self-similarity, it follows that in a uniform environment the rate of entrainment at the edge of turbulent plumes/jets is a constant fraction of some characteristic velocity at that height, called the 'entrainment coefficient' α. The development and applications of this entrainment assumption to various geophysical flows is discussed in depth by Turner (1986). To date, the exact numerical value of α cannot be obtained theoretically and has to be determined from other considerations, such as laboratory experiments or numerical simulations.

Determination of the numerical value of the entrainment constant for turbulent jet and plumes has received continuous attention over the past 65 years. The reported values from various experimental investigations, aggregated from Linden (2000) and Carazzo et al. (2006), are presented in table 1.1. These measurements show that under the top-hat representation, for which plume/jet properties are taken to be constant within the plume and zero outside, the typical ranges of values for α_T in jets and plumes are $0.065 < \alpha_T^j < 0.084$ and $0.10 < \alpha_T^p < 0.16$, respectively. The origin of this rather high variability remains unexplained. Among the commonly suggested reasons for such large discrepancies are the differences between measurement techniques, the nature of fluids and the particular geometries of the nozzles used (Carazzo et al., 2006). To the contrary, George (1989) argued that the differences in the measured values of α should not be attributed to the experimental errors, but instead explained by the inability of the concept of universal self-similarity to capture the multiplicity of self-preserving states determined by initial conditions. Despite the scatter, previous experimental measurements strongly suggest that $\alpha^p > \alpha^j$. The systematic difference between the entrainment values measured for jets and plumes suggests that it is likely to be caused by buoyancy-enhanced turbulence (List 1982; Kaminski et al. 2005).

Study	Flow	Fluid	Method	α_T
Forstall and Gaylord (1955)	J	L	w	0.070
Wang and Law (2002)	J	L	l	0.075
Papanicolaou and List (1988)	J	L	l	0.074
Rosensweig et al. (1961)	J	G	w	0.076
Panchapakesan and Lumley (1993)	J	G	w	0.095
Ruden (1933)	J	G	w	0.070
Papanicolaou and List (1988)	P	L	l	0.124
Wang and Law (2002)	P	L	l	0.124
Rouse et al. (1952)	P	G	w	0.120
George et al. (1977)	P	G	w	0.159
Shabbir and George (1994)	P	G	w	0.154
Baines (1983)	P	L	f	0.104
Ezzamel et al. (2015)	P	G	p	0.141
Nakagome and Hirata (1980)	P	-	-	0.170

Table 1.1 Experimentally measured values of the 'top-hat' entrainment coefficient for plumes and jets, aggregated from Linden (2000) and Carazzo et al. (2006). Flow: J = jet, P = plume; Fluid: L = liquid, G = gas; Method: w = hot-wire probe anemometers; l = laser-Doppler anemometry and laser-induced fluorescence concentration technique; p = particle image velocimetry; f = 'filling-box' technique by Baines (1983).

1.2.3 Origin of buoyancy

In many cases, the density difference, which gives rise to the buoyancy force that drives the plume/buoyant jet fluid motion, originates from the difference in concentration of only one scalar quantity, e.g. temperature or salinity. In this thesis, we refer to such flows as 'single-diffusive'. However, it is not uncommon for a plume/jet fluid to contain two (or more) scalar components which contribute to its density and diffuse at different rates, e.g. heat and salt. We refer to such flows as 'double diffusive', with one example being a plume of freshwater rising along a wall of a melting iceberg. The plume is double diffusive since the freshwater produced is normally colder than the saline ocean water and thus is different in both temperature and salinity. An example of a double-diffusive plume in an industrial context is the discharge of waste brine from a seawater desalination facility into the ocean (Del Bene et al., 1994). The injected brine is double-diffusive as it is typically warmer and saltier than the ambient ocean. Given that the purpose of this work is to investigate the effect of double diffusion on the dynamics of turbulent plumes/jets, we now turn to a brief overview of the field of double-diffusive convection.

1.3 Double-diffusive convection

The existence of an overall statically stable density distribution does not guarantee stability in a fluid system that consists of multiple scalar properties (Turner, 1979). Double-diffusive convection may occur if the density field is produced by two or more components with different molecular diffusivities (e.g. heat and salt), which make opposing contributions to the vertical density gradient (Huppert and Turner 1981; Hunt and Linden 2001a). This comparatively recent field of fluid mechanics was originally motivated by oceanographic field observations of layered thermohaline structures, and was later extended to applications in geology, metallurgy and astrophysics. As part of the early attempts to explain the nature of nearly discontinuous thermohaline oceanic structures, a number of theoretical and experimental studies have been performed. In one of the first experimental studies on the subject, Turner and Stommel (1964) observed various instabilities, arising in an initially hydrodynamically stable liquid column, but in which a stable gradient in one property (salinity or temperature) was counteracted by the distribution of the other property. Their experiments revealed that depending on whether the faster or slower component is unstably distributed, double diffusive processes can lead to two distinct types of instabilities. These two distinct cases are described in detail below.

1.3.1 Diffusive convection

In the situation where the faster diffusing component (T) is unstably distributed (e.g. when a layer of cold fresh water lies above warm salty water), the so-called 'diffusive' configuration is formed. Such a case was first considered on theoretical grounds by Stern (1960), and was for the first time observed experimentally by Turner and Stommel (1964). Their experiments showed that water, stabilised by an initially smooth linear salt gradient and then heated from below, convects in layers which are separated by thin stable interfaces. The layers formed through a turbulent convective mechanism, sustained by a more rapid vertical diffusive transport of heat relative to salt, and referred to as 'diffusive convection'. The thin interfaces that separated these layers were termed 'diffusive', as the heat and salt across the interfaces was transported by molecular diffusion alone. Diffusive interfaces can be frequently found in the oceans, for example where cold, Arctic water formed by the melting of sea ice interacts with the warmer, saltier water from the Atlantic (Schmitt, 1994). They can also be found during replenishment of some magma chambers Turner and Campbell (1986) and within industrial solar ponds (Newell and Boehm, 1982).

The phenomenological processes driving convection across the diffusive interface were described by Turner (1965), with the general idea that heat and salt are transferred by conduction until breaking of a wave occurs, followed by mixing through molecular processes. In this process, buoyancy associated with the temperature field is used to lift the salt elements. In line with Turner's view, later, Linden and Shirtcliffe (1978) proposed a theory in which heat and salt are diffused across a stable core region between the two layers and are carried away by convective elements that periodically break away from the edge of the core. Their model, which extended ideas proposed by Howard (1964) for high-Rayleigh-number convection, centres on the idea of a cyclical process, in which the boundary layers separating the diffusive core from the well-mixed layers grow by diffusion until a local critical Rayleigh number is exceeded, causing eruption and restoring the layers to their initial state. In general, among other factors, the dynamics of double-diffusive processes depends on the parameter $R_\rho = \beta_T \Delta T / \beta_S \Delta S$, commonly referred to as 'density' or 'stability' ratio, where β_T and β_S are the expansion coefficients for the faster-diffusing component T and the slower-diffusing component S, respectively and Δ refers to the difference in the quantity with respect to the ambient. Note that throughout this thesis we will follow the convention of $R_\rho = \beta_T \Delta T / \beta_S \Delta S = 1/R_\rho^*$. Linden and Shirtcliffe (1978) suggested that at large values of the density ratio R_ρ, where $\beta_T \Delta T$ and $\beta_S \Delta S$ are relative effects of temperature and salt on the total departure from a reference fluid density ρ_r, the cyclical eruption cannot return the layers to their initial state, leading to a build-up of heat and salt at the edges of the diffusive core, which cannot be removed by convection.

Within a certain range of governing parameters, diffusive processes can lead to an oscillatory diffusive instability. This range is narrow, owing to the fact that oscillatory modes can be easily damped by viscous drag (Linden, 2000). The process leading to an instability is described as follows. Consider a two-layered stratification with a layer of warm and salty fluid below one which is cold and fresh. Imagine a small parcel of warm and salty fluid displaced vertically upwards into the ambient which is fresh and cold. Heat will diffuse away from the parcel much faster than salt, leading to a build-up of negative buoyancy within the parcel. Reaching its terminal displacement, the negative buoyancy will generate vertical motion in the direction opposite to the initial perturbation. Upon its return to the original position, the parcel will find itself heavier than its surroundings, as well as itself originally. Thus, on its return to the initial position, the parcel experienced a buoyancy force greater than on its way up. This difference provides the parcel with some extra energy, making it overshoot its original equilibrium position. Below the equilibrium level, the parcel again quickly regains

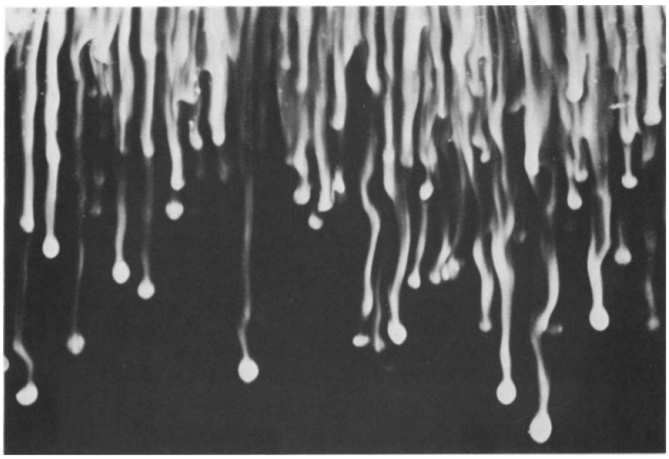

Fig. 1.3 A field of salt fingers formed by setting up a stable temperature gradient and pouring salt solution on top (Huppert and Turner, 1981).

temperature but not salinity, making it now fresher and therefore lighter than the surrounding fluid. In a similar fashion, gravity forces it upwards, the parcel overshoots, and the process repeats. The energy gained by the particle during each cycle leads to a gradual growth of the amplitude of oscillations, resulting in the so-called 'overstable' mode of instability.

1.3.2 Salt-fingering convection

The first hints of the possibility of convection in the opposite configuration to that described above were laid out by Stommel et al. (1956) in their work on the perpetual salt fountain. The authors realised that if a narrow heat-conducting pipe was inserted into a tank with a linear stratification of stable temperature and unstable salt, a salt fountain can be formed. The proposed explanation was that heat conduction through the pipe walls would rapidly equillibrate the temperature of water inside the pipe, while keeping it fresher (and therefore lighter) in the absence of salt diffusion. Shortly after, Stern (1960) realised that the presence of a physical boundary stopping salt diffusion is not a necessary condition, and that an instability can arise due to the difference between the molecular diffusivities of salt and temperature, as explained below.

Consider a two-layered stratification with warm and salty water lying on top of a cold and fresh layer. If a small parcel of warm salty fluid is perturbed to find itself in the lower layer, both heat and salt diffusion across its interface will ensue. The $O(100)$ times faster temperature diffusion will lead to rapid adjustment of the parcel temperature to that of its surroundings, but it will still retain most of its salt. The

parcel therefore ends up being denser than the ambient fluid and will start to sink. At the same time the adjacent fluid parcel raised into the upper layer will continue rising, as it will continue gaining heat but remain relatively fresh. In this manner, lateral diffusion processes will induce horizontal density variations, leading to convection in the form of 'salt fingers', shown in figure 1.3.

The diffusive nature of the origin of salt fingers implies that the spatial scale of convection cells is controlled by the diffusivity of the faster-diffusing component. This was confirmed by Stern using linear growth-rate calculations, showing that the fastest-growing convective cells are tall and thin. The obtained lengthscale of the salt fingers was based on the balance between the destabilising diffusive processes and stabilising viscous effects. Qualitatively, wide fingers do not lose enough heat laterally to fully engage double-diffusive mechanics and therefore they cannot grow as fast as intermediate width fingers. Overly thin fingers are damped by viscosity and ultimately by salt diffusion.

Visual observations (similar to that presented in figure 1.3) confirm that salt fingers normally take the form of long narrow convection cells moving alternately up and down through the fluid. The first indication of such finger structures came from an experiment of Stommel and Faller, cited in Stern (1960). Later, in an experimental study with two homogeneous layers of liquid, Turner (1967) presented an experimental photograph, which gave a good indication of the columnar nature of the salt fingers. Turner's experiment was performed with heat and salt and the two diffusing components. Only a few years later, Stern and Turner (1969) noted that the same phenomenon would occur if the fluid consisted of two solutes with much closer molecular diffusivities (e.g. sugar above a salt solution). Shirtcliffe and Turner (1970) obtained shadowgraphs showing the planforms of the fingers which existed between a layer of sugar solution above a layer of salt solution.

An important factor that may hinder the development and subsequent motion of salt fingers is turbulence. Motivated by the observations of layered structures in the ocean, where turbulence levels are generally high, Linden (1971) posed a question of whether salt finger convection may be altered by the presence of turbulence. In search for an answer, he investigated the nature of salt finger convection exposed to grid-generated turbulence within a two-layered stratification in a salt-fingering configuration within a tank containing stirring grids. His finding showed that unsteady shearing, produced by stirring on both sides of the interface, can rapidly disrupt the fingering interface, leading to a decrease of the vertical salt flux. An extension to this result was made by Linden (1974), where he performed a similar investigation in presence of a steady

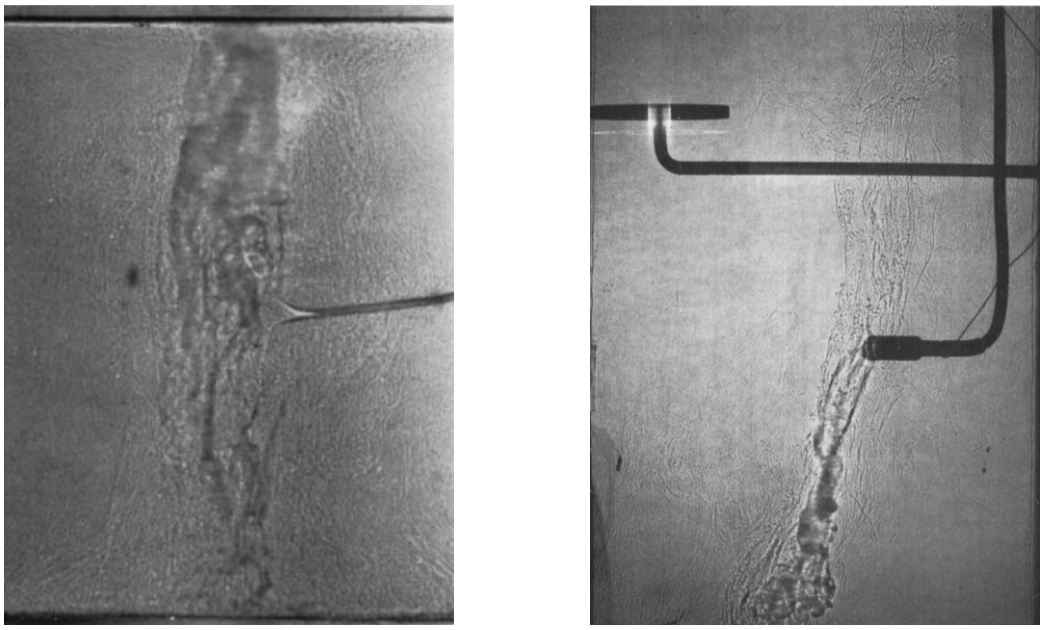

(a) (b)

Fig. 1.4 Shadowgraph photographs of two experiments with double-diffusive plumes, both of which developed vigorous convective motions both upwards and downwards: (a) photograph of a neutrally-buoyant sugar plume flowing into a homogeneous salt environment (Turner and Chen, 1974); (b) photograph of a slightly denser ($\Delta\rho \simeq 1\,\mathrm{kg\,m^{-3}}$) salt solution flowing into a sugar solution (McDougall, 1983).

shear flow. He showed theoretically and experimentally that a steady shear across a finger interface changes the fingers into two-dimensional sheets aligned with the shear. Experimental measurements showed that the flux of salt through the fingers is nearly unaffected by the steady shear, implying that the two-dimensional sheets are as efficient transporters of salt as the salt fingers. This result, has to be contrasted with experiments conducted in presence of unsteady shear.

1.4 Double-diffusive plumes and jets

Given their commonality, it is somewhat surprising that, unlike single-diffusive plumes and jets, details of which have been studied in considerable detail, availability of literature on their double-diffusive equivalents is rather limited: we have found no studies addressing the dynamics of entrainment in turbulent double-diffusive plumes, and only a few works on related phenomena in plumes and jets, which are described below. This gap in the literature could be the result of the extrapolation of a widespread assumption that for flows at high Reynolds numbers and Péclet numbers ($Pe = UL/\kappa$,

where κ is molecular diffusivity), slow molecular diffusive processes have little effect on the overall dynamics of the flow (Hunt and Van den Bremer, 2010). Although this assumption is valid for single-diffusive turbulent flows, demonstrated through previously noted agreement between heat-only and salt-only turbulent plumes at various scales (Briggs, 1982), as will be shown later in this work, double diffusion can have a considerable effect on the dynamics of turbulent free shear flows.

Turner and Chen (1974) conducted a series of exploratory, mostly qualitative, laboratory experiments, among which were, to the best of my knowledge, the first experiments with a double-diffusive plume. These involved horizontal injections of a sugar solution through a small (2 mm diameter) nozzle positioned at the mid-depth of the experimental tank into an initially homogeneous salt solution of the same nominal density. In this configuration, the faster-diffusing component T is salt and the slower-diffusing component S is sugar. Despite the slow injection flow rate, which in the case of salt-fresh water system would produce a laminar flow, the observed behaviour was significantly more violent. In particular, under the action of double-diffusive processes, the plume 'split' into two vertical motions, both upwards and downwards. The authors attributed this observation to the differences in molecular diffusivities of salt and sugar. In particular, they reasoned that the faster diffusion of ambient salt into the plume fluid was making the latter heavier, while the immediate surroundings were becoming lighter. This, in turn, rapidly generated vertical plume motions in opposite directions. Turbulence, developing in the plumes, acted to increase the concentration gradients and thus the rates of diffusion, further strengthening their vertical motions.

Later, McDougall (1983) conducted a similar, but more comprehensive experimental study (i.e. the buoyancy flux from the source was non-zero), in which the behaviour of heat-salt and salt-sugar doubly-diffusive plumes and their surroundings in confined and unconfined environments was investigated. The first part of his study addressed the influence of double-diffusive convection on the turbulent plume itself. For the qualitative description of plume behaviour, the author adopted a 'parcel argument', in which he assumed that although buoyancy is the driver of plume motion, the plume fluid parcels can exchange their scalar properties with the environment, leading to changes in their buoyancy. In some particular configurations with an unstable distribution of the faster-diffusing component, the action of double-diffusion reversed the initial buoyancy of a fluid parcel, making it move in the opposite direction to that of the main plume. McDougall (1983) captured this striking feature during a release of a slightly denser salt plume into sugar solution (see figure 1.4a).

Turner and Veronis (2000) studied experimentally the two-dimensional double-diffusive processes, motivated by the observations of layering and intrusions in the ocean reported by Schmitt (1994) and Carmack et al. (1997). Motivated to provide some explanation for some of the effects observed in a series of their experiments, the authors performed experiments with a plume of sugar flowing slowly into a homogenous salt solution. Their result, once again confirmed the earlier observations of plume splitting and motivated Turner to perform a more structured sequence of investigations, covering a wider range of possible plume/ambient configurations.

Consequently, Turner (2001) conducted laboratory experiments in which sugar plumes were fed into a homogeneous tank of salt solution, and salt plumes into a sugar solution, over a range of density ratios R_ρ. The experimental tank was fitted with a partition at mid-depth, which could be closed at the end of a known period of input so that the concentration changes above and below the source could be deduced. The resulting upward and downward transports of the two properties were thereby measured directly in both cases. The authors found large differences between the upward and downward transport of the two properties, which was again attributed to the difference in the rates of diffusion of salt and sugar in and out of the plumes, and to the subsequent transports through the interfaces that formed as the plumes spread out along the top and bottom boundaries.

The preliminary results of Turner (2001) were extended later in Turner (2003), where additional experiments were carried out to complement the existing measurements. The author concluded that sugar and salt plumes flowing into a homogeneous tank of the other solution with a small difference in density produce systematically different vertical transports. These results were depicted graphically and the reader is referred to Turner (2003) for details. In a particular case of density ratio $R_\rho = \beta_T \Delta T / \beta_S \Delta S$ close to 1, a salt plume produced nearly equal upward and downward transports of salt, whereas at the same density ratio a sugar plume experienced a much larger downward flux of sugar. Equal upward and downward transports of sugar occurred only when the sugar plume was substantially lighter than the ambient fluid in the tank.

In addition to investigating the dynamics of double-diffusive plumes, McDougall (1983) also studied the double-diffusive filling-box process, where a negatively buoyant plume was flowing into a confined environment from above. Here the author investigated double-diffusive convection within the environment, rather than in the plume itself. One of his observations was that, in contrast with the ordinary filling-box behaviour, the plume fluid did not always reach the base of the box and instead spread out at intermediate depths. Similar behaviour was reported earlier by Turner (1978)

who observed the formation of horizontal intrusions produced by localised releases of salt or sugar into a salinity gradient. Consequently, the stratified region below the first front could break up into a series of well-mixed layers layers and sharp density interfaces. The double-diffusive nature of these layers, their interaction and the consequent interface structures were extensively studied. In addition, McDougall (1983) suggested that double-diffusive processes in the lower layer may have an effect on the upper layer, potentially reducing its density. This, in turn, could have an effect on the plume behaviour, as the plume would entrain lighter fluid initially, later to find itself surrounded by denser fluid below the first front.

In application to jets, the importance of double-diffusive processes was first demonstrated by Thangam and Chen (1981) in their experimental investigation of two-dimensional surface discharges of heated and/or saline jets into a stable salinity gradient. They observed that for the case of heated saline buoyant discharges, temperature and salinity were able to spread significantly deeper as compared to an analogous heated jet, which was attributed to the action of salt-fingering convection. More recent observation of the presence of salt fingers in turbulent double-diffusive jets was made by Law et al. (2004). In this work they also reported that initially neutrally-buoyant round jets sink and found qualitative features that inspired us to explore this topic more quantitatively. Recent developments in the field of double-diffusive jet flows focus on modelling the discharges of concentrated brine from desalination facilities, where one of the major concerns is the localised increase in salinity of the near-field seawater due to poor initial mixing and consequent formation of layers inhibiting exchange of water mass (Del Bene et al., 1994).

More broadly, other related studies include the experimental investigations of double-diffusive lock-exchange flows (Yoshida et al., 1987) and gravity currents (Maxworthy, 1983). More recently, detailed numerical investigations of double-diffusive effects in gravity currents were performed by Konopliv and Meiburg (2016) and Penney and Stastna (2016).

We conclude this section by stating that although the influence of double diffusion on different aspects of plume and jet dynamics has been looked at in some detail, providing valuable insights into their behaviour, there seems to exist a significant gap in our understanding of the influence of double-diffusive processes on the dynamics of turbulent plumes and jets in a homogeneous environment. This is particularly true for double diffusive turbulent jets, which arguably have received even less research attention than plumes.

1.5 Problem formulation

The general motivation for this work is to enhance our understanding of the effect of double diffusion on turbulent free shear flows, restricting our attention to plumes and jets. To that end, we first study experimentally the role of double molecular diffusion on the dynamics of high-Péclet-number turbulent plumes. In particular, we focus on investigating the effect of double diffusion on the rate of turbulent entrainment. Previous investigations of single-diffusive plumes driven by temperature or solute concentration differences showed that, despite orders of magnitude difference in the molecular diffusivity κ of the scalar – in the case of heat or a solute in water the values of κ differ by a factor of order 100 – for high-Péclet-number $Pe = UL/\kappa$ turbulent single-diffusive plumes the rate of entrainment is a constant and independent of Pe (Partridge and Linden, 2013). However, the absence of relevant literature makes it unclear whether this constant value will remain valid for plumes which contain two scalar properties which diffuse at different rates.

Measurements are first made using the 'filling-box' technique, details of which are provided in section 3.1. These results are then complemented by high-resolution simultaneous velocity and scalar field measurements, obtained using Particle Image Velocimetry (PIV) and Laser Induced Fluorescence (LIF) techniques, respectively. Together, this part of our investigation aims to not only increase our understanding of the dynamics of turbulent double-diffusive plumes, but to potentially bring another viewpoint on the debate around the nature of the entrainment process itself, by which the irrotational fluid outside a sharp boundary of a turbulent buoyant fluid becomes rotational and is incorporated into the plume, as discussed in section 1.2.2.

In the second part of this study we investigate experimentally the effect of double diffusion on the dynamics of turbulent round jets discharged into a quiescent fresh ambient. In addition to being of relevance within the broader context of double diffusion in the presence of turbulence, this problem is of particular relevance to a number of industrial applications involving waste discharges. As mentioned earlier in this chapter, an example of such an application is the discharge of hot and salty brine from a water desalination facility into the cooler and fresher ocean water. In this particular context, the ability to predict the dynamics and ultimate fate of buoyant jet fluid is of crucial importance for near-coastal ecological and environmental considerations.

To simplify the experimental procedure and the subsequent analysis, we restrict our attention to initially neutrally-buoyant jets discharged horizontally with the only control parameters being the source scalar concentrations and the source Reynolds number.

Given the shortage of relevant literature on the subject matter, our investigation focuses on providing the answers to a number of seemingly basic questions. In particular, we examine whether double-diffusive effects are significant enough to alter the trajectory of a high-Reynolds-number and high-Péclet-number turbulent jet. Our further aim is to understand the processes leading to the observed trajectory deviations and to assess the relative importance of double-diffusive processes on the resulting jet behaviour.

Another objective of this study is to investigate whether salt-fingering and/or diffusive instabilities are able to develop along the jet-ambient interfaces. Salt fingers are of particular interest, as they could lead to significantly enhanced transport of the scalar components contained with a double-diffusive jet. This could be either desirable or undesirable, depending on the context. In the case of brine discharges, the slow-diffusing scalars would include various chemicals (such as copper and chlorine) used for water treatment at various stages of the desalination process, whose high-concentrations and premature contact with the coastal flora and fauna are definitely undesirable. It is therefore important to understand the mechanism of formation and the subsequent dynamics of both types of instabilities in the current context.

1.6 Outline

The rest of this thesis is structured as follows. Chapter 2 introduces the basic underlying theory used in our analysis. The details of the experimental techniques and apparatus used in gathering experimental data are laid out in chapter 3. Chapter 4 presents the results of direct measurements of the entrainment coefficient using emptying-filling box experimental technique, described in 3.1. Corresponding velocity and scalar field measurements of double-diffusive plumes are presented in chapter 5. Results of the investigation of double-diffusive jets are laid out in chapter 6. Finally, chapter 7 draws conclusions from this work and provides our vision for future work in this field.

At the time of submission of this thesis, the majority of the contents presented in chapter 4 had been published in the Journal of Fluid Mechanics (Dadonau, M. & Partridge, J. L.& Linden P. F. 2020 The effect of double diffusion on entrainment in turbulent plumes. *J. Fluid Mech.* 884, A6). In addition, the work presented in chapter 6 had been accepted and was, at the time, in preparation for publication in the Journal of Fluid Mechanics. A third paper on the basis of the findings presented in chapter 5 was in preparation.

Chapter 2

Fundamentals

This chapter introduces the fundamental concepts and governing equations relevant to the problem outlined in chapter 1 and studied in chapters 4, 5 and 6. An outline of the buoyancy force and the governing equations for fluid flow are presented first. We then introduce the non-dimensional parameters relevant to turbulent buoyant flows, providing their physical meaning, as these will be referred to frequently in the discussion of results. The chapter then proceeds to a brief derivation of the governing equations for plumes and jets. Finally, we provide a short outline of previous measurements of the fluxes across double-diffusive interfaces.

2.1 Buoyancy force

Given that this work is primarily focused on buoyant fluid flows, the terms 'buoyancy' and 'buoyant force' will arise frequently in our discussions, and hence it is necessary to provide a sound definition of what they are physically and mathematically.

Consider a parcel of fluid, shown pictorially in figure 2.1, whose density ρ depends on temperature T, the concentration of some scalar component S, and on the static pressure p, that is $\rho(T, S, p)$. In a gravitational field of strength $\mathbf{g}$, a local region of density ρ, surrounded by a quiescent ambient environment of higher density ρ_a, will be subject to an upward buoyancy force $\mathbf{B}$. Under the condition that this buoyancy force is able to overcome the retarding viscous forces and diffusive processes, the fluid element will be set in motion. This motion arises from the imbalance between the hydrostatic pressure gradient in the ambient $dp_a/dz = -\rho_a g$ and the localised pressure variations $dp/dz = -\rho g$ in the region of lower density ρ. The difference in the pressure gradients induces a buoyancy force, which drives fluid motion. Positive density differences result in vertical rising motion, whereas negative density difference results in sinking.

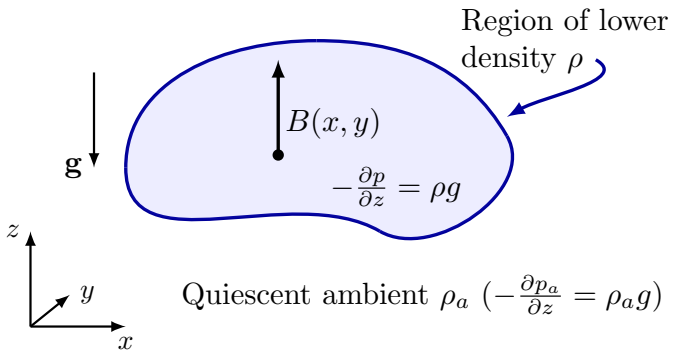

Fig. 2.1 A schematic representation of a finite fluid element of density ρ in a uniform stationary ambient of density ρ_a.

The magnitude of the buoyancy force per unit volume is calculated as $B = g(\rho_a - \rho)$, which is the difference between two body forces. The normal convention is to take B as positive if it, and hence the resulting flow, is upward. However, since most of the flows we will be describing in this work are negatively buoyant, for convenience we will change the definition of the buoyancy force to $B = g(\rho - \rho_a)$. Under this new definition, the buoyancy force resulting in downward motion is positive and this convention is used herein.

The modified gravitational acceleration g', commonly referred to as the 'reduced gravity' or 'buoyancy', quantifies the buoyancy force per unit mass and is defined as

$$g' = g\frac{\rho - \rho_r}{\rho_r} = g\frac{\Delta\rho}{\rho_r}, \tag{2.1}$$

where ρ_r is the reference fluid density. Throughout this work, the reference density is taken to be the fixed density of the unstratified ambient, i.e. $\rho_a \equiv \rho_r$.

2.2 Governing equations

Conservation of mass

For a fluid flow the rate of change of mass in a system is equal to the difference between the rates at which mass enters and leaves the system. This principle can be formulated in the differential form of the mass conservation equation as

$$\frac{\partial\rho}{\partial t} + \nabla\cdot(\rho\mathbf{u}) = 0, \tag{2.2}$$

Property	Diffusivity	Value, $m^2\,s^{-1}$
Momentum	ν	1.0×10^{-6}
Temperature	κ_T	1.4×10^{-7}
Salt	κ_S	1.5×10^{-9}
Sugar	κ_C	0.5×10^{-9}

Table 2.1 Values of key diffusivity constants (Shirtcliffe, 1973).

where t is time and $\mathbf{u}$ is the velocity field. Equation (2.2) can be expanded as

$$\underbrace{\frac{\partial \rho}{\partial t} + \mathbf{u} \cdot \nabla \rho}_{\text{Material Derivative}} + \rho \nabla \cdot \mathbf{u} = 0. \tag{2.3}$$

For incompressible fluids, we take the fluid density ρ to be a constant, implying that the total derivative is zero and yielding the incompressible mass continuity equation

$$\nabla \cdot \mathbf{u} = 0. \tag{2.4}$$

The assumption of incompressibility is valid provided the flow speed remains much less than the speed of sound. This is the case throughout our laboratory experiments and for most environmental flows. For a complete derivation of the continuity equation in differential form, the reader is referred to appendix A.

Conservation of momentum

The governing equations describing the conservation of momentum for an incompressible fluid with constant viscosity can be written as

$$\rho \left(\frac{\partial \mathbf{u}}{\partial t} + \mathbf{u} \cdot \nabla \mathbf{u} \right) = -\nabla p + \rho \mathbf{g} + \mu \nabla^2 \mathbf{u}, \tag{2.5}$$

where μ is the dynamic viscosity of the fluid. For fluid flows with negligible viscosity, the last term on the right-hand side (rhs) of the above equation may be dropped, leading to the incompressible Euler equations.

Conservation of temperature/solute

In an unsteady flow containing two scalar components (e.g. heat and salt), diffusing at constant rates, the transport of temperature T and salinity S within the flow can be

formulated using the unsteady advection-diffusion equations in the following form

$$\left(\frac{\partial}{\partial t} + \mathbf{u}\cdot\nabla\right) T = \kappa_T \nabla^2 T, \tag{2.6}$$

$$\left(\frac{\partial}{\partial t} + \mathbf{u}\cdot\nabla\right) S = \kappa_S \nabla^2 S, \tag{2.7}$$

where κ_T and κ_S are the molecular diffusion coefficients for heat and salt, respectively. Table 2.1 summarises the key diffusivity coefficients used in this work. Note that the molecular diffusivity of heat is $O(100)$ times greater than that of salt. Contrast this with the $O(1)$ ratio between the diffusivities of salt and sugar.

Conservation of vorticity

The curl of a velocity field gives rise to a quantity $\boldsymbol{\omega} = \nabla \times \mathbf{u}$, which describes the circulation density in a fluid, commonly termed as vorticity. With this in mind, taking the curl of the momentum conservation equation (2.5), and noting that $\mathbf{u}\cdot\nabla\mathbf{u} = \nabla(\frac{1}{2}\mathbf{u}\cdot\mathbf{u}) - \mathbf{u}\times\boldsymbol{\omega}$, we obtain the vorticity conservation equation in the form

$$\frac{\partial \boldsymbol{\omega}}{\partial t} + \mathbf{u}\cdot\nabla\boldsymbol{\omega} = \underbrace{\boldsymbol{\omega}\cdot\nabla\mathbf{u}}_{\text{Vortex stretching}} + \underbrace{\frac{1}{\rho^2}\nabla\rho\times\nabla p}_{\text{Baroclinic torque}} + \nu\nabla^2\boldsymbol{\omega}, \tag{2.8}$$

where $\nu = \mu/\rho$ denotes the kinematic viscosity. We follow the convention of anticlockwise vorticity being positive and denote its magnitude as $\psi = |\boldsymbol{\omega}|$. The middle term on the rhs of (2.8), called the baroclinic torque, is a vorticity generating mechanism. This buoyancy-induced vorticity term is non-zero, giving rise to the baroclinic torque, if the stratification gradients do not lie along surfaces of constant pressure (Linden, 2000). An example of such a situation is a stationary hydrostatic fluid with horizontal density variations. It is the action of the baroclinic torque that is widely believed to result in the increased rate of turbulent entrainment in plumes compared to jets, as discussed in section 1.2.2.

2.3 Boussinesq approximation

For all flows discussed in this work, the density differences between the flow fluid and the ambient are small compared to ρ_r, and we use the Boussinesq assumption to describe fluid motion. To obtain the equations of motion under the Boussinesq approximation,

originally formulated by Boussinesq (1903), we start with the momentum equations, rewritten for convenience in tensor notation

$$\rho\left(\frac{\partial u_i}{\partial t} + u_j\frac{\partial u_i}{\partial x_j}\right) = \frac{\partial p}{\partial x_i} + \rho g_i + \mu\frac{\partial^2 u_i}{\partial x_j^2}. \tag{2.9}$$

For a fluid of uniform density ρ_r at rest in a gravitational field $\mathbf{g} = (0, 0, -g)$, the pressure at any location is given by the weight of the fluid above. This statement is known as the hydrostatic condition and can be formulated as

$$0 = -\frac{\partial p_r}{\partial z} + \rho_r(-g). \tag{2.10}$$

Any small perturbations to the pressure and density fields can be represented using the modified Reynolds decomposition as

$$p(x_i, t) = p_r(x_i) + p'(x_i, t) \quad \text{and} \quad \rho(x_i, t) = \rho_r(x_i) + \rho'(x_i, t). \tag{2.11}$$

Substituting the above expression into the conservation of momentum equation we get

$$(\rho_r + \rho')\left(\frac{\partial u_i}{\partial t} + u_j\frac{\partial u_i}{\partial x_j}\right) = -\frac{\partial(p_r + p')}{\partial x_i} + (\rho_r + \rho')g_i + \mu\frac{\partial^2 u_i}{\partial x_j^2}. \tag{2.12}$$

Expanding the brackets on the rhs and using the hydrostatic condition, we obtain

$$(\rho_r + \rho')\left(\frac{\partial u_i}{\partial t} + u_j\frac{\partial u_i}{\partial x_j}\right) = -\frac{\partial p'}{\partial x_i} + \rho' g_i + \mu\frac{\partial^2 u_i}{\partial x_j^2} \tag{2.13}$$

Assuming that $\rho' \ll \rho_r$ we take the density differences to have negligible effect on the intertial term on the lhs. Dividing through by ρ_r, we get

$$\frac{\partial u_i}{\partial t} + u_j\frac{\partial u_i}{\partial x_j} = -\frac{1}{\rho_r}\frac{\partial p'}{\partial x_i} + \frac{\rho'}{\rho_r}g_i + \nu\frac{\partial^2 u_i}{\partial x_j^2}, \tag{2.14}$$

The equation above represents the momentum conservation equation under the Boussinesq approximation, which can be rewritten using general vector notation as

$$\frac{\partial \mathbf{u}}{\partial t} + \mathbf{u}\cdot\nabla\mathbf{u} = -\frac{1}{\rho_r}\nabla p' + \mathbf{g}' + \nu\nabla^2\mathbf{u}, \tag{2.15}$$

where $\mathbf{g}' = (0, 0, g')$. These equations are the starting point for deriving the plume conservation equations, presented in section 2.7.

2.4 Equations of state

For a Boussinesq fluid, the effects of temperature T and some scalar property, e.g. salt S, on the departure of the fluid density $\rho = \rho(T, S)$ from its reference value $\rho = \rho_r$ can be approximated using the linearised equation of state in the form

$$\rho = \rho_r(1 - \beta_T \Delta T + \beta_S \Delta S), \tag{2.16}$$

where β_T and β_S are linear volumetric expansion coefficients defined as

$$\beta_T = -\left(\frac{1}{\rho}\frac{\partial \rho}{\partial T}\right), \quad \beta_S = \left(\frac{1}{\rho}\frac{\partial \rho}{\partial S}\right). \tag{2.17}$$

The above coefficients give the change in density per unit change in temperature or scalar concentration. Note that under the Boussinesq approximation, $\beta_{T,S}$ are constants (Spiegel and Veronis, 1960). The linear equations of state are only valid for small changes in temperature and/or solute concentration. When these differences are large, or extra precision is needed, the cross term between temperature and solute concentration, along with higher order terms should be included in the equations of state. For our experiments we therefore used the equations of state with higher order terms, which are provided by Ruddick and Shirtcliffe (1979).

2.5 Non-dimensionalisation & key parameters

In order to demonstrate the nature and origins of key parameters governing the motion of fluid flow, we non-dimensionalise the full set of relevant equations in terms of characteristic quantities. It is convenient to make (2.5)–(2.7) dimensionless using the following (starred) non-dimensional variables

$$\mathbf{u} = U_0\,\mathbf{u}^*, \quad L = L_0\,L^*, \quad t = \frac{L_0}{U_0}\,t^*, \quad p = \rho_0 U_0^2\,p^*, \quad T = T_0\,T^*, \quad S = S_0\,S^*. \tag{2.18}$$

Replacing all variables in (2.5)–(2.7) with their non-dimensional equivalents yields

$$\left[\frac{U_0}{L_0}\right]\left(\frac{\partial}{\partial t^*} + \mathbf{u}^* \cdot \nabla^*\right)\begin{pmatrix}[U_0]\,\mathbf{u}^* \\ [T_0]\,T^* \\ [S_0]\,S^*\end{pmatrix} = \begin{pmatrix}-\left[\frac{U_0^2}{L_0}\right]\nabla^* p'^* + \mathbf{g}' + \left[\frac{U_0}{L_0^2}\right]\nu\nabla^{2^*}\mathbf{u}^* \\ \left[\frac{T_0}{L_0^2}\right]\kappa_T\nabla^{2^*}T^* \\ \left[\frac{S_0}{L_0^2}\right]\kappa_S\nabla^{2^*}S^*\end{pmatrix}, \tag{2.19}$$

which can be rewritten as

$$\left(\frac{\partial}{\partial t^*} + \mathbf{u}^* \cdot \nabla^*\right) \begin{pmatrix} \mathbf{u}^* \\ T^* \\ S^* \end{pmatrix} = \begin{pmatrix} -\nabla^* p'^* + Ri + Re^{-1} \nabla^{2^*} \mathbf{u}^* \\ Re\, Pr\, \nabla^{2^*} T^* \\ Re\, Sc\, \nabla^{2^*} S^* \end{pmatrix}. \tag{2.20}$$

The set of non-dimensionalised equations (2.20) gives rise to a number of non-dimensional governing parameters, including the Reynolds number Re, Prandtl number Pr, Schmidt number Sc and Richardson number Ri. Alternatively, the three governing equations can be non-dimensionalised using a different set of non-dimensional variables, defined as

$$\mathbf{u} = L_0^{-1} \kappa_T \, \mathbf{u}^*, \; L = L_0 \, L^*, \; t = L_0^2 \kappa_T^{-1} \, t^*, \; p = \rho_0 \kappa_T^2 L_0^{-2} \, p^*, \; T = T_0 \, T^*, \; S = S_0 \, S^*. \tag{2.21}$$

Using these non-dimensional variables gives rise to additional non-dimensional parameters, including the Rayleigh number Ra and the Lewis number Le, which are particularly relevant for double-diffusive buoyancy driven flows. Definitions and brief explanation of the meaning of these non-dimensional parameters are provided below.

Reynolds number

The Reynolds number is a key parameter for characterising the fluid flow, and arises from balancing viscous and advective terms upon non-dimensionalisation of the momentum equation. This non-dimensional parameter provides a measure of the relative significance of inertial and viscous effects in a fluid flow and is defined as

$$Re = \frac{UL}{\nu}, \tag{2.22}$$

where U and L are the characteristic velocity and length scales, respectively. At large Reynolds numbers, flow is generally turbulent and inertia dominates, meaning that the effects of viscosity may be ignored in the momentum equation.

For the plume/jet flows studied in this work, the source Reynolds numbers based on the source exit velocity U_0 and source radius r_0 were $300 < Re_0 < 1500$, which is not large enough for the flow field to be confidently treated as fully turbulent at the source. However, with the use of a specially-designed nozzle, described in section 3.6, it was possible to sufficiently excite the flow prior to discharge, thus ensuring that a turbulent flow is developed at the plume/jet source.

Rayleigh number

The relative importance of the buoyancy-induced destabilising effects, which lead to convective motions, and the stabilising viscous and molecular diffusive processes is quantified using the Rayleigh number, defined as

$$Ra = \frac{g' H^3}{\nu \kappa}, \tag{2.23}$$

where H is the vertical scale of interest. This non-dimensional parameter is commonly used as an indicator of whether convection, taking place in the region of interest, is laminar or turbulent. In most cases of practical interest, the density differences and length scales characterising the flow result in $Ra \gg 1$. For $Ra > O(10^5)$, convection is generally considered to be fully turbulent, and thus independent of the Rayleigh number.

Taking $H \sim O(10^{-1})$ m to be the height of the experimental tank filled with water for our experiments, and using the value of the temperature difference $\Delta T \sim O(10)$ °C, we get $Ra_T \sim O(10^8)$ implying that any thermally-driven convection in our experiments was turbulent. For an equivalent experimental configuration, the value of the salt-based Rayleigh number is $Ra_S \sim O(10^{10})$, implying that salt-driven convection in the tank was also turbulent.

Richardson & Froude numbers

In general, the Richardson number Ri is the dimensionless number that expresses the ratio of the buoyancy term to the flow shear term, and is defined as

$$Ri = \frac{g' L}{U^2}. \tag{2.24}$$

In the context of plumes and buoyant jets, Ri represents the relative importance of natural convection, driven by the density difference, and forced convection, driven by the source momentum flux. An alternative version of this non-dimensional parameter is the Froude number, defined as $Fr = 1/\sqrt{Ri}$. For a neutrally-buoyant ($\rho = \rho_a$) momentum-driven flow $Ri \to 0$ and $Fr \to \infty$. Conversely, the limits of $Ri \to \infty$ and $Fr \to 0$ correspond to a flow which is dominated by buoyancy. The two cases correspond to a pure jet and plume, respectively. Buoyant jets, forced and lazy plumes exist at intermediate values of the Richardson and Froude numbers.

Péclet number

The balance between the advective and diffusive transfer of heat/solute is given by the Péclet number, defined as

$$Pe = \frac{UL}{\kappa}. \tag{2.25}$$

For a high-Péclet-number flow, advective transport dominates, leading to an assumption that the diffusive effects are insignificant. In the context of plumes, the insignificant role of diffusive transport has been demonstrated by Partridge and Linden (2013), who showed that despite two orders of magnitude difference in the molecular diffusivity κ, for high-Péclet-number plumes driven by temperature or solute concentration difference the rate of entrainment is constant. For buoyancy-driven flows, taking $h \sim H$, the velocity scales as $U \sim \sqrt{g'H}$ and the expression for the Péclet number can be reconstructed as

$$Pe = \frac{\sqrt{g'H^3}}{\kappa}. \tag{2.26}$$

Using this definition, in the case of our plume experiments the typical values of Péclet numbers were $O(10^3)$.

Prandtl, Schmidt & Lewis numbers

Finally, we arrive at the ratios between the diffusivities involved in a particular fluid flow, including, respectively, the Prandtl, Schmidt and Lewis numbers defined as

$$Pr = \frac{\nu}{\kappa_T}, \quad Sc = \frac{\nu}{\kappa_S}, \quad Le = \frac{\kappa_T}{\kappa_S}. \tag{2.27}$$

Since all our experiments were conducted in water, the value of Prandtl number was fixed at $Pr \simeq 7$. The value of the Schmidt number depends on the choice of the solute used in the experiments. In the case of salt, $Sc \simeq 700$. For a heat-salt flow combination, the value of the Lewis number is $Le \simeq 100$.

2.5.1 Kolmogorov length scale

In a turbulent flow, motions occur over a wide range of length and time scales. While the largest eddies in the flow are normally constrained by their physical boundaries, the length scales of the smallest eddies are determined by viscosity. For a statistically steady turbulent flow, the energy supplied by the large eddies must equal the energy dissipated at the small scales by viscous effects. The only factors influencing the smallest eddies

are viscous diffusivity ν and the kinetic energy dissipation rate ϵ (Kolmogorov, 1941). Although the rate of dissipation is independent of viscosity, the length and time scales at which energy dissipation occurs depends on both ϵ and ν, and can be defined as

$$\eta_K = \left(\frac{\nu^3}{\epsilon}\right)^{1/4} \quad \text{and} \quad \tau_K = \left(\frac{\nu}{\epsilon}\right)^{1/2}. \tag{2.28}$$

The length scale η_K is referred to as the Kolmogorov length scale, and is the smallest velocity length scale in a turbulent flow, below which viscosity damps out any inhomogenieties in the velocity field. The time scale τ_K is the associated time scale for the energy in the smallest eddy to be dissipated by viscosity.

For a jet/plume flow emanating from a source with radius r_0 at velocity U_0, the scaling for the associated energy dissipation rate can be constructed as

$$\epsilon = \mathbf{u} \cdot \nu \nabla^2 \mathbf{u} \sim \nu \frac{U_0^2}{(2r_0)^2}. \tag{2.29}$$

For plumes, the typical source exit velocities were $U_0 \simeq 0.2\ \mathrm{m\,s^{-1}}$ and the source radius was $r_0 = 2.5 \times 10^{-3}\ \mathrm{m\,s^{-1}}$. Using these values, the energy dissipation rate was $\epsilon \simeq 1.6 \times 10^{-3}\ \mathrm{m^2\,s^{-3}}$ and hence the Kolmogorov length scale was $\eta_K \simeq 1.6 \times 10^{-4}$ m.

2.5.2 Batchelor length scale

Analogously to the Kolmogorov scale, the smallest length scale associated with the scalar field, the Batchelor scale, is determined by the molecular diffusivity κ. In our work, $\nu > \kappa$ and therefore velocity fluctuations will be dampened out at scales larger than those for the scalar, i.e. $\eta_K > \eta_B$. In this case, the appropriate time scale is the Kolmogorov time scale. From the scaling implied by the diffusion equation, $\eta_B^2 \sim \kappa \tau_K$ and using the Kolmogorov scale, $\eta_K = (\nu^3/\epsilon)^{1/4}$, we can construct the Batchelor scale as

$$\frac{\eta_B}{\eta_K} = (\kappa_S/\nu)^{1/2} = Sc^{-1/2}. \tag{2.30}$$

Using the value of the Kolmogorov length scale estimated above, the value of the Batchelor length scale for salt in our experiments was $\eta_B \simeq 6 \times 10^{-6}$ m. Replacing the Schmidt number in (2.30) with the Prandtl number for water, we obtain the Batchelor length scale for temperature $\eta_B \simeq 6 \times 10^{-5}$.

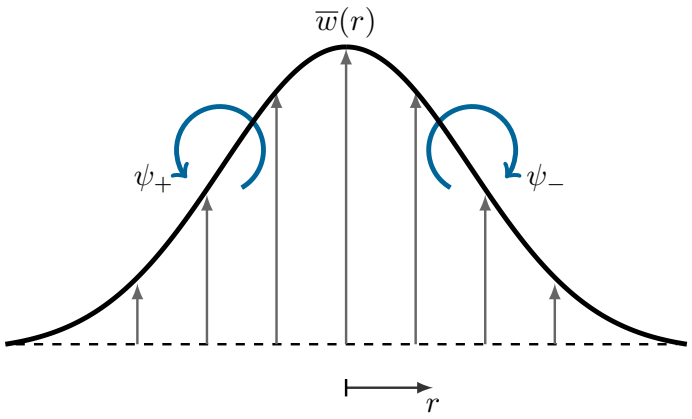

Fig. 2.2 A schematic representation of the time-average vertical velocity distribution $\overline{w}(r)$ in a turbulent jet/plume at some distance z from the source. The blue arrows indicate the orientation of the shear-induced vorticity of strength $\psi = |\boldsymbol{\omega}|$ within the flow. Note that the radial distribution of salinity S and temperature T in the case of salt-only and heat-only plumes, respectively, follow similar Gaussian profiles.

2.6 Plume/jet radial profiles

Turbulent plumes and jets in a uniform environment are geometrically self-similar, taking a mean conical shape (Turner 1979). More specifically, measurements made by Rouse et al. (1952), Ricou and Spalding (1961) and Papanicolaou and List (1988) demonstrate that the radial dependence of the time-averaged vertical velocity in jets and plumes can be well-approximated by a Gaussian profile of the form

$$\overline{w}(r,z) = \overline{w}_c(z)\,\exp(r^2/\overline{b}(z)^2), \tag{2.31}$$

where $\overline{w}_c(z)$ is the centreline vertical velocity, $\overline{b}(z)$ is the mean plume width at a given distance from the source z, and r is the plume radial coordinate. The nature of the observed time-average Gaussian distribution is mainly a result of the meandering motions of the flow rather than the actual physical velocity distribution.

There is an on-going debate on whether in a turbulent plume the ratio of radial distribution of buoyancy matches that of the vertical velocity. While measurements made by Papanicolaou and List (1988) suggest that the relative width of the buoyancy profile is greater than that of velocity, Shabbir and George (1994) reported an opposite observation. However, since all previously measured values of the buoyancy and velocity radii are close to unity, for simplicity, we will assume that the scalar distribution in a turbulent plume matches that of vertical velocity for every distance z.

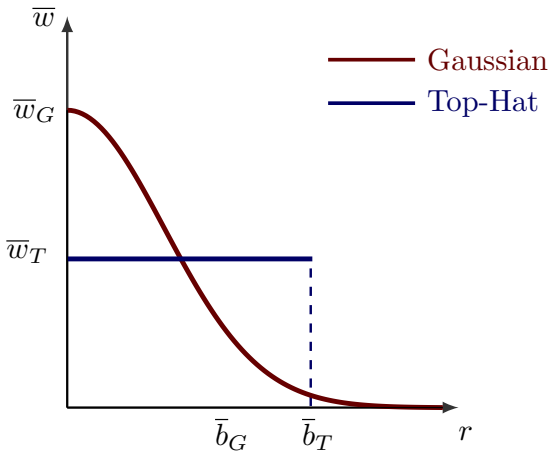

Fig. 2.3 A schematic representation of radial velocity distribution under the Gaussian and the 'top-hat' assumptions.

Shown schematically in figure 2.2, the non-uniform vertical velocity distribution in plumes and jets induces shear, which in turn generates vorticity. As explained in chapter 1, vortex dynamics is an important aspect of turbulent entrainment, since the entrainment process is largely dependent on the engulfment of ambient fluid by large-scale turbulent eddies.

2.6.1 Top-Hat vs. Gaussian representation

Given the experimental evidence, it is natural to use the Gaussian representation to describe integral properties of plume and jet flows. However, it is often more convenient to replace the Gaussian representation with a top-hat profile, in which the flow properties are assumed constant within the flow and zero outside. The two common representations of plume/jet radial distribution of the mean vertical velocity $\overline{w}(r)$ are therefore

$$\overline{w}(r) = \overline{w}_G \exp(-r^2/\overline{b}_G{}^2) \quad \text{for } 0 \le r \le \infty, \tag{2.32a}$$

$$\overline{w}(r) = \begin{cases} \overline{w}_T & 0 \le r \le \overline{b}_T \\ 0 & r > \overline{b}_T, \end{cases} \tag{2.32b}$$

where $\overline{w}_G$ and $\overline{b}_G$ are the centreline vertical velocity and radius under the Gaussian representation, and $\overline{w}_T$ and $\overline{b}_G$ are the centreline vertical velocity and radius under the top-hat representation. Using these definitions, the plume volume flux under the

Gaussian representation $\overline{Q}_G$ is

$$\begin{aligned}\overline{Q}_G &= \int_0^{2\pi}\int_0^{\infty} \overline{w}_G \exp(-r^2/\bar{b}_G{}^2)\, r\mathrm{d}r\mathrm{d}\theta \\ &= 2\pi\overline{w}_G \int_0^{\infty} \frac{1}{2}\exp(-r^2/\bar{b}_G{}^2)\,\mathrm{d}r^2 = \pi\overline{w}_G(-\bar{b}_G^2)\Big[\exp(-r^2/\bar{b}_G{}^2)\Big]\Big]_0^{\infty} = \pi\overline{w}_G\bar{b}_G^2.\end{aligned} \tag{2.33}$$

For the top-hat representation, the mean plume/jet volume flux $\overline{Q}_T$ can be written as

$$\overline{Q}_T = \int_0^{2\pi}\int_0^{\bar{b}_T} \overline{w}_T\, r\mathrm{d}r\mathrm{d}\theta = 2\pi\overline{w}_T \int_0^{\bar{b}_T} \frac{1}{2}\,\mathrm{d}r^2 = \pi\overline{w}_T\bar{b}_T^2. \tag{2.34}$$

In a similar fashion, the mean momentum flux of a plume/jet under the Gaussian representation can be written as

$$\begin{aligned}\overline{M}_G &= \int_0^{2\pi}\int_0^{\infty}\Big[\overline{w}_G \exp(-r^2/\bar{b}_G{}^2)\Big]^2\, r\mathrm{d}r\mathrm{d}\theta \\ &= 2\pi\overline{w}_G^2 \int_0^{\infty} \frac{1}{2}\exp(-2r^2/\bar{b}_G^2)\,\mathrm{d}r^2 = \frac{1}{2}\pi\overline{w}_G^2\bar{b}_G^2,\end{aligned} \tag{2.35}$$

and under the top-hat representation as

$$\overline{M}_T = \int_0^{2\pi}\int_0^{\bar{b}_T} \overline{w}_T^2 r\mathrm{d}r\mathrm{d}\theta = \pi\overline{w}_T^2\bar{b}_T^2. \tag{2.36}$$

Since using either representation, both the volume and momentum fluxes must be the same, i.e. $\overline{Q}_G = \overline{Q}_T$ and $\overline{M}_G = \overline{M}_T$, using the above expressions for the volume and momentum fluxes, we can establish the following relationships between the plume/jet velocity, radius and the entrainment coefficient

$$\overline{w}_G = 2\overline{w}_T, \quad \bar{b}_G = \bar{b}_T/\sqrt{2} \quad \text{and} \quad \alpha_G = \alpha_T/\sqrt{2}. \tag{2.37}$$

2.7 Plume theory

For an steady axisymmetric plume flow of an incompressible fluid with no diffusion of mass and momentum, under the Boussinesq assumption (density differences are small compared with the ambient density), and with a velocity field $\mathbf{u} = (u, 0, w)$ in

cylindrical polar coordinates (r, θ, z), the Navier-Stokes equations can be written as

$$r: \quad u\frac{\partial u}{\partial r} + w\frac{\partial u}{\partial z} = -\frac{1}{\rho_a}\frac{\partial p}{\partial r}, \tag{2.38a}$$

$$z: \quad u\frac{\partial w}{\partial r} + w\frac{\partial w}{\partial z} = -\frac{1}{\rho_a}\frac{\partial p}{\partial z} - g\frac{\rho}{\rho_a}, \tag{2.38b}$$

$$Continuity: \quad \frac{1}{r}\frac{\partial (ur)}{\partial r} + \frac{\partial w}{\partial z} = 0. \tag{2.38c}$$

In the above equations $w \to 0$ as $r \to \infty$, signifying that the vertical motion is confined to the plume. This assumption will be important in further derivations.

Using Reynolds decomposition, each variable in a turbulent plume can be broken down into a sum of a time-averaged profile and a fluctuating component,

$$w = \overline{w} + w', \quad \text{where} \quad \overline{w} = \frac{1}{t_T}\int_0^{t_T} w \, \mathrm{d}r, \tag{2.39}$$

where t_T is the total time for averaging. In our subsequent analysis we assume that the turbulent fluctuations are small compared to the mean values and the plume variables can therefore be replaced by their time-mean values. For simplicity we drop the overbar notation to signify the time-mean.

The dynamics of turbulent plumes are determined by the fluxes of mass, momentum, and the force arising from buoyancy. For high-Péclet-number, incompressible, Boussinesq plumes, conservation of mass can be approximated by conservation of volume, and the density changes are only important for determining the buoyancy force. We can therefore rewrite the aforementioned physical fluxes as the fluxes of volume Q, specific momentum M and buoyancy B in terms of time-averaged plume velocity $w(r, z)$, density $\rho(r, z)$ and buoyancy $g'(r, z) = g(\rho(r, z) - \rho_a)/\rho_a$ as

$$Q = 2\pi \int_0^\infty r \, w(r, z) \mathrm{d}r, \tag{2.40a}$$

$$M = 2\pi \int_0^\infty r \, w^2(r, z) \mathrm{d}r, \tag{2.40b}$$

$$B = 2\pi \int_0^\infty r \, w(r, z) \, g'(r, z), \mathrm{d}r, \tag{2.40c}$$

where ρ_a is the ambient fluid density. To model the process of turbulent entrainment and mixing of the ambient fluid into the plume we use the 'entrainment assumption', formulated by Morton et al. (1956), which takes the entrainment velocity of ambient fluid at the plume edge at a given height $u_e(z)$ to be proportional to the vertical velocity in the plume at that height by the entrainment coefficient α^P.

Using this model for self-similar plumes in a uniform environment under the top-hat representation, for which plume properties are taken to be constant within the plume and zero outside, and neglecting turbulent transport terms, which are small (Burridge et al., 2016), the solutions to (2.38) yield the plume conservation equations, which can be written as

$$\frac{\mathrm{d}Q}{\mathrm{d}z} = 2\pi b_T u_e = 2\pi^{1/2}\alpha_T^P M^{1/2}, \quad \frac{\mathrm{d}M}{\mathrm{d}z} = \pi b_T^2 g_T' = \frac{BQ}{M}, \quad \text{and} \quad \frac{\mathrm{d}B}{\mathrm{d}z} = 0, \tag{2.41}$$

where b_T, g_T' and α_T^P denote the top-hat plume radius, buoyancy and entrainment coefficient, respectively. For a complete derivation of similarity solutions to the conservation equations for a plume rising in a uniform environment from a point source of buoyancy with zero source volume and momentum fluxes, that is a pure plume, the reader is referred to appendix B. For the current purposes we will straightaway provide the solutions for a pure plume in their final form:

$$b_T(z) = \frac{6}{5}\alpha_T^P z, \tag{2.42a}$$

$$w_T(z) = \frac{5}{6\alpha_T^P}\left(\frac{9\alpha_T^P}{10}\right)^{1/3}\pi^{-1/3}B_0^{1/3}z^{-1/3}, \tag{2.42b}$$

$$g_T'(z) = \frac{5}{6\alpha_T^P}\left(\frac{9\alpha_T^P}{10}\right)^{-1/3}\pi^{-2/3}B_0^{2/3}z^{-5/3}, \tag{2.42c}$$

$$Q(z) = \frac{6\alpha_T^P}{5}\left(\frac{9\alpha_T^P}{10}\right)^{1/3}\pi^{2/3}B_0^{1/3}z^{5/3}, \tag{2.42d}$$

$$M(z) = \left(\frac{9\alpha_T^P}{10}\right)^{2/3}\pi^{1/3}B_0^{2/3}z^{4/3}, \tag{2.42e}$$

where the subscript '0' denotes the quantity at the physical plume source.

2.7.1 Plume parameter

Solutions of the conservation equations yield a dimensionless parameter, the plume Richardson number Γ_0, also referred to as the 'plume parameter', which represents the balance of volume flux, momentum flux and buoyancy flux at the plume source as

$$\Gamma_0 = \frac{5}{8\sqrt{2}\alpha_G^P\pi^{1/2}}\frac{Q_0^2B_0}{M_0^{5/2}} = \frac{5}{8\alpha_T^P\pi^{1/2}}\frac{Q_0^2B_0}{M_0^{5/2}}. \tag{2.43}$$

Introduced by Morton (1959), the plume Richardson number can be used to classify the plume source conditions. A value of $\Gamma_0 = 0$ corresponds to a pure momentum jet with no buoyancy, and values of $\Gamma_0 < 0$ are characteristic for a fountain, i.e. where the source momentum flux opposes the buoyancy flux (Turner, 1966). For idealised point sources of buoyancy with no momentum flux and no volume flux at the source, Γ_0=1. This type of plume is referred to as a 'pure' plume.

If the flow has initially more momentum than a pure plume, it is referred to as a 'forced' plume, with the source plume parameter $0 < \Gamma_0 < 1$ (Morton, 1959). To 'correct' the excess momentum flux, this flow initially entrains more ambient fluid and decelerates, converging towards the self-similar plume. The length scale of this adjustment corresponds to the distance travelled over which the plume develops momentum comparable in magnitude to the initial momentum, and hence begins to lose memory of the source conditions. Morton (1959) showed that this vertical distance scales with the momentum jet-length L_M, given by

$$L_M = (4\pi^{1/2}\alpha_T^P)^{-1/2}\frac{M_0^{3/4}}{B_0^{1/2}}. \tag{2.44}$$

Plumes with an initial deficit of momentum are referred to as 'lazy' plumes, and are defined by $\Gamma_0 > 1$ (Hunt & Kaye, 2001, 2005). The flow compensates for an initial momentum deficit by entraining less fluid. During that time excess buoyancy acts to generate momentum flux to correct the imbalance. The flow therefore accelerates and converges to the natural self-similar solution. Hunt and Van den Bremer (2010) showed that the adjustment length of lazy plumes is shorter than that of forced plumes, and in this case scales with the distance

$$L_Q = \frac{5}{6\alpha_T\pi^{1/2}}\frac{Q_0^{3/5}}{B_0^{1/5}}, \tag{2.45}$$

over which the plume entrains a mass comparable to the initial mass. Hunt and Kaye (2001) showed that the plume parameter can be rearranged in terms of the source area (πr_0^2) and the initial reduced gravity g_0', giving

$$\Gamma_0 \sim \frac{(\pi r_0^2)^{5/2} g_0'}{Q_0^{5/2}}. \tag{2.46}$$

In this form it is clearly seen that highly buoyant slow releases from large area sources result in lazy plumes. Conversely, forced plumes are obtained when the source plume

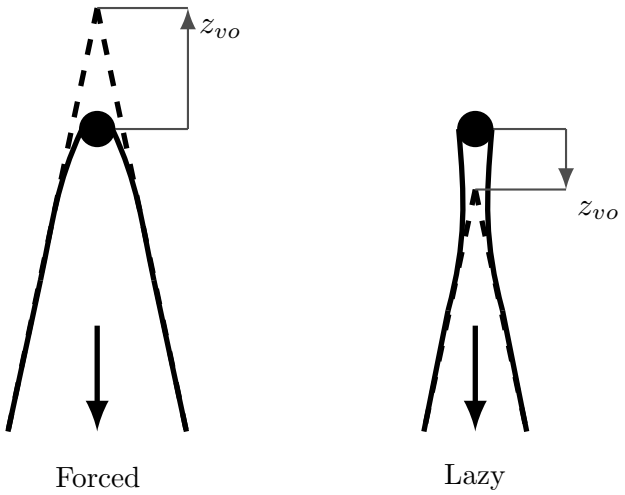

Fig. 2.4 Schematic representation of the virtual origin location z_{vo} for a forced ($\Gamma_0 < 1$) and a lazy ($\Gamma_0 > 1$) plume emanating downwards from a point source. Note that in the case of a lazy plume, the virtual origin in 'front' of the physical source.

fluid of low buoyancy is released at high flow rate from a small opening. In addition, for circular sources, $\Gamma_0 \sim r_0^5$, and thus the source plume parameter is highly sensitive to the choice of the source area size.

2.7.2 Virtual origin correction

In our experiments, as in most cases of practical interest (e.g. smoke plumes from chimneys), plumes had non-zero volume and/or momentum fluxes at the source, i.e. $\Gamma_0 \neq 1$. Therefore, in order to be able to use the similarity solutions (2.42) for accurate prediction of the flow evolution, a correction to the source position, called 'virtual origin correction' needs to be applied. We define the virtual origin correction z_{vo} as the distance from a physical plume source to a virtual location, from which an ideal point source pure plume, of buoyancy only, would develop fluxes identical to those in a real plume.

Hunt and Kaye (2001) extensively discussed a number of approaches to determining the virtual origin correction, for both forced and lazy plumes. These techniques, ranging from simple geometric methods, such as tracing the conical plume outline far from the source back to a point, to analytical methods using solutions for the plume fluxes to calculate the virtual origin, were grouped into four different categories: (i) corrections based on empirical measurements; (ii) 'conical' source correction; (iii) jet-length based correction; and (iv) source correction based on the source plume fluxes.

In the case of a plume emanating from a point source with an imbalance of source fluxes, the virtual origin can be located either 'in front of' or 'behind' the physical source, as illustrated schematically in figure 2.4. As discussed in the previous section, in the case of a forced plume the entrainment is greater in the early stages of the flow development and therefore the virtual source is located behind the physical source. Conversely, lazy plumes entrain less at the start, and therefore the virtual source is located in front of the actual source. However, these considerations are only valid for a flow coming from a point source. For any source of finite size, as in our experiments, an additional correction for the source volume flux needs to be applied.

In our calculations, we used the two-step source correction (iv) based on the initial properties of the plume (B_0, M_0, Q_0) developed by Morton (1959), which is particularly useful as it can be applied to lazy ($\Gamma_0 < 1$) and forced ($\Gamma_0 > 1$) plumes, both of which were present in our experiments. The first step involves replacing the general source (B_0, M_0, Q_0) with a virtual point source forced plume with no source volume flux of modified strength $(B_0, \chi M_0, 0)$ located at $z = z_1$. The second step relates the flow above this modified source to a pure buoyancy source $(B, 0, 0)$ at a distance $z = z_2$. Combining the two steps, the far-field flow produced by the general source may be related to the flow from a point source of buoyancy at the virtual origin $z_{vo} = z_1 + z_2$, which scales on the plume jet-length L_M. The exact calculations of the virtual origin depend on the value of plume parameter Γ_0, and are provided in detail by Hunt and Kaye (2001).

2.8 Jet theory

Derivation of the similarity solutions for a pure jet is analogous to those for a pure plume, with the major difference being the absence of a buoyancy term. This implies that in a homogeneous environment, the jet momentum flux is conserved. Neglecting turbulent transport terms, the equations describing steady, incompressible and inviscid jet flow with a velocity field $\mathbf{u} = (u, 0, w)$ in cylindrical polar coordinates (r, θ, x) are

$$x: \quad u\frac{\partial w}{\partial r} + w\frac{\partial w}{\partial x} = 0, \tag{2.47a}$$

$$Continuity: \quad \frac{1}{r}\frac{\partial (ur)}{\partial r} + \frac{\partial w}{\partial x} = 0. \tag{2.47b}$$

As for plumes, to model the process of turbulent entrainment and mixing of the ambient fluid into the jet we use the 'entrainment assumption', formulated by Morton et al. (1956), with the jet entrainment coefficient denoted as α^J. Using this model for

self-similar jets in a uniform environment under the Gaussian representation, neglecting turbulent transport terms, yields the jet volume and momentum conservation equations

$$\frac{\mathrm{d}}{\mathrm{d}x} 2\pi \int_0^\infty rw(r,x)dr = 2\pi b(\alpha_G^J w_G) \quad \text{and} \quad \frac{\mathrm{d}}{\mathrm{d}x} 2\pi \int_0^\infty rw^2(r,x)dr = 0. \tag{2.48}$$

Substituting the Gaussian profile of mean radial velocity distribution

$$w(r) = w_G \exp(-r^2/{b_G}^2) \tag{2.49}$$

into (2.48) yields

$$b_G(x) = 2\alpha_G^J x \quad \text{and} \quad w_G(x) = w_0 \frac{1}{\sqrt{2}\alpha_G^J} \frac{r_0}{x}, \tag{2.50}$$

where r_0 and w_0 are the source bore radius horizontal exit velocity, respectively.

2.9 Fluxes across double-diffusive interfaces

The motion in diffusive and salt-fingering double-diffusive systems is driven by the release of potential energy stored in the unstably stratified component. This potential energy is released through fluxes of heat and salt, determining the behaviour and properties of the layers and the interface that separates them. In this section we provide a brief outline of the flux measurements for double-diffusive systems.

2.9.1 4/3 flux law

In general, the term convection represents the total transfer of heat/mass by diffusion and advection. In the case of heat transfer, diffusion is replaced by conduction, and the relative magnitude of total heat transfer with respect to conductive transport can be measured by the Nusselt number

$$Nu = \frac{F_T}{k_T \Delta T H^{-1}}, \tag{2.51}$$

where F_T is the actual heat flux, $k_T = \rho C_p \kappa_T$ is the thermal conductivity, C_p is the specific heat capacity of the fluid, and ΔT is the temperature drop across the warm fluid layer of depth H. In the case of $Nu = 1$, heat transport is purely by conduction, whereas for cases where $Nu > 1$, the total heat transport is a result of some combination of conduction and advection.

As stated earlier, the strength of convection is governed by the Rayleigh number. For high Ra, the flow is turbulent and the heat flux is independent of fluid layer depth, implying, from dimensional considerations, that $Nu \sim Ra^{1/3}$. Despite the demonstrated effectiveness of this functional relationship in a number of previous experimental studies (Turner, 1965, 1967), the exact value of the scaling exponent continues to be the subject of an ongoing debate. As such, numerous experimental investigations and simulations with $Pr = O(1)$ yielded the values of the scaling exponent ranging between 0.27 and 0.40 (Ahlers et al., 2009; Roche et al., 2010). Although no universal agreement on the exact choice of the power has been reached to date, the alternatively proposed values are not substantially dissimilar from the value of 1/3. In addition, none of our calculations in this work rely sensitively on the exact choice of the power law used. Hence, for the purposes of our work, we decided to stick with the conventional 1/3 power law, allowing the turbulent heat flux into a deep layer to be written as

$$F_T = c_F k_T \Big(\frac{\beta_T g}{\kappa_T \nu}\Big)^{1/3} \Delta T^{4/3}, \tag{2.52}$$

where c_F is a dimensionless constant for a fixed Prandtl number fluid. The value of this constant has been obtained experimentally by several authors, with the best estimate being $c_F = 0.085$ (Chandrasekhar, 1961). Note that the expression for heat flux does not involve fluid layer depth, which is consistent with the idea that the depth of the fluid layer in unimportant. The dependence of heat flux on $\Delta T^{4/3}$ is the 'four-thirds' law.

2.9.2 Diffusive double-diffusive fluxes

Turner (1965) conducted the first experiment measuring the values of heat and salt flux across a double-diffusive diffusive interface. He used dimensional analysis to reason that the diffusive heat flux transferred across such an interface is

$$F_T = c_F k_T \Big(\frac{\beta_T g}{\kappa_T \nu}\Big)^{1/3} \Delta T^{4/3} f(R_\rho^*, Le, Pr), \tag{2.53}$$

where $R_\rho^* = (\beta_S \Delta S)/(\beta_T \Delta T)$. For a given physical system, for which Le and Pr are constants, a single functional relationship between F_T and R_ρ^* was sought. His work, along with some other more recent experiments by (Shirtcliffe 1973; Marmorino and Caldwell 1976; Stamp et al. 1998) has shown support of this functional form at low to moderate stability ratios $R_\rho^* < 10$. In particular, Turner's experiments demonstrated that both the heat flux and the relative rates of transfer of salt and heat through a

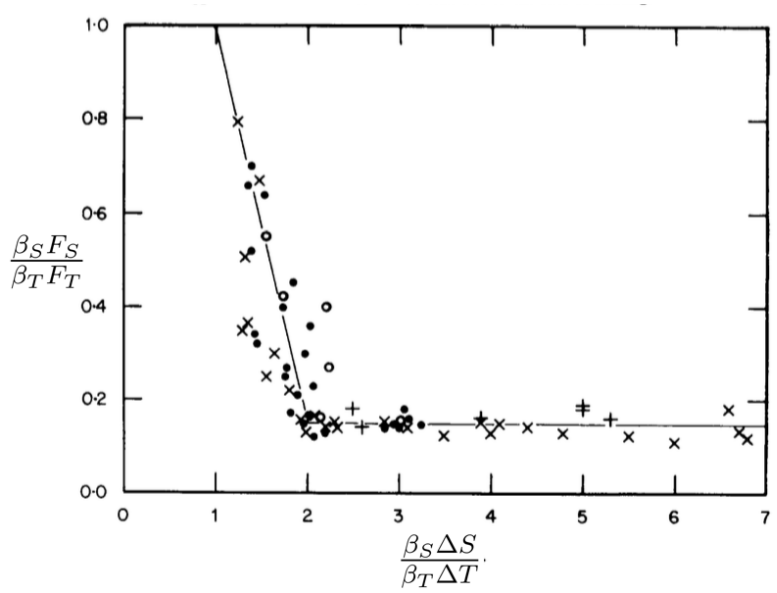

Fig. 2.5 The ratio of the potential energy changes due to the transfer of salt and heat across an interface between a hot salty layer below a cooler fresher layer, plotted as a function of the density ratio $R_\rho^* = \frac{\beta_S \Delta S}{\beta_T \Delta T}$ (Turner, 1965).

stable interface heated from below depend systematically on the stability ratio of the interface. For low values of stability ratios ($1 < R_\rho^* < 2$), the heat transfer normalised by an equivalent solid plate value was decreasing from ~ 10 to ~ 1, which was attributed to the effect of a wavy, breaking interface. At higher stability ratios, the heat flux was below the value appropriate to a solid surface, due to the inhibiting need for lifting of salt by the thermally driven motion.

Another important feature of the diffusive interface, shown in figure 2.5, is that the upward heat flux αF_T is larger than the downward flux of salt and becomes a constant of around 0.15 for $R_\rho^* > 2$. That implies that the potential energy of the system, consisting of cold and fresh fluid above a hot and salty layer, decreases and the density difference between the two layers increases in time. The net effect is such that the upward buoyancy flux is greater than that downwards. Note that the opposite process occurs in an analogous system with only one component contributing to density.

2.9.3 Salt-fingering double-diffusive fluxes

As with the diffusive interface, the first quantitative measurement of the fluxes of heat and salt carried by salt fingers across a density interface was performed by Turner (1967). Measurements were made with a layer of cold fresh water lying underneath a layer of warm and salty solution. Both layers were kept uniform by mechanical stirring

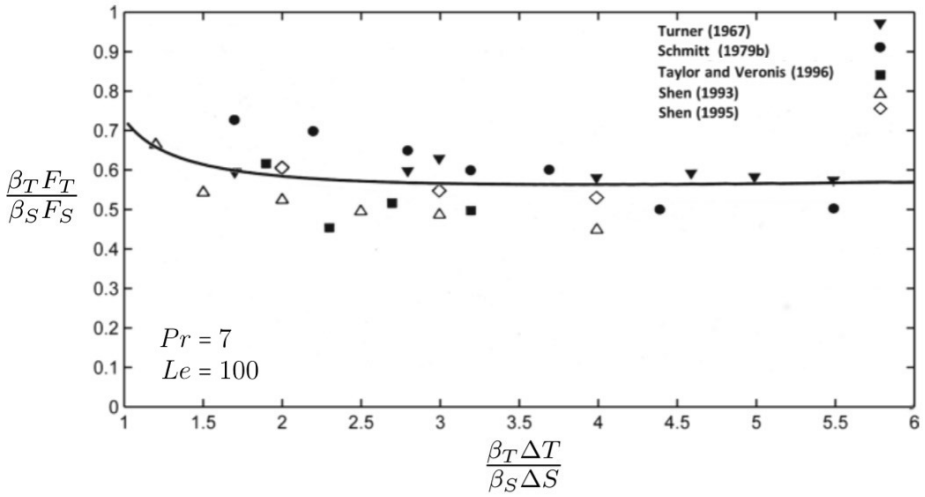

Fig. 2.6 Salt-finger flux ratio $\beta_T F_T/\beta_S F_S$ as a function of the stability ratio $R_\rho = \frac{\beta_T \Delta T}{\beta_S \Delta S}$. Symbols are experimental values, and the solid curves represent the theoretical estimate based on the fastest growing finger model (from Radko (2013)).

using vertically oscillating grids positioned at the centre of each layer. Measurements of temperature and salinity within both layers were used to estimate the values of heat and salt fluxes across the interface.

Symmetry between the two types of interfaces ('diffusive' and 'finger') allows many of the overall properties of the finger interface to be described using minor modifications to the dimensional results obtained for the diffusive interface (Turner, 1979). The important difference is that in this case the driving component across the interface is salt (ΔS), so that, for a given fluid with constant Le and Pr, the salt flux is

$$F_S = k_S \Big(\frac{\beta_s g}{\kappa_S \nu} \Big)^{1/3} \Delta S^{3/4} f(R_\rho), \tag{2.54}$$

where $R_\rho = (\beta_T \Delta T)/(\beta_S \Delta S)$. Turner (1967) found that: (i) like in the ordinary Rayleigh-Benard convection with no-slip impermeable boundary condition, the rate of transfer of salt depends mainly on the salinity difference; (ii) as for the diffusive interface, the salt flux is a function of the density ratio, reducing for larger values of R_ρ. The most striking feature of this result was the large magnitude of the ratio F_S/F_S^*, where F_S^* represents the solid plate diffusive salt flux for an equivalent ΔS. This is, perhaps, not very surprising, since advective motion, evident from visual observations of the salt fingering process (as shown in figure 1.3), suggest that fingers are a much more efficient means of transferring salt than a solid plane diffusive interface. Turner

was unable to make measurements for $R_\rho < 1.5$, as the experiment "run away" so rapidly that reliable measurements could not be made.

The ratio of the density fluxes $\gamma = \beta_T F_T / \beta_S F_S$ measured experimentally was found to be constant, $\gamma = 0.56$, over a wide range of density ratios, as shown in figure 2.6. This value is in agreement with more recent experimental measurements by Schmitt (1979), Taylor and Veronis (1996), and Shen (1993), despite that Turner (1979) supposed that this value could be much smaller as the conditions in his experiment were unsteady. Such a high flux ratio is particularly remarkable, as it implies that salt fingers are a very efficient means for transporting heat in the vertical. In fact, salt fingers are a much more efficient means for transporting heat than the heat flux is for transporting salt in the case where the relative density contributions are reversed.

Chapter 3

Methodology

The following chapter provides a summary of the experimental techniques and apparatus used to perform the collection of experimental data in accordance with the objectives outlined in the introduction chapter. For the exact experimental procedures (based on the techniques and using the apparatus described below) followed to collect the relevant data, the reader is referred to chapters 4, 5 and 6 individually.

3.1 Experimental techniques

3.1.1 Baines' emptying-filling box technique

One way of determining the entrainment coefficient α is using an experimental method first described and verified by Baines (1983), which allows direct measurement of the volume flux in a turbulent plume. The procedure involves the release of a plume into an enclosure through which a known ventilation flux Q_v is imposed on the ambient fluid via input openings at the top of the enclosure and removed through openings at the bottom. A turbulent, negatively buoyant plume initiated at the top of the enclosure descends and spreads out on reaching the bottom of the enclosure to form a dense layer. This dense bottom layer continues to increase in depth until the volume flux $Q(z)$, supplied by the plume into the dense layer at a distance z from the physical source, is balanced by the ventilation flux Q_v. At this point a steady-state is established with the interface at the top of the dense layer located at a fixed distance $\hat{z}$, measured from the plume virtual origin, as illustrated schematically in figure 3.1. In this schematic each distance from the source virtual origin to the interface $\hat{z}_i$ corresponds to a specific value of ventilation volume flux Q_{vi}. In steady state, there is no flow across the interface other than in the plume itself and, therefore, the imposed ventilation flow rate Q_v

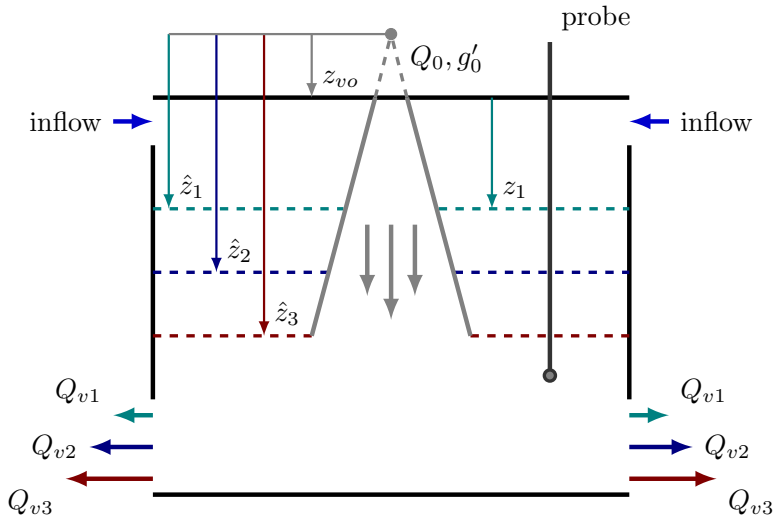

Fig. 3.1 A schematic representation of the 'filling-box' experimental technique. Larger values of ventilation volume fluxes Q_v, correspond to the lower positions of the interface $\hat{z}$, as the plume needs longer distance to develop an equal volume flux. Note that $\hat{z}_i = z_i + z_{vo}$.

equals the plume volume flux. Consequently, the plume volume flux can be determined as a function of distance from the source from measurements of the interface position and, therefore, the entrainment rate into the plume can be calculated directly.

Hence, in order to determine the value of the entrainment coefficient, we located the steady-state interface position $\hat{z}$ for a specific ventilation volume flux Q_v, which equals the plume volume flux at that distance $Q(\hat{z})$. This procedure was repeated for different source buoyancy fluxes B_0 (calculated as the product of the source volume flux Q_0 and source buoyancy g_0') and ventilation volume fluxes to measure the plume volume flux at various distances from the source. By substituting the obtained values of the interface position and plume volume flux, the top-hat value of entrainment coefficient α was determined using (2.42d), rearranged to solve for α as

$$\alpha = \left(\frac{5}{6}\left(\frac{10}{9}\right)^{1/3}\pi^{-2/3}\right)^{3/4} Q(\hat{z})^{3/4}\, B_0^{-1/4}\hat{z}^{-5/4}. \tag{3.1}$$

3.1.2 Shadowgraph technique

Visualisation of flows with spatio-temporal density variations can be done effectively using the shadowgraph technique. The technique is based on the effect of localised variations in the refractive index (in our case induced by the variations in heat and/or salt concentration) on the direction of light beams. In particular, as shown schematically

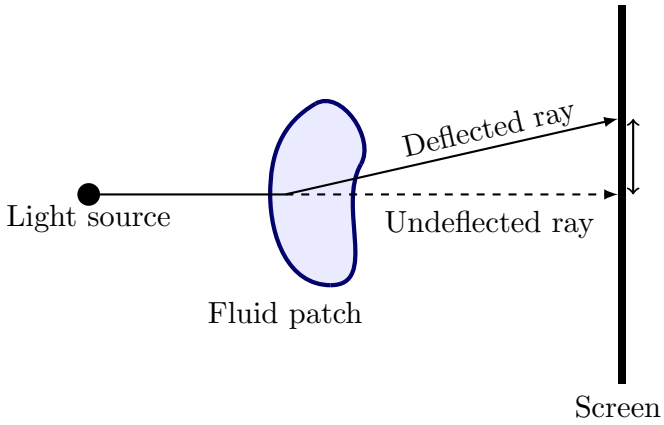

Fig. 3.2 A schematic diagram of the shadowgraph principle.

in figure 3.2, rays of light passing though a fluid patch are deflected according to the refractive properties of that fluid. Projection of the light source onto a screen (in our case a sheet of tracing paper attached to the front surface of the tank wall) produces a visible pattern. The position where the undeflected ray should have arrived becomes dark, while the position where the deflected ray arrives appears brighter than the undisturbed environment. The resulting pattern is a long-path-integrated result of the individual deflections across the entire thickness of the tank.

The technique has a wide range of applications and has been used for studying various effects in aerodynamics Weinberg and Weinberg (1963), combustion Holder and North (1963), as well as geophysical flows Turner (1979). For an extensive summary of the development of this technique, including examples of its applications to various fields of fluid mechanics the reader is referred to Settles (2012). In our work, this method was used to qualitatively visualise the flow only; it was not used for quantitative measurements of the density structures developed within the filling box/ambient tank during our experiments.

3.1.3 Particle Image Velocimetry

Particle image velocimetry or 'PIV' is a non-intrusive laser optical measurement technique used for determining the instantaneous velocity fields of a global (2D or 3D) flow with high accuracy. As follows from the name, PIV uses visual measurements, containing the temporal evolution of the positions of small tracer particles to extract the local fluid velocity.

In order to function, PIV requires four basic components: (1) an optically transparent test section containing the flow seeded with tracer particles; (2) a light source

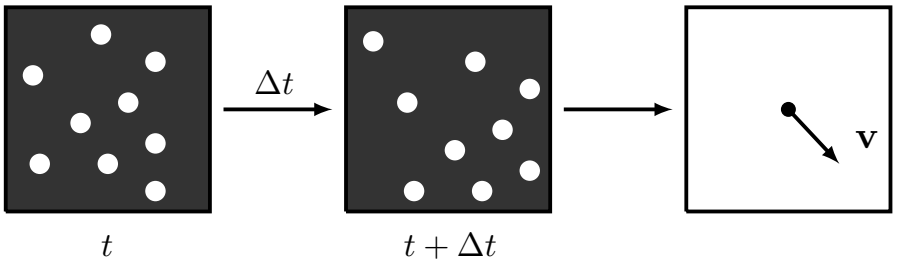

Fig. 3.3 A schematics representation of an interrogation window at times t and $t + \Delta t$. Cross correlation algorithm compares the two images to calculate the velocity vector $\mathbf{v}$.

(normally a laser) to illuminate the plane of interest; (3) a visual recording device (CCD camera); (4) computer for data storage and processing to extract velocity information from the obtained images of tracer particle positions.

Provided these four basic requirements are met, the PIV procedure is typically executed as follows. A camera (in our case Camera A described in section 3.2.8) captures a sequence of images of the flow field seeded with small particles at regular time intervals. The bright dots, present on the obtained images, are the result of the light being scattered from seeding particles in the plane of the laser sheet. Pairs of subsequent images are then used to calculated local displacement vectors for a known time step Δt using a matching algorithm.

The algorithm typically breaks down an image into a number of small regions (hereafter referred to as "interrogation windows") and interrogates the movement of small groups of particles within them. As such, a pattern matching algorithm uses a correlation function to determine the optimal pixel displacement shift sequentially for each interrogation window. The obtained displacement measurements are then used in conjunction with the camera calibration described in section 3.2.8 to construct velocity fields. This process is illustrated schematically in figure 3.3, where the white circles represent the seeding particles. Performing accurate, high-resolution PIV measurements depends on a number of factors, including the dynamical and optical properties of the particles used, the particle seeding density, the camera setup and the properties of the light sheet, all of which are discussed in detail in section 3.2.

3.1.4 Laser Induced Fluorescence

Laser Induced Fluorescence (LIF) is a non-intrusive spectroscopic measurement method, in which the spontaneous emission of light is triggered by exciting a molecule to a higher energy level using a laser. Depending on the thickness of the laser sheet, the obtained data can be typically treated as 2-dimensional, representing the instantaneous

planar scalar field within a flow. Similarly to PIV, the technique requires a light source (typically a laser), fluorescent dye (e.g. Rhodamine 6G), visual recording device (CCD camera) and a computer for image processing. This signal captured by the camera can be related to the concentration of the dye, and subsequently to the density field of the flow, by calibration.

Combined with PIV, these two techniques allow for simultaneous measurements of the velocity and the scalar fields within a flow, provided that the diffusivities of the dye and of the scalar quantities are similar. For example, in the context of turbulent plumes Burridge et al. (2017) performed simultaneous PIV and LIF measurements to combine the information about the scalar salinity edge of the flow with its velocity field and perform conditional analysis of plume properties.

3.1.5 Dye attenuation

Dye attenuation is a non-intrusive technique that allows measurements of either the concentration of dye in a fluid, or the depth of a dyed fluid patch. The method is based on an image processing routine developed by Dalziel in 1989 as part of the image processing system DigImage (Dalziel, 1992) and is explained in detail by Cenedese and Dalziel (1998). The technique uses Beer-Lambert theory of light absorption and requires a thorough calibration. The calibration used for our experiments is laid out in appendix F. A short summary of the theoretical underpinnings for this technique are laid out below.

According to the classical light absorption theory of Lambert-Beer, the rate of change of the intensity $I(y, c)$ of a beam of light, travelling in the y-direction through a dyed fluid of concentration c, is given by

$$\frac{\mathrm{d}I}{\mathrm{d}y} = -\xi I, \tag{3.2}$$

where ξ is the rate of absorption and is some function of dye concentration $\xi = \xi(c)$. Supposing that the concentration along a ray of light is a constant, i.e. $c(y) = c$, integration of (3.2) along the ray gives

$$I(h, c) = \hat{I}_0 \, e^{\xi(c)h}, \tag{3.3}$$

where h is the total distance a ray of light has travelled through the dyed water and $\hat{I}_0$ is the illuminating light intensity before it has travelled through the tank. The absorbency of the dye ξ is assumed to be a function of dye concentration only, and has

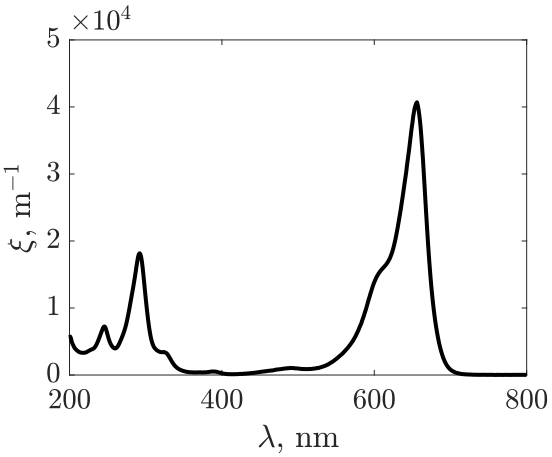

Fig. 3.4 Absorption spectra of Methylene Blue dye (courtesy of Masahiko Taniguchi).

to be determined using calibration experiments. Provided that the dye concentration is low, the absorbency function $\xi(c)$ can be approximated to be linear in concentration

$$\xi(c) = Ac + b, \quad \text{with} \quad A, b > 0, \tag{3.4}$$

where constant A determines how increasing the concentration affects the attenuation, and constant b is the attenuation of the undyed water. By using $I_0 = I(h, 0) = \hat{I}_0 e^{-bh}$, we may, in practice, take

$$\frac{I}{I_0} = e^{-Ach}, \tag{3.5}$$

where I_0 factors in any of the light attenuated by such factors as air, tank walls and ambient water.

In our experiments we used methylene blue, which is a common choice for dye attenuation measurements for multiple reasons. Most importantly, this dye is safe and its concentration can be controlled manually between batches, since unlike other dyes, such as food colouring, it can be hand-made in the laboratory.

Accurate measurements using the dye attenuation technique rely greatly on appropriate choice of the background light for a given choice of dye. As shown in figure 3.4, the peak in the absorption spectrum of methylene blue $\xi(c, \lambda)$ occurs at the wavelengths of $\lambda \sim 660$ nm. In principle, large values of absorption are preferred, since that would only require a small amount of dye to provide strong differences in the signal received by the visual recording device. In addition, linear approximation of the absorption function only works for a limited range of low values of dye concentration. Given the choice of methylene blue as the working dye, in order to maximise contrast, we therefore used red colour background lights to illuminate the field of view.

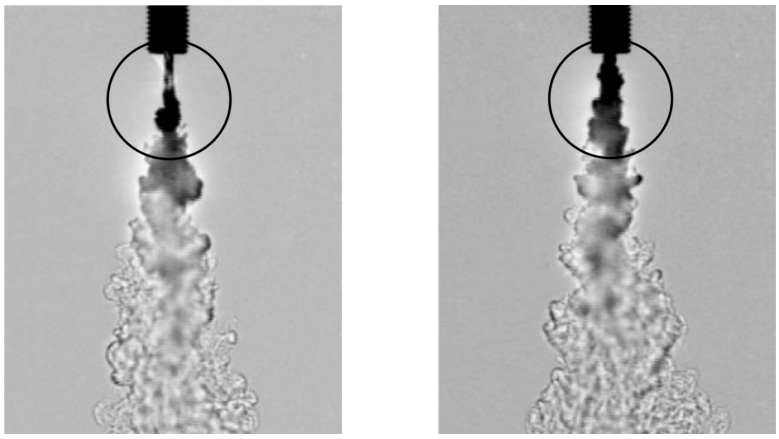

(a) (b)

Fig. 3.5 Shadowgraph images showing turbulent plumes ($Re_0 = 220$) produced by two different nozzle designs: (a) a cylindrical tube of constant cross-section with a fine mesh at the outlet and (b) nozzle based on Dr Paul Cooper's design Hunt and Linden (2001a). The vertical distance from the source to the point at which the plume becomes turbulent is approximately 3 source diameters in (a) and 1 source diameter in (b).

3.2 Experimental apparatus

3.2.1 Plume nozzle

The entrainment model of Morton et al. (1956) is only valid for fully turbulent flows. It was therefore essential for our experiments to ensure that the flow becomes turbulent immediately at the source. A simple way of promoting turbulence at the outlet is to increase the flow speed and hence the source Reynolds number. This method, however, would create a problem of introducing excessive momentum into the flow, shifting the balance of buoyancy and momentum, captured in the plume Richardson number (Γ_0), towards a momentum-dominated buoyant jet rather than a plume. This, in turn, would have direct implications on the accuracy of the entrainment coefficient measurements, and thus had to be avoided.

The solution to this problem, was to eject the fluid through a plume nozzle, specifically designed to promote turbulence within the flow. The nozzle, originally designed by Professor Paul Cooper and illustrated schematically in Hunt and Linden (2001b), achieves this by passing the flow through a 'pin-hole' (diameter 1 mm) and then into a wide expansion chamber (diameter 10 mm) before exiting through the nozzle bore (diameter 5 mm). The sharp expansion acts to excite turbulent flow in the chamber prior to discharge from the nozzle. Figure 3.5 demonstrates visually the effect of using the Professor Cooper's nozzle design.

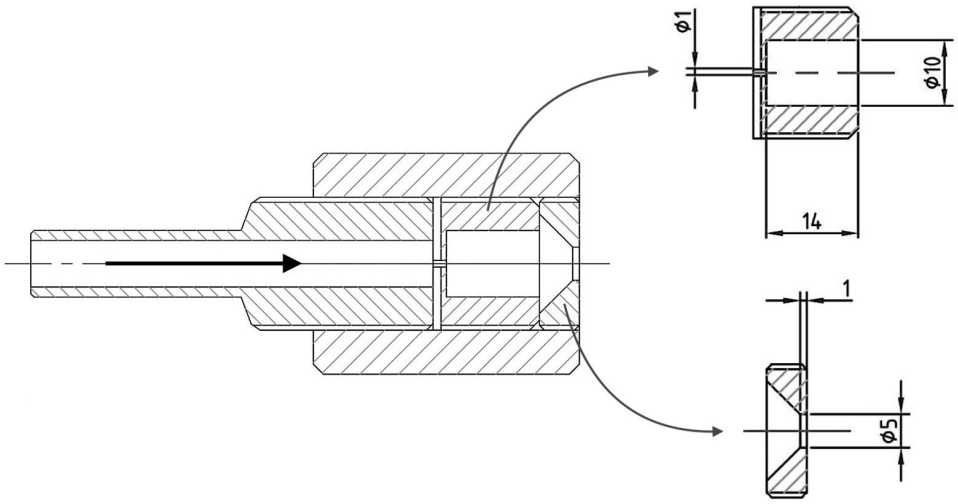

Fig. 3.6 Modified supply nozzle modular design (dimensions shown in mm), based on a design originally conceived by Professor Paul Cooper of the Faculty of Engineering, University of Wollongong, NSW, Australia.

A schematic diagram of the modified version of the original nozzle design, used for our experiments with turbulent plumes is shown in Figure 3.6. The nozzle was made up of three distinct sections: supply channel, expansion chamber and nozzle outlet. The internal dimensions of the expansion chamber and nozzle outlet are shown separately in figure 3.6. The modular design allowed for easy nozzle cleaning and agile design modifications, such as changing the bore radius. The final design had a circular bore of radius $r_0 = 2.5\,\text{mm}$. Despite the moderate source Reynolds numbers for typical experiments ($Re_0 = M_0^{1/2}/\nu \approx 300$), the additional excitation of the flow prior to discharge ensured that the vertical distance from the source to the point at which the plume becomes turbulent was approximately one source diameter. This distance was deemed sufficiently low for the entrainment assumption to be used.

The nozzle design used for the jet experiments was based on the nozzle design described above in this section with a few minor modifications specific for the experiment. For further details on the jet nozzle design, the reader is referred to chapter 6.

3.2.2 Water bath

Warming up a salt solution for both plumes and jets experiments to a set temperature of up to 80.0 ± 0.1 °C was performed using a 1 kW Grant LTC4 water bath. For our experimental setup, 80.0 °C was the highest temperature that could be safely supplied through the pumps to the nozzle. The total capacity of the water bath of 20 l was

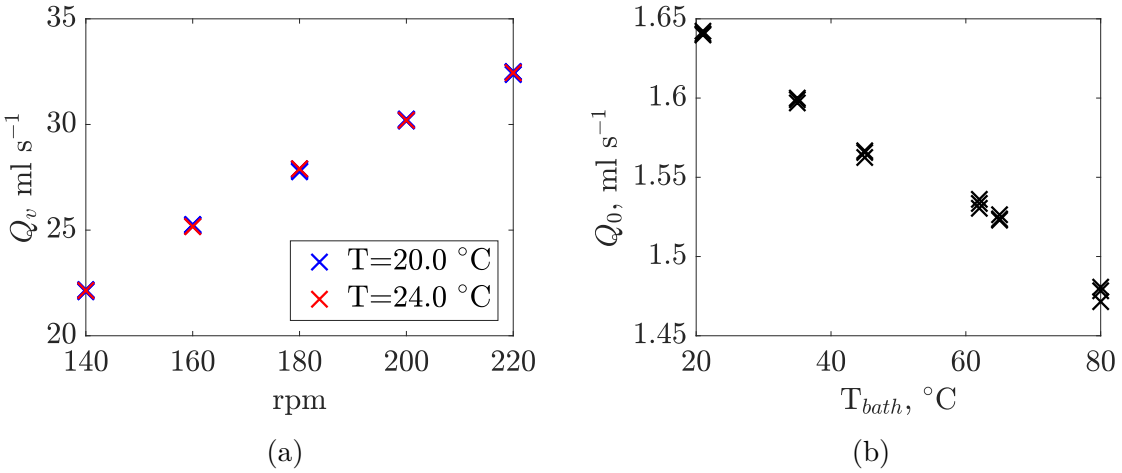

Fig. 3.7 Calibration plots for: (a) peristaltic pump at five different flow rates and two temperatures, with the experimental error of ±0.1 ml s^{-1}; (b) gear pump at a constant reference flow rate for six different temperatures of the fluid in the water bath, with the experimental error of ±0.045 ml s^{-1}.

sufficient to run an experiment continuously without resupply for ≈90 min. This was more than sufficient for the jet experiments. However, to perform multiple experiments with double-diffusive plumes at a known constant density without running out of warm fluid, the reservoir had to be continuously resupplied with the salt solution from a large tank at ambient temperature by a small peristaltic pump. The resupply flow rate was equal to the volume flux at the plume source, effectively setting up a ventilation flow. The flow rate of the incoming fluid was small (a minute of continuous resupply amounts to ≈ 0.5% of the total reservoir capacity), and therefore did not have any noticeable effect on the temperature of the salt solution in the water bath and hence the source plume fluid.

3.2.3 Supply, resupply & extraction pumps

Fluid supply, resupply and extraction (ventilation) was performed by means of a gear pump and two peristaltic pumps, respectively. The supply pump used for the ejection of source fluid in both plume and jet experiments consisted of a Cole-Parmer Masterflex Digital Pump System connected to a Micropump gear head with a resolution of 0.316 ml/rev. The ventilation pump used in the Baines' filling-box experiments was the Watson-Marlow 520Du Peristaltic Pump. An additional multi-channel peristaltic pump Watson-Marlow 505U was used for replenishment of the fluid in the water bath at a flow rate matching the flow rate of the supply pump.

The choice of using the higher precision gear pump for plume/jet fluid supply was based on the extreme sensitivity of flow dynamics to the source conditions, which thus had to be controlled with extra care. In addition to the lower instrumental error, in comparison to the peristaltic pump, the gear pump did not have the disadvantage of producing noticeable pulsation in the flow even at low volume fluxes. Although pulsations were inevitably produced by the gear pump as well, their amplitude was significantly lower, with the associated frequency being significantly higher, making the flow effectively uniform and continuous.

All pumps were carefully calibrated over the range of volume fluxes used. Calibration for the extraction peristaltic pump is shown in figure 3.7a, with the typical error of $\pm 0.1\,\mathrm{ml\,s^{-1}}$ ($\pm 0.5\,\%$), estimated as the average of two standard deviations about the mean values of calibration measurements. The gear pump was calibrated using a built-in calibration feature. Despite having rather high accuracy and repeatability, the pump had an important drawback in that the flow rate it produced was sensitive to the pressure difference between the points of intake and supply. For that reason, calibrations were performed in conditions closely matching an actual experiment, i.e. water bath full and the nozzle positioned at the correct height inside the experimental tank. Performed in this manner, the typical error of the source flow rate did not exceed $\pm 0.045\,\mathrm{ml\,s^{-1}}$ ($\pm 0.3\,\%$), estimated as two standard deviations about the mean values of the flow rate measurements during calibration. The resupply peristaltic pump was the least repeatable, with the typical error of $\pm 0.3\,\mathrm{ml\,s^{-1}}$ ($\pm 20\,\%$). It was, however, arguably the least critical component of the experimental setup, and therefore such level of uncertainty was tolerable.

We also observed a dependence of the pump volume flux output on the fluid temperature. In particular, for extreme cases of temperature in the water bath at $80\,^{\circ}\mathrm{C}$, we observed as much as 10% reduction in the volume flux, as shown in figure 3.7b. Such drastic reduction could not be accounted for by effects of volumetric thermal expansion, causing the fluid to reduce in volume on the way from the water bath to the supply nozzle. Experiments with thermohaline plumes therefore required additional volume flow rate calibrations at different fluid temperatures. Great care was taken to perform these calibrations before each experiment at a new temperature.

Temperature calibration of the extraction pump was performed at a fluid temperature of $24\,^{\circ}\mathrm{C}$, which was $0.5\,^{\circ}\mathrm{C}$ greater than the highest temperature difference ever observed in the bottom layer of the filling-box. As shown in figure 3.7a, such low temperature variations did not produce any noticeable deviations in the volume flux outputs.

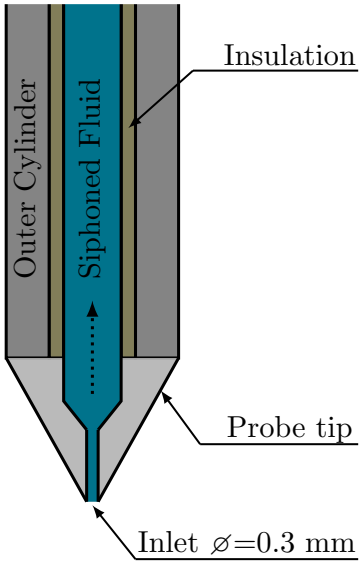

Fig. 3.8 A schematic diagram of the conductivity probe internal design around the tip. Dotted arrow indicates the direction of the ambient fluid siphoning through the probe.

3.2.4 Conductivity probe

We used an aspirating conductivity probe to measure the salinity stratification within the filling-box, and to consequently determine the location of the salinity interface. Shown schematically in figure 3.8, the probe consisted of two long concentric conductive cylinders, separated by an insulator, and connected to a 15 mm long conical probe tip, made of Delrin (acetal resin). The tip has a very narrow (0.3 mm diameter) hole which allows the ambient fluid to be siphoned through. This probe design originated at DAMTP in around 1995, and was subsequently modified to its current state, as used by Holford and Linden (1999).

The principle of operation of the conductivity probe is based on the direct relationship between electrical conductivity of a fluid and the concentration (and mobility) of the ionized solutes within it. When the fluid is siphoned through the probe, an electrical circuit is established between the inner and outer cylinders via the ambient fluid. Since the resistivity of the fluid at the tip is much larger than anywhere else within the probe, the conductivity between the inner and outer cylinders is dominated by the fluid currently at the tip. The measured values of conductivity can then be converted into salinity through an established calibration curve, and hence, assuming a single solute, to fluid density.

During measurements, the ambient fluid in the vicinity of the tip of the probe was siphoned through the head and subsequently expelled from the device at a rate of

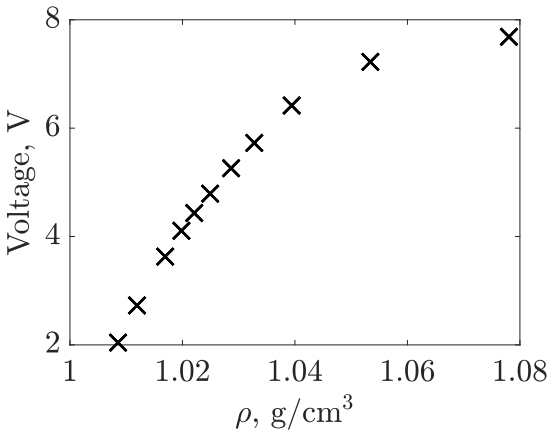

Fig. 3.9 Conductivity probe's voltage output for a range of solution densities $1.01 < \rho < 1.08\ \mathrm{g\,cm^{-3}}$. Figure shows the increasing non-linearity of the voltage output for greater density, indicating the need for multiple calibrations over short density intervals. The typical error for these measurements was ±0.05 V, estimated as one standard deviation of the temporal fluctuations of the voltage readings taken at a fixed fluid salinity.

$\approx 0.1\,\mathrm{ml\,s^{-1}}$. Given the miniature tip channel width, such siphoning volume flux is sufficient to move the fluid parcels through the head at $O(1\,\mathrm{m\,s^{-1}})$, thus allowing for a rapid response to any changes in salinity.

In our experiments, we used NaCl solution (containing dissolved Na^+ and Cl^- ions) as our conductive fluid for its availability, however, in principle any other conducting solute could be used. Probe calibration was performed by measuring the changes in the resistivity of the fluid for known changes in the concentration of NaCl. Care was taken to ensure no contamination of test beakers with other solutes, so as to relate fluid conductivity to its density directly. Figure 3.9 demonstrates an example of such calibration curve for solution densities of $1.01 < \rho < 1.08\ \mathrm{g\,cm^{-3}}$. It is clear from that figure that over a large range of densities, the voltage response to an increase in the solute concentration is nonlinear. This means that using a single calibration curve would yield a poor signal-to-noise ratio for large density fluids. We therefore performed multiple calibrations, shown in appendix D, 'zooming' into the specific sections of the density range to maximise the noise-to-signal ratio. The selection of a calibration file for a specific experiment was based on the approximate predicted maximum salinity within the stratification.

The conductivity of salt water is also temperature dependent. However, given that we were only interested in large spatial changes in salinity, rather then their absolute values, and that the temperature variations during our experiments never exceeded 3.5 °C, the effect of temperature on conductivity was negligible.

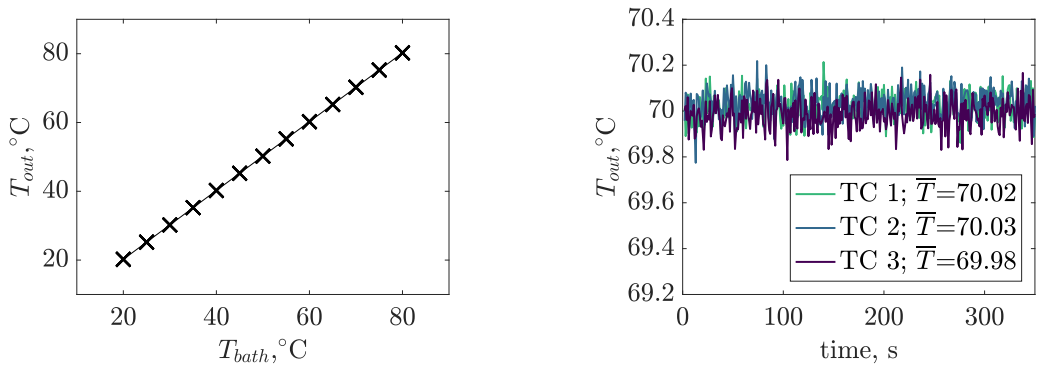

(a) (b)

Fig. 3.10 Thermocouples: (a) calibration plot for all seven thermocouples over an appropriate temperature range of 20–80±0.1 °C; (b) time series of temperature readings for three thermocouples placed into water bath at 70 °C upon calibration.

3.2.5 T-type thermocouples

For experiments with plumes and jets, temperature data was recorded at 5 Hz using seven T-type thermocouples connected to National Instruments equipment (NI 9213). The choice of type T was based on its stability and repeatability within a temperature range from -200 °C to 200 °C. The thermocouples were calibrated in DigiFlow by placing them in a water bath over an appropriate temperature range (20–80 °C). The obtained calibration curve, presented in figure 3.10a, shows a linear behaviour of the thermocouples over the entire temperature range and is well approximated using a linear fit with an accuracy of within ±0.05 °C. Figure 3.10b shows the time series output of three thermocouples tested inside a water bath at 70 °C for 350 s upon calibration. The figure shows that the thermocouples had a stable signal, with their time-averaged readings being well within the calibration uncertainty. Shown in figure 3.10b, the temporal temperature signal had considerable level of noise, present for all thermocouples. We therefore used ±0.1 °C, which represents two standard deviations around the mean of the temporal temperature fluctuations averaged for all thermocouples, as a measure of uncertainty of temperature readings.

3.2.6 Tracer particles

The ability to make robust PIV measurements relies critically on the appropriate choice of the tracer particles, with the two major considerations being the particle size d_p and density ρ_p. First, particles should be small enough to follow closely the fluid flow, yet large enough to be clearly seen by the camera, i.e. taking up to 2-3 pixels

in the obtained image (Prasad et al., 1992). The tendency of the particles to follow the fluid streamlines is described by the Stokes number, which, as discussed by Xu and Bodenschatz (2008), for particles smaller than the Kolmogorov lengthscale η_K, is commonly defined as

$$St = \frac{1}{18}\Big(\frac{\rho_p}{\rho_a}\Big)\Big(\frac{d_p}{\eta_K}\Big)^2. \tag{3.6}$$

Second, particle density should be close to that of the ambient, to minimise buoyancy-induced motion, otherwise particles will either quickly rise to the surface or sink down to the bottom of the tank, prohibiting the use of PIV. For spherical particles at low Re, the associated buoyancy-induced particle settling velocity is given by the Stokes settling velocity

$$U_p = g d_p^2\Big(\frac{\rho_p - \rho_a}{18\mu}\Big). \tag{3.7}$$

With these considerations in mind, we chose to use spheroidal polyamide particles (Orgasol 2002 ES5 NAT 3) in our experiments, with diameter $d_p = 50\,\mu\text{m}$. Particle density was determined by adding a small patch of particles into a linear stratification created within a measuring tube. By sampling the fluid density around the particles settlement locations, we identified a narrow bi-modal density distribution, with strong peaks at $\rho_{p-} = 1.023\,\text{kg}\,\text{m}^{-3}$ and $\rho_{p+} = 1.025\,\text{kg}\,\text{m}^{-3}$. We therefore approximate the particles density as the average of the two measurements, i.e. $\rho_p = 1.024\,\text{kg}\,\text{m}^{-3}$.

Using the estimate for the Kolmogorov lengthscale made in section 2.5.1, and assuming that the density of the particles matches that of the ambient fluid, we obtain $St \sim O(10^{-4}) \ll 1$. This implies that the selected particles acted as passive tracers in the flow, closely following the fluid motion. In addition, taking the difference between the density of the particles and that of the ambient fluid as $(\rho_p - \rho_a) \sim O(10)\ \text{kg}\,\text{m}^{-3}$, the resulting particle settling velocity is $U_p \sim O(10^{-5})\ \text{m}\,\text{s}^{-1}$. Such a low value of settling velocity means that it would take a particle positioned at mid-height of the experimental tank $O(10)$ hours to settle to the bottom of the tank with depth of $O(1)$ m. In addition, the value of U_p is substantially smaller than the typical velocity scales of the fluid flow in our experiments, further validating our choice.

3.2.7 Laser

We used two frequency-doubled dual-cavity Litron Nano L100 Nd:YAG pulsed lasers with wavelength 532 nm, operated at a frequency of 70 Hz, to create a light sheet with a thickness of 1 – 2 mm for the simultaneous PIV/LIF measurements of velocity and scalar fields of single- and double-diffusive plume flows, presented in chapter 5.

3.2.8 Cameras

Collection of visual data was done by means of three cameras. The first was the 12 megapixel ISVI B/W CXP digital CoaXPress camera, producing 8-bit output. Images were taken at a frame rate of 15 frames per second. This camera was used for visual measurements of experiments with plumes and jets described in chapters 4 and 6.

Two other cameras (Allied Vision Technologies, Bonito CMC-4000) were used to record the plume flow in the light sheet for the experiments summarised in chapter 5. Each camera had a resolution of 4 megapixels and was equipped with a 50 mm Nikon lens. One camera (referred to as "Camera A") was used to obtain PIV measurements (details of which are provided in section 3.1.3), and the other camera (referred to as "Camera B") was used to obtain LIF measurements (details of which are provided in section 3.1.3). The cameras were triggered simultaneously with the lasers via DigiFlow, allowing for precise synchronisation between the laser pulses and frame capture.

In an ideal case, one would want both cameras to be positioned at a single point, both looking perpendicularly onto the light sheet. However, due to the non-negligible physical dimensions of the cameras, this could not be achieved in practice. With this restriction, care was taken to position the two cameras in a way so to maximise the overlapping area in their field of view. We chose to position Camera A (taking the images for PIV) normal to the light sheet. This was done to collect higher quality images for the PIV measurements, as the accuracy of the obtained PIV measurements is significantly more sensitive to the quality of the input images than for the LIF measurements. In particular, by placing Camera A perpendicular to the light sheet, it was easier to focus the camera over the region of interest for the acquisition of high resolution data. Camera B was consequently facing the light sheet at a small angle to the normal, which was corrected for in subsequent image processing.

3.3 Conclusion

Equipped with the modern measurement instruments described in section 3.2, the multiplicity of experimental techniques outlined in section 3.1 allowed us to collect a range of repeatable and accurate experimental measurements, in line with the objectives summarised in chapter 1. The only significant experimental limitation related to the simultaneous PIV/LIF measurements was the inability to refractive index match the plume and ambient fluids in the presence of strong, simultaneous temperature and salinity gradients. This will be discussed in greater detail in chapter 5.

Chapter 4

Direct Measurements of Entrainment in Plumes

In this chapter we investigate experimentally the effect of double diffusion in the salt-fingering configuration on the rate of entrainment in turbulent plumes. Plumes over a range of source buoyancy fluxes B_0 and source density ratios R_ρ are examined. Measurements of the entrainment coefficient for single- and double-diffusive plumes were performed using the Baines' filling-box technique, described in section 3.1.1. In addition, we present visual observations of the flow made using simple dye visualisations and the shadowgraph technique described in section 3.1.2.

4.1 Introduction

Many of the previous experimental investigations on double-diffusive plumes (Turner and Chen (1974); McDougall (1983); Turner (2003)) were performed using salt-sugar combinations. Working with salt and sugar solutions is practical in many ways: both agents are cheap and readily available, they are safe to use and do not require special handling, and, unlike heat, are conserved in a physically-closed system. These attributes motivated us to perform initial experiments with sugar plumes in a salt environment. However, our preliminary test experiments uncovered a number of critical disadvantages of using this combination for turbulent plume experiments, as outlined below.

The first effect is associated with the unexpected and undesirable behaviour of the conductivity probe, in presence of strong sugar content. In theory, the signal obtained using the conductivity probe should not be affected by the presence of sugar molecules, since no ions are formed when sugar is dissolved in water. However, our test measurements showed a measurable effect. Fig.4.1 demonstrates the dependence

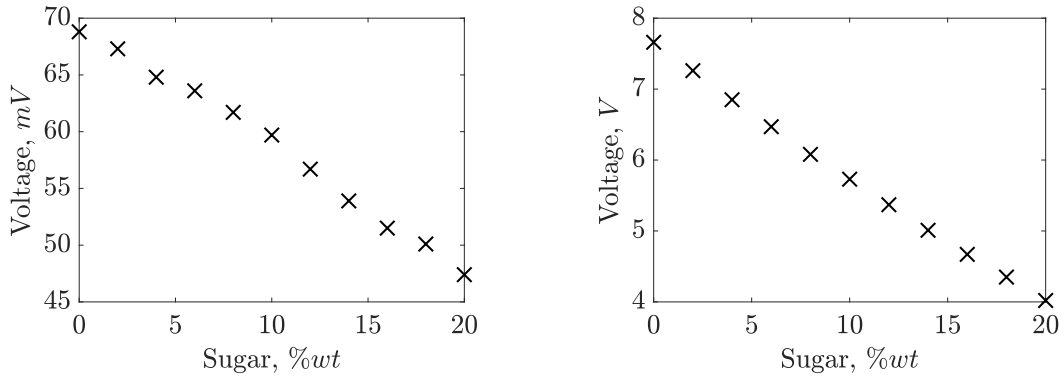

(a) (b)

Fig. 4.1 The dependence of the voltage output of the conductivity probe vs the concentration of sugar (a) in fresh water at a constant total solution mass of 300 g, with the experimental error of ±0.1 mV; (b) in a salt solution at a constant total solution mass of 300 g, with the experimental error of ±0.05 V.

of the conductivity probe output in volts on the sugar content by weight in fresh water and salt solution. Two cases were considered, (i) sugar in fresh water at a constant total solution mass (300 g); (ii) sugar in salt solution at a constant total solution mass (300 g). All solutions were prepared and left overnight to fully dissolve and equilibrate in temperature prior to measurements. As shown in figure 4.1, in all cases, the voltage output drops linearly with increase in the sugar content. This linear decrease could be the consequence of an increased number of sugar molecules in the solution which impede the motion of conductive ions, thereby reducing conductivity and hence voltage output. Given such behaviour, it was impossible to perform reliable measurements of the density structures within the filling-box without additional calibrations for the dependence on sugar concentration.

The second, perhaps more critical observation is associated with the effect of sugar content on fluid viscosity. The relatively low Lewis number for salt-sugar configuration ($\kappa_S/\kappa_C = 3$), implies that for the double-diffusive processes to have a significant effect, the concentration gradients of both scalars have to be high. However, using a relatively high concentration ($> 20\%wt$) sugar solution had an undesirable side effect of increasing the fluid viscosity, which, in turn had a drastic effect on the plume behaviour in the early stages of its development. Visual inspection of sugar plumes around the source revealed that the flow was considerably less turbulent than for a salt only plume at equivalent source volume/buoyancy flux. This effect is shown in figure 4.2, where salt and sugar plumes with equivalent source conditions were ejected through the nozzle designed by Professor Paul Cooper and described in section 3.6, which acts to

(a) Salt Plume (b) Sugar Plume

Fig. 4.2 Photographs showing the difference in the near-source behaviour of: (a) salt plume and (b) sugar plume at the same source density of $\rho_0 = 1.120\ \mathrm{g\,cm^{-3}}$ ejected into fresh ambient at $Q_0 = 1.27\ \mathrm{ml\,s^{-1}}$. Note the difference in the plume behaviour close to the source, where the sugar plume appears significantly less turbulent.

promote turbulence at the source. The lack of source turbulence in the case of the sugar plume, clearly seen in figure 4.2b, is likely to be a result of a $\simeq 3.2$ increase in viscosity at 30% sugar concentration (Swindells, 1958). Attempts were made to create additional excitation of plume fluid at the ejection point by changing the mesh and using mechanical vibrations. However, these did not provide a satisfactory improvement of the plume behaviour. Experiments at lower sugar concentrations could be performed, but for lower source concentration gradients the effects of double diffusion would be less pronounce, and even if sufficient to still make a difference to plume behaviour, we would not have had certainty that they are not due to the effect of viscosity. Therefore, for our experiments we chose to work with the aqueous heat-salt ('thermohaline') system in which a hot, salty plume descends into cooler, fresher water. For this combination, the component with the larger molecular diffusivity κ_T is temperature T and that with the smaller molecular diffusivity κ_S is salinity S. The ratio κ_T/κ_S is $O(100)$, and therefore for large concentration gradients of both components the system is strongly doubly-diffusive.

The rest of this chapter is structured as follows. In section 4.2, we describe the experimental procedure that was followed to collect the experimental data. We then derive a simple analytical model describing the filling box process and use it to validate the experimental procedure by comparing the analytical predictions against three test experiments in section 4.3. In section 4.4 we summarise and discuss the key observations and results, highlighting the differences in entrainment between single-diffusive and double-diffusive plumes. We also propose explanation for the observed differences. Finally, in section 4.5 a series of conclusions is drawn.

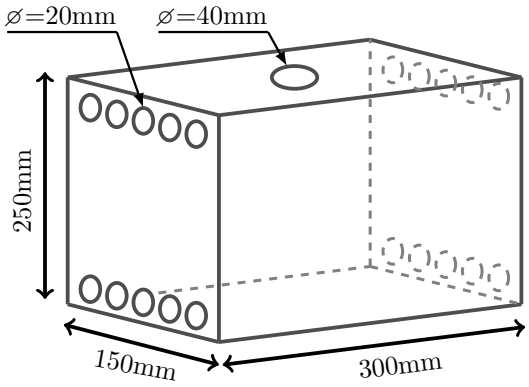

Fig. 4.3 A schematic representation of the 'filling-box' with its relevant dimensions.

4.2 Experimental procedure

All filling-box experiments were conducted in a clear Perspex (acrylic) tank, shown schematically in figure 4.3, submerged in a larger 'environmental' tank, measuring 2.5 m x 0.7 m x 0.8 m (L x W x H), filled with uniform ambient fluid. The submerged experimental tank, herein called the 'filling-box', had five identical circular openings with diameter of 20 mm on each side at the top and bottom, which were used for fluid drainage and resupply. The bottom openings of the filling-box were connected to a peristaltic pump, which extracted the dense bottom layer fluid during the experiment at a known constant volume flow rate in the range $21.8 - 32.4 \pm 0.1$ ml s^{-1}, where the error represents two standard deviations about the mean of the calibration measurements. To conserve volume, the top inlets were left open, allowing the ambient fluid to freely replace the extracted fluid at the same constant flow rate. Over this range of ventilation flow rates the maximum vertical velocity averaged over the area of the filling-box was less than 0.8 mm s^{-1}, which was much less than the typical plume velocities at the source of ~80 mm s^{-1} and had no effect on the plume itself. We also assumed that the filling-box is well-insulated, as verified in Appendix C. The entire experimental setup is shown schematically in figure 3.1.

Plumes were created by steadily ejecting negatively buoyant solution though the specifically designed plume nozzle located at the top of the filling-box using a gear pump. The pump was carefully calibrated over the range of volume fluxes used, i.e. $1.3 \leq Q_0 \leq 1.6$ ml s^{-1} ml s^{-1}. For the details of nozzle design and pump calibration, the reader is referred to subsection 3.2.1. Note that the plume source flow rate was approximately 5% of the ventilation rate and was accounted for using the virtual origin correction, described in section 2.7.2. As shown in table 4.2 the values of z_{vo} range from 10 – 31 mm which is small compared with the distance to the interface,

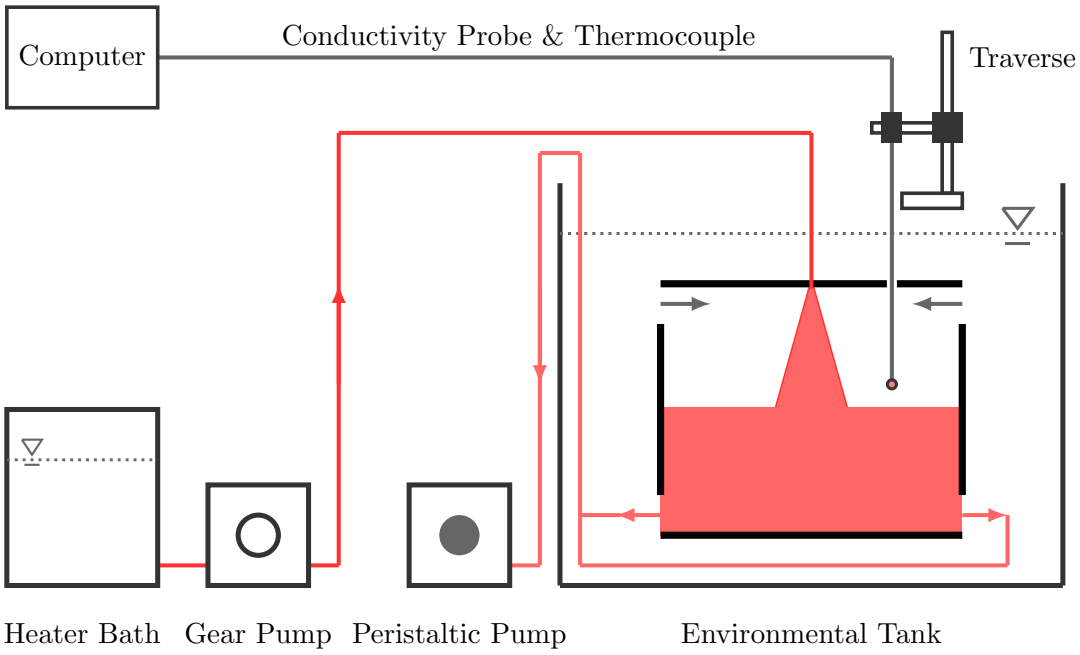

Fig. 4.4 A schematic representation of the 'filling-box' experimental setup.

typically 100 – 150 mm where measurements were taken. Validation of this correction was confirmed as we obtained a constant entrainment coefficient value for a range of interface heights of salt-only experiments (see section 4.4.2).

Thermohaline source fluid was created by heating a solution of known salt concentration to a set temperature of up to 80.0 ± 0.1 °C using the 1 kW Grant LTC4 heater bath. For our experimental setup, 80.0 °C was the highest temperature that could be safely supplied to the nozzle. The inevitable heat losses, occurring during the supply of the plume fluid from the heater bath to the discharge point, were reduced by thermally insulating the connecting pipework and minimising the total distance from the heater bath to the nozzle. Nevertheless, even the slightest variations in the ambient conditions created unavoidable fluctuations in the plume temperature at the discharge point, which thus had to be monitored. This was done by means of two T-type thermocouples inserted into the nozzle. The insertion of the thermocouples into the nozzle was done via a 3D printed custom designed V-connector, shown schematically in figure 4.5. The connector allowed to merge the plume fluid supply and the thermocouples into a single pipe, connected to the supply nozzle. Done in this way, the thermocouple tips were submerged fully into the fluid flow, minimising the noise temperature signal from the ambient, and had precise and secure positioning. These thermocouples were positioned with 10 mm vertical spacing, with the distance upstream from the nozzle outlet to the furthest thermocouple fixed at 35 mm. The geometry of the nozzle did not allow

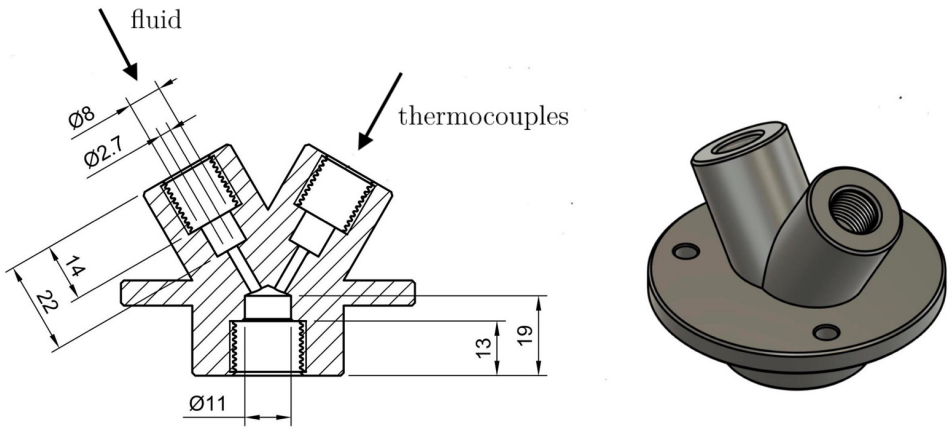

Fig. 4.5 A schematic diagram of a custom designed V-connector for insertion of thermocouples into the supply fluid flow (measurements in mm).

closer positioning of the thermocouples to the source outlet. The temperature at the point of discharge was then estimated by linearly extrapolating the temperature loss over the 10 mm spacing between the thermocouples to the nozzle outlet. As well as measuring the temperature within the nozzle, the readings were used to check that the supply temperature remained constant throughout an experimental run. Another four thermocouples were located in the environmental tank around the experimental tank inlets to monitor the temperature of the incoming ambient fluid. For the details of the heater bath and thermocouples calibration, the reader is referred to subsections 3.2.2 and 3.2.5, respectively.

The densities of the saline plume fluid and the ambient fluid were measured using the Anton Paar DMA5000 densitometer with the accuracy of $\pm 1\,\mu g\,cm^{-3}$, and, using the source volume flux, the source buoyancy flux was determined for the single-diffusive plumes. In the case of heat-salt combinations, the source density of the supply fluid was evaluated using the equations of state of Ruddick and Shirtcliffe (1979) from the known values of salinity and temperature at the source.

A probe, consisting of a conductivity sensor and a thermocouple (identical to the fixed thermocouples) was mounted on a traverse mechanism that was used to obtain vertical profiles of temperature $T(z)$ and conductivity $S(z)$ in the ambient fluid away from any regions directly affected by the plume. For greater detail on the conductivity sensor's principle of operation and calibrations, the reader is referred to section 3.2.4. Since the temperature variations in the ambient fluid were at most 3.5 °C in all experiments, the effect of temperature on conductivity was negligible compared to that of salt, and the conductivity measurements could be considered as a good

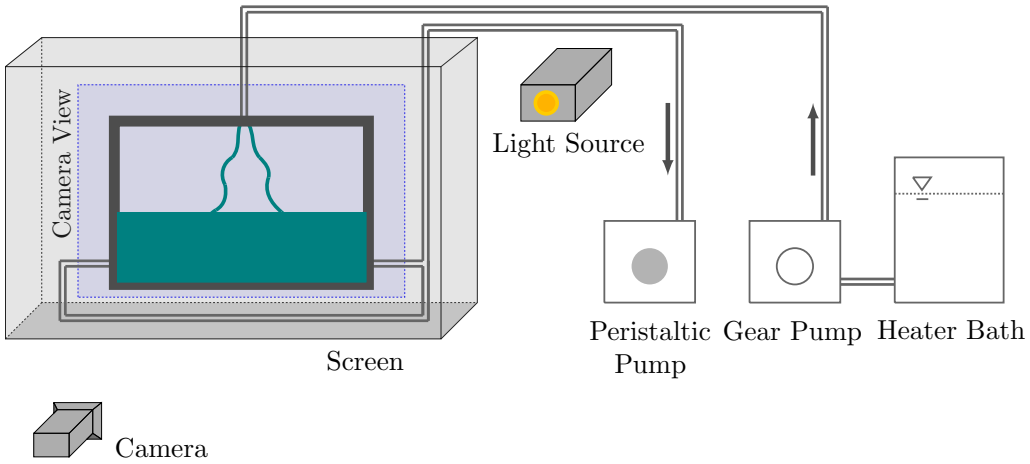

Fig. 4.6 A schematic representation of the visualisation procedure of the filling-box experiment using dye and/or shadowgraph technique. In the case of shadowgraph, the flow within the box was projected onto a 2-dimensional screen (tracing paper) attached to the frontal glass surface of the tank.

analogue for the salinity of the system, and therefore were used to identify the salinity interface. For all experiments traversing was initiated simultaneously with starting the plume fluid supply into the box. The traversing mechanism was driven by a UEI data acquisition card, to send pulses to a stepper motor, which was controlled via DigiFlow. The stepper motor was pulsed at 125 Hz and took approximately 3 min to traverse 241 mm through the tank. This traverse speed was chosen to minimise the lag associated with the conductivity probe and thermocouple. Reducing the speed of the stepper motor further made no difference to the density and temperature profiles recorded.

The majority of the experiments were visualised by adding dye to the brine, merely for the purpose of visual control of the experiment during its run. Additional visualisations, aimed at investigating qualitatively the processes occurring inside the box and making visual distinctions between those for single- and double-diffusive cases were performed using the shadowgraph technique, described in subsection 3.1.2. A schematic of the experimental setup for these visual experiments is shown in figure 4.6. Images were collected by a video camera (for details see section 3.2.8) at a frequency of 15 frames per second, and post-processed to remove background lighting and enhance the contrast between regions of mixing in the plume and the surrounding fluid. The light source and the camera were positioned approximately 8.5 m and 2.5 m from the screen, respectively.

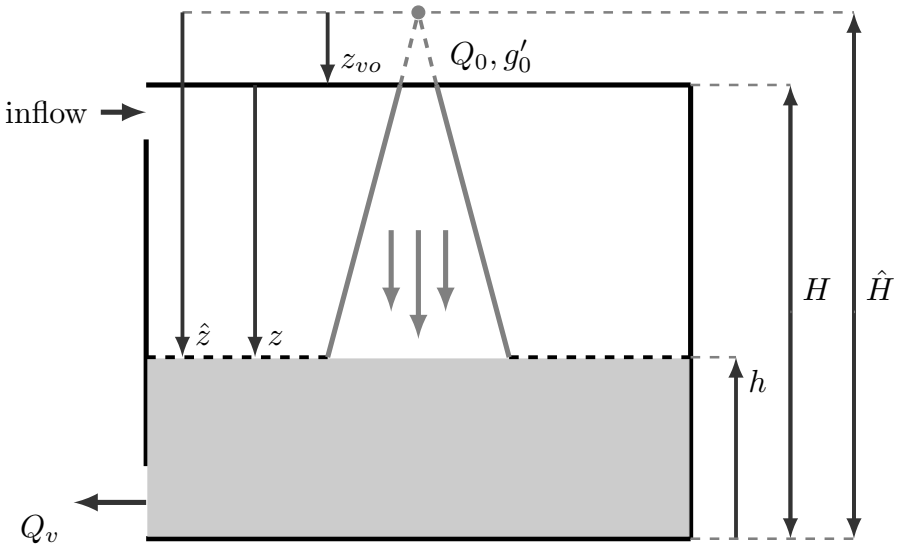

Fig. 4.7 A schematic representation of the 'semi-confined' filling box experiment, in which the bottom negatively buoyant layer is extracted at a constant ventilation flow rate Q_v.

4.3 Validation of the filling-box method

In this section we present the validation of the Baines' emptying-filling box experimental technique using a modified theoretical model, based on the work of Kaye and Hunt (2004). As in their work, this model predicts the temporal evolution of bottom layer depth h, with the modification that in our case the bottom layer fluid is extracted at a constant flow rate (using a pump), rather than outflowing due to the buoyancy difference with the ambient fluid. The plume flow described below is 'semi-confined', as the fluid within the box is exchanging with the external ambient fluid through openings.

The structure of this section is as follows. First, we derive a simple analytical solution for the problem, illustrated schematically in figure 4.7, predicting the transient evolution and steady state position of the interface between the two fluid layers. The obtained predictions are then validated against three experiments, which were performed at different source buoyancy fluxes. Once validated, the analytical model was used to estimate, for given experimental parameters, how long it would take for the emptying-filling box flow to reach a steady-state, i.e. $h = const$. From these estimates, we gain an insight into how long a typical experiment should last for in order to ensure that sufficient data is collected during the steady state.

4.3.1 Analytical model derivation

Assuming that diffusive transport is negligible, the rate of change of the depth of the bottom layer h is controlled by the difference between the volume flux supplied by the plume Q_p at the level of interface and the volume flux extracted by the pump Q_v. By mass conservation, for an incompressible fluid (i.e. $\rho = const$), this may be written as

$$\frac{\mathrm{d}V}{\mathrm{d}t} = Q_p - Q_v, \tag{4.1}$$

where V is the volume of the bottom negatively buoyant layer. For an enclosure of height H and base area S, the volume of the bottom layer can be written as

$$V = S\,h = S(H - z) = S(\hat{H} - \hat{z}), \tag{4.2}$$

where z and $\hat{z}$ are the distance from plume source and plume virtual origin to the interface, repsectively, and $\hat{H} = H + z_{vo}$, as illustrated schematically in figure 4.7.

Using the similarity solution for the volume flux of an axisymmetric plume, it is possible to rewrite the rate of change of bottom layer depth as

$$\frac{\mathrm{d}}{\mathrm{d}t}(\hat{H} - \hat{z}) = \frac{1}{S}\left(CB_0^{1/3}(z + z_{vo})^{5/3} - Q_v\right). \tag{4.3}$$

This can be simlified to

$$\frac{\mathrm{d}}{\mathrm{d}t}\hat{z} = \frac{1}{S}\left(Q_v - CB_0^{1/3}\hat{z}^{5/3}\right), \tag{4.4}$$

where $\hat{z} = z + z_{vo}$. We can now introduce the non-dimensional interface height and distance to the interface, respectively, as

$$\zeta_h = \frac{h}{\hat{H}} \quad \text{and} \quad \hat{\zeta} = \frac{\hat{z}}{\hat{H}}, \quad \text{where} \quad \zeta_h = 1 - \hat{\zeta}. \tag{4.5}$$

Dividing both sides by $\hat{H}$, we get the following relation

$$\frac{\mathrm{d}\hat{\zeta}}{\mathrm{d}t} = \frac{1}{T_d} - \frac{1}{T_f}\hat{\zeta^{5/3}}, \tag{4.6}$$

which gives rise to the two governing timescales T_d and T_f, defined as

$$T_d = \frac{S\hat{H}}{Q_v} \quad \text{and} \quad T_f = \frac{S}{CB_0^{1/3}\hat{H}^{2/3}}. \tag{4.7}$$

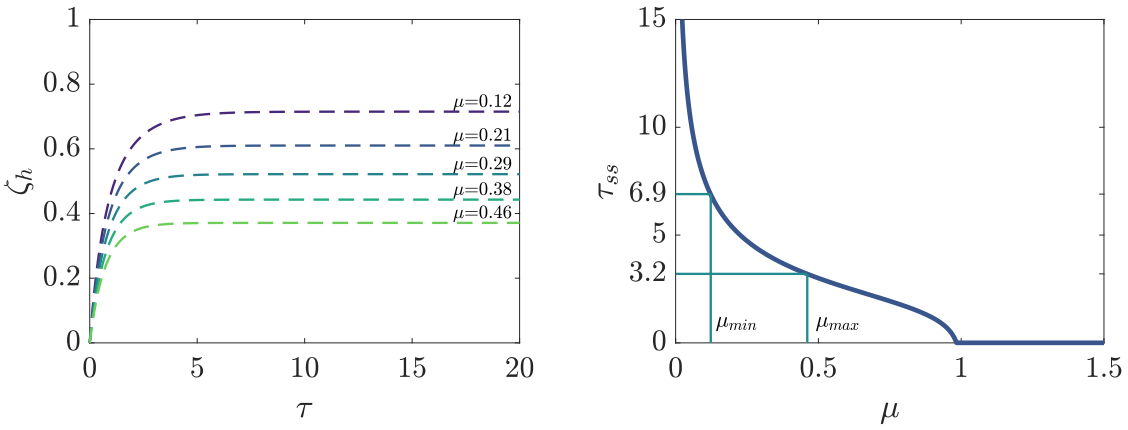

Fig. 4.8 Numerical predictions using (4.9) for (a) the interface depth ζ_h evolution over a range of the timescale ratios $\mu = T_f/T_d$; (b) the non-dimensional time τ_{ss} it takes to reach a steady state as function of the timescale ratio $\mu = T_f/T_d$.

The 'filling time' T_f, first identified by Baines and Turner (1969) in their paper on 'fully confined' plumes, provides a timescale for the process of filling an unventilated box with buoyant fluid at a constant source buoyancy flux. The timescale T_d, called the 'draining time', represents the amount of time required to drain completely a box full of fluid using an external pump alone at a constant rate Q_v. It is somewhat analogous to the draining timescale obtained by Linden et al. (1990), with the difference being that in their analysis, it was the buoyancy difference between the buoyant layer and the ambient that drove the draining/ventilation flow.

We now can fully non-dimensionalise the equation describing the evolution of the interface position by introducing the non-dimensional timescale τ and parameter μ as

$$\tau = t/T_f \quad \text{and} \quad \mu = T_f/T_d, \tag{4.8}$$

transforming (4.6) into

$$\frac{\mathrm{d}\hat{\zeta}}{\mathrm{d}\tau} = \mu - \hat{\zeta}^{5/3}. \tag{4.9}$$

The single parameter μ is the ratio of the two competing timescales for filling and draining the box. For a fixed geometry box (which is the case throughout this work), μ is a function of B_0 and Q_v only. In the case of a large μ, the time it takes to fill the box is greater than to drain it, and therefore we expect the lower layer to stay relatively thin. In the opposite case of $T_d > T_f$, the filling volume flux is large in comparison with

Exp	Solution	B_0	Γ_0	z_{vo}	L_m	Q_v	μ
-	-	$\times 10^{-8}$ m^{4}s^{-3}	-	m	m	$\times 10^{-6}$ m^{3}s^{-1}	–
1	Salt	32.3	0.64	0.019	0.010	27.4	0.32
2	Salt	76.3	1.31	0.015	0.007	27.4	0.25
3	Salt	143.8	2.48	0.013	0.005	27.4	0.21

Table 4.1 Experimental parameters for test experiments conducted with salt plumes. The source volume flux for all experiments was $Q_0 = 1.4 \times 10^{-6}$ m^3 s^{-1}.

Q_v and thus the bottom layer will grow to a substantial thickness before the drainage flux can balance the fluid supply provided by the plume.

For our numerical solutions we take the time $\tau = 0$ as the instant when the plume fluid first touches the bottom of the box. In that case $\hat{\zeta}(\tau = 0) = 1$. To calculate the plume volume flux we took the value of the entrainment coefficient $\alpha_T = 0.13$. Numerical solution of (4.9) using these initial conditions is presented in figure 4.8a for 5 particular cases of μ in the range of realistic parameters relevant to our experiments. These were obtained using a simple first order numerical scheme. The figure shows that as μ increases, the time it takes to reach a steady state decreases, and so does the interface height. This correlates with the physical intuition that for larger μ, the relative effect of draining is greater and so the plume is unable to build a fluid layer of considerable depth.

Figure 4.8b shows how the time to reach a steady state varies as a function of μ. In this case we define the state state as the time when the interface position has reached 99% of its theoretical steady-state value. The figure shows a non-linear relationship between τ_{ss} and μ. As expected, as the value of μ increases, the steady-state fluid depth decreases and is reached in less time. For $\mu \geq 1$, $\tau = 0$, indicating that the steady state is reached immediately, as the volume flux supplied by the plume is always smaller than the drainage volume flux and no fluid layer can form. The two particular cases marked as μ_{max} and μ_{min} provide the range of values that are relevant for our experiments, given the limitations of the pumps and the typical buoyancy fluxes B_0.

4.3.2 Model validation

Validation of the model was performed for three experiments with single-diffusive salt-only plumes. Table 4.1 summarises all three test experiments and their respective parameters. Determining the location of the interface was performed by means of a conductivity probe described in section 3.2.4 and following the procedure explained in

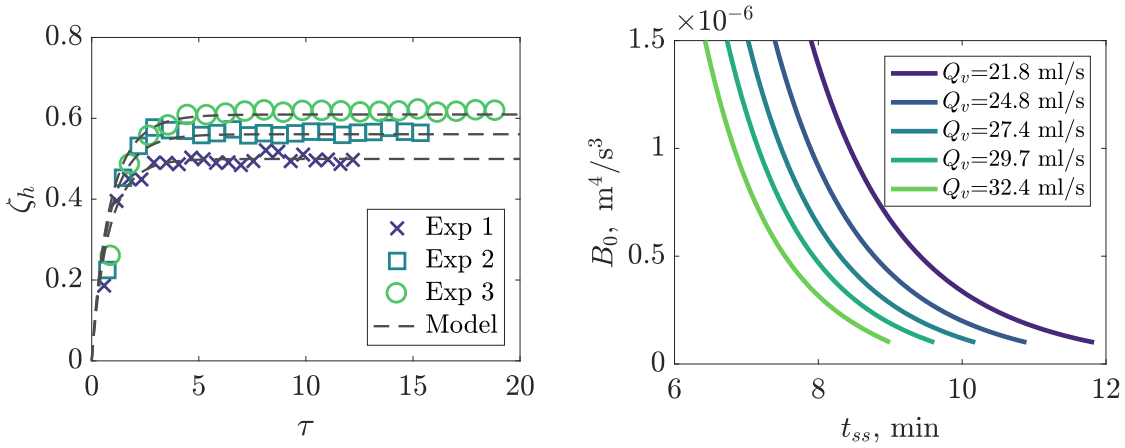

Fig. 4.9 (a) Comparison between the model predictions (shown as dashed lines) and the measured positions of the interface for three experiments; (b) theoretical prediction of the physical time to reach a steady state t_{ss} against the source buoyancy flux. Note that the error bars for the measurements presented in subfigure (a) are smaller than the marker sizes and are therefore omitted.

section 4.4.1. Figure 4.9a demonstrates the temporal evolution of the bottom layer fluid depth for three experiments. Each point in this plot represents a single measurement of the interface location. Predictions made by the model for each experiment, shown as dashed lines, are in a good agreement with both the observed temporal evolution and the final steady-state interface positions. This, therefore, validates the undertaken experimental procedure.

We performed all future experiments at five regular drainage flow rates spanning the range of $21.8 < Q_v < 32.4$ ml s^{-1}. Figure 4.9b shows the prediction of the physical time for the interface to reach a steady height as function of the source buoyancy flux B_0 for these five drainage volume fluxes. These predictions were made on the basis of the model, which at this stage has been validated against experimental measurements. The figure shows that in the worst case scenario over the range of possible experimental parameters the experiment should not take more than t_{ss} =12 min to reach a steady state. With that in mind, we performed all our experiments for at least 30 min to ensure that we obtain a sufficient number of measurements in the steady state.

We now proceed to presenting the actual experimental results obtained for single- and double-diffusive plumes. Note that, for simplicity, throughout this chapter we will denote the top-hat entrainment coefficient of a turbulent plume α_T^P as α.

Fig. 4.10 A series of images from a typical experiment (salt only in this case). The initial descent of the plume is shown in (a); (b, c) show the impact of the fluid on the base and its subsequent rise toward the source, and (d) final steady state with two uniform layers separated by the density interface.

4.4 Experimental results

Figure 4.10 shows a visualisation of a typical single-diffusive experiment, performed using simple blue food colouring and recorded using DigiFlow. The instant when the negatively buoyant axisymmetric turbulent plume, introduced into a fresh stationary ambient from the top, reached the base of the filling-box is shown in figure 4.10a. During its descent the plume entrained ambient fluid and thus grew in radius. Upon reaching the bottom of the box, the plume spread radially outwards as a gravity current and hit the walls, as shown in figure 4.10b. At this moment, the denser fluid began to exit through the bottom opening and was replaced by an equal volume (less source volume flux) of fresh ambient fluid, entering through the upper openings, to conserve volume. As the volume flux supplied by the plume initially exceeded that imposed by the drainage pump, a layer of salt solution began to form and grew in height, as shown in figure 4.10c. This layer continued to increase in depth and density until a steady-state flow was established. Figure 4.10d demonstrates that the steady flow consisted of a two-layer stratification: a fresh upper layer and a well-mixed lower layer of salt solution, separated by a horizontal interface.

As shown in figure 4.10, the interface between the two layers was not perfectly flat and horizontal throughout the experiment. The disturbances introduced by the plume caused interfacial waves between the fresh and saline layers. As the interface moved closer to the plume source, the amplitude of these interfacial waves reduced, but remained significant compared to the thickness of the interface. Since the fluctuations were oscillatory in time, it was necessary to perform multiple measurements of the interface position to average out any temporal variations. These measurements are discussed in detail in the next section.

Table 4.2 provides a summary of all experiments and their respective parameters. Each experiment was performed at five ventilation volume fluxes Q_v, with the values presented in table 4.2 being the averages over these five runs. The range of Q_v gave a range of steady-state interface heights $85\,\text{mm} \leq \hat{z} \leq 190\,\text{mm}$. Altogether 13 experiments (making a total of 65 runs) were performed, three with single-diffusive plumes (S1-S3), with the values of R_ρ being close to 0, and ten double-diffusive (HS4-HS13). Since for all double-diffusive experiments, the faster diffusing component (heat) was stably distributed and the slower diffusing component (salt) was unstable, as mentioned above the plumes were in the salt-fingering regime.

Experiment	Title	Source Solution	T_0	ΔT_0	B_0	Γ_0	z_{vo}	L_m	R_ρ
-	-	-	°C	°C	$\times 10^{-8}$ m^{4}s^{-3}	-	m	m	-
1	S1	Salt	20.8	0.7	65.6	0.92	0.017	0.008	0.004
2	S2	Salt	21.9	1.7	90.5	1.15	0.016	0.007	0.007
3	S3	Salt	20.9	1.3	33.8	0.47	0.021	0.011	0.014
4	HS4	Heat-Salt	67.7	47.7	133.2	1.94	0.014	0.006	0.100
5	HS5	Heat-Salt	40.8	20.4	65.1	0.82	0.017	0.008	0.101
6	HS6	Heat-Salt	55.8	35.6	51.3	0.72	0.018	0.009	0.186
7	HS7	Heat-Salt	68.6	48.1	55.1	1.04	0.016	0.008	0.198
8	HS8	Heat-Salt	56.2	36.1	35.3	0.47	0.020	0.011	0.253
9	HS9	Heat-Salt	54.3	34.4	28.0	0.37	0.022	0.013	0.291
10	HS10	Heat-Salt	55.8	35.3	17.8	0.31	0.024	0.014	0.371
11	HS11	Heat-Salt	67.2	47.9	20.8	0.30	0.024	0.014	0.404
12	HS12	Heat-Salt	61.1	41.1	12.6	0.17	0.029	0.019	0.492
13	HS13	Heat-Salt	67.4	47.7	9.5	0.14	0.031	0.021	0.572

Table 4.2 Experimental parameters for all experiments conducted with single- and double-diffusive plumes.

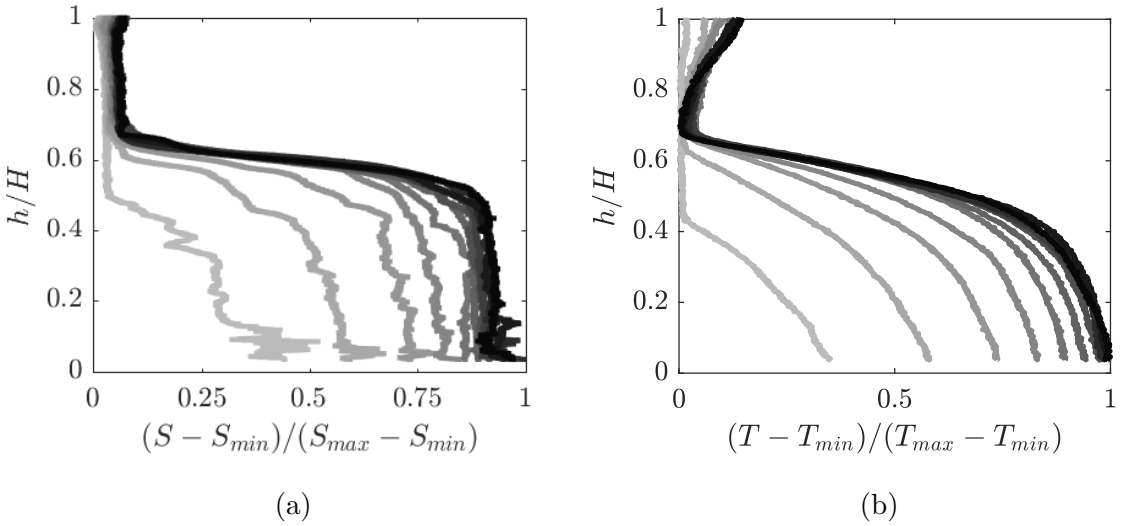

Fig. 4.11 Dimensionless conductivity and temperature profiles for experiment HS9 taken at regular time intervals of 178 s. The chronological order of obtained measurements is indicated by the darkness of the lines, with the darker ones corresponding to later profiles. Here the subscripts *max* and *min* denote the maximum and minimum values of the variables for this experiment.

4.4.1 Conductivity and temperature measurements

Figure 4.11 shows the outputs of the conductivity probe and thermocouple traversed through the box during the filling process of experiment HS9. Such profiles were typical for all experiments. The chronological order of the measurements is indicated by the darkness of the lines, with the darker ones corresponding to later profiles. The salinity profiles, shown in figure 4.11a can be roughly broken down into three sections from the top-down: (i) a region of constant low salinity (top layer); (ii) an intermediate region where the salinity increases to that of the bottom layer and (iii) a high salinity region (bottom layer). The sequence of profiles shows that the bottom layer grew in height and salinity during the filling process, until the steady state was reached with the salinity interface fluctuating around its mean position. The associated temperature profiles, shown in figure 4.11b, exhibit a similar behaviour, typical for all conducted thermohaline experiments, wherein the temperature of the bottom layer grew until reaching the steady state.

Two important observations about the profiles have to be made here. First, in comparison to the salinity profiles, the outputs of temperature measurements are considerably more diffuse, which cannot be explained by the slow response time of the thermocouple, as further reduction of the traversing speed did not make any noticeable

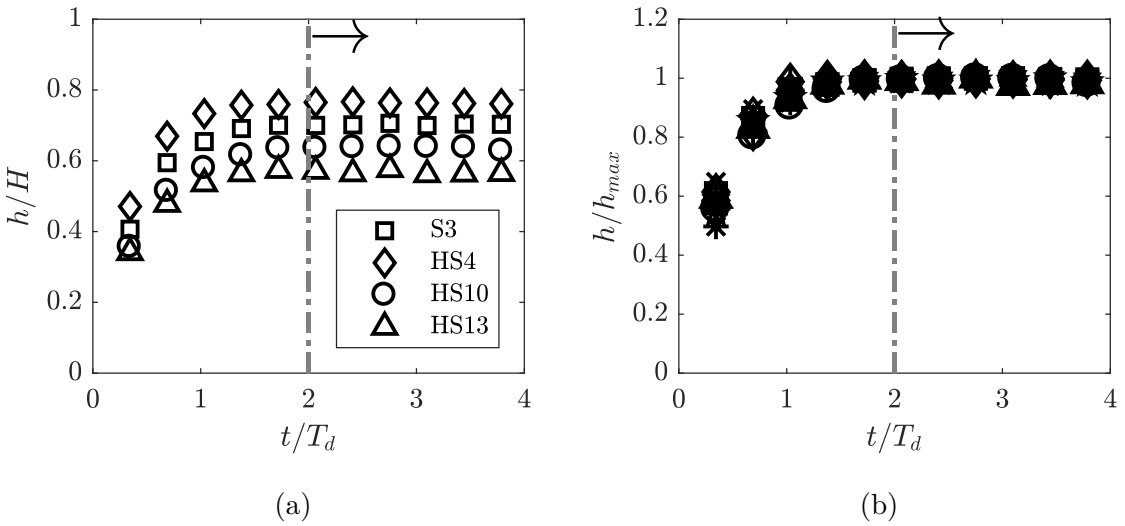

(a) (b)

Fig. 4.12 Evolution of the salinity interface in time t normalised with drainage timescale T_d: (a) for four individual experiments normalised by box height H; (b) for all 13 experiments, conducted at the lowest ventilation volume flux for each experiment, normalised by their respective maximum interface heights h_{max}.

difference to the obtained shape. Such diffuse temperature profiles make the definition of the temperature interface position ambiguous and, therefore, unsuitable for locating the interface. For that reason, salinity profiles only were used to locate the interface. Second, figures 4.11a and 4.11b demonstrate a small but persistent gradual increase in the salinity and temperature of the upper layer, respectively. While the salinity profiles appear to be nearly uniform at all times, the temperature in the upper layer forms a stable stratification.

This increase in both scalar properties could be a result of either double-diffusion acting across the plume, indicative of the counterbuoyancy flux observed by McDougall (1983) and Turner (2003), and/or double-diffusive convection occurring along the interface between the layers. Appendix E presents visual measurements obtained using the shadowgraph technique that did not reveal any significant convective motion occurring at the double-diffusive interface, signifying that it is likely that the cause of thermal stratification is heat diffusion from the plume. It is nevertheless hard to tell with certainty what is the dominating cause of the thermal stratification, but, given that the temperature difference between the top and bottom layers never exceeded 3.5 °C, its effect on plume buoyancy was negligible. Moreover, the reduction in temperature difference between the ambient and the plume due to the stratification is small, as at the source the ambient temperature increase had a mean value of 1.0±0.5% of ΔT_0,

where the error is one standard deviation. Further, although the temperature of the plume decreases as it descends, so does the ambient temperature anomaly, and the temperature difference between the plume just above the interface and the initial ambient temperature has a mean value of 3.2±2.6%.

To locate the instantaneous interface position, a hyperbolic tangent was fitted to each salinity profile and the height at the centre of the fitted profile was used to track the interface migration. Figure 4.12a shows the temporal evolution of the interface height determined in this manner for four different experiments. In this figure, the physical time t has been normalised with a timescale for emptying the tank T_d at a constant rate due to the ventilation volume flux Q_v, giving the non-dimensional time scale

$$\hat{t} = \frac{t}{T_d} = t\,\frac{Q_v}{SH}, \tag{4.10}$$

where S and H are the floor area and height of the tank, respectively. It is clear that for the four (typical) experiments shown, the interface height becomes approximately steady after about $\hat{t} = 2$.

Figure 4.12b shows the evolution of interface position normalised by the maximum interface distance z_{max} for all experiments conducted at the lowest ventilation volume flux $Q_v^{min} = 21.8\ \mathrm{ml\,s^{-1}}$. In line with figure 4.12a, we see that that after around $\hat{t} = 2$ all experiments reached a steady state. We also observed that for ventilation flow rates higher than $Q_v > Q_v^{min}$ the interface reached a steady state faster (in $\hat{t} \leq 2$), and therefore, for consistency, we took the last 6 profiles ($\hat{t} > 2$) for each experiment to calculate the time-averaged steady-state salinity $\overline{S}(z)$ and temperature $\overline{T}(z)$ profiles using

$$\overline{S}(z) = \frac{1}{(i_e - i_s + 1)} \sum_{i_s=6}^{i_e=11} S_i(z) \quad \text{and} \quad \overline{T}(z) = \frac{1}{(i_e - i_s + 1)} \sum_{i_s=6}^{i_e=11} T_i(z). \tag{4.11}$$

Figure 4.13 shows the typical calculated steady-state time-averaged salinity $\overline{S}(z)$ and temperature $\overline{T}(z)$ profiles. The figure demonstrates that the steady-state salinity profile is very well approximated by the hyperbolic tangent fit and can therefore be used to determine the interface position. The horizontal dashed bars represent the confidence levels of the interface position, estimated by extrapolating the slope at the centre of the interface to the edges of the profile. Although, as noted earlier, the averaged temperature profile is too diffuse to be used for accurate interface identification, figure 4.13 demonstrates that the temperature increase occurs within the confidence levels.

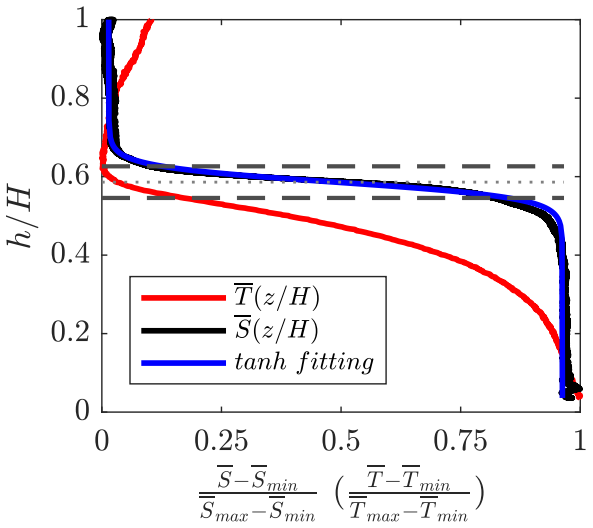

Fig. 4.13 Typical normalised time-averaged steady-state profiles of salinity $\overline{S}(h/H)$, fitted using hyperbolic tangent profile, and temperature $\overline{T}(h/H)$.

4.4.2 Entrainment coefficient

Figure 4.14 shows the calculated values of the top-hat entrainment coefficient α for three single-diffusive experiments (figure 4.14a) and four double-diffusive experiments (figure 4.14b) at five ventilation volume fluxes, evaluated using (3.1). The vertical error bars represent the combination of errors from temporal interface fluctuations, and the uncertainties in the temperature and supply volume flux measurements. These three sources of error were estimated as two standard deviations about their respective mean values for each experiment. Figure 4.14a demonstrates that the value of the entrainment coefficient for single-diffusive plumes is a constant, independent of plume buoyancy flux and ventilation volume flux, with a mean of $\alpha = 0.129 \pm 0.002$, where the error represents two standard deviations from the mean. This is in good agreement with the generally accepted value of $\alpha \approx 0.13$, reported in various experimental investigations (Linden, 2000), and was therefore used as a benchmark for further results.

In contrast to the results obtained from experiments with single-diffusive plumes, figure 4.14b shows that the values of the entrainment coefficient for double-diffusive plumes are (i) not constant, (ii) smaller than the single-diffusive entrainment constant. These two observations are surprising for a number of reasons. Observation (i) is contradictory to the general assumption that molecular diffusion plays no role in the dynamics of entrainment in high Péclet number turbulent plumes. Observation (ii) is also surprising, since we naively supposed that the small-scale double-diffusive

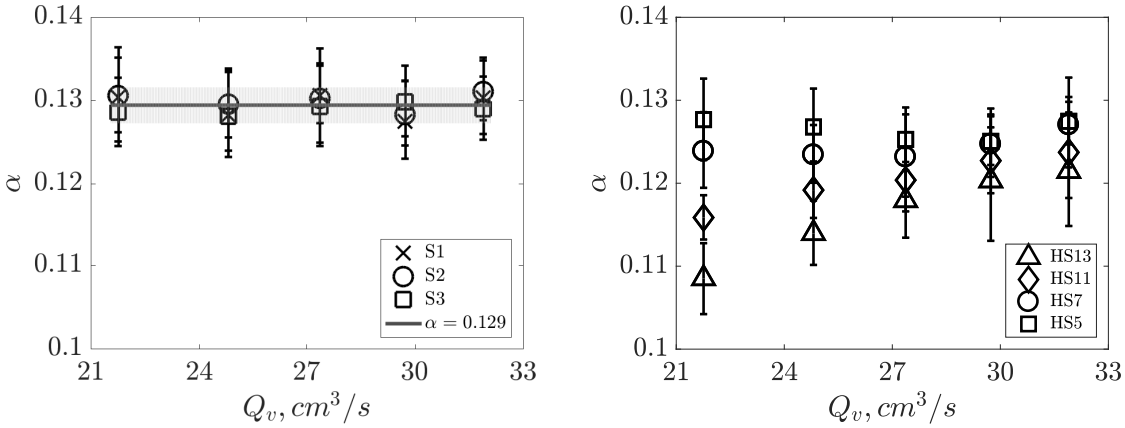

(a) (b)

Fig. 4.14 (a) Top-hat entrainment coefficient α for: (a) three single-diffusive experiments at five ventilation volume fluxes Q_v; (b) four double-diffusive experiments at five ventilation volume fluxes Q_v.

processes would enhance mixing of the engulfed fluid, leading to an increase of the effective entrainment coefficient. The observed reduction in the entrainment coefficient cannot be explained by the temporal change in the buoyancy flux of the plume during its descent. The faster diffusion of heat would result in an increase of the negative buoyancy flux, driving the flow, which in turn, would lead to an increase in the plume volume flux and 'move' the interface closer to the source than it should be for a given initial source buoyancy flux B_0. From (3.1), this reduction of $\hat{z}$ would yield an increased value of the entrainment coefficient, opposite to our observations.

Two additional important observations have to be made here. First, recalling that the experimental parameters presented in table 4.2 were tabulated in the ascending order of R_ρ, it is clear that the reduction of the entrainment coefficient is proportional to the strength of the double-diffusivity of the plume, represented by R_ρ. In particular, figure 4.14b shows that for all values of ventilation volume flux Q_v, the values of the entrainment coefficient for HS13 are lower than those of HS11, HS7 and HS5. This suggests that the intensity of the double-diffusive processes within the plume controls the magnitude of the reduction in entrainment. We also observe some non-monotonic behaviour of HS5 and HS7, in that their values of the entrainment coefficient appear to reduce at the intermediate range of Q_v. However, the magnitude of these variations in relation to experimental uncertainty for those experiments, makes it is difficult to comment reliably on this observation.

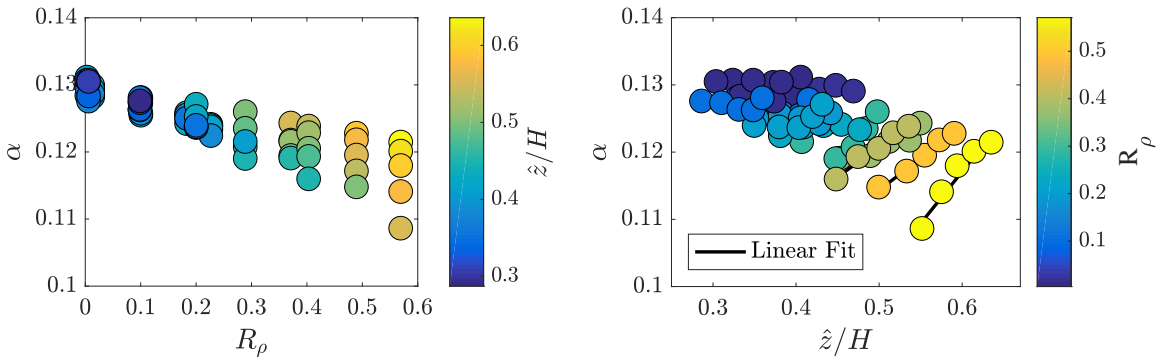

(a) (b)

Fig. 4.15 Entrainment coefficient results for all experiments at all ventilation volume fluxes as a function of: (a) density ratio R_ρ, where marker colour represents the normalised distance from the plume virtual origin to the interface $\hat{z}/H$; (b) normalised distance from the plume virtual origin to the interface $\hat{z}/H$, where marker colour represents stability ratio R_ρ.

Second, for highly doubly-diffusive experiments (HS11 and HS13), the values of the entrainment coefficient exhibit a clear dependency on the ventilation flux, i.e. for smaller values of the flux, the reduction of the entrainment coefficient is greater. Note that, in effect, a reduction in Q_v results in the migration of the interface towards the plume source. Therefore, the second observation can be transformed into a statement that, the reduction in the entrainment coefficient is greater when the interface is closer to the plume source. This observation is not explained by the need for the plume to adjust to a self-similar state, as the lowest ratio of the distance to the interface and jet-length is $\hat{z}/L_m$=6.6. Instead, this observation suggests that the strength of double diffusion in the plume varies with distance from the source.

To explore further the variation of double-diffusive effects within the plume, we present the results in a different fashion in figure 4.15. Figure 4.15a shows the dependence of the top-hat entrainment coefficient on the density ratio R_ρ for all experiments at all ventilation fluxes (making a total of 65 data points). The colour scheme in this figure represents the normalised distance from the plume virtual origin to the steady-state interface $\hat{z}/H$. Although no clear dependency between the entrainment coefficient and $\hat{z}$ is observed in the range $0 < R_\rho < 0.3$, there appears to be a pattern for strongly double-diffusive experiments in the range $0.3 < R_\rho < 0.6$. In particular, for a specific value of R_ρ, the values of the entrainment coefficient are consistently smaller for smaller $\hat{z}$, i.e. monotonically reducing with $\hat{z}$. The absence of such behaviour in the region $0 < R_\rho < 0.3$ is attributed to the fact that the magnitude of the dependence

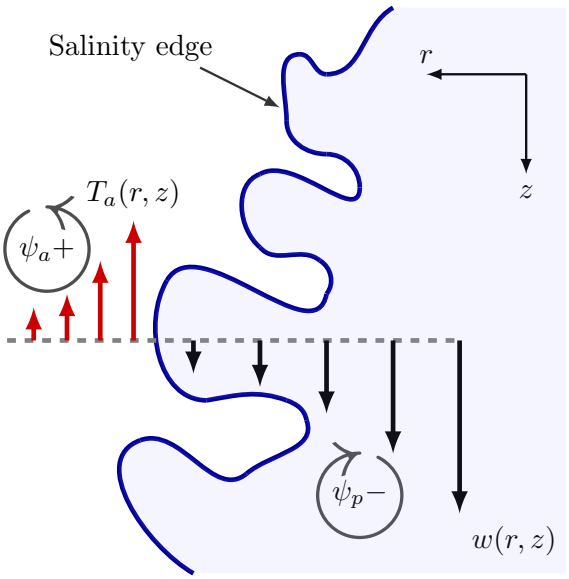

Fig. 4.16 A schematic snapshot of a thermohaline negatively-buoyant plume during its descent, showing the distribution of vertical velocity $w(r,z)$, temperature outside salinity edge T_a and vorticity fields ψ_p and ψ_a, within and outside the plume, respectively.

on $\hat{z}$ is comparable with the experimental uncertainty. Figure 4.15b displays the same results as a function of the distance to the interface. As expected, the figure shows that for single-diffusive plumes, represented by the dark blue markers, there is no dependency on the interface position, confirming the entrainment coefficient is a constant. In contrast, the strongly double-diffusive plumes exhibit a clear dependency on the distance travelled to the interface. The data, displayed in figure 4.15 lead to the conclusion that double-diffusive effects, acting to inhibit entrainment, vary along the plume and are stronger closer to the plume source. An attempt to explain these observations is made below.

4.4.3 Differential diffusion mechanism

One possible explanation for the observed reduction of entrainment is based on differential diffusion of the properties driving the plume motion. Consider a snapshot of a negatively-buoyant turbulent thermohaline plume during its descent, schematically illustrated in figure 4.16. We assume for simplicity that the flux of salt across the salinity interface is negligible, with only heat being transferred from the plume to the surrounding fluid by molecular diffusion (evidence of this heat diffusion across the plume/ambient interface is shown in figure 4.11b). Under these assumptions, the

ambient fluid just outside the salinity interface is fresh and warm, with the associated Gaussian distribution of temperature T_a in the radial direction. Such a temperature profile will create a corresponding buoyancy force distribution, which in turn will produce a vorticity field ψ_a oriented oppositely to the vorticity field ψ_p within the plume itself. This oppositely-orientated vorticity field outside the plume edge ψ_a will counteract ψ_p and thereby inhibit turbulent engulfment, which, as discussed in section 1.2.2, is widely believed to be the dominant mechanism of entrainment. This explanation, based on differential diffusion of heat and salt, is consistent with the observations of 'counterbuoyancy' fluxes and 'plume splitting' made by McDougall (1983), Turner and Veronis (2000) and Turner (2003).

From the above model it follows that the strength of the thermally-induced external vorticity field ψ_a is dependent on the temperature gradient at the salinity interface, with larger gradients inducing a stronger field. From our definition of R_ρ, for a fixed salinity difference, larger values of density ratio R_ρ are accompanied by stronger temperature gradients and thus the proposed counteracting effect of the external vorticity field on engulfment is greater. This explains the direct relationship between R_ρ and the scale of entrainment reduction. Such reasoning is consistent with large-scale engulfment being dominant in the entrainment process.

The proposed explanation is also supported by the observed inverse dependence of the reduction in entrainment with the distance travelled by the plume. Close to its source, the plume experiences a significant reduction in entrainment, as it has not yet lost its heat and the temperature gradients are still large. As the plume continues its downward motion, exchanging its properties with the ambient, heat is lost an $O(100)$ times faster than salt by the action of molecular diffusion, thereby decreasing the local value of the density ratio from that at the source. This reduction continues as the plume descends.

An estimate of the velocity scale in the region driven by the temperature alone can be constructed as

$$w \sim \sqrt{g\beta_T \Delta T L_T}. \tag{4.12}$$

To get an order of magnitude estimate, we take $g = 10\,\mathrm{m\,s^{-2}}$, $\beta_T = 10^{-4}\ ^\circ\mathrm{C}^{-1}$ and ΔT =1 °C. Assuming diffusive growth of the thermal boundary layer ($L_T \sim \sqrt{\kappa_T t}$), we take $L_T = 10^{-3}$ m. Using these values, the vertical velocity will be $O(10^{-3})\ \mathrm{m\,s^{-1}}$, which is approximately 10% of the typical entrainment velocity and, therefore, could hinder the entrainment process.

4.5 Conclusions

An experimental investigation of the role of double diffusion on the rate of entrainment in turbulent plumes has been conducted. We have restricted our attention to negatively buoyant saline and thermohaline plumes discharged vertically downwards into a stationary uniform freshwater ambient. Under this configuration, the thermohaline plumes were in the salt-fingering regime. As expected, the values of the top-hat entrainment coefficient obtained for single-diffusive (saline) plumes are a constant $\alpha = 0.129 \pm 0.002$, independent of the source buoyancy flux and the ventilation flux Q_v.

However, we observed a reduction in the value of the entrainment coefficient by up to 20% for double-diffusive thermohaline plumes. This reduction is not explained by the changes in the plume buoyancy flux, as this would yield the opposite result. As shown in figure 4.15a, the scale of reduction is in direct relation to the source density ratio R_ρ, indicating that double-diffusive processes alter the dynamics of turbulent entrainment. The reduction is also inversely related to the distance from the virtual origin to the interface $\hat{z}$, implying transiency of the double-diffusive effects. The exact functional relationship of α as a function of z and R_ρ remains to be established. As all of our experiments were in the salt-fingering configuration, it is also unclear at this stage as to what effect double-diffusion would have on the dynamics of a plume in the diffusive regime.

There are at least two important implications of this chapter. First, our findings may be useful in deciding whether double-diffusive effects would be of importance in modelling entrainment and subsequent dynamics of turbulent plumes in various environmental and industrial scenarios. Extrapolation to large-scale systems requires independence of the flow on Péclet and Reynolds numbers. The previously noted agreement between heat only and salt only plumes shows that these plumes are already independent of Pe and it is well known that laboratory scale plumes at lower Re capture the dynamics of large scale plumes (Briggs, 1982). One particular example is the already mentioned case of iceberg melting, the typical temperature and salinity differences between the produced meltwater and the ambient ocean are $\Delta T = 5$ °C and $\Delta S = 0.035$, respectively, yielding a density ratio of $R_\rho = 0.05$. Based on our experimental results, such a low source density ratio would result in a minor reduction in the entrainment coefficient. However, for cases where R_ρ is significantly greater, the double-diffusive effects should not be ignored. Second, this work shows that even for high-Péclet-number turbulent flows, in which advection dominates diffusion, the effect of molecular diffusion can be non-negligible, as it may alter the overall dynamics of the flow.

Chapter 5

PIV/LIF Measurements in Plumes

5.1 Introduction

In the previous chapter we presented the experimental measurements of the rate of turbulent entrainment in double-diffusive plumes in the salt-fingering configuration. In brief, these results, obtained using the Baines' filling-box technique, showed that (i) when plumes are double diffusive, the rate of turbulent entrainment is reduced, (ii) the reduction is greater for greater source stability ratio R_ρ, and (iii) the plume dynamics appears to evolve with the distance travelled. Although the Baines' filling-box technique serves as a relatively simple and robust way for determining the entrainment coefficient, it only allows the plume volume flux to be measured at a particular distance from the source and does not provide any insight into the flow field within the plume itself and the ambient fluid. To address these limitations, in this chapter we report our measurements of the flow fields in single- and double-diffusive plumes using simultaneous PIV and LIF measurements, with the aim of verifying the results presented in chapter 4 and gaining additional insights into the behaviour of double-diffusive turbulent plume flows.

Non-intrusive experimental investigations of turbulent plumes are not uncommon, and have been performed by multiple authors in the past. In one of the earliest, Kotsovinos and List (1977) performed an investigation of mean and turbulent properties of buoyant jets and plumes using the Laser-Doppler anemomentry (LDA). Their velocity measurements were combined with intrusive scalar (temperature) point measurements, obtained using bead thermistors. In doing so, the authors attempted to elucidate the mechanisms governing the transition of planar buoyant jets to plumes. To the best of our knowledge, their work presented the turbulence structure of planar turbulent buoyant jets for the first time. Later, in a similar fashion, Papanicolaou and List (1988) used LDA to investigate the dependence of the flow field in a turbulent forced plume

on its source Richardson number. This time the scalar concentration measurements were obtained using the laser-induced fluorescence technique (LIF), which is described in basic terms in section 3.1.4.

The approach of combining simultaneous measurements of velocity and scalar fields to study turbulent flows has been applied by multiple authors in the recent years. Modern technological advances in experimental systems and computational methods enabled experimental investigations of the dynamics of turbulent plumes and jets to be done with great accuracy. As such, high-resolution simultaneous velocity and scalar measurements using combined particle image velocimetry (PIV) and planar laser-induced fluorescence (PLIF) techniques were performed by Wang and Law (2002) and Mistry et al. (2016) to study round turbulent buoyant jets. In application to plumes, Burridge et al. (2017) used these two techniques to perform conditional analysis of the flow velocity measurements. In particular, the scalar field data (obtained using LIF) was used to distinguish the plume fluid from the ambient, providing the basis for conditional segregating of the plume velocity profiles according to specific criteria. The novel and insightful approaches used in their work inspired us to follow some of them in application to the current investigation.

As in chapter 4, for our experiments we chose to work with the aqueous heat-salt ('thermohaline') system in which a hot, salty plume descends into cooler, fresher water. The new experiments, however, required an additional modified experimental setup, since the setup described in chapter 4 was designed with no initial intention of performing simultaneous PIV/LIF measurements of the plume flow field. The modified experimental setup and the associated experimental procedure are described in section 5.2. The results of the experimental investigation are presented in section 5.3. We start with the validation of our experimental method by comparing the time-averaged results for the single-diffusive plumes against previously reported measurements. Similar analysis is then performed for double-diffusive plumes, enabling us to draw out the differences in the observed behaviour. We then proceed to the analysis, based on the combined PIV and PLIF measurements. In subsection 5.3.3.1 we explain the edge-detection procedure and demonstrate its effectiveness in differentiating the plume fluid from the ambient. Using the edge information, we then present the time-average flow field for both types of plumes in the plume coordinate system, as in Burridge et al. (2017). Ultimately, in section 5.4 a series of conclusions are drawn, bringing together the results from both chapters 4 and 5.

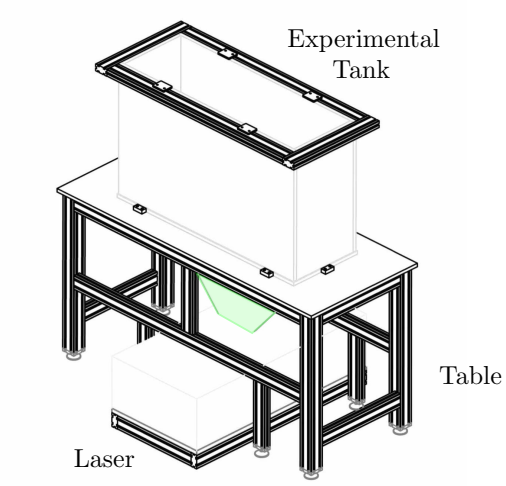

Fig. 5.1 A schematic representation of the experimental setup physical arrangement. A horizontal slit in the table allowed the laser beam (marked green) to enter the tank.

5.2 Experimental procedure

All experiments described in this chapter were performed in a Perspex (acrylic) tank, measuring $1.2\,\mathrm{m} \times 0.40\,\mathrm{m} \times 0.75\,\mathrm{m}$ ($L \times W \times H$). Only the front wall of the experimental tank was left transparent for visual data collection, with the three others masked using black cover for laser safety and ambient light noise reduction. The tank was positioned on a table, which had a horizontal slit spanning the width of the tank to pass the laser beam from underneath, as illustrated schematically in figure 5.1. For all experiments, the tank was filled with homogeneous aqueous NaCl solution and left overnight to equilibrate thermally.

As in chapter 4, turbulent plumes were created by steadily ejecting a negatively buoyant NaCl solution through the specifically designed plume nozzle located at the top of the tank using a gear pump. The pump was carefully calibrated over the supply volume fluxes used, that is, $Q_0 = 1.4 \pm 0.2\ \mathrm{ml\,s^{-1}}$. For the details of nozzle design and pump calibration, the reader is referred to subsections 3.2.1 and 3.2.3, respectively. For double-diffusive plume experiments, thermohaline source fluid was created by heating a solution of known salt concentration to a set temperature of up to 80.0 ± 0.1 °C using the Grant LTC4 water bath, described in section 3.2.2. The inevitable heat losses, occurring during the supply of the plume fluid from the heater bath to the discharge point, were reduced by thermally insulating the connecting pipework and minimising the total distance from the heater bath to the nozzle. As before, temperature of the plume fluid at the discharge point was measured using two T-type thermocouples, described in section 3.2.5, inserted into the nozzle. The densities of the saline plume fluid and the

ambient fluid were measured using the Anton Paar DMA5000 densitometer with an accuracy of $\pm 1\,\mu g\,cm^{-3}$. In the case of heat-salt combinations, the source density of the supply fluid was evaluated using the equations of state of Ruddick and Shirtcliffe (1979) from the known values of salinity and temperature at the source.

Thermohaline plume experiments required up to $\simeq 360\,s$ of warm-up to reach a steady-state temperature at the point of discharge. To avoid contamination of the tank with visualisation dye, heat and NaCl during the warm-up period, a siphon connected to a pump was temporarily placed near the nozzle outlet, collecting all the ejected plume fluid. Once the pre-heat was finished, the siphon was carefully removed away from the nozzle discharge point and the plume was allowed to run for another $\simeq 30\,s$ to re-establish a steady-state flow.

Simultaneous measurements of the velocity and scalar fields of both single- and double-diffusive plumes were performed using particle image velocimetry and laser induced fluorescence techniques, described in sections 3.1.3 and 3.1.4, respectively. The measurement section, shown schematically in figure 5.2, was illuminated using a frequency-doubled dual-cavity Litron Nano L100 Nd:YAG pulsed laser with a wavelength of 532 nm. Operated at a frequency of 70 Hz, with both cavities of the laser pulsed simultaneously, the laser system was used to create a light sheet with a thickness of 1–2 mm. The central plane of the light sheet was positioned in the mid-section of the experimental tank, parallel with the tank wall facing the cameras. To avoid inconsistencies in the intensity and/or spatial structure of the light sheet, present in the first $\simeq$30 s of the laser warm up, for each experiment both lasers were turned on at least 5 min before the start of data collection.

For the PIV measurements, polyamide particles with a mean diameter of 50 µm and density $1024\,kg\,m^{-3}$ were added to the ambient fluid. The choice of particles was based on minimising the Stokes' settling velocity, as described in section 3.2.6. To ensure homogeneous dispersion of particles in the experimental tank, for each set of experiments a fixed volume of particles was first added to a small beaker containing freshwater and a few millilitres of rinse aid. The resultant suspension was well stirred, ensuring that no particle lumps remained, and poured into the tank. Once added, the particles were thoroughly mixed within the tank, ensuring a practically uniform distribution, and the ambient water was allowed to settle for $\simeq$20 min. Given the pre-selected particle size and density, the final decision on the amount of particles to be added was based on the balance between the seeding density and optical permeability. In particular, while Keane and Adrian (1992) and Cowen and Monismith (1997) reported that for reliable PIV measurements, the seeding density should be greater

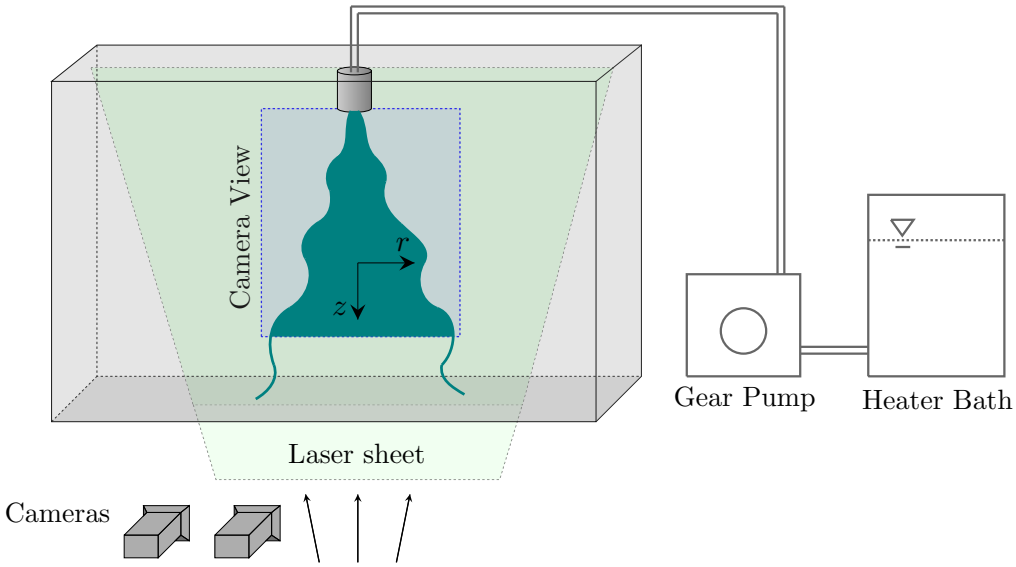

Fig. 5.2 A schematic representation of the PIV/PLIF experimental setup.

than 10 particles per interrogation window, excessive seeding can lead to a decrease in the quality of the images, as the optical path between the light sheet and the camera could be obscured. With both considerations in mind, a balanced seeding density was obtained experimentally and kept at three 10 ml scoops for a full tank.

To allow simultaneous LIF measurements, for all the experiments a low concentration ($1.0 \times 10^{-7}\,\mathrm{kg\,m^{-3}}$) of fluorescent dye Rhodamine 6G was added to the source fluid. To reduce the unwanted effect of attenuation, we minimised the amount of dye added by using a low f-number lens (f/1.2), which was close to fully open. With the optical device set, the volume of dye added was chosen such that the images were close to saturated at the top of the window, ensuring that the full range (8 bit of intensity resolution / 256 levels) of the camera capability was exploited.

Images of a section of the illuminated laser sheet were captured using two AVT Bonito CMC-4000 4 megapixel CMOS cameras. The lenses used on the PIV and LIF cameras were Nikkor 50 mm f/1.4 and Nikkor 50 mm f/1.2, respectively. Both cameras were placed approximately 1 m away from the front surface of the tank. Positioned at this distance, the resulting measurement window (camera view) had a height of 0.253 m (101 r_0), starting at 0.002 m above the physical source, and a width of 0.340 m (136 r_0). Done in this way, we were able to observe the entire process of the evolution of the plumes over a substantial vertical distance. To separate the two light signals, i.e. the light scattered from the polyamide particles and that fluoresced by the dye, a narrow (532 ± 1.5 nm) band-pass filter (centred at the wavelength of the laser) was mounted onto the PIV camera and a longpass (>570 nm) filter was mounted onto the

LIF camera. Images from both cameras were simultaneously captured at a frequency of 70 Hz, matching that of the laser pulsations, before being processed.

Perhaps the major limitation in studying thermohaline plume flows experimentally, is the effect of the large gradients of both heat and salt on the refractive index mismatch between the plume and ambient fluid. Generally, in situations where measurements of a flow with high density gradients are made using visually-based methods, it is necessary to eliminate refractive index variations within the experimental fluids. This is done to minimise the otherwise arising distortions to the light trajectories, leading to errors in determining particle positions and dye concentration measurements. Turbulent plume flows are characterised by the presence of large scalar gradients, creating sharp density gradients and thus making the above considerations particularly relevant. As a result, many previous similar studies performed refractive index matching using an additional solute within the ambient fluid (e.g. sodium nitrate) to match the optical properties of the flow and the ambient fluid while maintaining a density difference (McDougall, 1979). This was often possible because only a single scalar component was present within the flow that therefore had to be matched. However, in our case of thermohaline turbulent plume flows, the presence of two large scalar gradients, diffusing at rates with $O(100)$ difference, makes refractive index matching extremely challenging, as the local optical properties of the flow undergo significant rapid changes and thus cannot be accounted for. Without refractive index matching, it was therefore inevitable that some PIV and LIF data, particularly those obtained from the region close to the source, where the gradients of both scalars are large, were unreliable and could not be used. Physically, this effect was evident from the 'blurriness' of the particle images in the region close to the source, which, given that each frame is only illuminated for the pulse width of the laser (10 ns), could only be a result of the refractive index mismatch.

Using the scalings from the classical plume theory (i.e. $g'_p \sim z^{-5/3}$ and hence $\Delta n \sim z^{-5/3}$), where Δn is the difference in refractive index between the plume fluid and the ambient fluid, it is possible to obtain an estimate of the refractive index variations within the plume over the measurement region. Our calculations, based on the integral plume properties, showed that the largest values of refractive index variations ($\Delta n \sim 10^{-3}$) occur near the source, over the region where the concentration gradients are largest. It is therefore unsurprising that, with Δn spanning the entire width of the plume, the largest errors due to refractive index variations (~ 0.1 pixels) occurred near the source, as the incident light angle is also largest at that location.

As the plume travelled downstream, the incident light angle to the camera reduced, and so did the scalar gradients as a result of mixing through turbulent entrainment

and diffusive processes. Both of these effects acted to rapidly reduce the effect of the refractive index mismatch on the visual measurements error. It is, however, hard to predict with certainty on the basis of this greatly simplified theoretical model, the z-location where the refractive index mismatch would become insignificant and reliable data could be obtained. We therefore searched for this location experimentally by comparing the obtained data with the previously-verified model predictions. Using this approach, we determined that beyond a certain z-location ($\simeq 25r_0$) our measurements of the velocity field exhibit the scaling relations expected for self-similar turbulent pure plumes and compare well with existing datasets. For consistency, this procedure was followed for both single- and double-diffusive plumes, and is laid out in section 5.3.2.

The two orders of magnitude difference in the diffusivity of heat and salt (and hence dye) also makes it impossible to accurately determine the density field within the double-diffusive plume. We therefore used the LIF measurements for flow visualisation and edge detection purposes only, without concern for quantifying scalar concentration and relating it to the density field. Given the low concentrations of the dye in the measurement section, for LIF processing we used a linear relationship between the light intensity measured by the camera and the dye concentration to determine the scalar field. This relationship was established for each experiment through a two-point calibration, based on two images: first at background light intensity, and second at a known dye concentration. Both calibration images were captured with the polyamide particles within the tank, at the seeding density used for the experiment, to account for differences in the laser intensity due to the presence of the particles. As the maximum dye concentration in the measurement section was small and the scalar measurements were not used for determining the density field, attenuation of the laser beam was neglected in the LIF image processing. The spatial resolution of the processed LIF images was 0.29 mm per pixel. To determine the velocity fields, the raw particle images were first pre-processed by subtracting the background and then processed using the 2017b PIV algorithm of Digiflow (Olsthoorn and Dalziel, 2017). Interrogation windows were chosen to be 24×24 pixels^2 with a spacing of 12 pixels (an overlap of $\approx 50\%$). For these settings, we obtained one velocity vector for every 1.76 mm.

Once the processing of the PIV and LIF images was complete, the velocity and scalar fields were mapped onto a common world coordinate system. To that end, an image of a calibration grid containing a rectangular array of regular dots was captured by both cameras. The calibration grid was carefully aligned with the laser sheet. For each camera a mapping was obtained between the pixel co-ordinates of the dots and the known world coordinate system using a least squares fitting procedure. This

employs polynomial basis functions of up to third order to fit a polynomial with the dot locations on each image plane. The images obtained by the two cameras are then mapped onto a single world co-ordinate system by choosing a common origin for the world co-ordinates. Despite our best efforts to ensure alignment of the laser sheet with the calibration target, small misalignments were inevitable and had to be accounted for. To overcome this issue, we used a sequence of particle images, captured simultaneously on both cameras (with their filters removed) to determine a disparity map and shift the coordinate mappings, compensating for any small misalignment between the calibration target and the light sheet. This procedure is similar to stereo PIV calibration, as in Willert (1997).

For the source buoyancy fluxes used, the maximum downward plume volume flux (which developed just before hitting the base of the tank) can be estimated using the similarity solutions as $Q = 3.9 \times 10^{-4}\,\mathrm{m^3\,s^{-1}}$. To conserve volume, an equivalent upward volume flux had to be induced in the ambient. Averaged over the area of the experimental tank, the resulting velocity of the rising ambient fluid was $\simeq 0.8\ \mathrm{mm\,s^{-1}}$, which is much less than the typical plume velocities at the source ($Q_0/(\pi r_0^2) \simeq 70\ \mathrm{mm\,s^{-1}}$), and thus had no significant effect on the plume itself.

Each experiment was recorded for approximately 180 s, producing approximately 12,000 simultaneous velocity/scalar fields. Between every new experiment, the tank was well-mixed, ambient density and temperature re-measured, and sufficient time was given to allow any ambient motion to settle. A total of 6 plumes were studied, 3 single- and 3 double-diffusive, with the experimental source parameters given in table 5.1.

In addition to the source conditions, the table provides the Reynolds number $Re = \overline{w}_c \overline{R}_F/\nu$, where $\overline{w}_c$ is the the time-averaged velocity on the plume centreline, and the Péclet number $Pe = Re\,Sc$ at the same distance from the virtual origin $\hat{z} = 60 r_0$ around the mid height of the region examined. The Schmidt number ($Sc = \nu/\kappa$) for the saline plumes and the thermohaline plumes was based on the salt diffusivity $\kappa_S = 1.5 \times 10^{-9}$ and temperature diffusivity $\kappa_T = 1.4 \times 10^{-7}\ \mathrm{m^2\,s^{-1}}$, respectively. Following Papanicolaou and List (1988) we calculated the Kolmogorov length scale as $\eta_K = \overline{R}_F/Re^{3/4}$, and the Batchelor scale as $\eta_B = \eta_K/Sc^{1/2}$. Table 5.1 shows that the resolution of our PIV measurements were an order of magnitude larger than the Kolmogorov scale, implying that the velocities were captured at scales dominated by inertia. In addition, the resolution of our LIF images were well above the Batchelor scale, suggesting that the effects of diffusion at these scales may be ignored in our scalar edge analysis.

Parameter	Definition	Exp 1	Exp 2	Exp 3	Exp 4	Exp 5	Exp 6
Source solution	–	Salt	Salt	Salt	Heat-Salt	Heat-Salt	Heat-Salt
Source temperature	T_0 [°C]	21.2	21.2	21.1	62.6	62.5	62.6
Source temperature difference	T_0 [°C]	0.2	0.2	0.1	41.6	41.5	41.5
Source buoyancy flux	B_0 [$\times 10^{-4}$ m^4 s^{-3}]	33.4	33.4	33.4	8.1	8.1	8.1
Source plume parameter	Γ_0	0.62	0.62	0.62	0.19	0.19	0.19
Jet length	L_m [m]	0.011	0.011	0.011	0.020	0.020	0.020
Virtual origin	z_{vo} [m]	0.021	0.021	0.021	0.031	0.031	0.031
Individual marker	–	○	◇	△	○	◇	△
Averaged marker	–		□			□	
Plume half-width ($\hat{z} = 60\,r_0$)	$\overline{R}_F = \overline{Q}/(\pi\overline{M})^{1/2}$) [m]		2.57×10^{-2}			2.26×10^{-2}	
Reynolds number ($\hat{z} = 60\,r_0$)	$Re = \overline{w}_c\overline{R}_F/\nu$ [-]		1125			677	
Péclet number ($\hat{z} = 60\,r_0$)	$Pe = Re\,Sc$ [-]		7.87×10^5			4.74×10^3	
Kolmogorov length scale ($\hat{z} = 60\,r_0$)	$\eta_K = \overline{R}_F/Re^{3/4}$ [m]		1.32×10^{-4}			1.70×10^{-4}	
Batchelor length scale ($\hat{z} = 60\,r_0$)	$\eta_B = \eta_K/Sc^{1/2}$ [m]		5.01×10^{-6}			6.42×10^{-5}	
PIV vector spacing	[m/pixel]		1.764×10^{-3}			1.764×10^{-3}	
LIF pixel spacing	[m/pixel]		2.93×10^{-4}			2.93×10^{-4}	

Table 5.1 Experimental parameters for the six experiments with single- and double-diffusive plumes. The Schmidt number ($Sc = \nu/\kappa$) for the thermohaline plumes is based on the thermal diffusivity $\kappa_T = 1.4 \times 10^{-7}$ m^2 s^{-1}.

5.3 Experimental results

5.3.1 Visual observations

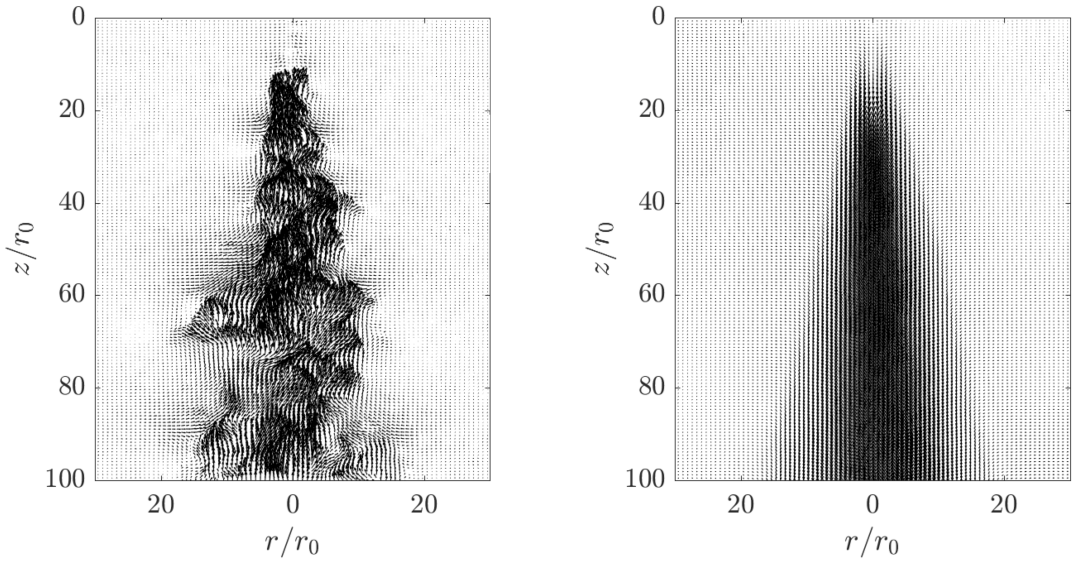

Fig. 5.3 Typical resolved two-dimensional PIV velocity field obtained for experiment S1 showing: (a) the combined instantaneous velocity field $w(r,z,t)$ and $u(r,z,t)$; (b) the combined time-averaged velocity field $\overline{w}(r,z)$ and $\overline{u}(r,z)$.

Figure 5.3a shows an instantaneous snapshot of the resolved PIV velocity field for experiment S1. The direction and length of the vectors illustrate schematically the direction and velocity of the fluid flow at each location, with the longer arrows corresponding to faster local flow. Such velocity fields were typical for all experiments with both single- and double-diffusive plumes. For each experiment, approximately 12,000 of such instantaneous velocity fields were constructed and used to obtain the time-average plume vertical velocity $\overline{w}(r,z)$ and horizontal velocity $\overline{u}(r,z)$ fields as

$$\overline{w}(r,z) = \frac{1}{t_T}\int_0^{t_T} w(r,z,t)\,\mathrm{d}t \quad \text{and} \quad \overline{u}(r,z) = \frac{1}{t_T}\int_0^{t_T} u(r,z,t)\,\mathrm{d}t, \tag{5.1}$$

where r and z are the the radial and vertical co-ordinates, respectively, as illustrated in figure 5.2, and t_T is the total PIV sampling time. Note that throughout this chapter we use the 'overbar symbol' to denote a time-average quantity.

The resulting time-average velocity field, which combines both $\overline{w}(r,z)$ and $\overline{u}(r,z)$, obtained for experiment S1 is shown in figure 5.3b. Importantly, this figure demonstrates

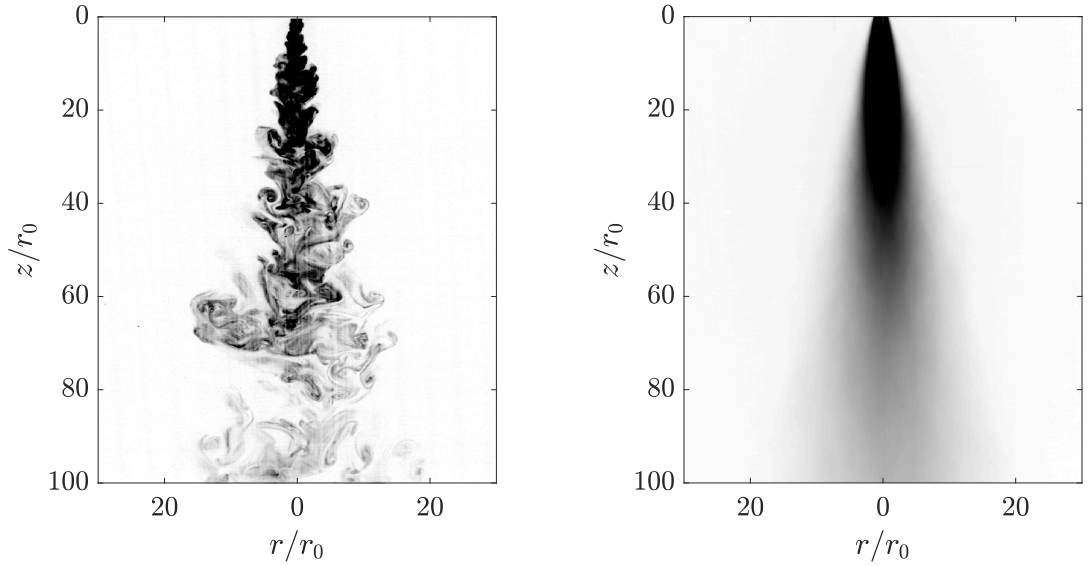

Fig. 5.4 LIF images obtained for experiment S1 showing: (a) the instantaneous scalar (fluorescent dye) field $c(r, z, t)$; (b) the time-averaged scalar field $\overline{c}(r, z)$. Both images were taken at the same time instant as in figure 5.3.

that in the time-average sense, the flow was visually symmetric around the vertical plume centreline at $r/r_0 = 0$, implying that the nozzle was correctly positioned and that there were no significant sources of disturbance to the flow, such as tank backflow or residual motion after stirring. Similarly to the instantaneous velocity fields, such time-averaged velocity fields were typical for all experiments.

Figure 5.4a shows an instant of the LIF image recorded for experiment S1, which was also typical for all experiments reported in this chapter. For visualisation purposes, the darkness in this figure corresponds to the concentration of the fluorescent dye $c(r, z)$, with the bright regions corresponding to the ambient fluid. This visualisation clearly demonstrates that despite the low values of the source Reynolds number ($Re_0 < 350$), the plume flow was fully-turbulent in the field of view. In a similar fashion to the velocity results obtained using PIV, the collected LIF data was time-averaged using

$$\overline{c}(r, z) = \frac{1}{t_T} \int_0^{t_T} c(r, z, t)\, \mathrm{d}t. \tag{5.2}$$

The resulting time-average dye concentration for experiment S1 is shown in figure 5.4b, which again was typical for all experiments. These were used to check that the time-average LIF data was sensible and in qualitative agreement with that from PIV.

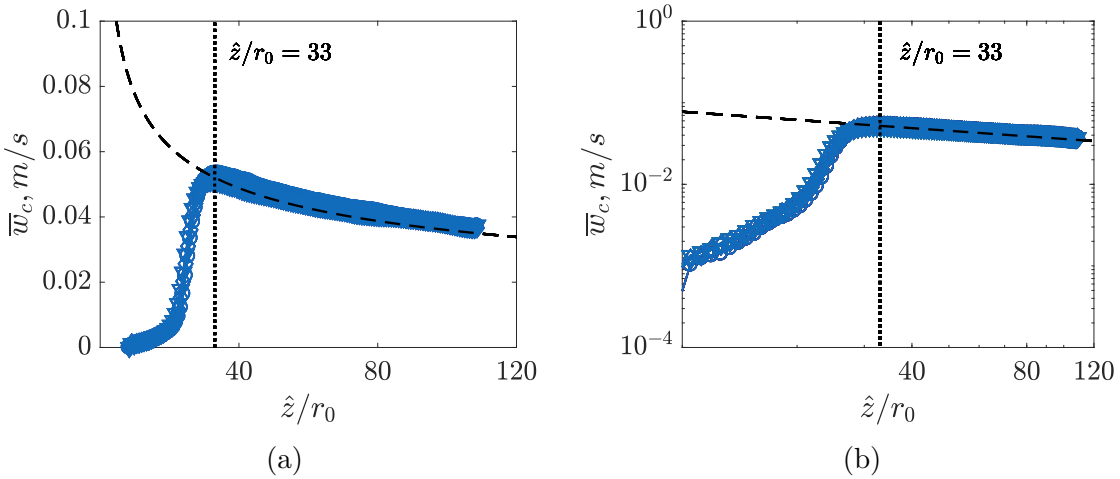

Fig. 5.5 The spatial evolution of the time-averaged vertical centreline velocity $\overline{w}_c$ for the three experiments with single-diffusive plumes (S1-S3) plotted on (a) physical scale; and (b) log-log scale. The dashed line marks the theoretical prediction based on the similarity solutions by Morton et al. (1956).

5.3.2 Results in an Eulerian coordinate system

5.3.2.1 Validation of the PIV data

As discussed in section 5.2, given the large source temperature and salinity gradients (ΔT_0, ΔS_0) and the two orders of magnitude difference in the diffusivities of temperature and salinity ($Le = 100$), accurate refractive index matching was not practically possible. As a result, it was inevitable that, over a significant measurement range, the refractive index mismatch was inhibiting reliable visual data collection. The turbulent nature of the plume motion makes it difficult to predict this region with certainty analytically, and therefore it had to be determined experimentally. To that end, we looked for the z-location beyond which the mismatch between the refractive indices of the plume fluid and the ambient fluid would become insignificant (as a result of dilution through mixing with the ambient fluid and diffusive processes) and, hence, where reliable data could be gathered. We did that by comparing the obtained results based on the velocity data against the well-known behaviour of single-diffusive turbulent plumes, reported in previous investigations.

Figure 5.5 shows the decay of time-averaged centreline vertical plume velocity $\overline{w}_c$ as a function of the normalised distance from the virtual origin $\hat{z}/r_0$ for three single-diffusive experiments (S1–S3) in both normal and log-log scales. In that figure, the dashed line represents the theoretical prediction for $\overline{w}_c$ based on the similarity solution for vertical centreline velocity decay (2.42b). Figure 5.5a shows that at early

stages of flow development ($10 < \hat{z}/r_0 < 20$), the obtained values of $\overline{w}_c$ were significantly lower than the model prediction, slowly adjusting to the theoretical values. Later, over the region of $20 < \hat{z}/r_0 < 33$, the measured values of $\overline{w}_c$ grew rapidly, ultimately reaching the model prediction. This adjustment could result from either an error in the PIV measurements, or because of the flow adjusting from the non-pure-plume behaviour at the source. It is unlikely to be the latter, as we expect the source velocity to be high ($\sim 0.07\ \mathrm{m\,s^{-1}}$) and then decay as the plume travels downstream, which is not observed in the measurements. Therefore, it is more likely that this adjustment process is associated with the plume dilution, reducing the mismatch in the optical properties of the plume fluid and the ambient fluid, and allowing reliable visual data to be collected. Beyond $\hat{z}/r_0 = 33$, the values of $\overline{w}_c$ for all three experiments follow well the theoretical model and each other. For the single-diffusive plumes, the distance of $\hat{z}/r_0 = 33$ corresponds to approximately 8 jet-lengths, and hence we anticipate the plume to have become self-similar. In addition, re-plotted on log-log axis and shown in figure 5.5b, the obtained centreline velocity measurements clearly attain the theoretical $-1/3$ slope (marked by the dashed line) after $\hat{z}/r_0 = 33$ and follow it well throughout the remainder of the measurement window. On the basis of these observations, we provisionally took the value of $\hat{z}/r_0 = 33$ as the distance beyond which velocity measurements for single-diffusive plumes were deemed satisfactory, and performed further checks to validate this choice. As such, we first analysed the time-averaged vertical $\overline{w}(r, z)$ and horizontal radial $\overline{u}(r, z)$ velocity distributions over the region $\hat{z}/r_0 \geq 33$ for the three single-diffusive plumes.

Figure 5.6 shows the normalised vertical velocity profiles $\overline{w}(r, z)/\overline{w}_c$ and horizontal velocity profiles $\overline{u}(r, z)/\overline{w}_c$ for experiments S1–S3 at 10 different vertical positions over the range $33 < \hat{z}/r_0 < 108$. The radial position in this figure was normalised by the e-folding plume radius $\overline{R}_e$, defined as the radial location at which the value of the normalised time-averaged vertical velocity reduced to $\overline{w}(r, z)/\overline{w}_c = 1/\exp$. The value of $1/\exp \simeq 0.37$ is represented in the figure as the horizontal dashed line and its intersections with the two vertical dashed lines denote the theoretical positions of the e-folding plume half-width. The figure demonstrates that the scaled time-averaged vertical velocity distributions exhibit Gaussian profiles at all distances over the range $33 < \hat{z}/r_0 < 108$. Such behaviour is expected for turbulent plumes as it has been reported previously by multiple authors, including Papanicolaou and List (1988) and Ezzamel et al. (2015). The obtained profiles collapse well onto a single curve for all three experiments at all distances from the virtual source, indicating that over the selected measurement range the single-diffusive plumes were in a self-similar regime.

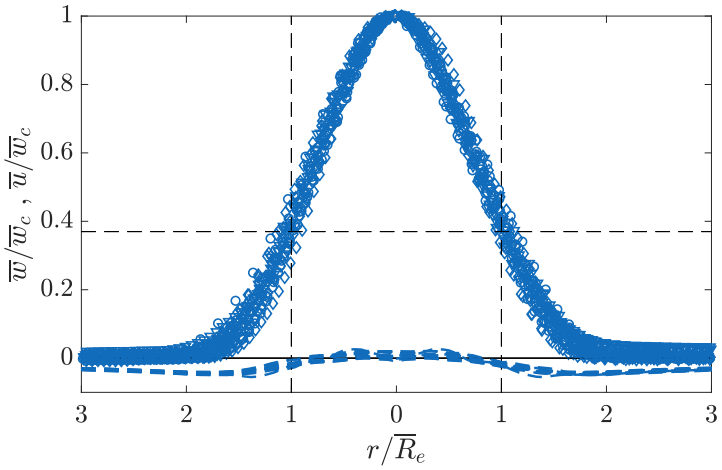

Fig. 5.6 The time-averaged scaled vertical velocities $\overline{w}/\overline{w}_c$ (represented using markers) and horizontal velocities $\overline{u}/\overline{w}_c$ (represented using dashed lines) for the three single-diffusive plumes at 10 different heights spanning $33 < \hat{z}/r_0 < 108$. The good collapse of data demonstrates that the flow exhibits the behaviour expected of a turbulent pure plume. The horizontal dashed line marks the theoretical value of $\overline{w}/\overline{w}_c$ at the e-folding width $\overline{R}_e$, which is in good agreement with the obtained profiles.

In addition, the figure illustrates a good agreement between the theoretical and the obtained e-folding predictions, with the vertical velocity profiles decaying to appropriate values at the radial distance of one e-folding radius $\overline{R}_e$.

The scaled time-averaged horizontal velocity profiles $\overline{u}(r,z)/\overline{w}_c$, marked by the dashed lines in figure 5.6, also exhibit the behaviour typical for turbulent plumes. In particular, looking from left to right, the horizontal velocities are first directed radially inward, toward the plume centreline ($r/\overline{R}_e = 0$), with their magnitude decreasing with the radial distance. After a certain point, a reversal of sign occurs, indicating that the flow begins to point radially outward. This outward-directed horizontal flow persists until the value of $\overline{u}(r,z)/\overline{w}_c$ once again reaches zero at the plume centreline. The reversal of radial flow direction acts as another confirmation for the validity of the flow measurements, as this behaviour is expected from theoretical considerations (continuity requires radial outflow, given the reduction in the local vertical velocity), and was previously observed for plumes by Shabbir and George (1994) and Ying et al. (2004).

Hence, over the region $33 < \hat{z}/r_0 < 108$, selected on the basis of the validity of the time-averaged centreline vertical velocity decay, the PIV measurements of the velocity field for single-diffusive plumes demonstrate the behaviour expected of turbulent pure-plumes on theoretical grounds and matches the previously-reported experimental

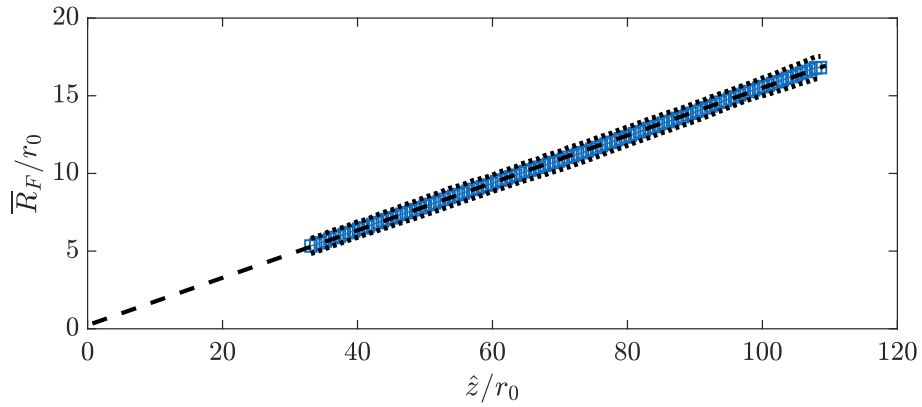

Fig. 5.7 Flux-based top-hat plume radius $\overline{R}_F/r_0$ averaged over the the three single-diffusive plumes (S1–S3). The confidence levels for these measurements, estimated as the standard deviation around their mean, are represented by the dotted lines. The dashed line represents the linear fitting to the plume radius over the region $33 < \hat{z}/r_0 < 108$, and extrapolated back to $\hat{z}/r_0 = 0$.

observations. This provides assurance that the velocity measurements were accurate and were not affected significantly by the refractive index mismatch beyond $\hat{z}/r_0 = 33$.

For further assurance, we evaluated the top-hat entrainment coefficient α_T of the single-diffusive plumes using two different approaches, as presented in the following section. In addition to providing further validation of the undertaken experimental procedure, these results provide a benchmark, against which the measurements of the double-diffusive plumes were compared.

5.3.2.2 Results for the single-diffusive plumes

Using the definition of the time-averaged vertical velocity (5.1), we introduce the time-averaged fluxes of volume and specific momentum, respectively, as

$$\overline{Q} = \pi \int_0^\infty r\,\overline{w}(r,z)\,\mathrm{d}r \quad \text{and} \quad \overline{M} = \pi \int_0^\infty r\,\overline{w}^2(r,z)\,\mathrm{d}r. \tag{5.3}$$

Using the above definitions, the characteristic plume radial scale $\overline{R}_F$, which represents the flux-based time-averaged top-hat plume radius, can be constructed as

$$\overline{R}_F = \frac{\overline{Q}}{(\pi\overline{M})^{1/2}}. \tag{5.4}$$

Figure 5.7 shows the result obtained for $\overline{R}_F$ as function of $\hat{z}/r_0$ averaged over the three single-diffusive experiments (S1–S3). In this figure, the dotted lines represent

the confidence levels, estimated as the standard deviation around the mean of the three sets of measurements, and the dashed line marks the linear approximation to the averaged $\overline{R}_F/r_0$ data, fitted over the region $33 < \hat{z}/r_0 < 108$ and extrapolated back to $\hat{z}/r_0 = 0$. The figure clearly demonstrates the linear growth of the single-diffusive plume radii through the ability of the linear fitting to well approximate the observed values of $\overline{R}_F/r_0$. This observation indicates that the entrainment coefficient was constant over the entire region $33 < \hat{z}/r_0 < 108$, allowing the value of the entrainment coefficient to be deduced. To that end, as the first method of estimating the value of the entrainment coefficient, we used the similarity solutions of Morton et al. (1956), rearranged as

$$\alpha_T = \frac{5}{6}\frac{\mathrm{d}\overline{R}_F}{\mathrm{d}z}. \tag{5.5}$$

Using the value of gradient extracted from the linear fit for $\overline{R}_F/r_0$, we estimated the value of the entrainment coefficient as $\alpha_T = 0.12 \pm 0.01$, which falls into the range of previous measurements presented in table 1.1 (where the median value is $\alpha_T = 0.12$) and corresponds well with the value of the top-hat entrainment coefficient for single-diffusive plumes determined experimentally using the Baines' filling box technique ($\alpha = 0.129 \pm 0.002$), as described in the previous chapter.

In addition to demonstrating the linear radial growth and providing the value of the entrainment coefficient for single-diffusive plumes, results presented in figure 5.7 allow for a verification of the virtual origin correction used. In particular, as outlined in section 2.7.2, in our analysis we used the two-step correction introduced by Morton (1959) described in detail by Kaye and Hunt (2004). Note that the results presented in figure 5.7 were plotted using this analytically-calculated virtual origin correction. In an ideal case of this correction being perfect, extrapolation of the linear fitting obtained for the plume half-width back to $\hat{z}/r_0 = 0$ should lead to the origin. In our experiments, such extrapolation resulted in the intersection value of $\overline{R}_F/r_0 \simeq 0.1$ at $\hat{z}/r_0 = 0$. Taking the previously-deduced value of the entrainment coefficient ($\alpha_T = 0.12$), we estimate the location at which the time-average plume width is zero as $\hat{z}/r_0 = -0.8$, which represents the deviation between the calculated virtual origin and the PIV-inferred virtual origin. Such a low value was deemed satisfactory and hence validated the use of the two-step virtual origin correction.

The second method of estimating the value of α_T for single-diffusive plumes was also based on the similarity solutions of Morton et al. (1956), but only used the values of the time-averaged plume volume flux $\overline{Q}$, which were calculated from the time-averaged velocity field measurements. These results, averaged over the three

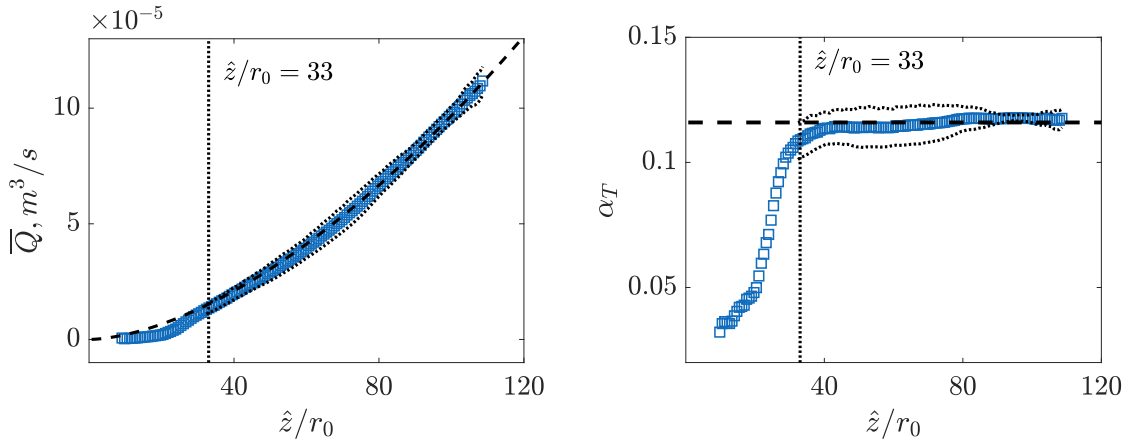

Fig. 5.8 The spatial evolution of (a) the time-averaged plume volume flux $\overline{Q}$ averaged for the three single-diffusive experiments; (b) the top-hat entrainment coefficient α_T averaged for the three single-diffusive experiments.

single-diffusive experiments, are presented in figure 5.8, where the dotted lines mark the confidence region for the obtained values, calculated as the standard deviation around the mean of the estimates for the three experiments. Figure 5.8a shows the evolution of the time-averaged plume volume flux $\overline{Q}$ against the normalised distance from the virtual origin. The theoretical prediction for $\overline{Q}(z/r_0)$, based on the similarity solutions and summarised in section 2.7, is marked in figure 5.8a using the black dashed line. The figure demonstrates that initially, over the region $\hat{z}/r_0 < 33$, there is a notable deviation between the theoretical prediction and the values of fluxes integrated from the time-averaged PIV velocity measurements. However, after around $\hat{z}/r_0 = 33$, the values of $\overline{Q}$ reach the theoretical prediction and follow it well (within the confidence levels) for the remainder of the measurement region, acting as a further re-assurance for the chosen confidence region of $\hat{z}/r_0 \geq 33$.

The validated measurements of the time-averaged volume flux were used to deduce the evolution of the the values of the entrainment coefficient over the entire measurement range. For that, we used the rearranged form of the similarity solution for pure plume volume flux (2.42d), written as

$$\alpha_T = \left(\frac{5}{6}\left(\frac{10}{9}\right)^{1/3}\pi^{-2/3}\right)^{3/4}\overline{Q}(\hat{z})^{3/4}\ B_0^{-1/4}\hat{z}^{-5/4}. \tag{5.6}$$

The result of this calculation is presented in figure 5.8b. In this figure, the dashed line represents the value of the entrainment coefficient obtained from (5.5), and the dotted

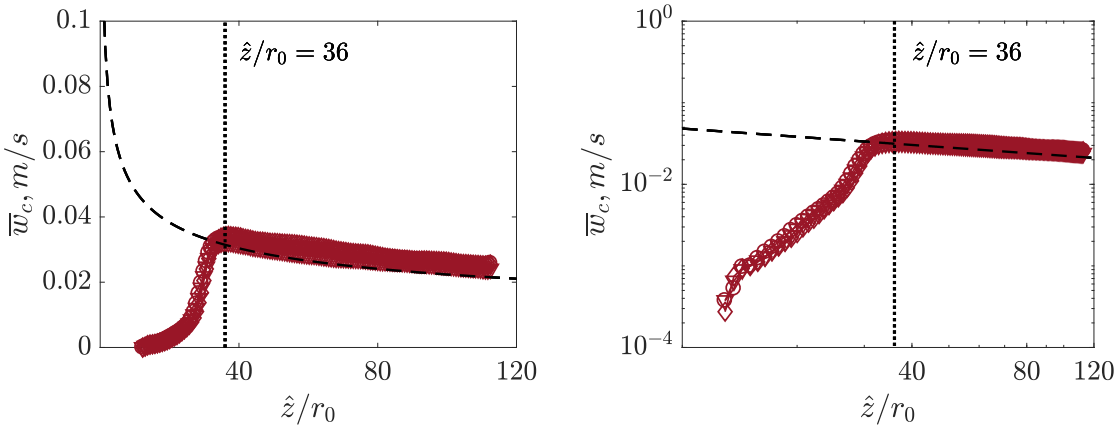

Fig. 5.9 The spatial evolution of the time-averaged vertical centreline velocity $\overline{w}_c$ for the three experiments with double-diffusive plumes (HS1–HS3) plotted on (a) physical scale; and (b) log-log scale. The dashed line marks the theoretical prediction based on the similarity solutions by Morton et al. (1956).

lines represent the confidence levels, estimated as the standard deviations around the mean of the three measurements for single-diffusive plumes. The figure shows that, beyond $\hat{z}/r_0 = 33$, the top-hat entrainment coefficient α_T is nearly a constant, fluctuating around the previously-deduced value of $\alpha_T = 0.12$.

Ultimately, there are two major conclusions that can be drawn from this section. First, the good agreement between the obtained results and the theoretical predictions show that beyond $\hat{z}/r_0 = 33$ the refractive index mismatch had negligible impact on the PIV measurements. This enabled reliable measurements to be collected over a substantial axial distance of $\simeq 75r_0$. Second, the observed sensible physical behaviour of single-diffusive plumes (manifested by self-similar velocity profiles and a reasonable value of the entrainment coefficient) implies that the general quality of the obtained PIV data was satisfactory. Importantly, these results provide the basis for comparison with the similar measurements for the double-diffusive plume experiments (HS1–HS3), which are presented in the next section.

5.3.2.3 Comparison with the double-diffusive plumes

We now proceed to comparing the time-averaged measurements of the single-diffusive plumes with their double-diffusive counterparts. Similarly to the procedure followed for the single-diffusive plumes, we first identified the region beyond which refractive index mismatch was insignificant and the obtained data could be reliably analysed.

Figure 5.9 shows the decay of time-averaged centreline vertical velocity $\overline{w}_c$ as a function of the normalised distance from the virtual origin $\hat{z}/r_0$ for three double-diffusive experiments (HS1–HS3). As in figure 5.5, in that figure, the dashed line represents the theoretical prediction for $\overline{w}_c$ based on the similarity solution for vertical centreline velocity decay (2.42b) at given source conditions. Similarly to the single-diffusive plume experiments, figure 5.9a shows that at early stages ($13 < \hat{z}/r_0 < 23$), the obtained values of $\overline{w}_c$ were significantly lower that the model prediction and were slowly adjusting to the corresponding theoretical values. Later, over the region of $23 < \hat{z}/r_0 < 36$, the measured values of $\overline{w}_c$ grew rapidly, ultimately reaching the model prediction. Note that the change in the cut-off region from $\hat{z}/r_0 = 33$ for single-diffusive plumes to the new value of $\hat{z}/r_0 = 36$ for double-diffusive plumes can be nearly fully accounted for by the difference in the virtual origin corrections, implying that it took the double-diffusive plume roughly the same distance from the physical source to dilute enough, so that the refractive index mismatch has negligible impact. Beyond $\hat{z}/r_0 = 36$, the values of $\overline{w}_c$ for all three double-diffusive experiments follow well the theoretical model and each other. As for the single-diffusive plumes, re-plotted on log-log axis and shown in figure 5.9b, the obtained centreline velocity measurements for the double-diffusive plumes attain the $-1/3$ slope after $\hat{z}/r_0 = 36$ and follow it well throughout the remaining measurement window. On the basis of these observations, we took the value of $\hat{z}/r_0 = 36$ as the distance beyond which velocity measurements for double-diffusive plumes were deemed satisfactory, and used them for comparison against the results for the single-diffusive plumes.

Figure 5.10 demonstrates the values of the entrainment coefficient for the single- and double-diffusive plumes, evaluated using (5.6). In figure 5.10a the blue and red markers represent the values of α_T, averaged for the three single- and double-diffusive plumes, respectively. The dotted lines represent the confidence levels, estimated as the standard deviations around the mean of the three respective measurements. The figure shows that, unlike the single-diffusive plumes, whose value of the entrainment coefficient beyond $\hat{z}/r_0 = 36$ was nearly a constant, the value of α_T for the double-diffusive plumes was evolving with the distance from the source. In particular, close to the source, starting from $\hat{z}/r_0 = 36$, double-diffusive plumes demonstrate significantly lower values of the entrainment coefficient, in comparison with their single-diffusive counterparts. This difference reduces as the plume travels further downstream, ultimately nearly reaching the value of α_T for the single-diffusive plumes at the end of the measurement window.

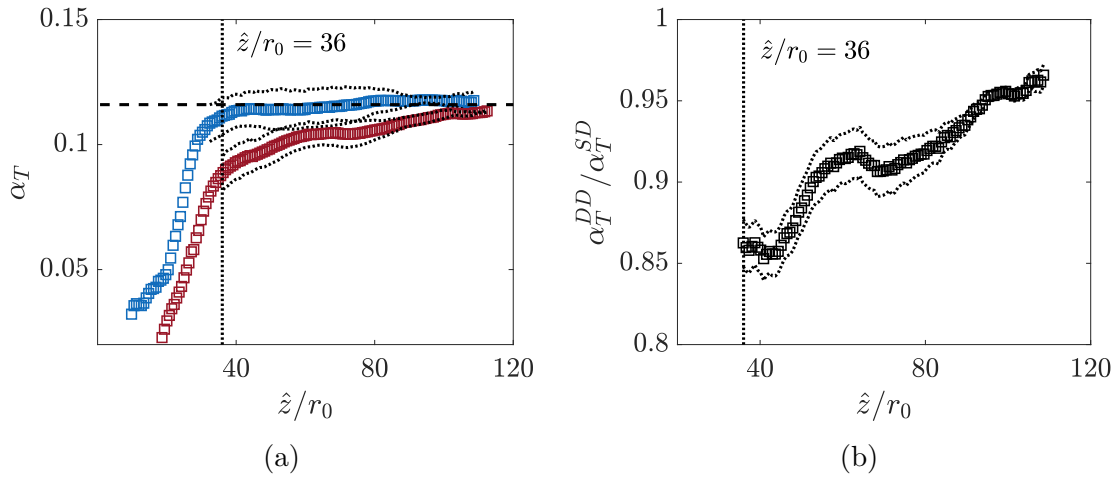

Fig. 5.10 The spatial evolution of the (a) average entrainment coefficient for the three single-diffusive plumes α_T^{SD} (represented by the blue markers) and for the three double-diffusive plumes α_T^{DD} (represented by the red markers); (b) the ratio between the values of the entrainment coefficient as a function of distance from the virtual origin.

The evolution of the ratio between the entrainment coefficients of the single- and double-diffusive plumes is shown in figure 5.10b. The figure shows that there is an up to 15% reduction in the value of α_T for double-diffusive plumes, which corresponds well with our measurements obtained using the Baines' filling-box technique and presented in chapter 4. Beyond the increasing trend of the ratio $\alpha_T^{DD}/\alpha_T^{SD}$, it is hard to comment reliably on the actual shape of the obtained profile.

Naive interpretation of the results presented in figure 5.10 may lead to the conclusion that, in the case of double-diffusive plumes, the local rate of entrainment, captured by the entrainment coefficient, is evolving with the distance from the source over the range $36 < \hat{z}/r_0 < 112$. Based on the entrainment assumption of Morton et al. (1956), the evolution of the entrainment coefficient would necessarily lead to the corresponding evolution of the time-averaged vertical and horizontal velocity profiles, which are examined below.

Figure 5.11 demonstrates the normalised vertical velocity profiles $\overline{w}(r,z)/\overline{w}_c$ and horizontal velocity profiles $\overline{u}(r,z)/\overline{w}_c$ plotted at 10 different vertical positions over the overlapping reliable measurement range $36 < \hat{z}/r_0 < 108$ for all six plume experiments (S1–S3, HS1–HS3). Note that in this figure the velocity profiles for double-diffusive plumes are laid over the corresponding profiles for single-diffusive plumes, which are shown separately in figure 5.5a. As for the single-diffusive plumes, the good collapse of the vertical velocity profiles onto a single Gaussian curve implies that for all experiments the double-diffusive plumes followed a self-similar regime over the region $36 < \hat{z}/r_0 < 108$.

Notably, the velocity profiles for the double-diffusive plumes closely match their single-diffusive counterparts. These observations act as the first contradiction to the idea of varying entrainment coefficient over the range $36 < \hat{z}/r_0 < 108$ as we would anticipate the obtained velocity profiles to be spatially evolving in this region.

To verify that the time-averaged dynamics of the double-diffusive plumes was similar to their single-diffusive counterparts in the reliable measurement range $36 < \hat{z}/r_0 < 108$, we now examine the turbulent statistics for both. We define turbulent velocity fluctuations using Reynolds decomposition as

$$u'(r,z,t) = u(r,z,t) - \overline{u}(r,z) \quad \text{and} \quad w'(r,z,t) = w(r,z,t) - \overline{u}(r,z). \tag{5.7}$$

The root mean square (rms) of the velocity fluctuations can then be defined as

$$u'_{rms} = \sqrt{\frac{1}{t_T}\int_0^{t_T} [u'(r,z,t)]^2 \, \mathrm{d}t} \quad \text{and} \quad w'_{rms} = \sqrt{\frac{1}{t_T}\int_0^{t_T} [w'(r,z,t)]^2 \, \mathrm{d}t}, \tag{5.8}$$

where t_T is the total averaging time. Figure 5.12 shows the turbulent fluctuations for the single- and double-diffusive plumes over the range $36 < \hat{z}/r_0 < 112$. The horizontal velocity fluctuations, shown in figure 5.12a, exhibit the profiles similar to those reported by Papanicolaou and List (1988), with the maximum value of $u'_{rms}/\overline{w}_c \simeq 0.2$. The vertical velocity fluctuations, presented in figure 5.12b, show a bi-modal peak, qualitatively similar to the observations made by Van Reeuwijk et al. (2016) in their direct numberical simulation (DNS) study of turbulent plumes. The mean profiles of the Reynolds stress, shown in figure 5.12c, are zero at the plume centreline, exhibit two peaks at $r/\overline{R}_e \simeq 0.6$, and reduce rapidly for larger radial positions. Such profiles of the Reynolds stress are also in agreement with the measurements by Van Reeuwijk et al. (2016).

Importantly, in addition to the closely-matching self-similar time-average velocity profiles shown in figure 5.11, the self-similarity and the good collapse of turbulent statistics data between single- and double-diffusive plumes provides further indication that their dynamics was indeed very similar over the region $36 < \hat{z}/r_0 < 108$. This leads to the conclusion that in the region of reliable measurements, the double-diffusive plumes attained self-similarity and behaved as normal single-diffusive plumes. This, in turn, contradicts the possibility of local evolution of the entrainment coefficient over that region and gives rise to the question on where does the reduction in entrainment come from.

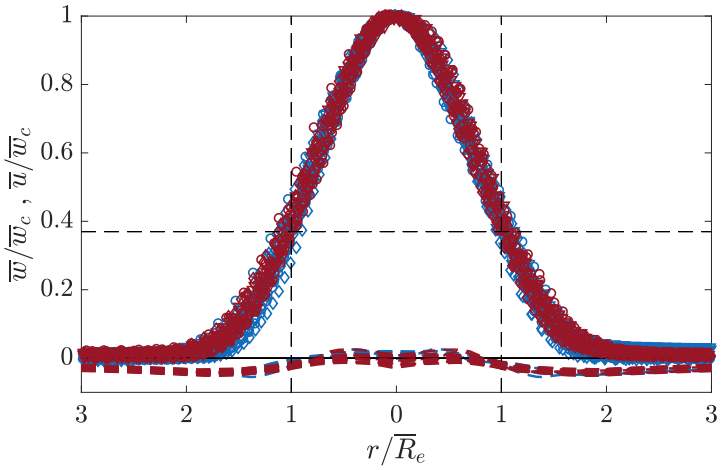

Fig. 5.11 The time-averaged scaled vertical $\overline{w}/\overline{w}_c$ and horizontal $\overline{u}/\overline{w}_c$ velocities for all six plume experiments (S1–S3, HS1–HS3) at 10 different heights spanning the overlapping region of $36 < \hat{z}/r_0 < 108$. The good collapse of data demonstrates that in all six cases the flow exhibits the behaviour of a turbulent self-similar pure plume. The black horizontal dashed line marks the theoretical value of $\overline{w}/\overline{w}_c$ the at the e-folding width $\overline{R}_e$, which is in good agreement with the obtained profiles.

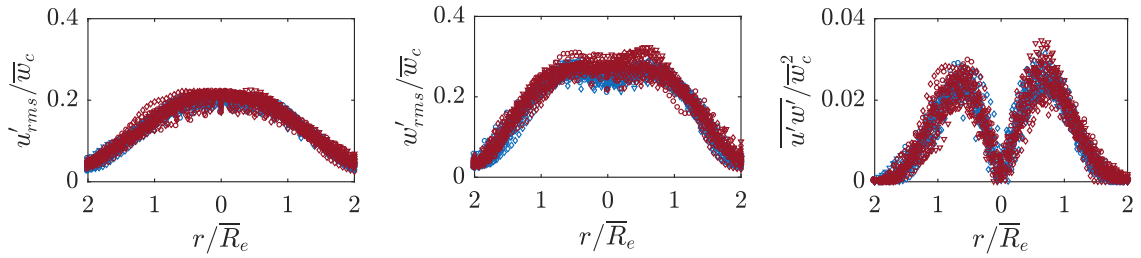

Fig. 5.12 Time-averaged scaled turbulent fluctuations of (a) horizontal velocity, (b) vertical velocity and (c) Reynolds stress, for all six experiments.

We hypothesise that, if not occurring locally, the observed reduction of the entrainment coefficient is likely to be a 'shadow' of the dynamic changes that the double-diffusive plumes were undergoing earlier in their travel. Recall that the method used to deduce the value of the entrainment coefficient is based on the similarity solution for the plume volume flux. In particular, the model predicts that at a given distance from the virtual origin, the pure turbulent plume should develop a certain volume flux. Based on that, the observed reduction in the entrainment coefficient could be the direct outcome of the underdeveloped plume volume flux at a given axial distance from the virtual origin $\hat{z}$, which occurred as a result of the reduction of the

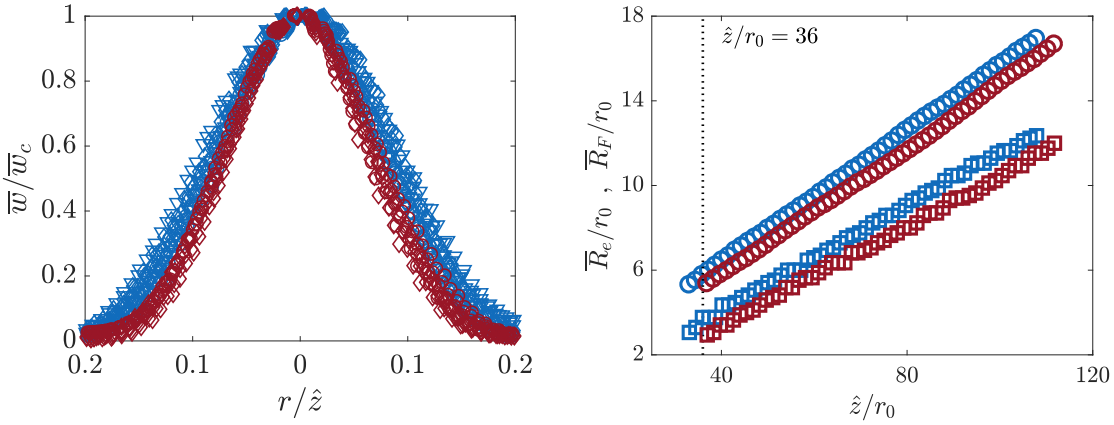

Fig. 5.13 The time-averaged (a) radial profiles of the scaled vertical velocities $\overline{w}/\overline{w}_c$ for the three single-diffusive plumes and three double-diffusive plumes at 10 different heights spanning $36 < \hat{z}/r_0 < 66$; (b) time-average normalised e-folding plume half-width $\overline{R}_e$ (represented by squares) and flux-based top-hat plume radius $\overline{R}_F/r_0$ (represented by circles), averaged for three respective experiments.

total volume of the entrained fluid along its journey. The observed reduction in the value of the entrainment coefficient is then the consequence of the deficit of volume flux, which diminishes as the plume travels further downstream and increases its total volume flux.

If the above hypothesis is true, the reduction in the rate of entrainment, leading to the deficit of the plume volume flux, should be reflected on the plume physical dimensions in the time-averaged sense. Figure 5.13a shows the time-averaged vertical velocity profiles for the three single- and three double-diffusive plumes at 10 different heights spanning the region of $36 < \hat{z}/r_0 < 66$. In contrast to the results presented in figure 5.11, in this figure, the radial position was normalised by the distance from the plume virtual origin $\hat{z}$. The figure shows that, over the entire range, the average normalised profiles of the double-diffusive plume vertical velocities are narrower in the normalised radial direction $r/\hat{z}$, than those of the single-diffusive plumes. This result is also demonstrated in figure 5.13b, where the spatial evolution of the e-folding $\overline{R}_e$ and flux-based $\overline{R}_F$ plume radii, averaged for three respective experiments are shown using squares and circles, respectively. The figure shows that, taken the same distance away from the virtual origin, the time-averaged e-folding radii of the double-diffusive plumes are smaller than those for the single-diffusive plumes. This is not surprising as these radii are deduced from the profiles, shown in figure 5.13a. However, importantly, the same holds true for $\overline{R}_F$, which is the characteristic flux-based (using volume and

specific momentum fluxes) plume width and hence is based on the overall time-averaged integral plume properties.

The fact that the plume is self-similar, yet narrower in the radial direction, implies that the effect of double-diffusion on the entrainment process must have occurred in the early stages of the plume development and vanished by the time the plume fluid got to $\hat{z}/r_0 = 36$. Travelling downstream, the plume becomes increasingly dilute through turbulent entrainment, rapidly weakening its initially large source temperature and salinity gradients, and hence the strength of the double-diffusive processes. As it does so, the plume ultimately attains self-similarity and behaves in a similar fashion to a normal single-diffusive plume.

Based on the above, it is to be expected that no significant difference in the dynamics of the double-diffusive plumes should be observed once the self-similar state has been attained. To gain further assurance that the single- and double-diffusive plumes behaved similarly in the reliable measurement region, we performed statistical analysis of the instantaneous velocity field measurements, by combining them with the scalar field measurements as laid out below. In that, we follow some of the techniques employed by Burridge et al. (2016).

5.3.3 Results in a plume coordinate system

5.3.3.1 Plume edges: detection and statistics

Given that, in our experiments, the Batchelor length scale (at which molecular diffusivity dominates) was small, that is, $5.01 \times 10^{-6} \leq \eta_B(\hat{z} = 60) \leq 6.42 \times 10^{-5}$ m, compared to the resolution of the LIF measurements (2.93×10^{-4} m), it was impossible to precisely detect the scalar interface between the plume and the ambient fluid. To that end, we employed a threshold-based technique, according to which, pixels containing values lower than a certain threshold were replaced by zeros. The remaining pixels were assigned the value of unity, thereby producing a black and white (binary) image. This approach was undertaken sequentially for each instantaneous image of the flow. Once converted into the binary scale, the images were processed using an algorithm, which detected the two outermost points of the plume as the first and the last locations for each pixel row where a change in the value of the pixel intensity occurred. The first such location, going from left to right, was marked as the plume left edge $E_L(z,t)$ and the second as the plume right edge $E_R(z,t)$. The difference between the locations of the two edges gives the instantaneous plume width $2\overline{R}_p$, which was used to calculate the instantaneous and the time-averaged plume half-widths $R_p(z,t)$ and $\overline{R}_p(z)$, respectively.

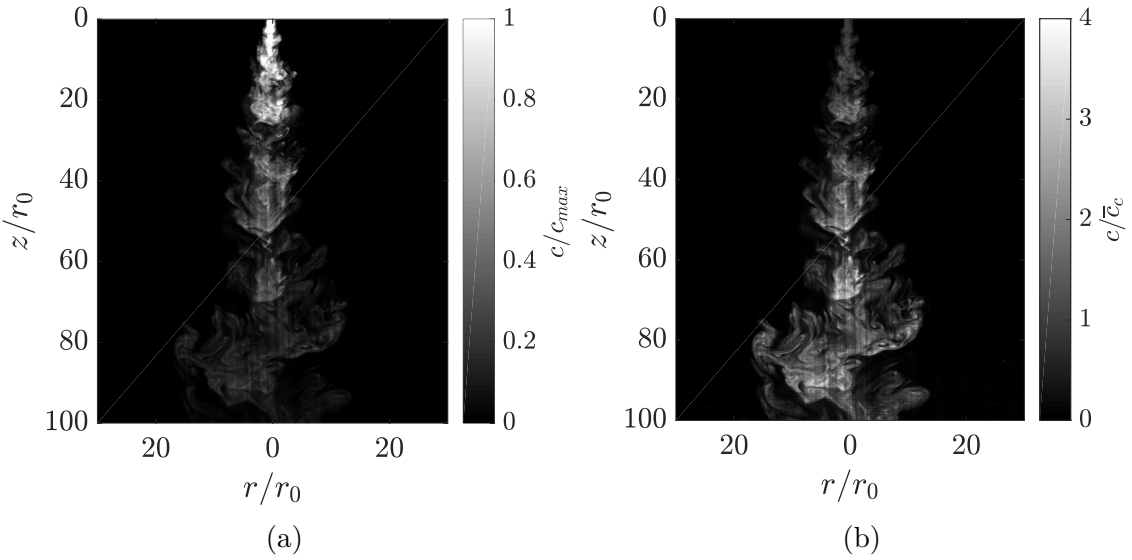

Fig. 5.14 Processed visualisations of the plume flow for experiment S1 at time $t = 9.7$ s with the obtained scalar field normalised by (a) maximum scalar concentration found within the image c_{max}; (b) centreline time-averaged scalar concentration $\overline{c}_c$. The colour scheme is as perceived by the camera.

The effectiveness of the above method in determining the plume edges depends critically on the choice of the threshold value used for converting images into the binary format. The exact value of the threshold can be determined in multiple ways, e.g. Burridge et al. (2016). In our analysis we employed a method similar to that used by Vanderwel and Tavoularis (2014), which relies on the observation that the histogram of the light intensities for a typical experimental image of a turbulent plume flow exhibits a bi-modal distribution.

Figure 5.14a shows the typical image of a plume normalised by the maximum scalar intensity c_{max} found within that image. The figure demonstrates that over such a large measurement range ($0 < z/r_0 < 100$), the entrainment process led to a substantial dilution of the plume fluid, resulting in a wide range of perceived scalar intensities. In order for a universal value of the threshold to be effective for all images over the entire z-range, all raw images had to be normalised by some global quantity. For consistency, this was taken to be the plume time-average centreline scalar intensity $\overline{c}_c(z)$. The result of such normalisation of the snapshot shown in figure 5.14a, is presented in figure 5.14b. Similar images were obtained for all other frames in all experiments and were sequentially sampled to produce the total distribution of scalar concentrations for further sampling analysis.

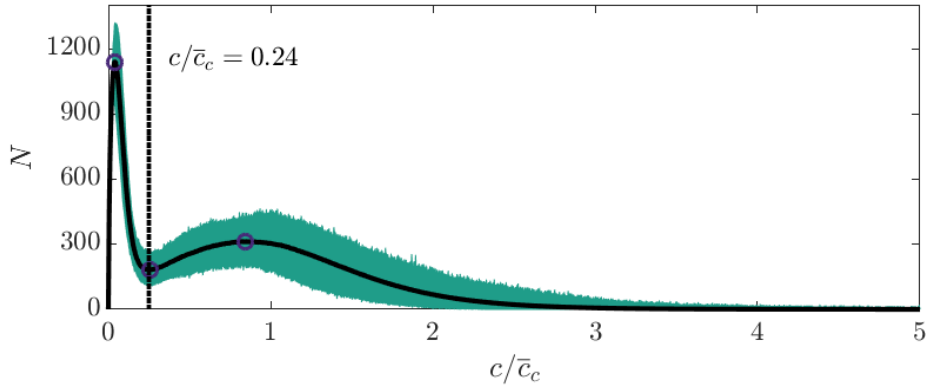

Fig. 5.15 Histogram of the normalised scalar concentrations for all frames in experiment S1. Circles mark the locations of the first three inflection points and the black line marks the average over all images. The dotted vertical line represents the value of selected threshold $c/\overline{c}_c = 0.24$ for experiment S1.

Figure 5.15 shows the output of the sampling procedure for experiment S1, where all pixels from all normalised images were 'binned' by their intensities into a range of 5 bins, discretised into 1024 buckets. The solid black line represents the average profile over the total of $\simeq$ 12,000 images. Similar to the result reported by Vanderwel and Tavoularis (2014), the obtained result exhibits a bi-modal distribution, with the first peak (of low pixel intensities) corresponding to the ambient. The high number of occurrences of pixels with very low scalar concentration ($c/\overline{c}_c \simeq 0$) arises from the relatively large area within each image occupied by the ambient fluid. The second peak (occurring at around $c/\overline{c}_c = 0.8$) is associated with the plume fluid, which, as expected, has a larger variance of the obtained pixel intensities and a much lower N-peak. Vanderwel and Tavoularis (2014) showed that in application to slender plumes the local minimum value between the two peaks can be effectively used as the threshold for differentiating the plume fluid from the ambient. Following this approach, such minima were determined from the average histogram profile for each experiment individually, using a computer algorithm. The obtained values of the threshold fell into the range of $0.24 < c/\overline{c}_c < 0.26$, and were used for each experiment to detect the instantaneous scalar plume edges ($E_L(z,t)$ and $E_R(z,t)$) using the method described earlier in this subsection.

Figure 5.16 shows the result of the edge detection procedure for the snapshot shown in figure 5.14. In that figure the resulting left and right plume edges are marked as solid lines, and the white horizontal arrows indicated the positions of the left ($E_L(z,t)$) and right ($E_R(z,t)$) edges for a particular distance from the source. The result of such an edge detection procedure was typical for all experimental images. The figure

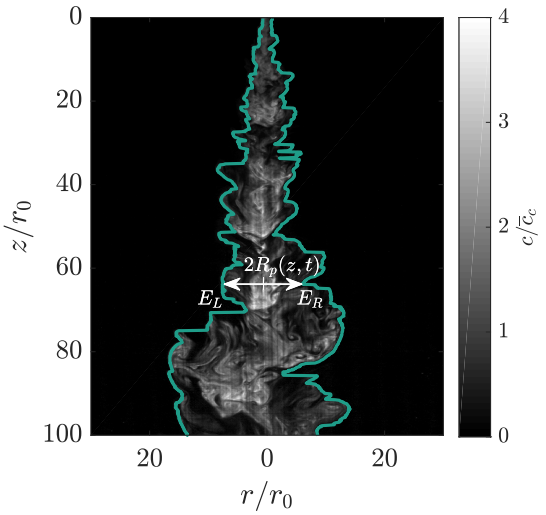

Fig. 5.16 Typical experimental image normalised by the time-average centreline scalar concentration $\overline{c}_c$, with both detected edges E_L and E_R represented by solid lines. The white horizontal arrows indicated the positions of the left edge $E_L(z,t)$ and the right edge $E_R(z,t)$ for a particular distance from the source.

demonstrates that using the threshold value determined by following the methodology described above, the obtained plume scalar edges (defined as the plume outermost points) were in good visual agreement with the qualitatively perceived plume scalar edges.

For a more quantitative verification of the validity of the obtained plume edges, in figure 5.17 we plotted the histograms of the radial locations of the left and right edges obtained for all experiments, as well as the associated instantaneous plume centre $C(z,t) = [E_L(z,t) + E_R(z,t)]/2$. In this figure, the results for experiments HS1–HS3 were overlaid on top of S1–S3, and the radial distance was normalised by the time-average local plume half-width $\overline{R}_p = [\overline{E}_R(z,t) - \overline{E}_L(z,t)]/2$. Results, presented in this plot lead to the following two conclusions. First, the ability of the Gaussian profiles, shown as black solid lines, to approximate the obtained data for the single-diffusive plumes acts as a validation for the employed edge detection algorithm, as similar behaviour was reported previously by Burridge et al. (2017). In particular, the obtained distributions for single-diffusive plumes follow well the best-fit Gaussian profiles with $E_L \sim N(\mu = -1, \sigma^2 = 0.033)$, $E_R \sim N(\mu = 1, \sigma^2 = 0.034)$ and $C \sim (\mu = 0, \sigma^2 = 0.017)$. Second, the good overlay of the data for single- and double-diffusive plumes show that in the reliable measurements range, their meandering was statistically similar.

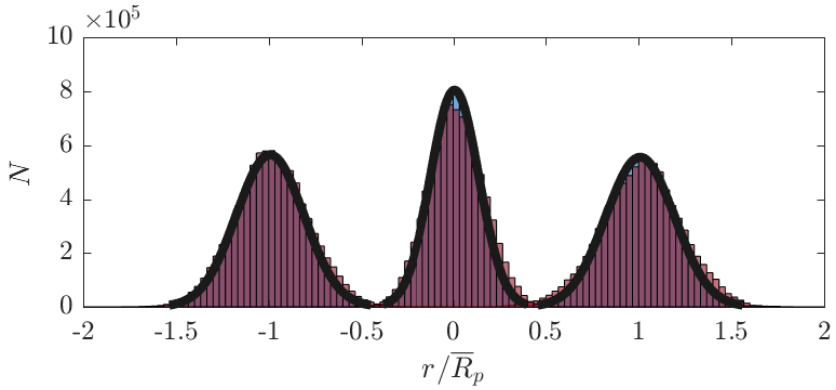

Fig. 5.17 Histogram of the locations of centre, left, and right edges of the plume for all six experiments normalised by the time-average local plume half-width $\overline{R}_p$. The average result for the double-diffusive plumes (marked in red) is overlaid on top of the result for the single-diffusive plumes (marked in blue). In both cases, the result is presented for the region over which reliable measurements could be obtained ($\hat{z} > 36$). The best-fits Gaussian curves for the single-diffusive plume data is presented as a solid black line for each distribution.

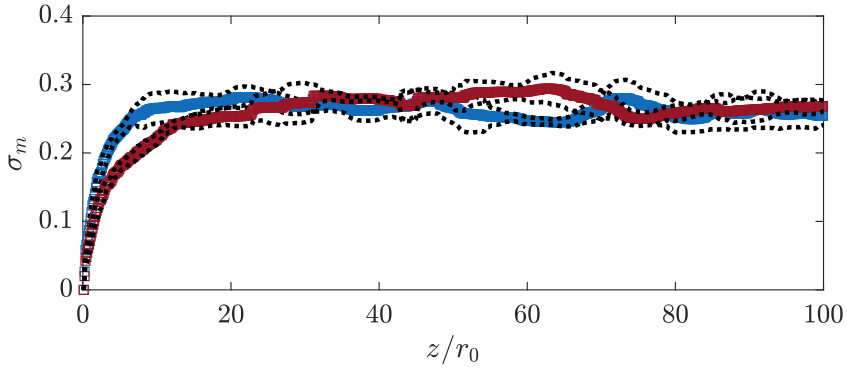

Fig. 5.18 Spatial evolution of plume meandering, defined as $\sigma_m = std[(E_R + E_L)/2 - \overline{C}]$, with the physical normalised distance from the source, averaged for the three single- and double-diffusive plumes. The confidence levels for the obtained results are represented using dotted lines.

The second observation also follows from figure 5.18, represents the plume meandering in a slightly different manner. In particular, from the obtained and verified instantaneous locations of the plume scalar edges and the associated centreline, it is possible to define a quantity $\sigma_m = std[(E_R + E_L)/2 - \overline{C}]$, which may be used as a representation of the scale of meandering of the plumes. The obtained values of σ_m, averaged over the groups of single- and double-diffusive plume experiments, are shown in figure 5.18. From that figure, it is clear that far enough downstream ($\hat{z} > 30$), meandering was statistically similar with the value of $\sigma_m \simeq 0.25$. It appears that

the meandering of the double-diffusive plumes was slightly lower close to the source, which could be related to the changes in the entrainment process. It is, however, hard to comment reliably on this observation, as any measurements taken in the region $\hat{z}/r_0 < 36$ could not be verified due to the refractive index mismatch.

5.3.3.2 Scalar and velocity field measurements in the plume coordinates

To perform further analysis of the behaviour of the single- and double-diffusive plumes, we followed the approach first introduced by Burridge et al. (2017), examining the flow field in a new 'dynamic' coordinate system, which uses both scalar edges to follow the plume as it evolves. In particular, for each time instant and z-position, we defined a local coordinate system in which the position $r_p = 0(z,t)$ was the instantaneous plume centre-point between the two edges at that distance from the source, and the left- and right-hand edge positions were denoted respectively as $r_p(z,t) = -R_p(z,t) = E_L(z,t)$ and $r_p(z,t) = R_p(z,t) = E_R(z,t)$. The plume scalar and velocity fields in the Eulerian frame were then mapped onto this new coordinate system using linear interpolation, so that $c(r,z,t) \rightarrow c(r_p,z,t)$, $w(r,z,t) \rightarrow w(r_p,z,t)$ and $u(r,z,t) \rightarrow u(r_p,z,t)$.

Figures 5.19a and 5.19b show two snapshots of the resulting scalar field in the plume coordinates for experiments S1 and HS1, respectively, taken at time $t = 20$ s. Such images were typical for all experiments at all time instants. Both figures clearly demonstrate that in the plume coordinates, the plume fluid was predominantly distributed between $r_p/R_p < 1$ on both sides from the centreline, with a sharp drop in the scalar concentration just outside $r_p/R_p = 1$ at all distances from the source. This observation provides another confirmation of the accuracy of the undertaken edge detection methodology, and indicates that the mapping procedure was performed correctly. Notably, both snapshots of the concentration field demonstrate the presence of plume fluid with high concentration (bright patches), not only around the plume centreline, but throughout its envelope, as well as near the instantaneous edges.

The instantaneous velocity field in the plume coordinates exhibits a somewhat different behaviour, and can be clearly contrasted with the scalar field. Most notably, figures 5.19c and 5.19d demonstrate that for both single- and double-diffusive plumes, significant vertical motion was present outside the instantaneous plume edges throughout the entire measurement window. This observation is in agreement with that made by Burridge et al. (2017), where they reported significant volume fluxes (of up to 5% of the total vertical transport on average) occur outside the plume scalar edge. In addition, in contrast to the scalar field, the regions with high vertical velocities tend to be concentrated around the plume instantaneous centreline.

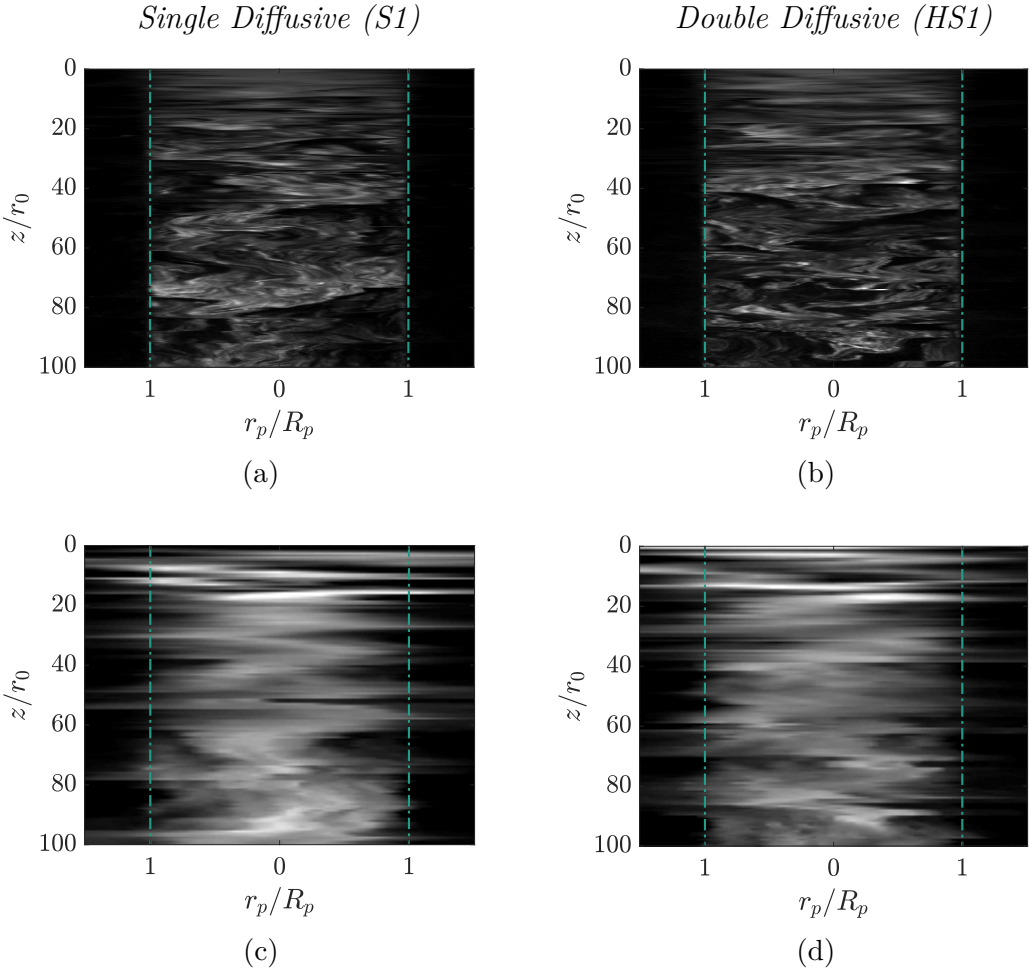

Fig. 5.19 Instantaneous fields of (a, b) scaled scalar concentration $c_p(r_p, z, t)/\overline{c}_c$; (c, d) scaled vertical velocity $w(r_p, z, t)/\overline{w}_c$ for single- and double-diffusive plume experiments S1 and HS1, respectively, taken at time t = 20 s. In all figures, the bright vertical dash-dot lines represent the locations of the plume left and right edges.

To proceed further, the scalar concentration fields $c_p(r_p, z, t)$ were time-averaged in the plume coordinate system using

$$\overline{c}_p = \overline{c}(r_p, z) = \frac{1}{t_T} \int_0^{t_T} c(r_p, z, t) \mathrm{d}t. \tag{5.9}$$

Similarly, the time-averaged plume-coordinate vertical and horizontal velocity fields were obtained using

$$\overline{w}_p = \overline{w}(r_p, z) = \frac{1}{t_T} \int_0^{t_T} w(r_p, z, t)\, \mathrm{d}t, \quad \overline{u}_p = \overline{u}(r_p, z) = \frac{1}{t_T} \int_0^{t_T} u(r_p, z, t)\, \mathrm{d}t. \tag{5.10}$$

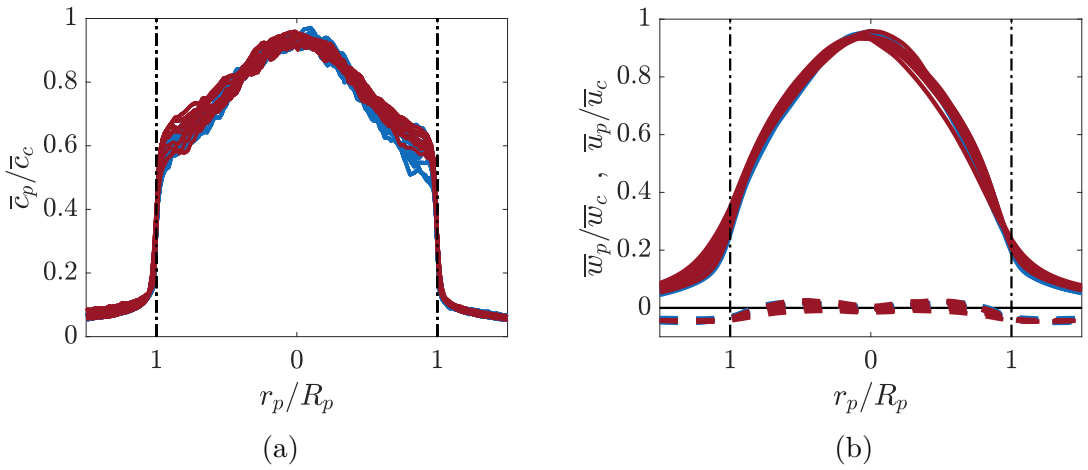

Fig. 5.20 Time-averaged radial profiles in the plume coordinates of (a) normalised scalar concentration $\overline{c}_p/\overline{c}_c$; (b) normalised vertical $\overline{w}_p/\overline{w}_c$ and horizontal $\overline{u}_p/\overline{u}_c$ velocities, taken at 10 different heights spanning the region $36 < \hat{z}/r_0 < 108$. The red and blue lines represent the averages over the three single- and double-diffusive plumes, respectively, and the dashed lines represent the horizontal velocity. The dash-dot vertical lines represent the locations of the plume left and right edges. Note the significantly more Gaussian-like shape of the vertical velocity profiles.

Figure 5.20 presents the result of the averaging procedure for the three properties across all six experiments. In particular, figure 5.20a shows the normalised concentration profiles in the plume coordinates for single- and double-diffusive plumes, marked using blue and red lines, respectively. The obtained profiles are self-similar and collapse well on top of each other, but instead of following the conventional Gaussian shape, they exhibit a rather more top-hat profile, with a sharp change in the value of $\overline{c}_p/\overline{c}_c$ at the plume edges. This is consistent with the observations made from the instantaneous scalar distributions, where we noted that the plume fluid was rather evenly distributed across its envelope.

The normalised vertical and horizontal velocity profiles in the plume coordinates, shown in figure 5.20b, are also self-similar and collapse well on top of each other, but, in contrast to the concentration profiles, the vertical velocity profiles demonstrate a clearly more Gaussian-like shape. This is consistent with the observation made from figures 5.19 (c, d), demonstrating that even in the absence of the intermittency, the vertical velocity profiles are nearly normally distributed. For both single- and double-diffusive plumes, the vertical velocities at the instantaneous plume edges were approximately $20 - 30\%$ of the local centreline vertical velocity. This is in good agreement with the measurements of Burridge et al. (2017), and the visual measurements of the coherent

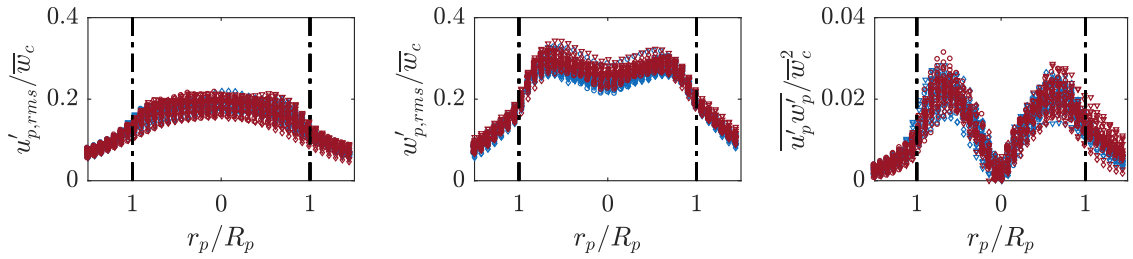

Fig. 5.21 Time-averaged scaled turbulent fluctuations in the plume coordinates of (a) horizontal velocity, (b) vertical velocity and (c) Reynolds stress, taken at 10 different heights spanning the region $36 < \hat{z}/r_0 < 108$.

plume structures done by Burridge et al. (2016). In the latter, the authors found the structures to be travelling at ~ 30% of the plume centreline velocities.

From the obtained vertical and horizontal velocities in the plume coordinates we define the fluctuating terms using Reynolds decomposition with respect to the time-averaged velocities in plume coordinates as

$$u'_p(r_p, z, t) = u(r_p, z, t) - \overline{u}(r_p, z) \quad \text{and} \quad w'_p(r_p, z, t) = w(r_p, z, t) - \overline{w}(r_p, z). \tag{5.11}$$

The root mean square of the velocity fluctuations in the plume coordinates can then be defined as

$$u'_{p,rms} = \sqrt{\frac{1}{t_T}\int_0^{t_T} [u'_p(r, z, t)]^2 \, \mathrm{d}t} \quad \text{and} \quad w'_{p,rms} = \sqrt{\frac{1}{t_T}\int_0^{t_T} [w'_p(r, z, t)]^2 \, \mathrm{d}t}. \tag{5.12}$$

The turbulent properties for all experiments are shown in figure 5.21, where, as before, the blue and red lines represent the single- and double-diffusive plumes. The figure shows that all three quantities behave qualitatively similar to their equivalents in the Eulerian frame of reference, with a single flat peak for the $u'_{p,rms}$ and the bi-modal peaks for the $w'_{p,rms}$ and the Reynolds stress. In line with the results of Burridge et al. (2017), the locations of the peaks for the bi-modal distributions $r_p \simeq 0.5R_p$, roughly correspond to the locations at which the radial velocities in the plume were zero. Importantly, all profiles were self-similar and collapsed well on top of each other.

Altogether, this section shows that in the plume coordinates no systematic differences in the time-averaged plume concentration and velocity fields between the single- and double-diffusive plumes were present in the region $36 < \hat{z}/r_0 < 108$. Additional measurements of the velocity field conditioned on the local absence and presence of an eddy were performed, but also did not reveal any systematic differences between the

single- and double-diffusive plumes, and were hence omitted. In conjunction with the observations made in section 5.3.2.3, the absence of notable differences in the plume coordinates is, perhaps, unsurprising. In fact, it is consistent with the idea that by the time the thermohaline plumes reached $\hat{z}/r_0 = 36$, the double-diffusive processes were too weak to be of significance, hence the plumes became self-similar and evolved in a similar fashion to the normal single-diffusive plumes.

5.4 Conclusions

Simultaneous velocity and scalar field measurements of single- and double-diffusive plumes emanating from a point source into a homogeneous quiescent environment were performed. The flux-based measurements of the entrainment coefficient revealed that for the single-diffusive plumes the entrainment coefficient had a constant value of $\alpha_T = 0.12 \pm 0.1$. This is in good agreement with the values reported by previous investigators, summarised in table 1.1, and with the direct filling-box measurements reported in chapter 4. In contrast, the measured value of the entrainment coefficient for the double-diffusive plumes in the salt-fingering configuration ($R_\rho = 0.46$) was not a constant but varied with the distance from the virtual origin.

The refractive index mismatch inhibited reliable measurements closer than $\hat{z}/r_0 = 33$ and $\hat{z}/r_0 = 36$ for single- and double-diffusive plumes, respectively. Taken from $\hat{z}/r_0 = 36$, the measured value of α, averaged over three double-diffusive plumes, was $\sim 14\%$ lower than that of the single-diffusive plumes. A similar reduction of $10 - 15\%$ was observed for the thermohaline plumes at comparable source stability ratio ($R_\rho \simeq 0.49$) using the filling-box measurements, providing further confidence in the obtained result. Moreover, in agreement with the filling-box measurements, the observed difference in α continuously reduced as the double-diffusive plumes travelled further downstream, ultimately nearly reaching the value of α for the single-diffusive plumes. This suggests that double-diffusive effects weaken with the distance from the source.

Normalised by the plume e-folding width $\overline{R}_e$, the time-averaged velocity measurements, and the associated turbulent properties, of the single- and double-diffusive plumes in the Eulerian coordinates display no systematic differences. However, if normalised by the distance from the virtual origin $\hat{z}$, the Gaussian profiles of the vertical velocities for the double-diffusive plumes appear systematically narrower than those for their single-diffusive counterparts. Moreover, taken the same distance from the virtual origin, the characteristic e-folding radius $\overline{R}_e$ and the flux-based half-width $\overline{R}_F$ of the double-diffusive plumes appeared systematically smaller that those of the

single-diffusive plumes. These observations are consistent with the reduction in the rate of entrainment, which leads to the double-diffusive plumes being unable to develop equivalent fluxes and length scales through entrainment.

Although double-diffusive plumes appear to be narrower throughout the measurement range, the self-similarity of the time-averaged velocity profiles, and the associated turbulent properties in both Eulerian and the plume coordinates imply that the effect of double-diffusion on the dynamics of the flow, and hence on the entertainment coefficient, was insignificant over the region of reliable measurements. The same conclusion follows from the observation that the difference in the plume radii ($\overline{R}_e, \overline{R}_F$) between the single- and double-diffusive plumes remained constant throughout $\hat{z}/r_0 > 36$. This, in turn, implies that double-diffusion only had significant effect on the plume dynamics at very early stages and vanished as the plume travelled downstream, attaining and preserving self-similarity. The difference in the entrainment coefficient between the single- and double-diffusive plumes, present throughout the measurement range, can therefore be though of as a 'shadow' of the changes that occurred to the plume close to the source. If true, this suggests that, the local reduction to the entrainment coefficient near to the source could be much greater.

The weakening effect of double-diffusion on the rate of turbulent entrainment is consistent with the differential diffusion proposal, laid out in section 4.4.3. For a fixed fluid-solute combination, the key factor determining the importance of this mechanism is the concentration gradient of the two scalar properties. Close to the source, both concentration gradients are large and the effect of double-diffusion on the plume behaviour is significant. However, turbulent entrainment leads to a rapid dilution of the plume, and hence reduction of the concentration gradients, with less than $\sim 20\%$ of its original temperature and salinity difference remaining at $\hat{z}/r_0 = 33$. It is perhaps unsurprising that such insignificant scalar gradients, reducing even further as the plume travels downstream, are unable to noticeably alter the dynamics of the plume flow.

Ultimately, this study shows that in order to gain the complete picture of the processes governing the dynamics of high-Péclet-number turbulent double-diffusive plumes, is it necessary to be able to interrogate the flow field at the source, where double-diffusive effects are the strongest. With the current lack of a technique allowing to refractive index match for large gradients of both heat and salt, experimental methods based on the visual data collection fail to do so reliably, and thus have to be either replaced by intrusive direct measurements or, perhaps more preferably, numerical computation.

Chapter 6

Double-Diffusive Jets

6.1 Introduction

In the previous two chapters we demonstrated that double diffusion may have considerable effect on the dynamics of turbulent plumes. In this chapter, we proceed further, and investigate experimentally the effect of double diffusion on the dynamics of turbulent round jets discharged into a quiescent fresh ambient.

As for plumes, for these experiments we chose to work with the aqueous system in which a hot and salty (thermohaline) jets were discharged into cooler fresh water. For this combination, the component with the larger molecular diffusivity κ_T is temperature T and that with the smaller molecular diffusivity κ_S is salinity S. The Lewis number $Le = \kappa_T/\kappa_S$ is $O(100)$, and therefore even for moderate concentration gradients of both components, the system can be strongly doubly-diffusive. Jets over a range of source Reynolds numbers and source temperature/salinity combinations were examined. To simplify our analysis, we restricted our attention to initially neutrally-buoyant jets discharged horizontally, with the only control parameters being the source scalar concentrations $(\Delta S_0, \Delta T_0)$ and the source Reynolds number $Re_0 = U_0 r_0/\nu$, where U_0 and r_0 are the source horizontal velocity and outlet radius, respectively.

The rest of this chapter is structured as follows. In section 6.2 we describe the experimental setup and the procedure followed to create neutrally-buoyant double-diffusive jets. Visual observations of the differences between single- and double-diffusive jets are presented in section 6.3.1. We then summarise and discuss the time-averaged results in section 6.3.2, highlighting the systematic features of double diffusive jets as function of the control parameters. An explanation for the observed sinking behaviour is proposed in section 6.3.3. The prediction of the onset of salt fingers is made in section 6.3.5, and, finally, in section 6.4 a series of conclusions are drawn.

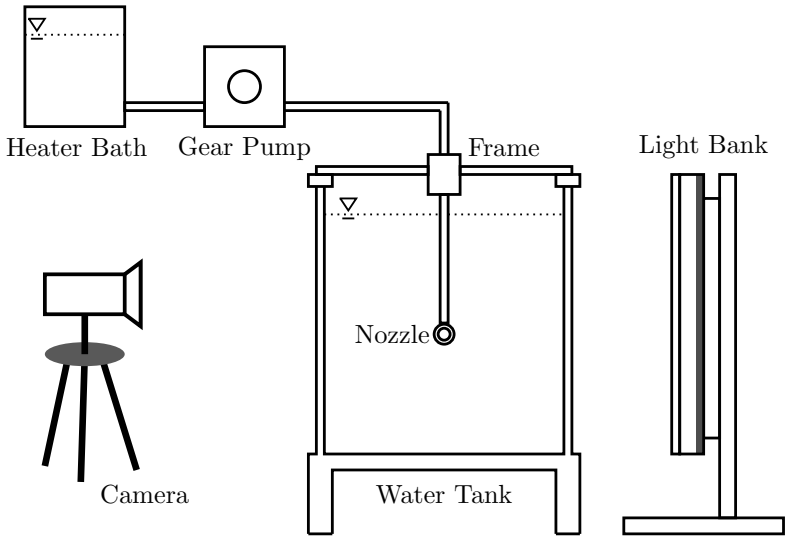

Fig. 6.1 A schematic representation of the experimental setup.

6.2 Experimental procedure

All experiments were conducted in a large transparent tank, measuring 2.5 m × 0.70 m × 0.80 m ($L \times W \times H$), filled with fresh water. Figure 6.1 shows a schematic diagram of the entire experimental setup. Turbulent jets were created by steadily ejecting source solution through a nozzle into the ambient fluid using a gear pump, which was carefully calibrated over the range of volume fluxes used, $3.0 < Q_0 < 7.0$ ml s^{-1}. The typical error of the source flow rate did not exceed ± 0.05 ml s^{-1}, which was estimated as two standard deviations about the mean flow rates measured during calibration. For the details of the pump, the reader is referred to section 3.2.3.

Given the moderate source Reynolds numbers ($700 < Re_0 < 1500$), the jet fluid had to be additionally excited to produce turbulent flow at the point of discharge. As with plumes, this was achieved by ejecting the fluid through a nozzle, specifically designed to promote turbulence within the flow. The jet nozzle, allowing horizontal ejection of the source fluid, was based predominantly on the plume nozzle design, originally developed by Professor P. Cooper, and illustrated schematically in section 3.2.1. Similar to the plume nozzle, the jet nozzle produced turbulent flow by passing the incoming fluid through a 'pin-hole' (diameter 1 mm) and then into a wide expansion chamber (diameter 10 mm), ultimately leading to the circular nozzle outlet of radius r_0 =1.5 mm.

Temperature measurements of the source fluid in all experiments were obtained from two T-type thermocouples inserted into the nozzle, as shown schematically in figure 6.2. The nozzle had two insulated channels leading to the expansion chamber, allowing direct access to the source fluid near the ejection point. Done in this way, the thermocouple

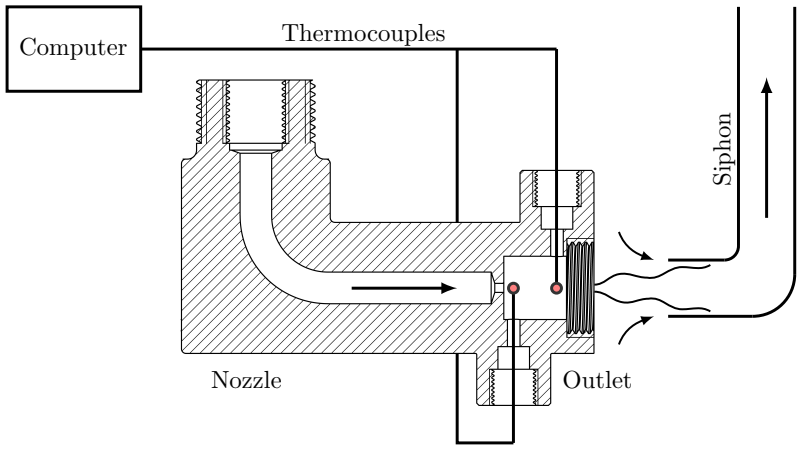

Fig. 6.2 A schematic representation of the jet nozzle with inserted thermocouples and the siphon collecting the ejected jet fluid (see text for dimensions). Note the the siphon was only used during the purging stage of an experiment.

tips were submerged fully into the fluid flow in the expansion chamber, minimising the noise signal from the ambient, and had precise and secure positioning. The slots were positioned with 10 mm horizontal spacing, with the distance upstream from the nozzle outlet to the nearest thermocouple fixed at 10 mm. The geometry of the nozzle did not allow closer positioning of the thermocouples to the source outlet. The temperature drop between the upstream and downstream thermocouples varied for different source volume fluxes and temperatures, but was always of order $O(10^{-1})$ °C. The temperature at the point of discharge was estimated for each experiment individually by linearly extrapolating the temperature loss over the 10 mm spacing between the thermocouples to the nozzle outlet. Temperature of the ambient fluid was measured using four additional T-type thermocouples, located near the nozzle at a regular vertical spacing of 150 mm inside the tank. All thermocouples were calibrated in DigiFlow by placing them in a water bath over an appropriate temperature range (15–70 °C), with an accuracy of ±0.1 °C. For further details on the thermocouples and their calibration, the reader is referred to section 3.2.5. Measurements were taken at 5 Hz using National Instruments equipment (NI 9213).

In order to create neutrally-buoyant double-diffusive jets, the density of the source fluid at the point of discharge had to be carefully matched to that of the ambient. This was achieved with great care for every experiment individually, as even small fluctuations of the source/ambient water temperature would lead to immediate deviation from neutral buoyancy. These temperature fluctuations would normally arise as a result of varying ambient room conditions, or as an expected consequence of changing the

injection volume flux, which altered the amount of time the source fluid would spend exchanging heat with the ambient on its way to the nozzle.

With these challenges in mind, we developed the following experimental procedure. The experimental tank was always filled with fresh water and left overnight to equilibrate with the ambient room temperature. Each time, prior to the actual experiment, we first performed a test experiment, aimed at determining the temperature of the jet fluid at the point of discharge for given ambient conditions. To that end, source fluid of some unknown low salinity (unimportant at this stage) was warmed up using the 1 kW Grant LTC4 water bath to some fixed temperature (e.g. 50 °C). Once a steady-state temperature was reached, fluid ejection into the tank and temperature measurements were simultaneously initiated. Throughout each test experiment, a siphon (diameter 10 mm) was used to collect the ejected source fluid, thus avoiding thermal and dye contamination of the tank prior to the actual experiment. The siphon was connected to an additional gear pump, running at double the ejection volume flux and positioned 5 mm away from the nozzle outlet, ensuring that all ejected fluid was collected. Visual inspection using a small amount of dye showed that the siphoning process did not introduce noticeable disturbances to the ambient fluid. Moreover, the siphoning had no significant effect on the temperature readings. For all experiments, we found that steady-state temperature was reached within 500 s. To determine the steady-state source temperature we averaged the values taken over 50 s in steady state. This was used as a prediction of source temperature T_0 for the actual experiment, which was performed in the same conditions shortly after.

For the actual experiment, we first measured the density of the ambient fluid. This was then used to calculate the required source fluid salinity S_0 such that the jet would be neutrally buoyant, given the source fluid temperature T_0 measured in the test experiment as detailed above. The required salinity S_0 was evaluated using the third-order equations of state of Ruddick and Shirtcliffe (1979). Densities were measured by an Anton Paar DMA5000 density meter with an accuracy of $\pm 10^{-6}$ kg m^{-3}. Once prepared, the source fluid solution was tested in the densitometer at the expected ejection temperature to ensure that its density matched that of the ambient. Deviations of up to $O(10^{-2})$ kg m^{-3} between the source fluid density and the ambient fluid density were deemed satisfactory, as this is comparable to the uncertainties of the temperature measurements. For such low values of the source fluid density deviations, the resulting plume 'jet length', defined by Morton (1959), was greater than the length of the experimental tank. This implies that in all experiments, the effect of source density mismatch had negligible impact on the jet dynamics close to the source.

Each experiment began with a 500 s purging stage over which the source fluid was allowed to once again reach the predicted steady-state source temperature prior to discharge. The standard deviations between the predicted and the actual steady-state temperatures were always below 0.1 °C, corresponding to the measuring accuracy of the thermocouples, implying that the source fluid was well-mixed at the outlet. As before, during the purging stage the siphon was used to collect the ejected source fluid to avoid contamination and disturbance of the ambient. Once the steady temperature was reached, an experiment was started by retracting the siphon vertically upwards, allowing the jet to emerge into the tank. The siphon was fully retracted within ~1 s and caused little disruption to the emerging flow. Occasionally, small volumes of jet fluid were initially lifted upwards by the motion of the siphon, but were quickly re-entrained into the jet.

All experiments were recorded using a 12 megapixel ISVI B/W CXP digital camera at a rate of 15 frames per second. Recording durations of ~200 s provided visual datasets of ~ 3000 frames, sufficient for our analysis. Due to the restricted tank dimensions, reliable data collection over a longer period of time was not possible, as after ~200 s the jet fluid was filling the bottom of the tank and re-emerging into the field of view. For visualisation purposes, the jet fluid was dyed using methylene blue. The obtained images were then processed following the dye attenuation technique, described in section 3.1.5. The processing step used the calibration, details of which are laid out in appendix F. Given their similar molecular diffusivities we assumed that the dye followed the salt and used the processed images as the depth-integrated salinity field. The tank was backlit using a lightbank constructed from a series of red LEDs positioned at a sufficient distance behind a diffuser and approximately 0.3 m away from the tank, such that the light appeared uniform. For the purposes of image processing, all images were normalised by a background image, taken in the absence of any flow prior to each experiment.

Table 6.1 provides a summary of all experiments and their respective parameters. Altogether 9 experiments with double-diffusive jets were conducted at 3 different Re_0 and ΔT_0. Experiments 1, 3 and 5 were each repeated twice to check the experiment for consistency. The repeats showed excellent agreement and hence were omitted to avoid duplication of data. Additional experiments with neutrally-buoyant freshwater jets over the same range of Re_0 were conducted to check that the ejection was horizontal, and to provide a visual benchmark for qualitative comparison. In addition, these experiments were conducted to test that the tank was sufficiently large, so that the jet injection did not induce any circulation that could impact the trajectories of the jet.

Exp No	Source solution	Q_0	ΔS_0	ΔT_0	$\rho_0 - \rho_a$	Re_0	Images
-	-	$\mathrm{ml\,s^{-1}}$	%	°C	10^{-2} $\mathrm{kg\,m^{-3}}$	-	-
1	Heat-salt	3.3	0.656	15.8	-8.7	700	3,027
2	Heat-salt	3.3	1.192	25.2	-0.8	700	3,021
3	Heat-salt	3.3	1.998	38.3	-2.3	700	3,044
4	Heat-salt	5.2	0.690	16.2	-1.4	1,100	3,054
5	Heat-salt	5.2	1.192	24.6	-7.7	1,100	3,036
6	Heat-salt	5.2	2.089	39.1	-9.1	1,100	3,016
7	Heat-salt	7.0	0.702	16.2	-4.2	1,500	3,023
8	Heat-salt	7.0	1.122	25.2	-1.6	1,500	3,024
9	Heat-salt	7.0	2.145	39.9	-4.1	1,500	3,024

Table 6.1 Source conditions and the number of images taken for all experiments with double-diffusive jets.

6.3 Experimental results

6.3.1 Visual observations

Figure 6.3 shows a visualisation of a pair of experiments with source Reynolds number $Re_0 = 1,100$ made using methylene blue dye. The images arranged within the left column, figures (6.3a, 6.3c, 6.3e), show the temporal evolution of a neutrally-buoyant single-diffusive freshwater jet, while the right column, figures (6.3b, 6.3d, 6.3f), contains those for an initially neutrally-buoyant double-diffusive thermohaline jet. Figures 6.3a and 6.3b demonstrate that both jets became turbulent immediately upon discharge and grew in radius. The shear-induced large-scale turbulent eddies present around the edges of the jets acted to rapidly entrain ambient fluid, which was consequently irreversibly mixed into the core. This turbulent entrainment led to a further growth in jet radius, shown in figures 6.3c and 6.3d, as both jets continued to propagate downstream. Although still qualitatively very similar, figure 6.3d shows that 30 s after the ejection, the double-diffusive jet started to develop a slight sinking trajectory and the first hints of small (compared to local jet radius) negatively-buoyant structures forming along the lower surface. Taken less than a minute later, the image in figure 6.3f shows that these negatively-buoyant structures were able to fully form, separate and fall off downwards from the lower surface of the double-diffusive jet. Such structures were absent along the upper surface of the double-diffusive jet, creating clear asymmetry in the flow. They were also absent in the single-diffusive jet experiment (see figure 6.3e), with the jet preserving visual symmetry around the centreline throughout the duration of the experiment. We believe that these structures are a result of the salt-fingering instability, and explain the mechanism for their formation below.

In a typical experiment, as the hot and salty jet fluid leaves the nozzle, it immediately finds itself surrounded by fresh and cold ambient fluid and two surfaces with very different dynamics form. The upper surface is in the diffusive regime, since the hot and salty jet fluid lies beneath a layer of cold and fresh ambient. In contrast, the lower jet surface is in the salt-fingering regime, as the hot and salty jet fluid is atop cold and fresh ambient. Heat and salt exchange occurs across both surfaces, but the mechanisms that govern these exchanges are rather distinct.

Along the upper diffusive surface, heat and salt diffusion act to produce two boundary layers: thermal and saline. As heat diffusion is $O(100)$ times faster than salt, the thermal boundary layer will quickly grow to a critical thickness, leading to the formation of convective heat elements (Howard, 1964). Taking the values of $g = 10\,\mathrm{m\,s^{-2}}$, $\beta_T = 10^{-4}\,^{\circ}\mathrm{C}^{-1}$, $\Delta T = 10\,^{\circ}\mathrm{C}$, $\kappa_T = 10^{-7}\,\mathrm{m^2\,s^{-1}}$ and $\nu = 10^{-6}\,\mathrm{m^2\,s^{-1}}$, we get the

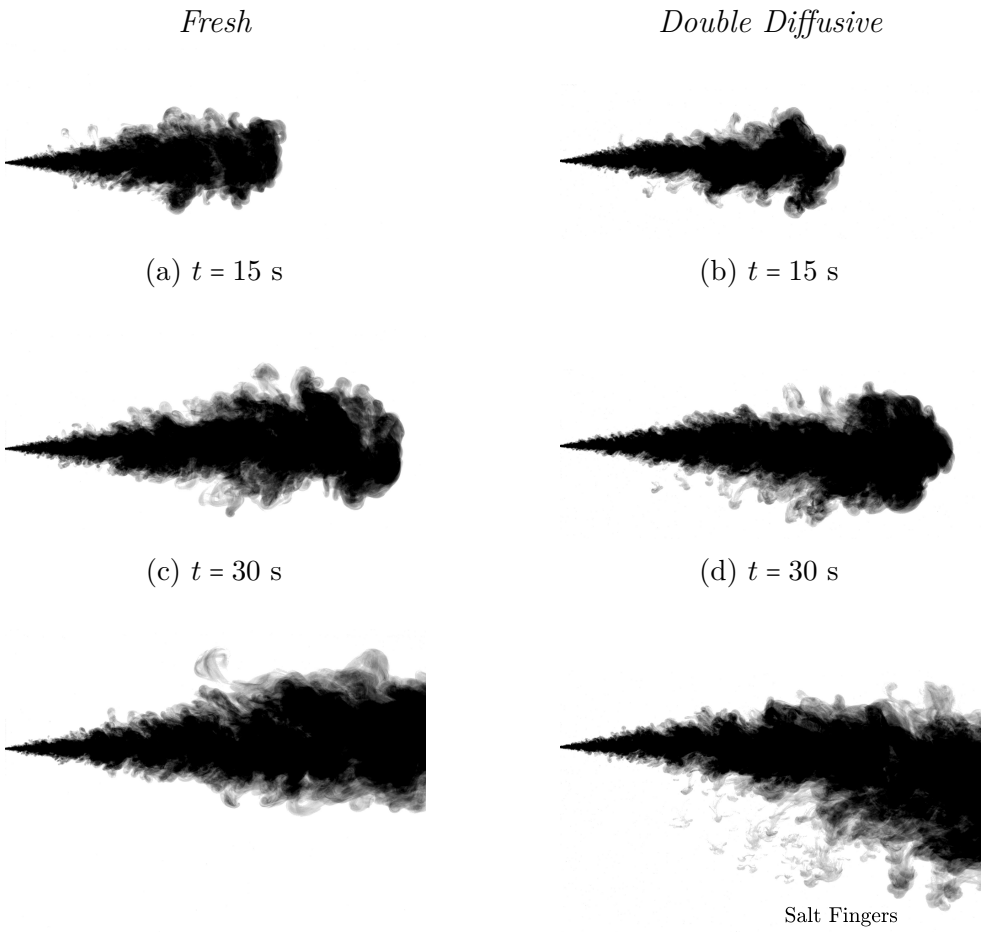

(a) $t = 15$ s (b) $t = 15$ s

(c) $t = 30$ s (d) $t = 30$ s

(e) $t = 85$ s (f) $t = 85$ s

Fig. 6.3 A series of images taken for two turbulent jet experiments ejected at the source Reynolds number $Re_0 = 1,100$ and visualised using blue dye. The left column (images (a), (c) and (e)) shows the development of a neutrally-buoyant jet injected into a quiescent fresh ambient water. The right column (images (b), (d) and (f)) shows the development of an initially neutrally-buoyant double-diffusive thermohaline jet with source salinity difference $\Delta S_0 = 0.690\,\%$ and temperature difference $\Delta T_0 = 16.2\,^{\circ}\mathrm{C}$, injected into a quiescent fresh ambient water (experiment 4).

value of the Rayleigh number $Ra = (g\beta_T \Delta T L^3)/(\kappa_T \nu) \sim 10^{11} L^3$. Then, assuming that turbulent convection ensues for $Ra \sim 10^3$, the critical depth of the thermal boundary layer is $L \sim 10^{-8/3}$. The source temperature differences for most experiments were two-three times greater than 10 °C, therefore let us round to $L \sim 10^{-3}$. Hence, the diffusive growth time of the thermal boundary layer to the critical thickness was $\tau_T = L^2/\kappa_T = O(1)$ s. The formed convective elements carry away salt, as well as heat, which are consequently irreversibly mixed with the ambient through molecular processes, and the fluid in the jet becomes more dense as a result of the differential loss of heat compared to salt. The dynamics of diffusive interfaces were studied in detail by Turner (1965) and the reader is referred to his work for more detail.

Along the lower surface, heat and salt are exchanged through the jet-ambient interface in a substantially different manner. When a patch of warm and salty jet fluid lying above a layer of cold and fresh ambient is perturbed, the $O(100)$ times faster heat diffusion acts rapidly to adjust the temperature of the perturbed patch towards that of the ambient, while most of its salt is retained. The fluid parcel therefore quickly finds itself denser than its surroundings and starts to sink. The convective elements, formed in this way, will carry heat, as well as salt, as they sink and irreversibly mix with the ambient through molecular diffusion. Owing to their long and thin geometry, such structures are commonly called 'salt fingers'. In this case the higher salt flux compared to the heat flux, in density terms, results in a decrease in density of the jet. For greater detail on the processes governing the dynamics of a salt-fingering interface, the reader is referred to Turner (1967). Consequently, taken together, the double diffusion over the upper surface of the jet will increase the density of the jet, while over the lower surface of the jet it will decrease the density. The ultimate trajectory of the jet depends on which of these two processes is dominant. We will return to this point later in section 6.3.3.

Figure 6.4 allows closer visual examination of the temporal evolution of the observed salt fingers for experiment 2. In the early stages of the jet development, there was an absence of 'clear' salt-finger structures (shown in figure 6.4a). Shortly after, salt fingers began to emerge at a distance beyond $x/r_0 \simeq 100$ as seen in figure 6.4b. Indeed, snapshots at later times, see figures 6.4 (c,d), show that no fingers form in the region close to the source ($x/r_0 < 100$) throughout the experiment. Note that this distance varied between different experiments and this will be discussed in detail in section 6.3.5. Visually it appeared that in many instances the salt plumes, attempting to form along the lower surface and separate from the jet, were not able to do so as they were re-entrained into the jet through the action of turbulent entrainment. This was

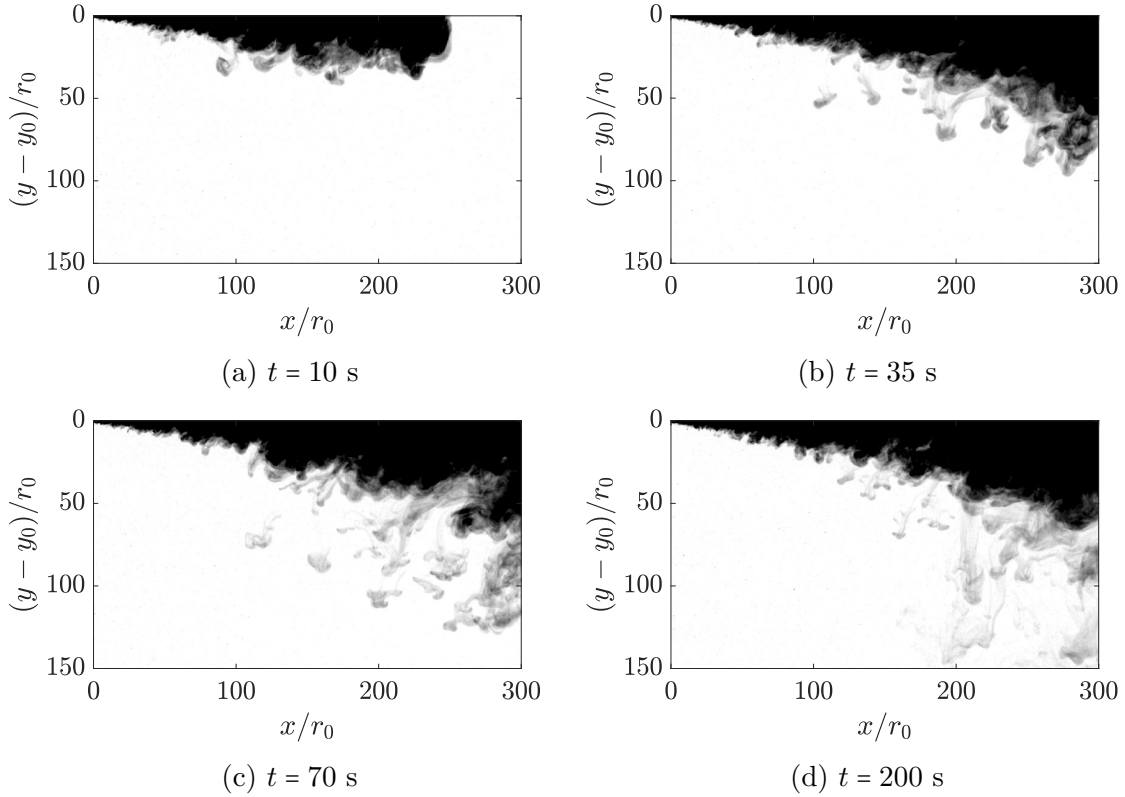

(a) t = 10 s (b) t = 35 s

(c) t = 70 s (d) t = 200 s

Fig. 6.4 Instantaneous images showing the emergence and temporal evolution of salt fingers along the lower jet surface for experiment 2.

particularly clear in the region near the source, where turbulent entrainment is the strongest.

Fingers that managed to detach from the jet, shown in figure 6.4c, fall downwards and interact with one another. As the jet propagates, more fingers emerge, forming a persistent 'rain' of salt and heat underneath the jet, as shown in figure 6.4d. Visual examination of the recorded videos revealed that many fingers formed from turbulent eddies that had been 'thrown' out from the jet core by the action of jet-generated turbulence. Once out in the ambient, these eddies were able to rapidly reject their heat, build up negative buoyancy and fall downwards as salt-fingers. In cases where the scales of detached eddies were sufficiently large, they broke down into a number of smaller fingers during descent. This observation is consistent with the idea that the horizontal length scale of a salt finger is limited by the competing diffusive processes (Turner and Chen, 1974). In particular, while eddies that are too wide are not able to reject heat effectively, the motion of narrow eddies is restrained by viscosity, and therefore fingers exist at intermediate scales.

Ultimately, it is the origin of the observed deviation from a horizontal trajectory, seen clearly in figure 6.3e, and the nature of the salt fingers, shown in figure 6.4, that we aim to investigate further in this chapter.

6.3.2 Time-average analysis

Figure 6.5 shows the time-averaged images for all experiments obtained by averaging over ~ 3000 snapshots, with the exact quantity for each experiment provided in table 6.1. These snapshots for time-averaging were taken at regular time intervals over the entire duration of the experiment, with the first snapshot taken 2 seconds after the retraction of the siphon. Note that in all cases, the trajectories of the jets did not vary with time, implying that all jets were in a quasisteady state. Two observations have to be made at this stage. First, this figure shows that for a given source Reynolds number, as the source temperature difference ΔT_0 increases, the jet horizontal propagation is reduced and a more curved trajectory is observed. Take, as an example, the three experiments performed at $Re_0 = 700$. Ejected at $\Delta T_0 = 15.8\,^{\circ}\mathrm{C}$, the jet reached the end of the viewing window at $x/r_0 \simeq 600$. This distance reduced significantly, to $x/r_0 \simeq 400$ and $\simeq 250$, as the source temperature differences increased to $\Delta T_0 = 25.2\,^{\circ}\mathrm{C}$ and $\Delta T_0 = 38.3\,^{\circ}\mathrm{C}$, respectively. This trend holds consistently for the other two groups with three experiments in each, performed at $Re_0 = 1100$ and $Re_0 = 1500$, indicating clearly that double-diffusive processes have a strong impact on the paths followed by the jets.

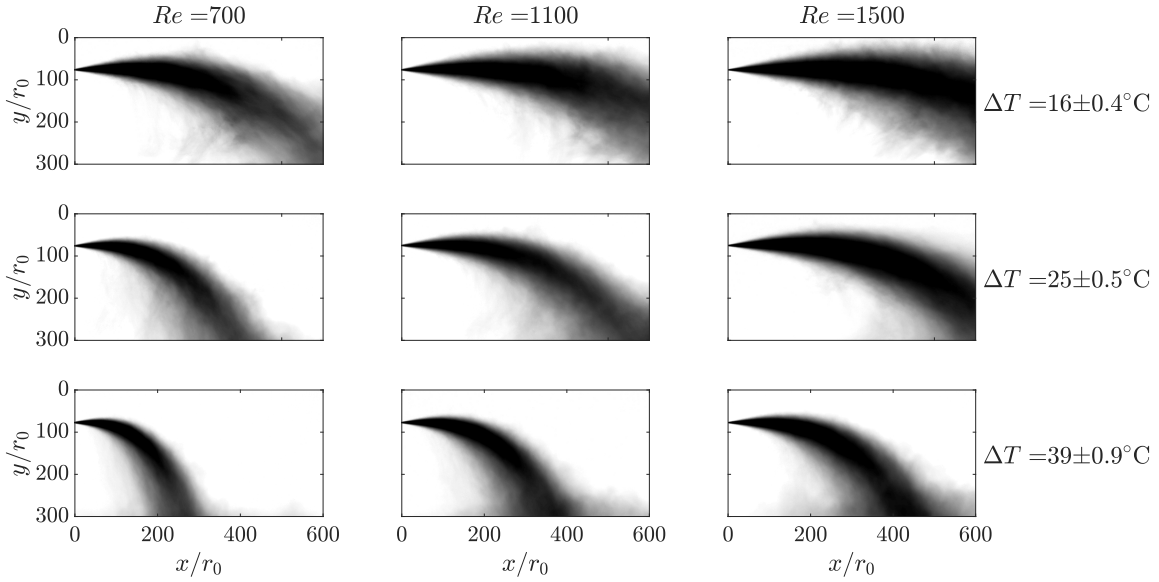

Fig. 6.5 Time-average images of the jets for all experiments plotted against source temperature difference (rows) and Reynolds number (columns).

Evidently, the potential for double-diffusive processes to alter the jet trajectory is greater for larger source temperature differences.

The second trend seen clearly in figure 6.5 is that for a given source temperature difference, as the source Reynolds number was increased, the jets followed a less curved trajectory. This is consistent with the idea that the momentum flux acts against the negative buoyancy driving the jet downwards. As explained above, this buoyancy is introduced by the action of double-diffusive processes and is controlled by the source temperature difference. The balance between buoyancy-driven velocity and jet velocity is commonly expressed using the densimetric Froude number $Fr = U/\sqrt{g'L}$, where U is the horizontal velocity scale, L is the characteristic length scale, for example the jet radius, and $g' = g(\rho - \rho_a)/\rho_a$ is the buoyancy scale. Neutrally-buoyant jets, for which $Fr \to \infty$, follow a perfectly horizontal trajectory. Buoyant jets with large buoyancy differences and thus low Fr numbers exhibit strongly-curved trajectories. In our experiments an increase in the source Reynolds number corresponds to an increase in the source horizontal velocity U_0. For a fixed ΔT_0 the effective Froude number is therefore higher for higher Re_0, so as Re is increased, the jet trajectory remains closer to the horizontal. We attempt to explain the origin of the development of negative buoyancy within the jet in the next section.

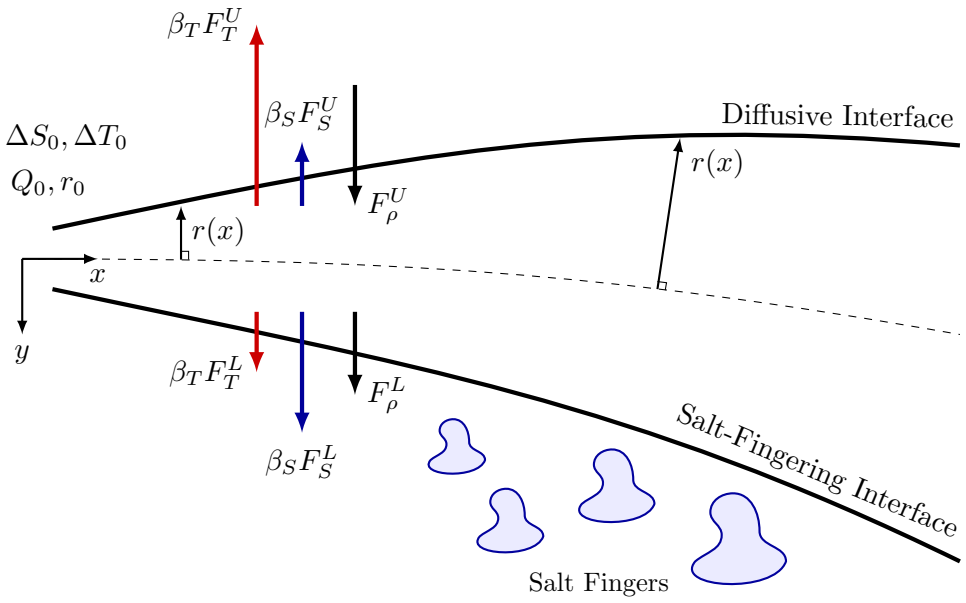

Fig. 6.6 Schematic representation of the double-diffusive thermohaline jet in a stationary uniform freshwater ambient.

6.3.3 Sinking trajectory explanation

One possible explanation for the build-up of negative buoyancy and the observed sinking jet motion is based on the differences in salinity and temperature fluxes across the two double-diffusive surfaces. We denote the double diffusive temperature and salt fluxes across the upper diffusive surface as F_T^U and F_S^U, respectively. The associated salt-fingering salt and temperature fluxes across the lower surface are denoted as F_S^L and F_T^L, respectively. The difference between the net density gain as a result of turbulent diffusive fluxes across the upper surface F_ρ^U, and the net density loss through the lower fingering surface F_ρ^L determines the net density flux from/into the jet and hence the build-up of negative buoyancy. This difference, illustrated pictorially in figure 6.6, can be written as

$$\frac{F_\rho^U}{F_\rho^L} = \frac{\beta_T F_T^U - \beta_S F_S^U}{\beta_T F_T^L - \beta_S F_S^L}. \tag{6.1}$$

The problem at this stage relies on the accurate determination of the double-diffusive fluxes involved in the process. From dimensional considerations, Turner (1965, 1967) showed that for high Rayleigh number diffusive and fingering interfaces, the turbulent fluxes of temperature F_T^U and salinity F_S^L, respectively, can be related to the turbulent fluxes from a 'solid wall' (i.e. the fluxes from a fixed temperature/salinity boundary

held at a constant temperature/salinity difference from the values in the fluid away from the boundary) as

$$F_T^U = c\kappa_T^{2/3}\Big(\frac{\beta_T g}{\nu}\Big)^{1/3}\Delta T^{4/3} f(R_\rho^*), \tag{6.2a}$$

$$F_S^L = c\kappa_S^{2/3}\Big(\frac{\beta_S g}{\nu}\Big)^{1/3}\Delta S^{4/3} f(R_\rho), \tag{6.2b}$$

where c is an experimentally determined constant and $R_\rho^* = 1/R_\rho$. Turner (1965, 1967) measured experimentally over a range of density ratios the numerical coefficients $R_D = f(R_\rho^*)$ and $R_S = f(R_\rho)$, which relate the double-diffusive diffusive temperature and salt fluxes to their reference solid wall values (i.e. the fluxes from a fixed temperature/salinity boundary), respectively. He also measured how the flux ratios $\gamma_D = (\beta_S F_S^U)/(\beta_T F_T^U)$ and $\gamma_S = (\beta_T F_T^L)/(\beta_S F_S^L)$ for diffusive and salt-fingering interfaces, respectively, vary as a function of the density ratio R_ρ. Using the above definitions, the ratio of density fluxes in 6.1 can be rewritten as

$$\frac{F_\rho^U}{F_\rho^L} = \frac{R_D}{R_S}\Big(\frac{\kappa_T}{\kappa_S}\Big)^{2/3}\Big(\frac{1-\gamma_D}{1-\gamma_S}\Big)\Big(\frac{\beta_T \Delta T}{\beta_S \Delta S}\Big)^{4/3}. \tag{6.3}$$

Precise calculations of the fluxes require exact measurements of numerical flux coefficients for double-diffusive interfaces in the presence of turbulence, which are not readily available. Another factor complicating the problem is the unknown non-trivial effect of differential diffusion in the presence of turbulence on the evolution of the density ratio R_ρ of a double-diffusive jet. This governs the choice of numerical coefficients that go into the flux calculations. To get an order of magnitude estimate using Turner's measurements, we take $R_D/R_S = 10^{-1}$, $(\kappa_T/\kappa_S)^{2/3} = 10$ and $(1-\gamma_D)/(1-\gamma_S) = 1$. Using these values, the density flux ratio is $O(1)$, implying that it is a delicate balance between the temperature and salinity fluxes that determines the net density flux.

Although the precise spatial evolution of the density ratio is unknown, visual observations of the sinking jet trajectories suggest that as the jet propagates its density ratio becomes $R_\rho < 1$. Taking as an example the value of $R_\rho = 2/3$ and substituting the associated numerical coefficients from Turner's experimental measurements yields a value of $F_\rho^U/F_\rho^L \simeq 0.8$. Further reduction in R_ρ would lead to a further decrease in the density flux ratio, implying that, contrary to our observations, the jets in this configuration should become positively buoyant. This simple balance calculation, however, uses numerical coefficients that do not take into account two important factors: (i) the effect of turbulence on the fluxes across both surfaces; (ii) continued absence of salt fingers close to the source, as shown in figure 6.4. It is the combined

effect of these two factors, that leads to the reversal of flux balance, leading to the development of negative buoyancy.

With respect to the first factor, turbulent motions generated by the jet affect its upper and lower surfaces in two distinct ways. Along the upper diffusive surface, turbulence acts to stretch the interface between the jet and the ambient, continuously sharpening the temperature gradient, and hence leading to an increased diffusive heat flux. The impact of jet turbulence on the dynamics of the lower fingering surface is somewhat more complicated. Linden (1971) investigated experimentally the effect of grid-generated turbulence on heat and salt transport across salt-fingering interface in a two-layered aqueous system. For the purpose of our work we will focus on two of his major findings. First, he showed that turbulent shear disrupts the formation of salt fingers and thus reduces the total salt-fingering flux across an interface. Second, he found that the ratio of buoyancy fluxes γ_S was greater than unity for all the grid frequencies (except zero), reaching up to $\gamma_S \approx 4$ for particularly high intensities of the grid turbulence. This means that the density step between two layers was decreasing with time, that is, the top layer was becoming heavier. Ultimately, this first factor implies that the numerical coefficients used in the above flux calculations, determined from experiments with stationary interfaces, are unlikely to be appropriate for a highly turbulent flow and instead flux ratios favouring greater heat exchange should be used. The implication of the second factor is, perhaps, even more pronounced. In the absence of salt fingers along the lower surface, the resulting salt flux is significantly reduced, that is, $F_\rho^L \sim 0$. This, in turn, means that thermal exchange through the diffusive surface will be the dominant mechanism, leading to a rapid build-up of negative buoyancy. Diffusive heat exchange will dominate for as long as there are no salt fingers forming, which in our experiments was for at least $x/r_0 = 40$, as will be shown in section 6.3.5. By that point, the dilution through entrainment alone will have reduced the jet temperature and salinity to $\simeq 0.2\Delta T_0$ and $\simeq 0.2\Delta S_0$ (Hirst, 1971), meaning that although salt-fingers will be formed beyond this stage, their impact on the total density flux will be relatively small.

6.3.4 Centreline analysis

With the aim of demonstrating the significance of diffusive processes on the dynamics of double-diffusive jets, we tracked their time-averaged trajectories. To that end, we processed the normalised time-averaged images to extract centrelines, which were used as proxy for trajectories. Each centreline was constructed as a collection of centrepoints for every pixel column, that is, for every x-coordinate, for a given time-averaged image.

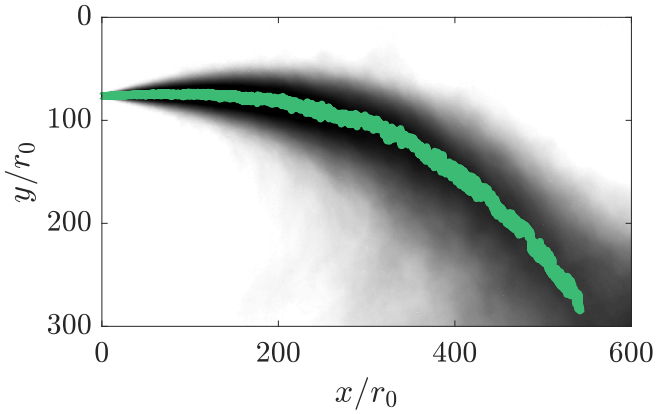

Fig. 6.7 Image showing that the centreline follows well the time-average jet trajectory for experiment 5, typical for all experiments.

A centrepoint was defined as the y-location of a pixel with the minimum intensity (corresponding to the darkest point) within a particular column of pixels. Using the above definitions, a one-dimensional array with the locations of all centrepoints was obtained for every time-average image, and used to reproduce centrelines. Figure 6.7 demonstrates the result obtained for experiment 5, which was typical for all experiments. The figure shows that the centrepoints, shown as bright dots, visually follow well the time-averaged jet image and can be used to approximate the jet trajectory.

Figure 6.8 shows the trajectories for all nine experiments, obtained using the procedure described above, and grouped by the source temperature differences ΔT_0. The colours of the markers represent the source Reynolds number, with the brighter lines corresponding to higher values of Re_0. We approximated the obtained trajectories using a well-established model for single-diffusive negatively-buoyant jets developed by Fan and Brooks (1969), which uses the similarity solutions derived on the basis of an integral model for incompressible Boussinesq turbulent round buoyant jets in a uniform ambient fluid. For their model, the authors introduced the dimensionless volume flux parameter μ and the momentum flux parameter m as

$$\mu = \frac{(Ur^2)}{(U_0 r_0^2)} \quad \text{and} \quad m = \left(\frac{g\lambda^2 U_0^3 r_0^6(\rho_0 - \rho_a)}{4\sqrt{2}\alpha\rho_0}\right)^{-2/5} \frac{U^2 r^2}{2}, \tag{6.4}$$

where $\lambda = 1.16$ is the turbulent Schmidt number. The horizontal and vertical components of the momentum flux parameter were defined as $h = m\,cos(\theta)$ and $v = m\,sin(\theta)$, respectively, where θ is the angle between the local jet trajectory and the horizontal. Using the above definitions, the model for the single-diffusive jet motion can be

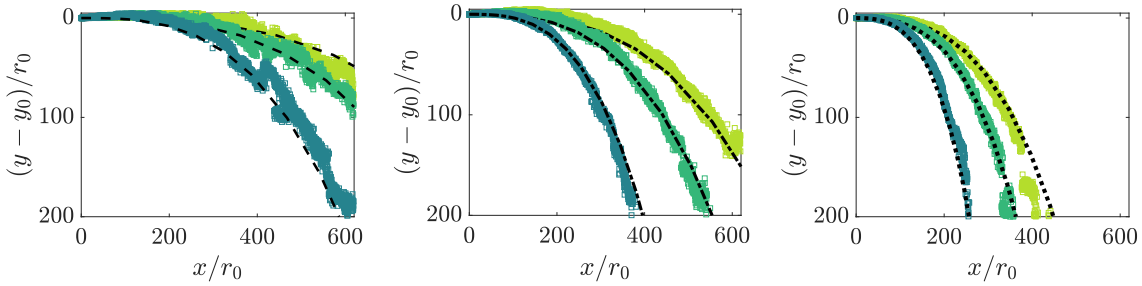

(a) $\Delta T_0 = 16.0 \pm 0.4$ °C (b) $\Delta T_0 = 25.0 \pm 0.5$ °C (c) $\Delta T_0 = 39.0 \pm 0.9$ °C

Fig. 6.8 Trajectories for all experiments grouped by the source temperature differences. The colour indicates the source Reynolds number, with the brighter colours corresponding to the larger values of Re_0. The black lines in each plot represent the numerical solution for trajectory of single-diffusive jets at a fixed source temperature difference, ---- $\Delta T_0^m = -0.7\,°\text{C}$, ----- $\Delta T_0^m = -2.2\,°\text{C}$, ····· $\Delta T_0^m = -7.5\,°\text{C}$, and varying source Froude number.

summarised using the following set of governing equations

$$\frac{\mathrm{d}\mu}{\mathrm{d}\zeta} = \sqrt{m}, \quad \frac{\mathrm{d}v}{\mathrm{d}\zeta} = \frac{\mu}{m}, \quad \frac{\mathrm{d}\eta}{\mathrm{d}\zeta} = \frac{h}{m}, \quad \text{and} \quad \frac{\mathrm{d}\psi}{\mathrm{d}\zeta} = \frac{v}{m}. \tag{6.5}$$

The associated coordinate system can be defined as

$$\zeta = \frac{\rho_0 U_0^2 r_0^4}{32\alpha^4\lambda^2 g(\rho_0 - \rho_a)}^{-1/5} s, \quad \eta = \frac{\rho_0 U_0^2 r_0^4}{32\alpha^4\lambda^2 g(\rho_0 - \rho_a)}^{-1/5} x, \quad \psi = \frac{\rho_0 U_0^2 r_0^4}{32\alpha^4\lambda^2 g(\rho_0 - \rho_a)}^{-1/5} y, \tag{6.6}$$

with the s-axis following the centreline of the jet. For a detailed derivation and description of the model the reader is referred to the original work of Fan and Brooks (1969). The set of governing equations (6.5) was solved numerically in Matlab using the value of the entrainment coefficient for buoyant jets $\alpha = 0.08$ (Carazzo et al., 2006). To approximate the trajectories for three sets of experiments, we varied the source buoyancy flux via the source temperature difference. The numerical solutions, presented as dashed lines in figures 6.8 (a), (b) and (c) were obtained for temperature differences of $\Delta T_0^m = -0.7\,°\text{C}$, $\Delta T_0^m = -2.2\,°\text{C}$ and $\Delta T_0^m = -7.5\,°\text{C}$, respectively. The trajectories obtained for these three manually-selected temperature differences follow well each group of the experimentally-obtained trajectories, which leads to three conclusions.

First, the observed sinking trajectories cannot be attributed to an experimental uncertainty, since the already mentioned experimental error in temperature measurements of $\pm 0.1\,°\text{C}$ is significantly less than the temperature difference required to produce the deviations observed in figure 6.8. Second, the fact that $|\Delta T_0^m| < |\Delta T_0|$ for all groups of

experiments implies that we cannot assume that all the heat simply diffused out and the jets were driven by the remaining salt. This suggests that within the measurement range, all jets continued to carry some amount of potential energy stored in the form of heat within them. Third, the fact that a single source buoyancy flux is able to approximate the trajectory so well suggests that the diffusive processes play little role relatively soon after discharge. It follows that accumulation of negative buoyancy of the jet happens rapidly and, once developed, stays relatively constant throughout the rest of its propagation. This third conclusion is consistent with the idea of the dominant heat diffusion being responsible for the build-up of negative buoyancy in the absence of salt fingers, as outlined in the previous section. Close to the source, temperature gradients are large, causing vigorous heat exchange with the ambient and resulting in a rapid build-up of negative buoyancy. As the jet propagates, the dilution through entrainment makes these gradients fall, reducing the ability for the diffusive flux to reject heat and thereby accumulate negative buoyancy. As a result, the trajectories followed by the jet are preconditioned by the density excess which is established by strong double-diffusive effects near the source where ΔT and ΔS are both large. This explains the observation that jets reached a quasisteady state and followed the same trajectory throughout an experimental run.

6.3.5 The onset of salt fingers

We now return to the discussion of the development of the salt fingers. As described in section 6.3.1, visual observations indicate the presence of a competition between the diffusive processes driving the formation of salt fingers and the entrainment acting to inhibit their separation from the jet. We propose that it is the balance between the two competing velocity scales, the salt-fingering velocity $w_f(x)$ and entrainment velocity $u_e(x)$, that determines the location of the onset point for fingering formation x_f, and provide experimental evidence in support of this hypothesis.

For an axisymmetric turbulent round jet emanating from a point source of momentum, using the entrainment assumption (Morton et al., 1956), the expression for the centreline horizontal velocity as a function of distance travelled by the jet can be written as

$$U(x) = \frac{1}{\sqrt{2}\alpha} U_0 \frac{r_0}{x}. \tag{6.7}$$

Given that $U(x)$ decays as x^{-1} with distance, so does the jet entrainment velocity $u_e(x) = \alpha U(x)$, indicating that the ability for the jet to re-entrain the salt fingers reduces rapidly with distance. In contrast, the diffusive nature of salt fingers suggests

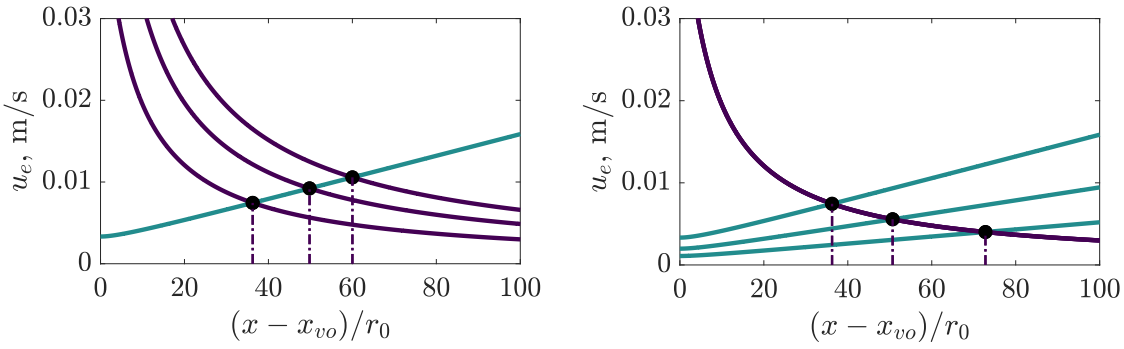

Fig. 6.9 Fingering onset prediction for two cases: (a) at fixed source salinity ΔS_0 and varying Re_0 using source values for experiments 1, 4 and 7, with the upper lines corresponding to the larger values of Re_0; (b) at fixed source Reynolds number Re_0 and varying ΔS_0 using source values for experiments 1, 2 and 3, with the upper lines corresponding to the larger values of ΔS_0. The black dots and connected dashed lines indicate the distance from the source x_f where the first salt fingers should form.

that their velocity scale $w_f(x)$ should be some growing function of time, or in this case distance along the jet. By considering a balance between thermal diffusion and viscosity, Linden (1971) constructed the salt-fingering velocity scale of the form

$$w_f(x) = \frac{gl^2(x)\beta_S \Delta S(x)(\gamma_S - 1)}{2\nu\pi^2} \tag{6.8}$$

where $l(x)$ and $\Delta S(x)$ are the finger horizontal length scale and salinity scale, respectively. Visual observations of salt fingers in our experiments showed that they often emerged from turbulent eddies, with their size growing with distance from the source. Burridge et al. (2016) showed that in a turbulent plume, the length scale of the largest turbulent eddies is 0.44 times its local half-width $r(x)$. Given the similarity in the turbulent properties between jets and plumes, as demonstrated by Van Reeuwijk et al. (2016), and assuming that the length scales of salt fingers are directly linked to that of the turbulent eddies, we take $L(x) = 0.44r(x)$. We assume that the salinity profile matches that of velocity, that is

$$S_m(x) = \frac{1}{\sqrt{2}\alpha} S_0 \frac{r_0}{x}, \tag{6.9}$$

and take the top-hat values $\Delta S(x) = S_m(x)/2$ to describe the salinity scale of the fingers.

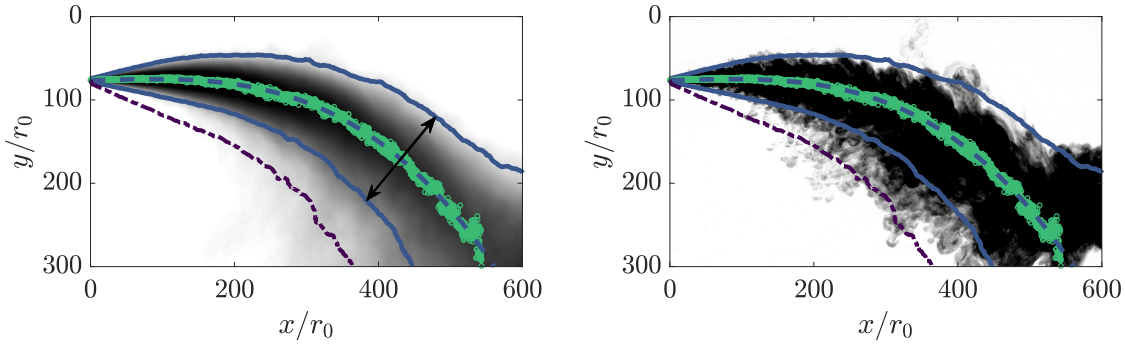

Fig. 6.10 An illustration of the 'gate' line construction procedure and application: (a) gate line construction using the time-averaged image for experiment 5; (b) an overlay of the centreline, edges and the gate line onto an instant capturing salt fingers crossing the gate line. In both sub-figures, the centreline fit is represented by the dashed line, the edges are represented by the solid lines and the dotted line represents the gate line. The arrow in (a) represents the local jet co-ordinate system.

Using the above definitions, it is possible to predict the fingering onset location x_f by determining where the two velocity scales become comparable $w_f(x_f) = u_e(x_f)$, as illustrated pictorially in figure 6.9. In this figure, the dark and bright solid lines represent the entrainment and salt-fingering velocity scales, respectively, with the locations where the two velocity scales reach a balance (x_f) marked using black dots and connected dashed lines. This balance was considered for two distinct cases. In the first case, shown in figure 6.9a we fixed the source salinity ΔS_0 and varied Re_0. The source values used in this model were taken as those for experiments 1, 4 and 7, allowing us to compare the obtained predictions against the experiments. The model predicts that an increase of Re_0 results in a delay in the formation of salt fingers, consistent with our qualitative observations. For the second case, shown in figure 6.9b, we fixed the source Reynolds number Re_0 and varied ΔS_0, using the source values for experiments 1, 2 and 3. As expected, for larger source salinity, the velocity scales of salt fingers are larger, resulting in the earlier formation of the salt fingers. To check the validity of the proposed balance between the two competing velocity scales, we compared the obtained predictions against the visual measurements of the onset of salt fingers, obtained using the procedure described below.

Detection of the salt fingers was performed by temporal sampling of the instantaneous jet images along the so-called 'gate' lines, with an example represented by the dotted lines in figure 6.10. The choice of the term 'gate' is arbitrary, and was adopted to signify that only those structures which were able to cross the 'gate' were considered.

Such gate lines were obtained individually for every experiment from their respective time-averaged images using the following procedure. As a first step, we extracted the centreline, as described earlier, and approximated it using a third order polynomial least-squares fit. We chose to approximate the measured centreline using a polynomial to both smooth the data and to easily find the derivative of the function defining the centreline. Using polynomials of higher orders did not make a noticeable difference to the obtained trajectory and therefore the third order was deemed sufficient. We checked that the obtained fittings, with a typical example shown as a dashed line in figure 6.10a, displayed a satisfactory agreement with the centreline points and visually followed the time-averaged jet trajectories well. For the next step, we detected the top edge of the time-averaged jet image. This was done by first filtering out any noise from the image using a single threshold value (signal below a threshold value was considered noise and removed) and then detecting the positions where the intensity changed abruptly within every pixel column. The threshold value was set as the average plus two standard deviations of the value of the ambient in absence of any flow. Using the derivative of the centreline position, the upper edge was located by searching on a line perpendicular to the centreline until the upper edge was located. The obtained upper edge was then mirrored perpendicularly around the centreline to create a lower interface (shown as a solid line below the centreline), which could not be detected otherwise due to the presence of salt fingers. The gate line was then constructed by scaling the bottom edge by a fixed multiple of the local jet radius. As can be seen in 9b, the jet width fluctuates about the time-average envelope. For this reason, and to avoid detecting intermittent events that remain attached to the plume, we choose the scaling factor to be ×2, meaning that any structure found one radius away from the time-averaged bottom edge is considered to be a finger that has managed to escape the re-entrainment process, rather than a turbulent eddy. Figure 6.10b shows an overlay of the obtained lines onto an instantaneous image from experiment 5. The figure shows that for this particular instance, the gate line will not pick up any signal of salt-fingers until up to $x/r_0 \simeq 80$ and will have a strong signal of the presence of salt fingers thereafter until $x/r_0 \simeq 350$. The region $x/r_0 \simeq 350$ and $x/r_0 \simeq 380$ will once again contain no salt-fingering signal.

Figures 6.11 and 6.12 show the obtained time-series of the jet images, sampled along the gate line as described above. In line with the visual observation made in figure 6.4, both figures show that in all cases there were consistently no fingers forming until some distance away from the source, which varied between experiments. The dashed vertical lines present in all figures are the predictions made using the model

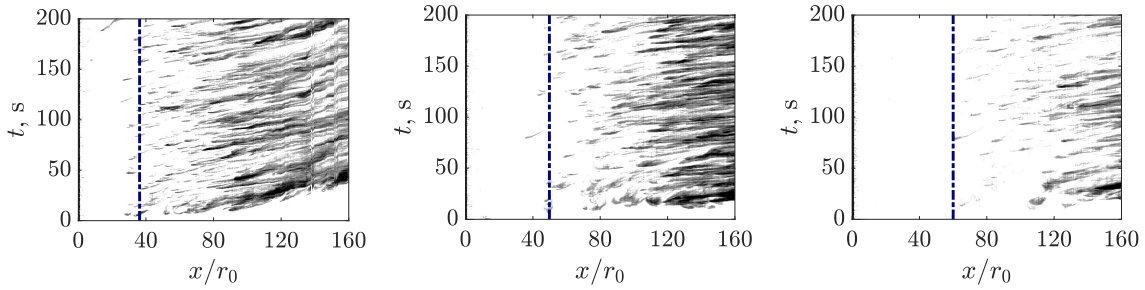

(a) $Re_0 = 700$ (b) $Re_0 = 1,100$ (c) $Re_0 = 1,500$

Fig. 6.11 Time series of dye concentration profiles taken along the gate lines for three experiments at fixed $\Delta T_0 = 15 \pm 0.4$ °C. The dashed lines represent the prediction for the fingers onset location x_f for respective source conditions shown in figure 6.9a.

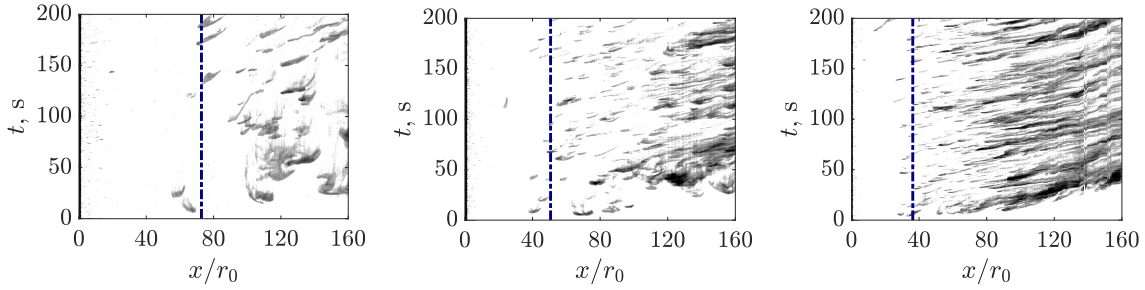

(a) $\Delta T_0 = 15.8$ °C (b) $\Delta T_0 = 25.2$ °C (c) $\Delta T_0 = 38.3$ °C

Fig. 6.12 Time series of dye concentration profiles taken along the gate lines for three experiments at fixed $Re_0 = 700$. The dashed lines represent the prediction for the fingers onset location x_f for respective source conditions shown in figure 6.9b.

described above and shown in figure 6.9. As seen in figure 6.11, experimental results are in good agreement with the model prediction, confirming that the formation of salt fingers is delayed as the source Reynolds number is increased. Similarly, there seems to be a good agreement between the predicted and observed onset points for a fixed Re_0 and varying ΔT_0 (see figure 6.12). As expected, the formation of salt fingers is earlier for larger values of ΔT_0, that in our experiments is equivalent to larger values of ΔS_0. These two observations confirm that it is the balance between the double-diffusive processes and turbulent entrainment that controls the formation of salt fingers in a horizontal jet.

6.4 Conclusions

An experimental investigation of the effect of double diffusion on the dynamics of turbulent jets has been conducted. We have restricted our attention to the simplest case of initially neutrally-buoyant thermohaline jets discharged horizontally into a stationary uniform freshwater ambient. Visual observations revealed that, in contrast to their freshwater equivalents, neutrally-buoyant double-diffusive jets develop considerable sinking trajectories, with significant salt-fingering convection forming along the lower jet-ambient surface some considerable distance away from the source. The tendency for the jets to sink is greater for larger source temperature differences ΔT_0, demonstrating the significance of double-diffusive processes for turbulent jet motion.

We associate the observed sinking trajectories with the impact of internal jet-generated turbulence on the fluxes of heat and salt across its upper and lower surfaces. Importantly, turbulent entrainment hinders the formation of the salt fingers for a considerable distance from the jet source. In the absence of advective salt transport through salt-fingering motion, the diffusive heat losses dominate, resulting in the build-up of negative buoyancy which drives the jet downwards. Note that other effects, such as the impact of salt-fingering motion on the turbulent entrainment processes along the lower surface of the jet, could be partially responsible for the observed sinking behaviour. However, given that we were able to explain our results without involving any additional effects, we feel that they are likely to be at best of secondary importance to the double-diffusive processes.

Double-diffusive jet trajectories can be well approximated by a trajectory of a single-diffusive buoyant jet with a fixed source buoyancy g'_0, indicating that accumulation of negative buoyancy happens quickly, since otherwise the diffusive processes would continuously change the jet buoyancy and hence trajectory. In addition, a simple model predicting the onset point of the salt fingers works well by balancing entrainment and salt-fingering velocity scales, confirming our physical understanding of the formation of salt fingers in this context.

This work has important modelling implications for industrial discharges involving double-diffusive jets, such as the brine discharges from desalination plants. First, it shows that using the standard single-diffusive buoyant jet equations for the case of thermohaline double-diffusive discharges may lead to a significant underestimation of the curvature of jet trajectory, overpredicting the distance travelled by the effluent, and consequently its dilution. Such models should therefore be used with caution. The second implication concerns various chemicals, such as copper and chlorine, added to the seawater at different stages in the desalination process to control bacterial

growth and/or reduce corrosion (Jones et al., 2019). Based on our results, it is likely that instead of propagating with the jet (going through continuous dilution to low concentrations through entrainment), these slow-diffusing chemicals may tend to fall out in the form of salt fingers, causing additional pollution in the near-coastal region, which is unaccounted for by the current single-diffusive models.

Finally, in addition to our findings on the importance of double diffusion on the dynamics of turbulent plumes, presented in chapters 4 and 5, this investigation provides a further confirmation that for high-Péclet-number flows, in which advection dominates diffusion, diffusive processes may have a considerable impact on the large-scale dynamics of turbulent free shear flows, as well as on the structure of the turbulent/non-turbulent interface.

Chapter 7

Conclusions & Future Work

7.1 Conclusions

An experimental investigation of the effect of double diffusion on the dynamics of turbulent plumes and jets has been performed. In brief, our measurements showed that for high-Reynolds-number and high-Péclet-number flows, in which advection dominates diffusion (both viscous and molecular), diffusive processes may have a considerable impact on the dynamics of turbulent free shear flows in general, and on the structure of the turbulent/non-turbulent interface in particular.

Throughout this work, heat and salt were used as the two agents to create double-diffusive flow configurations. This choice was motivated predominantly by the $O(100)$ difference in the molecular diffusivities of the two scalar properties, implying that even for moderate concentration gradients, the resulting flows were strongly doubly-diffusive. Attempts to create double-diffusive flows using salt-sugar combinations were made, but had to be terminated due to a number of drawbacks, as discussed in section 4.1. It is important that these drawbacks are taken into consideration by anyone intending to perform similar investigations in future.

In application to plumes, the effect of double diffusion was predominantly analysed in the context of the rate of turbulent entrainment, manifested through the value of the entrainment coefficient α. In doing so, we challenged the widespread assumption that for flows at high Reynolds and Péclet numbers, slow molecular diffusive processes have little effect on the overall dynamics of the flow (Hunt and Van den Bremer, 2010). Indeed, comparisons between single-diffusive plumes driven by temperature or solute concentration difference alone show that, despite orders of magnitude variations in the molecular diffusivity of the scalar, for high Péclet number turbulent single-diffusive plumes the rate of entrainment α is a constant (Partridge and Linden, 2013). The

question, however, remaines as to whether that would still be the case if both properties were present within the flow simultaneously, making it double-diffusive.

It may be worth mentioning that we initially naively supposed that if anything, the small-scale double-diffusive processes would enhance mixing of the engulfed fluid, leading to an increase of the effective rate of entrainment. To the contrary, our measurements of the entrainment coefficient for plumes over a range of source buoyancy fluxes and source density ratios, performed using the Baines' filling-box technique, revealed the opposite. In particular, our findings, presented in chapter 4, show an up to 20% reduction in α for double-diffusive plumes in the salt-fingering configuration. The scale of the reduction was found to be in direct relation to the source density ratio and was inversely related to the distance travelled by the plume, indicating that double-diffusive effects decrease as the plume evolves. On the basis of these observations, we proposed an explanation for the observed reduction in the entrainment coefficient on the basis of differential diffusion hindering large-scale engulfment at the edge of the plume, laid out in section 4.4.3.

The findings obtained using the Baines' filling-box technique were then confirmed by simultaneous high-resolution measurements of the velocity and scalar fields, presented in chapter 5. In particular, the results obtained using particle image velocimetry confirmed that the value of the entrainment coefficient for double-diffusive plumes in the salt-fingering configuration is reduced, and varies with the distance from the source. In line with our filling-box measurements, the reduction was the greatest close to the source – from as much as $\sim 15\%$ at $\hat{z}/r_0 = 36$, going down to $\sim 3\%$ at $\hat{z}/r_0 = 100$, thereby confirming that the effect of double-diffusion was transient, and strongest close to the plume source. Limited by our inability to refractive index match the flow in the presence of large gradients in heat and salt, as explained in section 5.2, reliable measurements of α closer to the source were not possible.

In addition to verifying our preceding results obtained using the Baines' filling-box technique, the simultaneous PIV/LIF measurements of the flow field provided additional insights into the dynamics of double-diffusive plumes. Most importantly, the self-similarity and good collapse of the velocity profiles, and the associated turbulent statistics, in both the Eulerian and the plume coordinates, indicated that the effect of double diffusion on the rate of turbulent entrainment was insignificant over the region beyond $\hat{z}/r_0 = 36$. However, when normalised by the distance from the virtual origin, the vertical velocity profiles (taken over the same region) appeared systematically narrower in the radial direction for the double-diffusive plumes. The flux-based plume

half-widths were also systematically smaller for the double-diffusive plumes, consistent with the reduction in the entrainment coefficient.

By combining the above observations, we conclude that the effect of double-diffusion on the entrainment coefficient is only important at the very early stages of the flow development. The self-similarity of the flow beyond $\hat{z}/r_0 = 36$ indicates that the effect of double-diffusion dies out very rapidly. That is, perhaps, unsurprising given that, based on the similarity solution of Morton et al. (1956), the scalar concentrations within the plume at $\hat{z}/r_0 \sim 35$ fall down to $\sim 20\%$ of their source values.

The effect of double-diffusion on the dynamics of turbulent jets was investigated in chapter 6. Unlike the preceding plumes experiments, where delicate measurements were required to observe the effect of double diffusion on the flow dynamics, the impact of double-diffusive processes on the evolution of initially neutrally-buoyant jets discharged horizontally into quiescent fresh ambient could be easily seen with a naked eye. Visual measurements over a range of source Reynolds numbers and temperature/salinity differences revealed that: (i) in contrast to their freshwater equivalents, the double-diffusive jets develop considerable sinking trajectories, and (ii) significant salt-fingering convection was present along the lower jet-ambient surface.

Qualitative inspection of the experimental records led us to believe that turbulent entrainment acts to hinder the formation of the salt fingers over a considerable distance from the jet source. Visually it appeared that in many instances the salt plumes, attempting to form along the bottom surface and separate, were not able to do so as they were re-entrained into the jet. This was particularly clear in the region near the source, where turbulent entrainment is the strongest. Based on these observations, a simple model predicting the onset point of the salt fingers was proposed by balancing entrainment and salt-fingering velocity scales. The good match between the model predictions and experimentally-determined locations of the onset of the salt fingers confirmed our physical understanding of the processes involved in this context.

We also observed that the tendency for the jets to sink was greater for larger source temperature differences, demonstrating the significance of double-diffusive processes for turbulent jet motion. The sinking trajectories were associated with the impact of internal jet-generated turbulence on the fluxes of heat and salt across its top and bottom surfaces. Importantly, in the absence of advective salt transport through salt-fingering motion over some considerable distance from the source, the diffusive heat losses dominated, resulting in the build-up of negative buoyancy which drove the jet downwards.

We showed that for a fixed source temperature difference, the double-diffusive jet trajectories can be well approximated by the trajectories of a single-diffusive buoyant jet with a fixed source buoyancy. This suggests that the accumulation of negative buoyancy as a result of double-diffusive processes happens quickly, since otherwise the jet buoyancy and hence trajectory would be changing continuously. Importantly, this effect is in line with the observations from the plume experiments, where the effect of double diffusion on turbulent entrainment was shown to be largest at the source, diminishing quickly as a result of turbulent dilution.

Importantly, even if the strength of the double-diffusive processes is greatest near the source (as it is predominantly controlled by the concentration gradients which tend to be largest at the point of discharge), it is the interplay of the diffusive and other processes governing the flow, that in the end determine its overall dynamics. This is well demonstrated by the contrast in what effect double-diffusion had on turbulent plumes and jets. For plumes, the reduction of the entrainment coefficient was greatest near the source, colliding with the region where double-diffusive processes were the strongest. However, for the case of turbulent jets, the development of the sinking trajectories and the fall-off of the salt-fingers occurred in the region where the concentration gradients, and hence the vigour of the double-diffusive processes were considerably reduced. This illustrates that the effect of double diffusion on the flow evolution and the structure of the turbulent/non-turbulent interface may only become important once other processes, such as entrainment processes, become relatively insignificant.

The findings presented in this thesis may have important considerations for modelling of environmental fluid flows. As shown in chapters 4 and 5, the double-diffusive effects on the rate of entrainment, and hence mixing, in turbulent plumes with high source concentration gradients and stability ratios may be significant. These effects, however, are transient in nature, and may be ignored when the concentration gradients fall down to sufficiently low levels.

The double-diffusive jets investigation, presented in chapter 6, may be of particular relevance for industrial waste disposal, such as the brine discharges from desalination plants. Our results show that that using the standard single-diffusive buoyant jet equations for the case of thermohaline double-diffusive discharges may lead to a significant underestimation of the curvature of the jet trajectory, overpredicting the distance travelled by the pollutant, and consequently its dilution. Such models should therefore be used with caution. Another implication of our work is that instead of propagating with the jet (going through continuous dilution to low concentrations through entrainment), the slow-diffusing scalar properties present within the jet may

tend to fall out in the form of salt fingers, causing additional pollution in the near-coastal region, which is unaccounted for by the current single-diffusive models.

Ultimately, this work show shows how limited our understanding of the interplay between turbulent and double-diffusive processes is, and opens up a multiplicity of potential avenues for future research in the field. These are briefly summarised below.

7.2 Future work

In this work, double-diffusive plume experiments were only conducted in the salt-fingering configuration, with the hot and salty plume fluid supplied into a colder and fresher ambient from above. Such a combination (based on heat and salt as the scalar properties) is, however, not unique for creating plumes in the salt-fingering configuration. The alternative, using the same scalar components, is to have a cold and fresh plume rising in a warm and salty ambient. This scenario is, perhaps, experimentally more challenging, mainly because of the need to maintain the ambient fluid at a constant elevated temperature, sufficiently high to produce large enough source temperature gradients. Experiments in this configuration may, however, be worth conducting, as they would provide additional measurements, which could be used for comparison with the results reported in this investigation.

Recalling that double-diffusion may exist in two distinct configurations, that is, salt-fingering and diffusive, there is potential in exploring the dynamics of double-diffusive plumes in the diffusive regime. In particular, it remains unclear as to what effect might double diffusion in the diffusive regime have on the rate of entrainment in turbulent plumes. Plumes in the diffusive configuration could be produced using heat and salt as the scalar components in either of the two following ways. The first option is to have a warm and salty plume rising into a cold and fresh ambient. The second option is to introduce a cold and fresh plume from above, descending into a warm and salty ambient. It is, however, important to note that both of these configurations are very challenging to implement experimentally. In the first case, as the plume rises, the warm and salty elements of the plume fluid will find themselves above colder and fresher ambient, creating the potential for the salt-fingering instability and leading to the formation of salt fingers. This would be of a particular problem in the case of the Baines' filling-box experiment, which relies on the establishment of a distinct two-layered stratification, with only the plume flow crossing the interface. The salt-fingering double-diffusive processes, occurring across the interface, would not only inhibit the formation of a distinct two-layered stratification, but also potentially induce advective fluxes of heat

and salt across the interface, making reliable measurements of the volume flux in the plume impossible. In the second case, as already mentioned, the key challenge would be the ability to maintain a constant elevated temperature in the environmental tank.

Finally, in relation to the double-diffusive plumes, perhaps the key remaining question is what exactly is happening to the flow near the source. Filling this gap experimentally may also be very challenging, mainly because of the effect of the two scalar properties with large gradients and $O(100)$ difference in the molecular diffusivities on the optical properties of the fluid, as discussed in detail in section 5.2. Unless a novel experimental methodology, allowing us to overcome the difficulties arising from the large refractive index mismatch becomes available, it may be more appropriate to address this problem computationally rather than experimentally. Direct numerical simulations of double-diffusive plumes with high Reynolds and Lewis numbers would, however, require very fine computational meshes to resolve the finest scales of the flow, and hence are likely to be computationally expensive. In that regard, the first step would be to simulate a relatively small near-source region, as this is where double-diffusive processes are most vigorous.

In relation to the double-diffusive jets, the potential for future research appears even greater. First, similar to the suggestions made for plumes, double-diffusive jets in the alternative case of the salt-fingering surface above the diffusive surface could be used as a comparison for the results presented in this investigation. In theory, this configuration should result in a mirror image of the behaviour described in chapter 7, with the jets tending to rise and salt fingers travelling upwards. One way of achieving this flow regime would be a jet of cold freshwater discharged into a warm and salty ambient. Given that, even for moderate source temperature differences of ~ 15 °C, the double-diffusive effects were readily observed in our experiments, these experiments could be performed even with the ambient water at room temperature, and would therefore require only minor modifications to the setup described in chapter 6.

As discussed in section 6.3.3, the inability to predict the exact evolution of the double-diffusive jet buoyancy, and hence its trajectory, mainly results from the absence of the exact parameters that determine the double-diffusive fluxes of heat and salt across turbulent interfaces in the diffusive and salt-fingering regimes. Early experiments of Linden (1971, 1974) provide some useful insights into the dynamics of salt-fingering interface in the presence of turbulence. However, these experiments were performed using a very particular setup for turbulence and shear generation, making the extrapolation of the obtained measurements onto the case of a turbulent jet very challenging. To make progress, more general parametrisations of the fluxes across a

double-diffusive interface in the presence of shear and turbulence are required and should to be pursued. If available, these parameters would enable modelling of scalar fluxes between the jet and the ambient, thereby allowing the predictions of the jet buoyancy, and hence trajectory, to be developed. Ideally, this could then lead to a general model for predicting the trajectory of a double-diffusive jet on the basis of the source parameters and the ambient conditions only.

In our experiments, the 3-dimensional structure of the flow resulted in salt fingers forming all around the lower surface of the jet at various depths into the plane of view, causing them to visually collide, and thus making it difficult to isolate and investigate the resulting structures accurately. To gain a better understanding of the mechanism of formation and the subsequent evolution of the salt fingers in turbulent double-diffusive jets, it could be useful to perform quasi-two-dimensional experiments, in which jets are confined in the spanwise direction. This would greatly simplify visual identification and tracking of individual fingers, while preserving many features of the three-dimensional jets.

Visual measurements of the slower diffusing component (salt) were made possible because of the similarity between its own molecular diffusivity and that of the methylene blue dye, used for visualisation. The $O(100)$ times faster diffusivity of heat, made it impossible to simultaneously visualise the evolution of the temperature field. To gain a better understanding of the processes occurring within the double-diffusive jets and their surroundings, measurements of the spatio-temporal temperature distributions are necessary. One way of doing this experimentally is to use the Thermochromic Liquid Crystals (TLC), which have become increasingly common for temperature visualisation in various flow field configurations in the recent decades, as discussed in considerable detail by Smith et al. (2001).

An area for potential investigations with more immediate practical applications is related to studying the effect of the discharge angle (both upwards and downwards) on the dynamics of double-diffusive jets in both configurations. Such work could have practical use in the field of waste disposal in the form of a jet flow (e.g. desalination brine discharge into the ocean), where the ejection angle is one of the critical design parameters.

Ultimately, looking at the bigger picture, investigations on the effect of double diffusion on the dynamics of other types of turbulent free shear flows, including thermals, gravity current and mixing layers, may uncover additional surprising effects arising from the interplay of turbulent and diffusive processes, and hence are strongly encouraged.

References

Ahlers, G., Grossmann, S., and Lohse, D. (2009). Heat transfer and large scale dynamics in turbulent rayleigh-bénard convection. *Rev. Mod. Phys*, 81(2):503.

Baines, W. D. (1983). A technique for the direct measurement of volume flux of a plume. *J. Fluid Mech.*, 132:247–256.

Baines, W. D. and Turner, J. S. (1969). Turbulent buoyant convection from a source in a confined region. *J. Fluid Mech.*, 37(1):51–80.

Bloomfield, L. J. and Kerr, R. C. (2002). Inclined turbulent fountains. *J. Fluid Mech.*, 451:283–294.

Boussinesq, J. (1903). *Théorie analytique de la chaleur*, volume 2. Gauthier-Villars.

Briggs, G. A. (1982). Plume rise predictions. In *Lectures on air pollution and environmental impact analyses*, pages 59–111. Springer.

Brown, G. L. and Roshko, A. (1974). On density effects and large structure in turbulent mixing layers. *J. Fluid Mech.*, 64(4):775–816.

Burridge, H. C., Parker, D. A., Kruger, E. S., Partridge, J. L., and Linden, P. F. (2017). Conditional sampling of a high péclet number turbulent plume and the implications for entrainment. *J. Fluid Mech.*, 823:26–56.

Burridge, H. C., Partridge, J. L., and Linden, P. F. (2016). The fluxes and behaviour of plumes inferred from measurements of coherent structures within images of the bulk flow. *Atmos. Ocean*, 54(4):403–417.

Carazzo, G., Kaminski, E., and Tait, S. (2006). The route to self-similarity in turbulent jets and plumes. *J. Fluid Mech.*, 547:137–148.

Carmack, E. C., Aagaard, K., Swift, J. H., MacDonald, R. W., McLaughlin, F. A., Jones, E. P., Perkin, R. G., Smith, J. N., Ellis, K. M., and Killius, L. R. (1997). Changes in temperature and tracer distributions within the arctic ocean: Results from the 1994 arctic ocean section. *Deep Sea Res. Part 2 Top. Stud. Oceanogr.*, 44(8):1487–1502.

Cenedese, C. and Dalziel, S. B. (1998). Concentration and depth fields determined by the light transmitted through a dyed solution. In *Proceedings of the 8th International Symposium on Flow Visualization*, volume 8, pages 1–37.

Chandrasekhar, S. (1961). Hydrodynamic and hydromagnetic stability, 652 pp., clarendon.

Chen, C. J. and Rodi, W. (1980). Vertical turbulent buoyant jets: a review of experimental data. *NASA Sti/Recon Technical Report A*, 80.

Cowen, E. A. and Monismith, S. G. (1997). A hybrid digital particle tracking velocimetry technique. *Exp. Fluids*, 22(3):199–211.

Dalziel, S. B. (1992). Digimage: system overview. *Cambridge Environmental Research Consultants, Ltd.*

Del Bene, J. V., Jirka, G., and Largier, J. (1994). Ocean brine disposal. *Desalination*, 97(1-3):365–372.

Ezzamel, A., Salizzoni, P., and Hunt, G. R. (2015). Dynamical variability of axisymmetric buoyant plumes. *J. Fluid Mech.*, 765:576–611.

Fan, L. and Brooks, N. H. (1969). Numerical solutions of turbulent buoyant jet problems. *Calif Inst. Technol., W. M. Keck Lab. Rep. No. KH-R-18.*

Forstall, W. and Gaylord, E. W. (1955). Momentum and mass transfer in a submerged water jet. *J. Appl. Mech*, 22:161–164.

Gartshore, I. S. (1966). An experimental examination of the large-eddy equilibrium hypothesis. *J. Fluid Mech.*, 24(1):89–98.

George, W. K. (1989). The self-preservation of turbulent flows and its relation to initial conditions and coherent structures. *J. Turbul.*, 3973.

George, W. K., Alpert, R. L., and Tamanini, F. (1977). Turbulence measurements in an axisymmetric buoyant plume. *Int. J. Heat Mass Transf.*, 20(11):1145–1154.

Hirst, E. (1971). Buoyant jets discharged to quiescent stratified ambients. *J. Geophys. Res.*, 76(30):7375–7384.

Holder, D. W. and North, R. J. (1963). *Schlieren methods*, volume 31. HM Stationery Office.

Holford, J. M. and Linden, P. F. (1999). Turbulent mixing in a stratified fluid. *Dynamics of atmospheres and oceans*, 30(2-4):173–198.

Howard, L. N. (1964). Convection at high rayleigh number. In *Applied Mechanics*, pages 1109–1115. Springer.

Hunt, G. R. and Kaye, N. G. (2001). Virtual origin correction for lazy turbulent plumes. *J. Fluid Mech.*, 435:377–396.

Hunt, G. R. and Linden, P. F. (2001a). Steady-state flows in an enclosure ventilated by buoyancy forces assisted by wind. *J. Fluid Mech.*, 426:355–386.

Hunt, G. R. and Linden, P. F. (2001b). Steady-state flows in an enclosure ventilated by buoyancy forces assisted by wind. *J. Fluid Mech.*, 426:355–386.

Hunt, G. R. and Van den Bremer, T. S. (2010). Classical plume theory: 1937–2010 and beyond. *IMA J. Appl. Math.*, 76(3):424–448.

Hunt, J. C. R. (1991). Industrial and environmental fluid mechanics. *Annu. Rev. Fluid Mech.*, 23(1):1–42.

Huppert, H. E. and Turner, J. S. (1981). Double-diffusive convection. *J. Fluid Mech.*, 106:299–329.

Jirka, G. H. (2004). Integral model for turbulent buoyant jets in unbounded stratified flows. part i: Single round jet. *Environ. Fluid Mech.*, 4(1):1–56.

Jones, E., Qadir, M., van Vliet, M. T. H., Smakhtin, V., and Kang, S. (2019). The state of desalination and brine production: A global outlook. *Sci. Total Environ*, 657:1343–1356.

Kaminski, E., Tait, S., and Carazzo, G. (2005). Turbulent entrainment in jets with arbitrary buoyancy. *J. Fluid Mech.*, 526:361–376.

Kaye, N. B. and Hunt, G. R. (2004). Time-dependent flows in an emptying filling box. *J. Fluid Mech.*, 520:135–156.

Keane, R. D. and Adrian, R. J. (1992). Theory of cross-correlation analysis of piv images. *Appl. Sci. Res.*, 49(3):191–215.

Kolmogorov, A. N. (1941). On degeneration (decay) of isotropic turbulence in an incompressible viscous liquid. In *Dokl. Akad. Nauk SSSR*, volume 31, pages 538–540.

Konopliv, N. and Meiburg, E. (2016). Double-diffusive lock-exchange gravity currents. *J. Fluid Mech.*, 797:729–764.

Kotsovinos, N. E. and List, E. J. (1977). Plane turbulent buoyant jets. part 1. integral properties. *J. Fluid Mech.*, 81(1):25–44.

Lane-Serff, G. F., Linden, P. F., and Hillel, M. (1993). Forced, angled plumes. *J. Hazard. Mater.*, 33(1):75–99.

Law, A. W., Ho, W. F., and Monismith, S. G. (2004). Double diffusive effect on desalination discharges. *J. Hydraul. Eng.*, 130(5):450–457.

Linden, P. F. (1971). Salt fingers in the presence of grid-generated turbulence. *J. Fluid Mech.*, 49(3):611–624.

Linden, P. F. (1974). Salt fingers in a steady shear flow. *Geophys. Astrophys. Fluid Dyn.*, 6(1):1–27.

Linden, P. F. (2000). *Convection in the environment. In Perspectives in Fluid Dynamics: A Collective Introduction to Current Research (ed. G. K. Batchelor, H. K. Moffatt & M. G. Worster).* Cambridge University Press.

Linden, P. F., Lane-Serff, G. F., and Smeed, D. A. (1990). Emptying filling boxes: the fluid mechanics of natural ventilation. *J. Fluid Mech.*, 212:309–335.

Linden, P. F. and Shirtcliffe, T. G. L. (1978). The diffusive interface in double-diffusive convection. *J. Fluid Mech.*, 87(3):417–432.

List, E. J. (1982). Turbulent jets and plumes. *Annu. Rev. Fluid Mech.*, 14(1):189–212.

Marmorino, G. O. and Caldwell, D. R. (1976). Heat and salt transport through a diffusive thermohaline interface. *Deep-Sea Res. Oceanogr. Abstr.*, 23(1):59–67.

Mathew, J. and Basu, A. J. (2002). Some characteristics of entrainment at a cylindrical turbulence boundary. *Phys. Fluids*, 14(7):2065–2072.

Maxworthy, T. (1983). The dynamics of double-diffusive gravity currents. *J. Fluid Mech.*, 128:259–282.

McDougall, T. J. (1979). On the elimination of refractive-index variations in turbulent density-stratified liquid flows. *J. Fluid Mech.*, 93(1):83–96.

McDougall, T. J. (1983). Double-diffusive plumes in unconfined and confined environments. *J. Fluid Mech.*, 133:321–343.

Mistry, D., Philip, J., Dawson, J. R., and Marusic, I. (2016). Entrainment at multi-scales across the turbulent/non-turbulent interface in an axisymmetric jet. *J. Fluid Mech.*, 802:690–725.

Morton, B. R. (1959). Forced plumes. *J, Fluid Mech.*, 5(1):151–163.

Morton, B. R., Taylor, G. I., and Turner, J. S. (1956). Turbulent gravitational convection from maintained and instantaneous sources. In *Proc. Royal Soc. A: Mathematical, physical and engineering sciences*, volume 234, pages 1–23. The Royal Society.

Nakagome, H. and Hirata, M. (1980). The structure of turbulent diffusion in a two-dimensional thermal plume. *Trans. Jpn Soc. Mech. Eng. B*, 46:2023–2036.

Newell, T. A. and Boehm, R. F. (1982). Gradient zone constraints in a salt-stratified solar pond.

Olsthoorn, J. and Dalziel, S. B. (2017). Three-dimensional visualization of the interaction of a vortex ring with a stratified interface. *J. Fluid Mech.*, 820:549–579.

Panchapakesan, N. R. and Lumley, J. L. (1993). Turbulence measurements in axisymmetric jets of air and helium. part 1. air jet. *J. Fluid Mech.*, 246:197–223.

Papanicolaou, P. N. and List, E. J. (1988). Investigations of round vertical turbulent buoyant jets. *J. Fluid Mech.*, 195:341–391.

Partridge, J. L. and Linden, P. F. (2013). Validity of thermally-driven small-scale ventilated filling box models. *Experiments in Fluids*, 54(11):1613.

Penney, J. and Stastna, M. (2016). Direct numerical simulation of double-diffusive gravity currents. *Phys. Fluids*, 28(8):086602.

Philip, J. and Marusic, I. (2012). Large-scale eddies and their role in entrainment in turbulent jets and wakes. *Phys. Fluids*, 24(5):055108.

Prasad, A., Adrian, R., Landreth, C., and Offutt, P. (1992). Effect of resolution on the speed and accuracy of particle image velocimetry interrogation. *Exp. Fluids*, 13(2-3):105–116.

Priestley, C. B. and Ball, F. K. (1955). Continuous convection from an isolated source of heat. *Q. J. Royal Meteorol. Soc*, 81(348):144–157.

Radko, T. (2013). *Double-diffusive convection*. Cambridge University Press.

Ricou, F. P. and Spalding, D. B. (1961). Measurements of entrainment by axisymmetrical turbulent jets. *J. Fluid Mech.*, 11(1):21–32.

Roberts, P. J. W., Ferrier, A., and Daviero, G. (1997). Mixing in inclined dense jets. *J. Hydraul. Eng*, 123(8):693–699.

Roche, P., Gauthier, F., Kaiser, R., and Salort, J. (2010). On the triggering of the ultimate regime of convection. *New J. Phys.*, 12(8):085014.

Rosensweig, R. E., Hottel, H. C., and Williams, H. C. (1961). Smoke-scattered light measurement of turbulent concentration fluctuations. *Chem. Eng. Sci.*, 15(1-2):111–129.

Rouse, H., Yih, C. S., and Humphreys, H. W. (1952). Gravitational convection from a boundary source. *Tellus*, 4(3):201–210.

Ruddick, B. R. and Shirtcliffe, T. G. L. (1979). Data for double diffusers: Physical properties of aqueous salt-sugar solutions. *Deep Sea Res. Part A. Oceanographic Research Papers*, 26(7):775–787.

Ruden, P. (1933). Turbulente ausbreitungsvorgänge im freistrahl. *Naturwissenschaften*, 21(21-23):375–378.

Schmidt, W. (1941). Turbulente ausbreitung eines stromes erhitzter luft. *ZAMM-Journal of Applied Mathematics and Mechanics/Zeitschrift für Angewandte Mathematik und Mechanik*, 21(5):265–278.

Schmitt, R. W. (1979). Flux measurements on salt fingers at an interface.

Schmitt, R. W. (1994). Double diffusion in oceanography. *Annu. Rev. Fluid Mech.*, 26(1):255–285.

Settles, G. S. (2012). *Schlieren and shadowgraph techniques: visualizing phenomena in transparent media*. Springer Science & Business Media.

Shabbir, A. and George, W. K. (1994). Experiments on a round turbulent buoyant plume. *J. Fluid Mech.*, 275:1–32.

Shen, C. Y. (1993). Heat-salt finger fluxes across a density interface. *Phys Fluid A, Fluid Dyn*, 5(11):2633–2643.

Shirtcliffe, T. G. L. (1973). Transport and profile measurements of the diffusive interface in double diffusive convection with similar diffusivities. *J. Fluid Mech.*, 57(1):27–43.

Shirtcliffe, T. G. L. and Turner, J. S. (1970). Observations of the cell structure of salt fingers. *J. Fluid Mech.*, 41(4):707–719.

Smith, C. R., Sabatino, D. R., and Praisner, T. J. (2001). Temperature sensing with thermochromic liquid crystals. *Exp. Fluids*, 30(2):190–201.

Spiegel, E. A. and Veronis, G. (1960). On the boussinesq approximation for a compressible fluid. *Astrophys. J*, 131:442.

Stamp, A. P., Hughes, G. O., Nokes, R. I., and Griffiths, R. W. (1998). The coupling of waves and convection. *J. Fluid Mech.*, 372:231–271.

Stern, M. E. (1960). The "salt-fountain" and thermohaline convection. *Tellus*, 12(2):172–175.

Stern, M. E. and Turner, J. S. (1969). Salt fingers and convecting layers. *Deep-Sea Res. Oceanogr. Abstr.*, 16(5):497–511.

Stommel, H., Arons, A. B., and Blanchard, D. (1956). An oceanographic curiosity: the perpetual salt fountain. *Deep-Sea Res.*, 3:152–153.

Swindells, J. F. (1958). *Viscosities of sucrose solutions at various temperatures: tables of recalculated values*, volume 440. For sale by the Supt. of Docs., USGPO.

Taylor, J. R. and Veronis, G. (1996). Experiments on double-diffusive sugar–salt fingers at high stability ratio. *J. Fluid Mech.*, 321:315–333.

Thangam, S. and Chen, C. F. (1981). Salt-finger convection in the surface discharge of heated saline jets. *Geophys. Astrophys. Fluid Dyn.*, 18(1-2):111–146.

Tollmien, W. (1926). Berechnung turbulenter ausbreitungsvorgänge. *ZAMM-Journal of Applied Mathematics and Mechanics/Zeitschrift für Angewandte Mathematik und Mechanik*, 6(6):468–478.

Townsend, A. A. (1970). Entrainment and the structure of turbulent flow. *J. Fluid Mech.*, 41(1):13–46.

Turner, J. S. (1965). The coupled turbulent transports of salt and and heat across a sharp density interface. *Int. J. Heat Mass Transf.*, 8(5):759–767.

Turner, J. S. (1967). Salt fingers across a density interface. *Deep-Sea Res. Oceanogr. Abstr.*, 14(5):599–611.

Turner, J. S. (1978). Double-diffusive intrusions into a density gradient. *J. Geophys. Res.: Oceans*, 83(C6):2887–2901.

Turner, J. S. (1979). *Buoyancy effects in fluids*. Cambridge University Press.

Turner, J. S. (1986). Turbulent entrainment: the development of the entrainment assumption, and its application to geophysical flows. *J. Fluid Mech.*, 173:431–471.

Turner, J. S. (2001). Double-diffusive plumes in a homogeneous environment. In *Proc. 14th Australasian Fluid Mech. Conf. Adelaide*, pages 905–908.

Turner, J. S. (2003). Vertical transports produced by double-diffusive plumes in a confined homogeneous environment. *J. Fluid Mech.*, 493:131–149.

Turner, J. S. and Campbell, I. H. (1986). Convection and mixing in magma chambers. *Earth-Sci. Rev.*, 23(4):255–352.

Turner, J. S. and Chen, C. F. (1974). Two-dimensional effects in double-diffusive convection. *J. Fluid Mech.*, 63(3):577–592.

Turner, J. S. and Stommel, H. (1964). A new case of convection in the presence of combined vertical salinity and temperature gradients. *Proc. Natl. Acad. Sci. U. S. A.*, 52(1):49.

Turner, J. S. and Veronis, G. (2000). Laboratory studies of double-diffusive sources in closed regions. *J. Fluid Mech.*, 405:269–304.

Van Reeuwijk, M., Salizzoni, P., Hunt, G. R., and Craske, J. (2016). Turbulent transport and entrainment in jets and plumes: A dns study. *Phys. Rev. Fluids*, 1(7):074301.

Vanderwel, C. and Tavoularis, S. (2014). On the accuracy of plif measurements in slender plumes. *Exp. Fluids*, 55(8):1801.

Wang, H. and Law, A. W. (2002). Second-order integral model for a round turbulent buoyant jet. *J. Fluid Mech.*, 459:397–428.

Weinberg, F. J. and Weinberg, F. J. (1963). *Optics of flames: including methods for the study of refractive index fields in combustion and aerodynamics*. Butterworths London.

Westerweel, J., Fukushima, C., Pedersen, J. M., and Hunt, J. R. (2005). Mechanics of the turbulent-nonturbulent interface of a jet. *Phys. Rev. Lett.*, 95(17):174501.

Willert, C. (1997). Stereoscopic digital particle image velocimetry for application in wind tunnel flows. *Meas. Sci. Technol*, 8(12):1465.

Xu, H. and Bodenschatz, E. (2008). Motion of inertial particles with size larger than kolmogorov scale in turbulent flows. *Physica D: Nonlinear Phenomena*, 237(14-17):2095–2100.

Ying, C., Davidson, M. J., Wang, H. W., and Law, A. W. K. (2004). Radial velocities in axisymmetric jets and plumes. *J. Hydraul. Res.*, 42(1):29–33.

Yoshida, J., Nagashima, H., and Ma, W. J. (1987). A double diffusive lock-exchange flow with small density difference. *Fluid Dyn. Res.*, 2(3):205.

Appendix A

Derivation of key equations

Conservation equation

Integral form

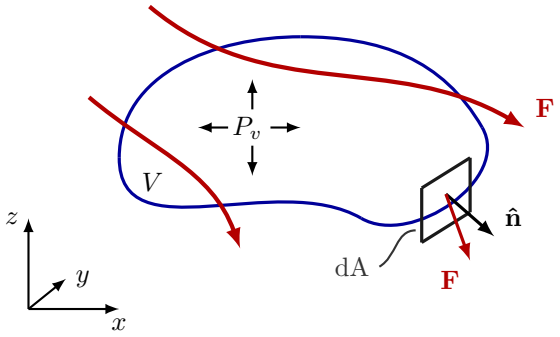

Fig. A.1 A schematic representation of control volume of conserved quanitity c.

The general statement of conservation of some quantity c, in a volume V can be expressed in an integral form as follows

$$\frac{\mathrm{d}}{\mathrm{d}t}\int_V c\,\mathrm{d}V = -\oint_A \hat{\mathbf{n}}\cdot\mathbf{F}\,\mathrm{d}A + \int_V P_v\,\mathrm{d}V. \tag{A.1}$$

We can transform the first term on the rhs of the above equation by applying the divergence theorem

$$\oint_A \hat{\mathbf{n}}\cdot\mathbf{F}\,\mathrm{d}A = \int_V \nabla\cdot\mathbf{F}\,\mathrm{d}V. \tag{A.2}$$

The divergence of a vector is defined as

$$\nabla\cdot\mathbf{F} = \mathrm{div}(\mathbf{F}) = \frac{\partial F_x}{\partial x} + \frac{\partial F_y}{\partial y} + \frac{\partial F_z}{\partial z}. \tag{A.3}$$

For cases, with no production term P_v, the general integral form of conservation equation becomes

$$\int_V \left(\frac{\partial c}{\partial t} + \nabla \cdot \mathbf{F}\right) \mathrm{d}V = 0 \tag{A.4}$$

Differential form

Taking the limit as $\mathrm{d}V$ approaches zero, we obtain the general differential form of conservation equation

$$\frac{\partial c}{\partial t} + \nabla \cdot \mathbf{F} = 0. \tag{A.5}$$

For a fluid flow the differential form of mass conservation equation can be written as

$$\frac{\partial \rho}{\partial t} + \nabla \cdot (\rho \mathbf{u}) = 0, \tag{A.6}$$

where ρ is fluid density. Equation above can be expanded as

$$\underbrace{\frac{\partial \rho}{\partial t} + \mathbf{u} \cdot \nabla \rho}_{\text{Material Derivative}} + \rho \nabla \cdot \mathbf{u} = 0. \tag{A.7}$$

For incompressible fluids, we can assume that density ρ is a constant, implying that the total derivative is zero and yielding the incompressible continuity equation

$$\nabla \cdot \mathbf{u} = 0. \tag{A.8}$$

The velocity vector in cartesian and cylindrical polar co-ordinate systems is

$$Cartesian : \mathbf{u} = u\mathbf{e_x} + v\mathbf{e_y} + w\mathbf{e_z}, \tag{A.9a}$$

$$Cylindrical\ polar : \mathbf{u} = u\mathbf{e_r} + v\mathbf{e}_\theta + w\mathbf{e_z}, \tag{A.9b}$$

and thus the continuity equation can be, respectively, written as

$$Cartesian : \frac{\partial u}{\partial x} + \frac{\partial v}{\partial y} + \frac{\partial w}{\partial z} = 0, \tag{A.10a}$$

$$Cylindrical\ polar : \frac{1}{r}\frac{\partial (ru)}{\partial r} + \frac{1}{r}\frac{\partial (rv)}{\partial \theta} + \frac{\partial w}{\partial z} = 0. \tag{A.10b}$$

Diffusion equation

The diffusive flux of a quantity c can be defined by Fick's law as

$$F = -D\nabla c. \tag{A.11}$$

In case of no advection, substitution of equation A.11 into the differential form of conservation equation yields the diffusion equation

$$\frac{\partial c}{\partial t} = \nabla \cdot (D\nabla c). \tag{A.12}$$

If the diffusion coefficient D is a constant, the equation above can be simplified to

$$\frac{\partial c}{\partial t} = D\nabla^2 c, \tag{A.13}$$

where ∇^2 is the Laplacian with the definition in cartisean coordinates as follows

$$\nabla^2 c = \frac{\partial c}{\partial x^2} + \frac{\partial c}{\partial y^2} + \frac{\partial c}{\partial z^2}. \tag{A.14}$$

For cases of diffusive flows in a constant velocity field, the total flux is a combination of both advective and diffusive fluxes

$$\mathbf{F} = c\mathbf{u} + D\nabla c. \tag{A.15}$$

Substitution of total flux $\mathbf{F}$ into the general form of continuity equation (A.5), yields

$$\frac{\partial c}{\partial t} + \nabla \cdot (c\mathbf{u}) = D\nabla^2 c. \tag{A.16}$$

Assuming a steady state, incompressible flow we can simplify the above equation to the general form of the advection-diffusion equation as below

$$\mathbf{u} \cdot \nabla c = D\nabla^2 c. \tag{A.17}$$

Appendix B

Plume theory

Scaling considerations

Consider a plume emanating from a point source with buoyancy flux B_0 defined as

$$B_0 = Q_0 \, g \, \frac{\rho_a - \rho}{\rho_a} = Q_0 \, g', \tag{B.1}$$

where Q_0 is the source volume flux, ρ is the density of the plume, ρ_a is the ambient density, and g' is the buoyancy, or reduced gravity. It is observed that turbulent plumes in a uniform environment are geometrically self-similar, taking a mean conical shape (Turner, 1986). The time-mean velocity and scalar distributions across the plume have the same shape profiles at all heights above the source, with only their amplitudes and widths varying with height. It follows that in the case of a uniform stationary ambient, the properties of the plume can be described by source buoyancy flux B_0 and vertical distance from the source z only. Dimensional analysis shows that at each height the mean radius b, mean vertical velocity w and mean buoyancy g' are given as

$$b = k_1 z, \qquad w = c_1 B_0^{1/3} z^{-1/3}, \qquad g' = c_2 B_0^{2/3} z^{-5/3}, \tag{B.2}$$

where k_1 is a dimensionless constant, and c_1 and c_2 are dimensionless functions of the dimensionless radius r/b. To date, these dimensionless functions cannot be accurately captured by theoretical models and thus have to be determined experimentally. Measurements made by Rouse et al. (1952) and Ricou and Spalding (1961) show that the radial dependence of time-averaged vertical velocity and density profiles can be

well-approximated by Gaussian profiles of the form

$$c_1 = \hat{c}_1 \exp(-r^2/b^2) \qquad \text{and} \qquad c_2 = \hat{c}_2 \exp(-r^2/\lambda b^2), \tag{B.3}$$

where $\hat{c}_1$ and $\hat{c}_2$ are dimensionless constants. Rouse et al. (1952) observed that the rates of spread, and thus the relative widths (given by λ), of velocity and buoyancy are not the same, but are close to unity. Papanicolaou and List (1988) later confirmed this finding with a value reported of buoyancy to velocity radii of λ=1.06. Very recent findings of Burridge et al. (2017) suggest that the time-averaged buoyancy can be wider due to its distribution being relatively well-mixed instantaneously. To simplify further analysis, it is assumed that λ=1. Using the above assumptions, the volume flux Q, defined as

$$Q = 2\pi \int_0^\infty wr \, \mathrm{d}r, \tag{B.4}$$

which for a self-similar plume is given by

$$Q = \pi \hat{c}_1 k_1^2 B^{1/3} z^{5/3}. \tag{B.5}$$

The key result of the dimensional analysis is that the plume volume flux increases through entrainment of ambient fluid. The leads to a rapid deceleration of the flow and an increase in radius to keep constant volume flux. It also shows that the plume volume flux depends weakly on buoyancy flux and strongly on the distance traveled.

Plume equations of motion

We start with a general form of the Navier-Stokes equations for an incompressible fluid

$$\rho(\frac{\partial \mathbf{u}}{\partial t} + \mathbf{u} \cdot \nabla \mathbf{u}) = -\nabla \mathbf{p} + \mu \nabla^2 \mathbf{u} + \rho \mathbf{g}, \tag{B.6a}$$

$$\nabla \cdot \mathbf{u} = 0. \tag{B.6b}$$

For an steady axisymmetric flow of an inviscid incompressible fluid with no diffusion of mass and momentum, under the Boussinesq assumption ($\rho = \rho_0$ in the inertial term), and with a velocity field $\mathbf{u} = (u, 0, w)$ in cylindrical polar coordinates (r, θ, z) the above

equations can be rewritten as

$$r: \quad u\frac{\partial u}{\partial r} + w\frac{\partial u}{\partial z} = -\frac{1}{\rho_0}\frac{\partial p}{\partial r}, \tag{B.7a}$$

$$z: \quad u\frac{\partial w}{\partial r} + w\frac{\partial w}{\partial z} = -\frac{1}{\rho_0}\frac{\partial p}{\partial z} - g\frac{\rho}{\rho_0} \tag{B.7b}$$

$$Continuity: \quad \frac{1}{r}\frac{\partial (ur)}{\partial r} + \frac{\partial w}{\partial z} = 0. \tag{B.7c}$$

In the above equations $w \to 0$ as $r \to \infty$, signifying that the vertical motion is confined to the plume. This assumption will be imporant in further derivations.

Using Reynolds decomposition, each variable in a turbulent plume can be broken down into a sum of a mean and a fluctuating components, as shown below

$$\rho = \overline{\rho} + \rho', \quad \text{where} \quad \overline{\rho} = \frac{1}{t_T}\int_0^{t_T} \rho \, \mathrm{d}r, \tag{B.8}$$

and where t_T is the total averaging time. In our subsequent analysis we assume that the turbulent fluctuations are small compared to the mean values and the plume variables can therefore be replaced by their time-mean values. For simplicity we drop the overbar notation to signify time-mean.

Entrainment assumption

Formulated by Morton et al. (1956), the entrainment assumption takes the entrainment velocity of ambient fluid at the plume edge at a given height $u_{edge}(z)$ to be linearly related to the vertical velocity in the plume at that height $w(z)$ by the entrainment coefficient α.

Volume flux

We start with a continuity equation in cylindrical polar co-ordinate system and assume incompressibility and axysymmetric geometry, (i.e. $\frac{\partial}{\partial \theta} = 0$)

$$\frac{1}{r}\frac{\partial (ur)}{\partial r} + \frac{\partial w}{\partial z} = 0. \tag{B.9}$$

Integrate over entire radial domain

$$\int_0^\infty \frac{\partial (ur)}{\partial r}\, \mathrm{d}r + \int_0^\infty r\frac{\partial w}{\partial z}\, \mathrm{d}r = 0. \tag{B.10}$$

Rearrange to

$$-\int_0^\infty \frac{\partial(ur)}{\partial r}\,\mathrm{d}r = \frac{\mathrm{d}}{\mathrm{d}z}\int_0^\infty wr\,\mathrm{d}r. \tag{B.11}$$

Recalling that $Q = 2\pi\int_0^\infty wr\,\mathrm{d}r$, we obtain

$$-ru|_\infty = \frac{1}{2\pi}\frac{dQ}{dz}. \tag{B.12}$$

The inflow from infinity is driven by the turbulent entrainment into the plume at the edge, therefore

$$-ru|_\infty = bu_{edge}. \tag{B.13}$$

Using the MTT entrainment assumption that $u_{edge} = \alpha w$, the volume conservation equation can be written as

$$\frac{\mathrm{d}Q}{\mathrm{d}z} = 2\pi b\,\alpha w. \tag{B.14}$$

Momentum flux

Recall the z-momentum equation

$$u\frac{\partial w}{\partial r} + w\frac{\partial w}{\partial z} = -\frac{1}{\rho_0}\frac{\partial p}{\partial z} - g\frac{\rho}{\rho_0}. \tag{B.15}$$

Since outside the plume, $\rho_a = \rho_a(z)$ and $w = 0$, from the above equation, we obtain the hydrostatic relation

$$\frac{\partial p}{\partial z} = -g\rho_a. \tag{B.16}$$

The vertical momentum equations for a thin ($\partial/\partial r >> \partial/\partial z$) plume therefore becomes

$$u\frac{\partial w}{\partial r} + w\frac{\partial w}{\partial z} = g(\frac{\rho_a - \rho}{\rho_0}). \tag{B.17}$$

Rate of change of vertical momentum flux

$$\frac{\mathrm{d}M}{\mathrm{d}z} = \int_0^\infty \frac{\partial}{\partial z}w^2 2\pi r\mathrm{d}r = 2\int_0^\infty w\frac{\partial w}{\partial z}2\pi r\mathrm{d}r, \tag{B.18}$$

and recalling that $g(\frac{\rho_a-\rho}{\rho_0}) = g'$ and using equation B.17 to replace one instance of $w\frac{\partial w}{\partial z}$, obtain

$$\frac{\mathrm{d}M}{\mathrm{d}z} = \int_0^\infty w\frac{\partial w}{\partial z}2\pi r\mathrm{d}r + \int_0^\infty g' 2\pi r\mathrm{d}r - \int_0^\infty u\frac{\partial w}{\partial r}2\pi r\mathrm{d}r \tag{B.19}$$

Take a step back here and perform a side derivation below

$$\frac{\partial}{\partial r}(ru\ w) = w\frac{\partial}{\partial r}(ru) + ru\frac{\partial w}{\partial r}. \tag{B.20}$$

From the continuity equation ($\nabla \cdot \mathbf{u} = 0$), we have

$$\frac{\partial}{\partial r}(ru) = -r\frac{\partial w}{\partial z}, \tag{B.21}$$

therefore, by substitution we get

$$\frac{\partial}{\partial r}(ru\ w) = -wr\frac{\partial w}{\partial z} + ru\frac{\partial w}{\partial r}, \tag{B.22}$$

which can be rearraged as follows

$$ru\frac{\partial w}{\partial r} = \frac{\partial}{\partial r}(ru\ w) + wr\frac{\partial w}{\partial z} \tag{B.23}$$

Substituting $ru\frac{\partial w}{\partial r}$ into equation B.19 yields

$$\begin{aligned}\frac{\mathrm{d}M}{\mathrm{d}z} = &\int_0^\infty w\frac{\partial w}{\partial z}2\pi r\mathrm{d}r + \int_0^\infty g'2\pi r\mathrm{d}r \\ &- \int_0^\infty \frac{\partial}{\partial r}(ru\ w)2\pi r\mathrm{d}r - \int_0^\infty w\frac{\partial w}{\partial z}2\pi r\mathrm{d}r.\end{aligned}$$

Given that $w|_\infty = 0$ and $(ru)|_0 = 0$, it follows that

$$\int_0^\infty \frac{\partial}{\partial r}(ru\ w)2\pi r\mathrm{d}r = (ru\ w)|_0^\infty = 0, \tag{B.25}$$

finally leading to the momentum conservation equation in the form

$$\frac{\mathrm{d}M}{\mathrm{d}z} = 2\pi\int_0^\infty g'r\mathrm{d}r. \tag{B.26}$$

Buoyancy flux

We begin with an expression for the plume buoyancy flux

$$B = 2\pi\int_0^\infty wg'r\,\mathrm{d}r, \tag{B.27}$$

with its rate of change in the vertical direction being

$$\frac{\mathrm{d}B}{\mathrm{d}z} = 2\pi \int_0^\infty \frac{\partial}{\partial z}(wg')\, r\mathrm{d}r = 2\pi \int_0^\infty w\frac{\partial g'}{\partial z}\, r\mathrm{d}r + 2\pi \int_0^\infty g'\frac{\partial w}{\partial z}\, r\mathrm{d}r. \tag{B.28}$$

Recalling that $g' = g\frac{\rho_a - \rho}{\rho_0}$ and using B.21, we obtain

$$\frac{\mathrm{d}B}{\mathrm{d}z} = 2\pi \int_0^\infty w\frac{g}{\rho_0}\frac{\partial \rho_a}{\partial z}\, r\mathrm{d}r - 2\pi \int_0^\infty w\frac{g}{\rho_0}\frac{\partial \rho}{\partial z}\, r\mathrm{d}r - 2\pi \int_0^\infty g'\frac{\partial}{\partial r}(ru)\,\mathrm{d}r \tag{B.29}$$

Recall the differential form of steady-state mass conservation

$$\mathbf{u}\cdot\nabla\rho + \rho\nabla\cdot\mathbf{u} = 0. \tag{B.30}$$

Given that $\nabla\cdot\mathbf{u} = 0$, it follows that $\mathbf{u}\cdot\nabla\rho = 0$, i.e.

$$u\frac{\partial\rho}{\partial r} + w\frac{\partial\rho}{\partial z} = 0. \tag{B.31}$$

Substitution of $w\frac{\partial\rho}{\partial z}$ into B.29 yields

$$\frac{\mathrm{d}B}{\mathrm{d}z} = \underbrace{\frac{g}{\rho_0}\frac{\partial\rho_a}{\partial z}}_{-N^2}\ \underbrace{2\pi\int_0^\infty wr\mathrm{d}r}_{Q} - 2\pi\int_0^\infty u\frac{g}{\rho_0}\frac{\partial\rho}{\partial r}r\mathrm{d}r - 2\pi\int_0^\infty g'\frac{\partial}{\partial r}(ru)\mathrm{d}r. \tag{B.32}$$

Let us now use the statement that

$$\frac{\partial g'}{\partial r} = \frac{\partial}{\partial r}\Big(g\frac{\rho_a - \rho}{\rho_0}\Big) = \frac{g}{\rho_0}\frac{\partial\rho}{\partial r}, \tag{B.33}$$

to obtain

$$\frac{\mathrm{d}B}{\mathrm{d}z} = -N^2Q - 2\pi\int_0^\infty ru\frac{\partial g'}{\partial r}\mathrm{d}r - 2\pi\int_0^\infty g'\frac{\partial}{\partial r}(ru)\mathrm{d}r. \tag{B.34}$$

Using the chain rule, rewrite the above equation as

$$\frac{\mathrm{d}B}{\mathrm{d}z} = -N^2Q - 2\pi\int_0^\infty \frac{\partial}{\partial r}(ru\,g')\mathrm{d}r. \tag{B.35}$$

Since $g'|_\infty = 0$ and $(ru)|_0 = 0$, the buoyancy conservation equation is reduced to

$$\frac{\mathrm{d}B}{\mathrm{d}z} = -N^2Q. \tag{B.36}$$

In case of an unstratified environment, $\frac{\partial \rho_a}{\partial z} = 0$, it follows that

$$\frac{\mathrm{d}B}{\mathrm{d}z} = 0. \tag{B.37}$$

Altogether the three conservation equations are

$$\frac{dQ}{\mathrm{d}z} = 2\pi b\,\alpha w, \quad \frac{\mathrm{d}M}{\mathrm{d}z} = 2\pi \int_0^\infty g' r \mathrm{d}r \quad \text{and} \quad \frac{\mathrm{d}B}{\mathrm{d}z} = 0. \tag{B.38}$$

Plume Top-Hat vs. Gaussian representation

In this section, we describe the two most common representations of plume integral properties and derive the solutions to the three conservation equations using them. The two classical representations of the radial distribution of vertical velocity $w(r)$ are

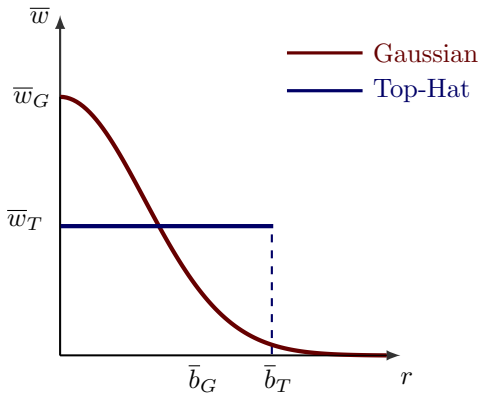

Fig. B.1 A schematic representation of radial velocity distribution under gaussian vs top-hat representations.

a gaussian and top-hat, with the following definitions

$$\overline{w}(r) = \overline{w}_G \exp(-r^2/\bar{b}_G{}^2) \quad \text{for } 0 \le r \le \infty, \tag{B.39a}$$

$$\overline{w}(r) = \begin{cases} \overline{w}_T & 0 \le r \le \bar{b}_T \\ 0 & r > \bar{b}_T, \end{cases} \tag{B.39b}$$

where $\overline{w}_G$ and $\bar{b}_G$ are the centreline vertical velocity and radius under the Gaussian representation, and $\overline{w}_T$ and $\bar{b}_G$ are the centreline vertical velocity and radius under the top-hat representation. Using these definitions, the plume volume flux under the

Gaussian representation $\overline{Q}_G$ is

$$\begin{aligned}\overline{Q}_G &= \int_0^{2\pi}\int_0^{\infty} \overline{w}_G \exp(-r^2/\bar{b}_G{}^2)\, r\mathrm{d}r\mathrm{d}\theta \\ &= 2\pi\overline{w}_G \int_0^{\infty} \frac{1}{2}\exp(-r^2/\bar{b}_G{}^2)\,\mathrm{d}r^2 = \pi\overline{w}_G(-\bar{b}_G^2)\Big[\exp(-r^2/\bar{b}_G{}^2)\Big]\Big]_0^{\infty} = \pi\overline{w}_G\bar{b}_G^2.\end{aligned} \tag{B.40}$$

For the top-hat representation, the mean plume/jet volume flux $\overline{Q}_T$ can be written as

$$\overline{Q}_T = \int_0^{2\pi}\int_0^{\bar{b}_T} \overline{w}_T\, r\mathrm{d}r\mathrm{d}\theta = 2\pi\overline{w}_T \int_0^{\bar{b}_T} \frac{1}{2}\,\mathrm{d}r^2 = \pi\overline{w}_T\bar{b}_T^2. \tag{B.41}$$

In a similar fashion, the mean momentum flux of a plume/jet under the Gaussian representation can be written as

$$\begin{aligned}\overline{M}_G &= \int_0^{2\pi}\int_0^{\infty}\Big[\overline{w}_G \exp(-r^2/\bar{b}_G{}^2)\Big]^2\, r\mathrm{d}r\mathrm{d}\theta \\ &= 2\pi\overline{w}_G^2 \int_0^{\infty} \frac{1}{2}\exp(-2r^2/\bar{b}_G^2)\,\mathrm{d}r^2 = \frac{1}{2}\pi\overline{w}_G^2\bar{b}_G^2,\end{aligned} \tag{B.42}$$

and under the top-hat representation as

$$\overline{M}_T = \int_0^{2\pi}\int_0^{\bar{b}_T} \overline{w}_T^2 r\mathrm{d}r\mathrm{d}\theta = \pi\overline{w}_T^2\bar{b}_T^2. \tag{B.43}$$

Since using either representation, both the volume and momentum fluxes must be the same, i.e. $\overline{Q}_G = \overline{Q}_T$ and $\overline{M}_G = \overline{M}_T$, using the above expressions for the volume and momentum fluxes, we can establish the following relationships between the plume/jet velocity, radius and the entrainment coefficient

$$\overline{w}_G = 2\overline{w}_T, \quad \bar{b}_G = \bar{b}_T/\sqrt{2} \quad \text{and} \quad \alpha_G = \alpha_T/\sqrt{2}. \tag{B.44}$$

Plume conservation equations

Take top-hat representation of properties within the plume

$$Q = 2\pi\int_0^{\infty} w r\mathrm{d}r = \pi b_T{}^2 w_T, \tag{B.45a}$$

$$M = 2\pi\int_0^{\infty} w^2 r\mathrm{d}r = \pi b_T{}^2 w_T{}^2, \tag{B.45b}$$

$$B = 2\pi\int_0^{\infty} w g' r\mathrm{d}r = \pi b_T{}^2 w_T g'_T. \tag{B.45c}$$

In terms of the volume and momentum fluxes, the top-hat variables are

$$w_T = \frac{M}{Q}, \qquad b_T = \frac{Q}{\pi^{1/2} M^{1/2}} \qquad \text{and} \qquad g'_T = \frac{B}{Q}. \tag{B.46}$$

Recalling the plume conservation equations and using the top-hat definitions above, obtain

$$\frac{\mathrm{d}Q}{\mathrm{d}z} = 2\pi b\, \alpha w = 2\pi^{1/2} \alpha_T M^{1/2}. \tag{B.47a}$$

$$\frac{\mathrm{d}M}{\mathrm{d}z} = 2\pi \int_0^\infty g' r \mathrm{d}r = \frac{QB}{M}, \tag{B.47b}$$

$$\frac{\mathrm{d}B}{\mathrm{d}z} = 0. \tag{B.47c}$$

The above equations can be solved directly. Use the following source conditions

$$Q = Q_0, \quad M = M_0, \quad B = B_0, \quad \text{at} \quad z = z_0 = 0. \tag{B.48}$$

Equation B.47c states that the buoyancy flux is conserved and, using the above source conditions, we get that $B = B_0 =$ constant. Equation B.47a may be rearranged for $\mathrm{d}z$ as

$$\mathrm{d}z = \frac{\mathrm{d}Q}{2\pi^{1/2} \alpha_T M^{1/2}}, \tag{B.49}$$

which may be substituted into B.47b to get

$$\frac{\mathrm{d}M}{\mathrm{d}Q/(2\pi^{1/2} \alpha_T M^{1/2})} = \frac{QB_0}{M}. \tag{B.50}$$

Separate variables and intergrate both sides as

$$\int_{M_0}^{M} M^{3/2} \mathrm{d}M = \frac{B_0}{2\pi^{1/2} \alpha_T} \int_{Q_0}^{Q} \mathrm{d}Q, \tag{B.51}$$

to get

$$M^{5/2} - M_0^{5/2} = \frac{5B_0}{8\pi^{1/2} \alpha_T} (Q^2 - Q_0^2). \tag{B.52}$$

We can rearrange the above equation into the following form

$$M^{5/2} = \frac{5B_0}{8\pi^{1/2} \alpha_T} Q^2 + \underbrace{\left(M_0^{5/2} - \frac{5B_0}{8\pi^{1/2} \alpha_T} Q_0^2\right)}_{\text{Source Balance}}. \tag{B.53}$$

In case of a plume with rising from a point source of buoyancy or with zero/ideal balance of source buoyancy and momentum fluxes, the source balance term is zero and the above equations reduces to

$$M^{5/2} = \frac{5B_0}{8\pi^{1/2}\alpha_T}Q^2. \tag{B.54}$$

To proceed, raise the above relation to a power of $1/5$ and substitute into B.47a

$$\frac{\mathrm{d}Q}{\mathrm{d}z} = 2\pi^{1/2}\alpha_T\left(\frac{5B_0}{8\pi\alpha_T}Q^2\right)^{1/5}. \tag{B.55}$$

Integrate and use $Q_0 = 0$ at $z_0 = 0$ to get

$$Q^{3/5} = \left(\frac{6}{5}\pi^{1/2}\alpha_T\right)\left(\frac{5B_0}{8\pi^{1/2}\alpha_T}\right)^{1/5} z \tag{B.56}$$

Rearrange the above equation for Q as

$$Q = \frac{6\alpha_T}{5}\left(\frac{9\alpha_T}{10}\right)^{1/3}\pi^{2/3}B_0^{1/3}z^{5/3} \tag{B.57}$$

To obtain an expression for M, square the above expression for Q, substitute into B.54 and take the both sides of the relation to power $2/5$ to get

$$M = \left(\frac{9\alpha_T}{10}\right)^{2/3}\pi^{1/3}B_0^{2/3}z^{4/3}. \tag{B.58}$$

Recalling the top-hat relations, laid out in B.46, use the solutions for Q and M establish the relations for w_T, b_T and g'_T

$$b_T = \frac{6}{5}\alpha_T z, \tag{B.59a}$$

$$w_T = \frac{5}{6\alpha_T}\left(\frac{9\alpha_T}{10}\right)^{1/3}\pi^{-1/3}B_0^{1/3}z^{-1/3}, \tag{B.59b}$$

$$g'_T = \frac{5}{6\alpha_T}\left(\frac{9\alpha_T}{10}\right)^{-1/3}\pi^{-2/3}B_0^{2/3}z^{-5/3}. \tag{B.59c}$$

Appendix C

Filling-box conductivity test

To verify that the conductive heat losses were insignificant, a series of experiments, measuring the thermal conductivity of the filling-box were performed. To this end, we determined the effective heat transfer coefficient U of the container, which enters the rate of conductive heat loss relation as

$$H_c = U\Delta T A_T, \tag{C.1}$$

where A_T is the total conductive surface area, and $\Delta T = T_H - T_C$ is the temperature difference between the interior and the exterior of the box.

The experiments were performed by filling the box with hot fluid, and then sealing it and placing it inside the environmental tank to cool. An array of four T-type thermocouples with 40 mm vertical spacing was placed inside the box and another two into the ambient fluid to monitor the temperature difference. A magnetic stirrer was inserted into the box to keep the interior well mixed. A schematic representation of the experimental arrangement is shown in figure C.1. From the temperature measurements, we estimated the value of U using Newton's law of cooling, in the form

$$\theta = \exp(-\gamma t), \tag{C.2}$$

where $\theta = \frac{T-T_C}{T_0-T_C}$ is the non-dimensional temperature, $\gamma = \frac{A_T U}{mc_p}$, m is the mass of warm fluid and c_p is the specific heat capacity of water.

Two pairs of experiments, each with hot water levels of $h_T = 0.195\,\mathrm{m}$ and $h_T = 0.245\,\mathrm{m}$, respectively, were performed. Figure C.2 demonstrates the time series of the obtained temperature measurements. On both plots, the lines represent the average readings from thermocouples inside and outside the tank, with respective accuracies

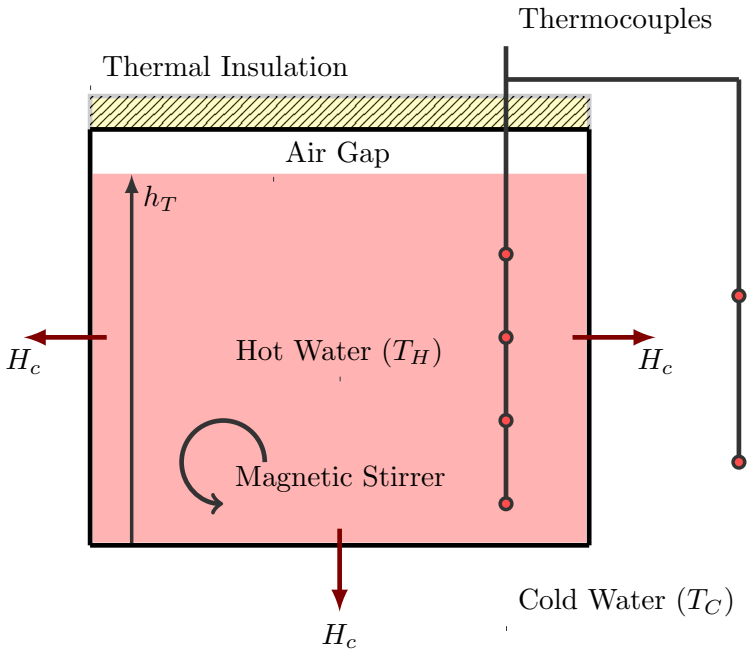

Fig. C.1 A schematic representation of the conductive heat losses experiment.

of ±0.16 °C and ±0.12 °C, estimated as two standard deviations of the time-average fluctuations between thermocouple readings. Such a small error shows that both the interior of the tank and the fluid in the larger environmental tank remained well-mixed throughout the experiment. Figure C.2a demonstrates that, as expected, the temperature difference between the interior and the exterior of the tank decays exponentially. Normalising the temperature differences to get θ and plotting it on a logarithmic y-scale, as shown in figure C.2b, we obtain a linear decay in time, whose gradient represents the value of γ. By performing a linear fit for the obtained measurements of θ and substituting the obtained values of gradient into the relation for γ we found a U-value of 18.5 ± 0.3 W m^{-2} K, where the error represents two standard deviations around the mean of the four obtained results.

Using the experimentally obtained U-value for the filling-box, we estimated conductive heat losses H_c, using equation C.1. In this calculation, we used an appropriate A_T, based on the interface height, and assumed that the bottom layer is well mixed with its temperature equal to the temperature measured at the bottom of the box T_b. The obtained losses were compared to thermal flux into the box from the supply nozzle, defined as

$$H_{in} = \dot{m}_{in} c_p (T_{in} - T_{amb}), \tag{C.3}$$

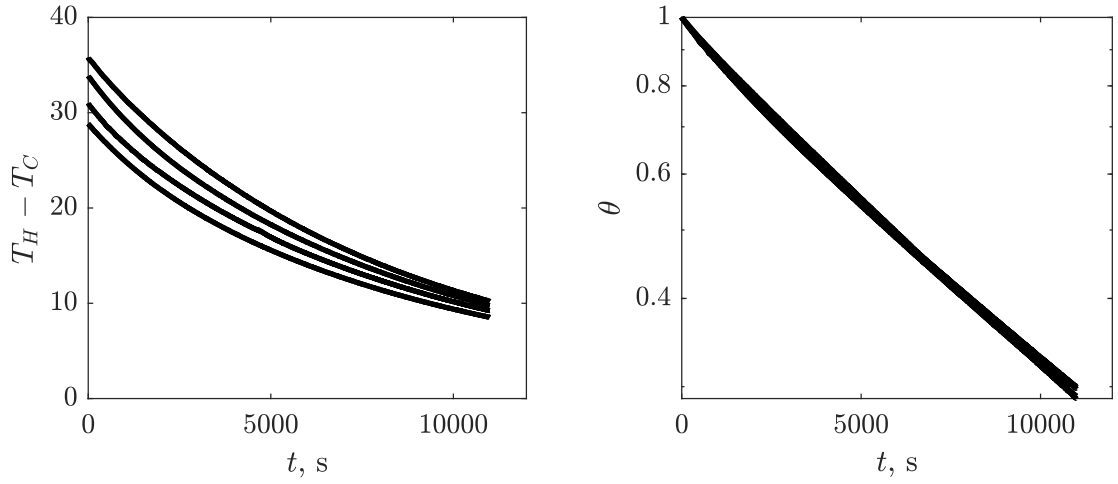

Fig. C.2 Time evolution of (a) temperature differences $T_H - T_C$ between the interior and exterior of the box; (b) normalised temperature differences θ between the interior and exterior of the box. Plot (b) shows good collapse of the obtained measurements from four different experiments.

where $\dot{m}_{in}$ is the mass flux of the supply fluid, and T_{in} and T_{amb} are the temperatures of the supply fluid and the ambient, respectively. In this way, we estimated that the typical thermal losses by conduction through the side tank walls H_{loss} were up to $3.0 \pm 0.3\%$ of the total heat input H_{in}, confirming that the heat losses were insignificant and did not have an impact on the experimental results.

As a further check of the experimental data, we performed the heat budget of each experiment, which, assuming no losses, can be written as

$$Q_0 T_{in} + (Q_v - Q_0) T_{amb} = Q_v T_b. \tag{C.4}$$

We find that the overall heat budget for all filling-box experiments is accurate up to $14.5 \pm 0.4\%$. However, this is extremely sensitive to temperature differences, i.e. a change by 0.3 °C only, comparable to the uncertainty of the temperature measurements, would result in a perfect balance.

Appendix D

Conductivity probe calibrations

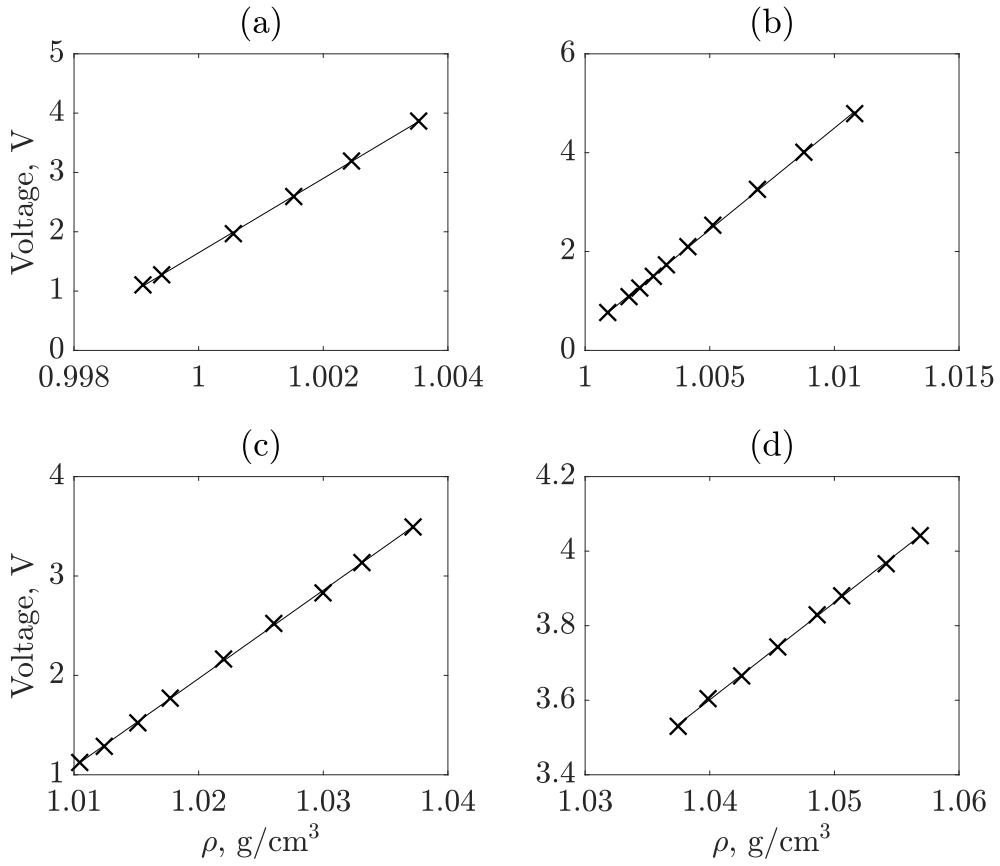

Fig. D.1 Conductivity probe calibrations for four different density ranges.

Appendix E

Shadowgraph flow visualisations

To investigate the cause of thermal stratification of the filling-box in the upper layer, a series of visual experiments were performed using the shadowgraph technique. For details of the technique, the reader is referred to section 3.1.2. The details of the experimental procedure are laid out in section 4.2 and a schematic representation of the experimental setup used to collect the shadowgraph images is shown in figure 4.6. In all experiments, small amount of blue dye was added to the source fluid to aid the visualisation. Images were post-processed to remove the background and thereby increase contrast.

Altogether, we conducted 6 experiments over a range of source buoyancy fluxes and source temperature differences. Representative of all other experiments, we restrict our attention to just two particular cases. For both experiments, the source supply volume flux was $Q_0 = 1.5\ \mathrm{ml\,s^{-1}}$ and the ventilation volume flux was $Q_v = 20.0\ \mathrm{ml\,s^{-1}}$. Performed at the room temperature $T_0 = 21.1\ ^\circ\mathrm{C}$, the source buoyancy flux of the single-diffusive plume was $B_0 = 67.5 \times 10^{-8}\ \mathrm{m^4\,s^3}$. Warmed up to the source discharge temperature of $T_0 = 65.4\ ^\circ\mathrm{C}$, the resulting buoyancy flux of the double-diffusive plume was $B_0 = 43.6 \times 10^{-8}\ \mathrm{m^4\,s^3}$.

Figure E.1 shows the shadowgraph visualisation for two experiments with single- and double-diffusive plumes taken at times $t = 650, 900$ s. For both experiments, a distinct interface is observed, with vigorous convection taking place below it in the mixed bottom layer. Visually, there appears to be no notable dissimilarities between the dynamics occurring along the single-diffusive interface in the case of a salt-only experiment and the diffusive interface in the case of a double-diffusive experiment. Interface fluctuations, triggered by the action of the plume crossing the interface, result in occasional wave-breaking events, with salt (and in the case of double-diffusive experiments heat) being transported from the bottom layer upwards. Although,

Salt Only *Double Diffusive*

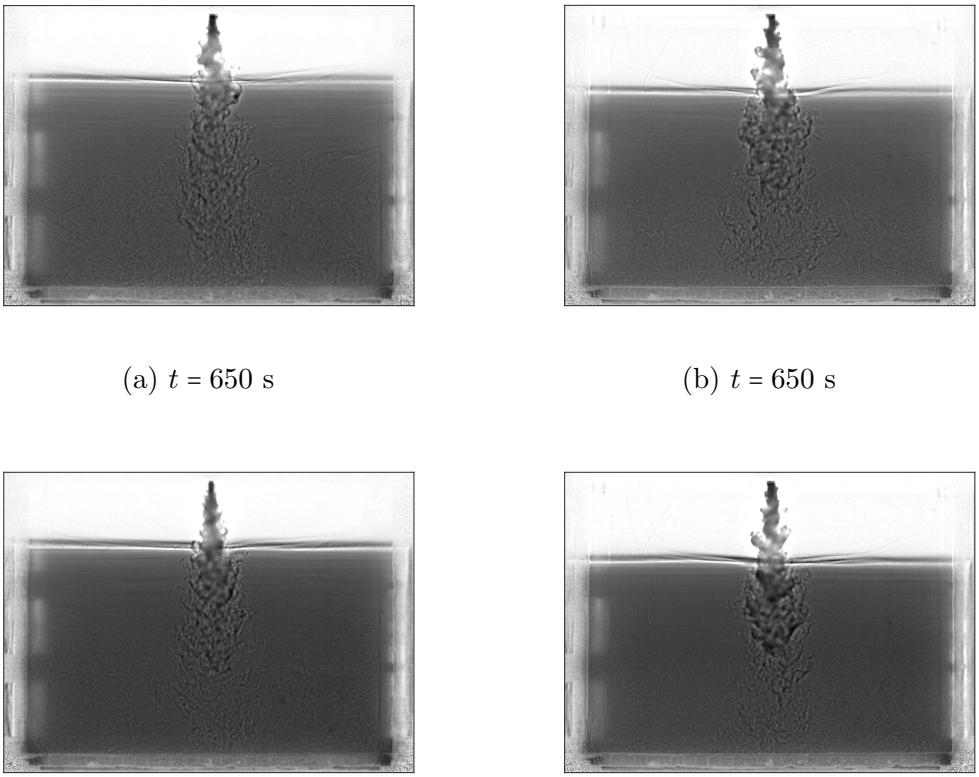

(a) t = 650 s (b) t = 650 s

(c) t = 900 s (d) t = 900 s

Fig. E.1 Examples of images taken using the shadowgraph technique for two experiments: one with a single-diffusive salt only plume and the other with a double-diffusive thermohaline plume (see text for details). In both cases, small amount of blue dye was added to aid the visualisation.

given the tank dimensions and typical temperature differences across the interface, $Ra \sim O(10^7)$ is high enough for turbulent convection to set in, the convective plumes, characteristic for high-Rayleigh-number convection, were visually not observed to form along the interface.

It is therefore likely that the cause of the thermal stratification, observed using thermocouple measurements described in section 4.4.1, is predominantly the result of heat diffusing out of the plume, however, it is hard to state with certainty what are the relative magnitudes of the two transport mechanisms and which of the two dominates. Importantly, given that the temperature difference between the top and bottom layers never exceeded 3.5 °C, the effect of thermal stratification on plume buoyancy was negligible.

Appendix F

Dye attenuation calibration

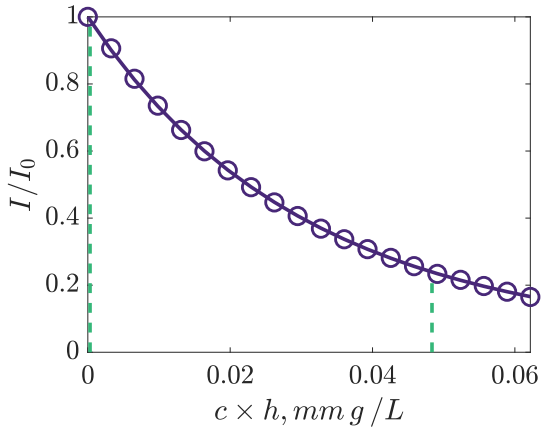

Fig. F.1 Dye attenuation calibration curve for Methylene Blue dye in fresh water. The dashed line represent the upper/lower confidence bounds.

To perform the calibration a tank with a known length L = 30 cm, width W = 25 cm and height H = 15 cm was filled with a known volume of water and partially submerged into the environmental tank. Both tanks were then illuminated from behind using red LED's, and a background image of the tank containing no dye was taken. Known volumes of dye were then added incrementally to the calibration tank and after each addition an image of the tank was taken. This process was repeated until the recorded image became saturated so that the light intensity could not be reliably measured by the camera. A total number of 20 such measurements were made. The background image was then subtracted from all calibration images and the average values of light intensity within the dyed section of the tank were taken. These average values are, in effect, the values of I/I_0 for a given product of dye concentration c and a fixed distance $h = W$ in the y-direction.

Figure F.1 shows that the value of I/I_0 is exponentially decaying for increasing values of $c \times h$. The fitting, shown using the solid line on this figure, follows closely the obtained calibration points and hence was used to determine the coefficient A. Two additional dashed lines present on the figure represent the the upper and lower confidence limits for I/I_0. The upper limit on I/I_0 was set to the value of $I/I_0 = 0.99$, as it is important to ensure that the camera pixels are never saturated (i.e. $I/I_0 \neq 1$). The lower limit, corresponding to a value of $I/I_0 = 0.24$ was estimated as the point at which the gradient of the fitted curve dropped below five time its value near origin. This, somewhat arbitrary cut-off, was based on the diminishing sensitivity of our visual measurements: as $c \times h$ increases, for a given change in $c \times h$ the corresponding change to I/I_0 gets smaller, ultimately leading to insensitive measurements. While the upper limit acted as the point below which measurements should not be made due to near-saturation of the camera, the bottom line was used to decide on the initial concentration of the dye in the source fluid so that the value of $c \times h$ is never in the "insensitive" range beyond the threshold.